Study of Electromagnetic Scattering from Randomly Rough Ocean-Like Surfaces Using Integral-Equation-Based Numerical Technique

Jakov V. Toporkov

Dissertation submitted to the Faculty of the
Virginia Polytechnic Institute and State University
in partial fulfillment of the requirements for the degree of

DOCTOR OF PHILOSOPHY

in

PHYSICS

Royce K. P. Zia, Chairman

Gary S. Brown, Co-Chairman

Brian K. Dennison

David A. DeWolf

Beate Schmittmann

April 28, 1998
Blacksburg, Virginia

Keywords: Electromagnetic scattering, numerical analysis, Pierson-Moskowitz spectrum, rough surfaces, Monte Carlo simulations.

Study of Electromagnetic Scattering from Randomly Rough Ocean-Like Surfaces Using Integral-Equation-Based Numerical Technique

by

Jakov V. Toporkov

Dr. Royce K. P. Zia, Chairman

Physics

Dr. Gary S. Brown, Advisor and Co-chairman

Electrical Engineering

(ABSTRACT)

A numerical study of electromagnetic scattering by one-dimensional perfectly conducting randomly rough surfaces with an ocean-like Pierson-Moskowitz spectrum is presented. Simulations are based on solving the Magnetic Field Integral Equation (MFIE) using the numerical technique called the Method of Ordered Multiple Interactions (MOMI). The study focuses on the application and validation of this integral equation-based technique to scattering at low grazing angles and considers other aspects of numerical simulations crucial to obtaining correct results in the demanding low grazing angle regime.

It was found that when the MFIE propagator matrix is used with zeros on its diagonal (as has often been the practice) the results appear to show an unexpected sensitivity to the sampling interval. This sensitivity is especially pronounced in the case of horizontal polarization and at low grazing angles. We show – both numerically and analytically – that the problem lies not with the particular numerical technique used (MOMI) but rather with how the MFIE is discretized. It is demonstrated that the inclusion of so-called "curvature terms" (terms that arise from a correct discretization procedure and are proportional to the second surface derivative) in the diagonal of the propagator matrix eliminates the problem completely. A criterion for the choice of the sampling interval used in discretizing the MFIE based on both electromagnetic wavelength and the surface spectral cutoff is established. The influence of the surface spectral cutoff value on the

results of scattering simulations is investigated and a recommendation for the choice of this spectral cutoff for numerical simulation purposes is developed.

Also studied is the applicability of the tapered incident field at low grazing incidence angles. It is found that when a Gaussian-like taper with fixed beam waist is used there is a characteristic pattern (anomalous jump) in the calculated average backscattered cross section at incidence angles close to grazing that indicates a failure of this approximate (non-Maxwellian) taper. This effect is very pronounced for the horizontal polarization and is not observed for vertical polarization and the differences are explained. Some distinctive features associated with the taper failure are visible in the surface current (solution to the MFIE) as well. Based on these findings we are able to refine one of the previously proposed criteria that relate the taper waist to the angle of incidence and demonstrate its robustness.

Acknowledgements

I am deeply indebted to many people who shared with me their knowledge, expertise and time, provided advice, encouragement and friendship.

My deepest thanks and gratitude go to my advisor, Prof. Gary S. Brown. These past three and a half years of working under his guidance were a truly invaluable and rewarding experience. Thank you Dr. Brown, for the advice and support, for the interest and concern that you take in my career and in my life.

I am extremely grateful to Prof. Royce K. P. Zia who served as a Chairman of my Committee and whose care and concern I constantly felt. The discussions that we had were always very beneficial and provided me with new insights and ideas. Also, his class on the advanced statistical and quantum mechanics that I was very fortunate to attend in 1994-95, was a profound and memorable experience.

I would also like to express my special thanks to Prof. Beate Schmittmann for her advice, readiness to help, kindness and the time she gave to serve on my Committee.

Thanks are due to other members of my Committee. I would like to express my gratitude and appreciation to Prof. David A. DeWolf who has always been willing to give his advice and help, and Prof. Brian K. Dennison who agreed to serve on the Committee on a very short notice. I am also thankful to Prof. Guy Indebetouw who devotedly served on the Committee through all these years but was not able to continue because of a research leave. His advice, encouragement and kindness are greatly appreciated.

I would also like to thank Prof. Warren L. Stutzman under whose supervision I got a first exposure to research here at Virginia Tech in the summer of 1994. Then and later, in his classes and during conversations, I learned a lot.

My thanks would not be complete if I did not mention Chris Thomas and an immense assistance she provides to graduate students. She is an outstanding secretary and a wonderful person.

I also wish to thank the Office of Naval Research (Remote Sensing Division) and the Army Research Office (Electronics Division) for the support they provided for this research.

Through all these years, I was very fortunate to be a part of the ElectroMagnetic Interactions Laboratory. Its unique climate of cooperation and support provided a perfect environment for both research and occasional relaxation. I would like to thank Dr. Ra'id Awadallah, Rob Adams and Brad Davis for being wonderful co-workers and friends. My thanks and appreciation also go to Bryan Browe, Albert Garcia and Greta Soechting. I would like to specially acknowledge Dr. David Kapp and Dr. Roger Marchand, two former members of the EMIL, interaction and discussions with whom continue to be of the most help.

I am lucky to have many friends, both near and far away. It would be impossible to mention all of them here, but without their moral support and standing by my side, accomplishing this work would be difficult if not impossible. However, I would like to express my special thanks and gratitude to Valeriy Marfitsin and his wife Tatyana for their lasting friendship and help in time of need. It was their advice and encouragement that helped me to make many important decisions in my life.

And foremost, I would like to thank my parents, Nadezhda and Vladimir Toporkov, who recognized my interest in physics, mathematics and engineering early in life and did everything possible to gently encourage it. You have set me on a long and exciting journey on which I have just reached yet another milestone. Thank you for everything. To you, I dedicate this work.

Contents

List of Figures

List of Tables

Chapter 1

Introduction

Studies of wave scattering by rough surfaces date back to the 19th century and the pioneering works of Rayleigh who considered scattering of sound waves by a sinusoidal surface [Rayleigh, 1896]. In the mid-20th, century the inventions of radar and underwater sonar renewed the interest in this problem, with the emphasis being put on the irregular surfaces. Since then, fueled by advancements in radar technology and expanded applications, interest in the problem of rough surface scattering has been ever-growing. Depending on the type and the purpose of a radar system, surface scattering may either constitute an unwanted "clutter" (target-detection radars) or be a source of useful information (remote sensing systems). In either case, a study of rough surface scattering (i.e. establishing the relationship between the properties of the surface and the properties of the scattered signal) is necessary to either minimize the impact of the surface "clutter" on the system performance or enhance the extraction of information about the surface features and related environmental parameters.

Numerical simulations emerged as a tool in studies of surface scattering as early as 1970s, e.g. [Lentz, 1974]. With the introduction of increasingly powerful computers and the invention of advanced numerical techniques, numerical simulation is quickly becoming one of the principal tools in this area of study. Not only can numerical simulations confirm be used to confirm theoretical findings, they also often lead the way to new theory or provide the results for the problems where no closed-form analytical answers are available or feasible.

One of the problems that has to rely extensively on numerical simulations is surface backscattering at low grazing angles (LGA). This problem is of interest in many practical radar applications, one of the important examples being radar systems operating on naval ships and designed to provide protection against low cross section sea-skimming anti-ship missiles. However, analytical studies of surface scattering at low grazing angles

have so far met with little success. Identifying the physical phenomena (multiple interactions) that need to be accounted for and the quite complex mathematical description hinder the progress in this direction. Approximations that are usually made in analytical approaches to make results tractable lead to significant errors for this demanding LGA geometry.

Numerical studies of LGA scattering also prove to be a challenging problem. As the direction of incidence approaches horizontal, surfaces of increasingly large size are required for simulations (the reasons behind this requirement will be discussed in detail in in Chapter 5). Larger surfaces mean, in turn, larger matrix sizes and higher computational and storage expenses. Until recently, these considerations forced researchers to consider only 2-dimensional problems with incident angles far away from grazing where the requirements on the surface length are far less prohibitive. Only recently have advances in computer technology and, even more importantly, the development of new numerical techniques began to remove these limitations. In particular, a new integral equation-based technique called the Method of Ordered Multiple Interactions [Kapp and Brown, 1996] reduced the computational and storage requirements dramatically thus making studies of LGA scattering, though still restricted to a 2-D space, conceivable. Another remarkable feature of this technique is that since it inherently accounts for multiple scattering, its performance does not deteriorate at low grazing angles where multiple scattering is significant. The MOMI technique is described in Chapter 2; it was used extensively to obtain the results reported in this work.

Another trend in surface scattering research in general and numerical scattering studies in particular is to use surfaces that more closely resemble those that appear in the real-world problems. The interest is increasingly shifting from simplistic surface models (e.g. surfaces with Gaussian spectra) that were used due to the analytical convenience to obtain closed-form results and to test these analytical results numerically, to models that bear more resemblance to natural surfaces. An important class of surfaces that are understandably of large practical interest, are ocean-like surfaces. This study focuses on such surfaces characterized by the Pierson-Moskowitz (P-M) spectrum; details on the description of randomly rough surfaces and the definition of the P-M spectrum are given in Chapters 3 and 4.

In running LGA scattering simulations with ocean-like surfaces we found that the results may be sensitive to quite a number of factors and parameters many of them not studied and some not even anticipated previously. Therefore, the purpose of this study was to investigate the problems that may adversely affect or completely invalidate the results of scattering simulations and formulate the solutions and recommendations to allow future researchers to apply numerical simulation techniques with confidence. The following issues were found to be of critical importance for LGA scattering simulations and were investigated.

We examine the discretization of the integral equation that is usually employed for the surface scattering problem (the Magnetic Field Integral Equation, or MFIE). Such a discretization should be performed before this governing equation can be solved numerically; unless done correctly, it can have an adverse impact on the precision of the results no matter what particular numerical technique is used to solve the discretized MFIE. It is shown that certain terms that were previously regarded as additional optional corrections must appear in the discretized kernel (propagator matrix). The results of simulations confirm that failure to include these terms leads to distorted values of the calculated scattered field and this effect is especially pronounced at low grazing angles and horizontal polarization. The choice of the sampling interval for the MFIE discretization is proposed based on the electromagnetic wavelength and the spectral cutoff of the ocean-like randomly rough surfaces. Such a cutoff occurs for natural ocean surfaces and is due to certain physical mechanisms that may vary depending on circumstances, but for numerical purposes a much lower, artificial cutoff is often introduced. We study the sensitivity of the scattering simulation results to the value of this cutoff and develop recommendations for its choice.

Another factor that affects the precision and validity of numerical simulation results is the form of the incident field used in the simulations. Usually numerical simulations use surfaces of finite length and tapering of incident field towards the surface ends is necessary. Such tapering, in particular, prevents distortions in calculated average scattering cross sections that are associated with a finite surface size (usually referred to as “edge effects”) and makes the results relatively insensitive to this parameter. The most commonly used form of the incident field is a plane wave with a Gaussian-like envelope.

However, such a field satisfies Maxwell equations only approximately and this can also be a factor in the scattering calculations. It has been previously noted ([Ngo and Rino, 1994], [Kapp, 1995]) that as the incident angle approaches grazing, the waist of the tapered incident field should increase. Consequently, criteria for the beam waist size as function of the incident angle have been proposed for both a pure Gaussian tapering function and more detailed, but still approximate, taper proposed by Thorsos [Thorsos, 1988]. However, these criteria, being somewhat heuristic, involve arbitrary and ill-defined constants which limit their usefulness. Also, their robustness has never been rigorously checked. In our simulation results we observed distinctive anomalous patterns, both in cross section and surface current (solution to the MFIE) that we were able to identify with the failure of the approximate Gaussian-like taper. Based on this finding we refine one of the above-mentioned "beam waist - angle of incidence" criteria and demonstrate its reliability at LGA for the case of the P-M surfaces. Various related questions such as sensitivity of the results to taper levels at the surface edges and use of a tapered incident field that satisfies the wave equation exactly are considered as well.

Our study is restricted to the 2-D case. Full-scale 3-D numerical simulations of rough surface scattering still presents a challenging problem although attempts are being made into this area as well, e.g. [Pak *et al,* 1995]. However, no extensive 3-D numerical simulations are yet conceivable, especially in the LGA mode where surfaces have to be large. This is in part because of the restrictions posed by a current computer technology (we used a state-of-the-art multiprocessor SGI "Power Challenge" computer), but more importantly, the absence of such efficient and reliable numerical techniques like MOMI for the 3-D case. However, 2-D simulations can be used as an important guideline giving an insight into the full 3-D scattering problem; under certain circumstances the 2-D results can be related to their 3-D counterparts [Thorsos, 1990]. The factors affecting the results in 2-D simulations such as sampling interval and tapering of the incident field will play a role in 3-D situation as well. We expect that most of our findings and methods of analysis will remain valid and useful for the 3-D simulations as well.

The dissertation is organized as follows. Chapter 2 provides the "electromagnetic background" of the scattering simulations reported in this work. It reviews the derivation of the MFIE for the surface scattering problem and discusses how the quantities of

interest such as the scattered field and normalized radar cross section can be obtained once the MFIE is solved. This chapter also discusses ways to solve the MFIE numerically and gives an overview of the numerical technique used throughout this study – the MOMI.

Chapter 3 considers another issue of importance to the Monte Carlo simulations: the statistical description and generation of randomly rough surfaces. There we give a detailed development of the so-called spectral method of random surface generation. It is shown that this method is very convenient and efficient in generating realizations of spatially homogeneous surfaces with the Gaussian statistics and a given spectrum or correlation function; it allows easy generation of higher surface derivatives as well.

Results of scattering simulations with the ocean-like Pierson-Moskowitz surfaces that show discretization-related problems are presented and discussed in Chapter 4. They are followed by the examination of the procedure of discretizing the MFIE. This analysis confirms the numerical finding that certain terms proportional to the second surface derivative ("curvature terms") previously regarded as an additional correction must appear on the diagonal of the propagator matrix. The choice of the sampling interval and effects of the surface spectral cutoff on the calculated cross section are also considered in this chapter.

Chapter 5 focuses on the question of using the tapered incident field in LGA simulations. It reviews Gaussian-like tapers most often used in numerical scattering simulations and "beam waist – angle of incidence" criteria that have been proposed for such tapers. Based on simulation results that consistently show certain anomalous pattern in the backscattered cross section, one of these criteria is refined and its robustness is demonstrated. It is shown that the failure of the Gaussian-like taper due to insufficient waist results in the distinctive patterns in the calculated surface current (solution to the MFIE) as well. Simulation results demonstrating the sensitivity of the average cross section at LGA to the taper levels at surface ends are also presented.

The summary of the results and findings is given in Chapter 6 of this dissertation.

In several chapters, it was deemed appropriate to arrange some of the supportive material in form of appendices. These appendices appear at the end of the relevant chapter. The background and related work is usually reviewed and referenced in chapter

bodies as becomes necessary through the course discussion; the list of the references completes this dissertation.

Chapter 2

Development and Solution of the Integral Equations for Rough Surface Scattering

This chapter establishes the "electromagnetic background" for the results reported in Chapters 4 and 5. Here we focus on the development of the integral equation method for solving rough surface scattering problems, discuss the numerical solution to the magnetic field integral equation (MFIE), and consider the associated question of calculating the scattered field and normalized radar cross section (NRCS). We limit our discussion to the two-dimensional geometry and perfectly conducting surfaces.

First, we outline the derivation of a useful integral formula, i.e. the Helmholtz integral formula, and then use it to develop the integral equations for the electromagnetic field or its derivative on the surface. We then briefly discuss possible numerical techniques to solve the MFIE and give a detailed description of the method of ordered multiple interactions (MOMI) – a recently developed, very robust, and efficient solution technique that will be exclusively used in our simulations. Finally, the task of calculating the scattered field from the solution to the MFIE is addressed and the NRCS is defined.

All fields, currents and charge densities are assumed to be time-harmonic, with the time dependence $e^{j\omega t}$ suppressed.

2.1 Scattering from an Irregular Boundary: Two-Dimensional Case

2.1.1 Helmholtz Integral Formula

In deriving the integral equations for surface scattering we will rely on the Helmholtz integral formula e.g. [Ogilvy, 1991, p. 40]. It can be derived following the steps outlined below [W. C. Chew, 1995].

Consider a scalar field $\psi(\vec{r})$ in the region V_1 bounded by the surface S and the infinitely remote surface S_∞, as shown in Fig. 2-1. This region can also contain some sources with the charge density $Q(\vec{r})$. The equation that governs ψ in this region is

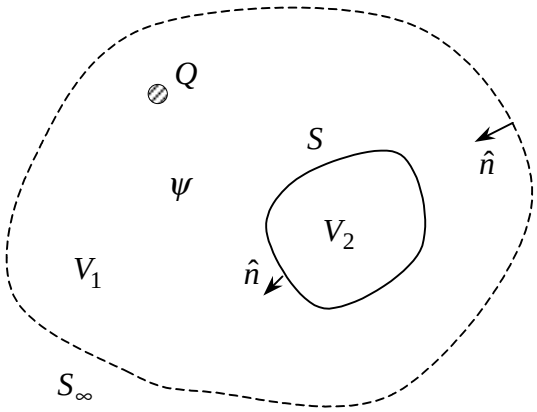

Figure 2-1. Geometry for the derivation of the Helmholtz integral formula.

$$(\nabla^2 + k^2)\psi(\vec{r}) = Q(\vec{r}) \tag{2.1}$$

where k is the wavenumber in the region V_1. For the region V_1, one can also define the Green's function $G(\vec{r},\vec{r}')$ that satisfies the equation

$$(\nabla^2 + k^2)G(\vec{r},\vec{r}') = -\delta(\vec{r}-\vec{r}') \tag{2.2}$$

This statement implicitly assumes that the propagation properties in the part of the region V_1 occupied by the sources Q are no different from the rest of this region. If this is not the case, a more careful treatment may be required, but we will continue with this assumption.

Let us now multiply equation (2.1) by $G(\vec{r},\vec{r}')$, equation (2.2) by $\psi(\vec{r})$, subtract them and integrate the result over the region V_1. This yields

$$\int_{V_1} dV\left\{G(\vec{r},\vec{r}')\nabla^2\psi(\vec{r}) - \psi(\vec{r})\nabla^2 G(\vec{r},\vec{r}')\right\} = \int_{V_1} dV\, G(\vec{r},\vec{r}')Q(\vec{r}) + \psi(\vec{r}'), \quad \vec{r}' \in V_1 \tag{2.3}$$

Applying the Green's theorem to the left-hand side of (2.3) and identifying the volume integral on the right as the incident field (the field that would be present in the region V_1 in the absence of the scatterer V_2):

$$\psi^i(\vec{r}') = -\int_{V_1} dV G(\vec{r},\vec{r}')Q(\vec{r}), \tag{2.4}$$

we obtain

$$-\int_{S+S_\infty} dS\,\hat{n}\cdot\{G(\vec{r},\vec{r}\,')\nabla\psi(\vec{r})-\psi(\vec{r})\nabla G(\vec{r},\vec{r}\,')\}=-\psi^i(\vec{r}\,')+\psi(\vec{r}\,'),\quad \vec{r}\,'\in V_1 \qquad (2.5)$$

The minus sign on the left-hand side appears because of the chosen direction of the normal $\hat{n}$. If we further require that the fields and the Green's function satisfy the radiation condition [Ishimaru, 1991, p. 124], the contribution over the S_∞ can be neglected. Thus, we finally get

$$\psi(\vec{r}\,')=\psi^i(\vec{r}\,')+\int_S dS\left\{\psi(\vec{r})\frac{\partial G(\vec{r},\vec{r}\,')}{\partial n}-G(\vec{r},\vec{r}\,')\frac{\partial\psi(\vec{r})}{\partial n}\right\},\quad \vec{r}\,'\in V_1, \qquad (2.6)$$

which is the Helmholtz integral formula. This equation is valid for three (3-D) and two (2-D) dimensional geometries.

2.1.2 Integral Equations for Scattering from 2-D, Rough, Perfectly Conducting Surfaces

We now use the Helmholtz integral formula to obtain the integral equations for rough surface scattering. We consider a 2-D case and assume the surface to be a perfect electric conductor (PEC) with the free space above it. The geometry in Fig. 2-1 that we considered when deriving the Helmholtz formula can be modified for the rough surface scattering problem; it is shown in Fig. 2-2. Here, the effect of the sources Q has already

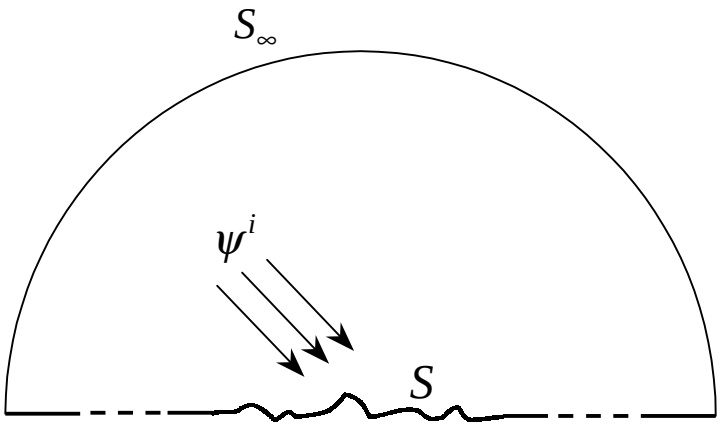

Figure 2-2. Application of the Helmholtz integral formula to the rough surface scattering.

been replaced by the incident field ψ^i that they produce in free space.

In the 2-D case there are no depolarization effects, so the problem becomes essentially a scalar one and the Helmholtz integral formula (2.6) developed for a scalar field can be applied. The two polarization cases are illustrated in Fig. 2-3. In this Figure, a Cartesian coordinate system is introduced, with the x-axis in the mean surface plane and the z-axis pointing upwards. In the 2-D case, there is no variation along the *y*-axis.

In each polarization case, we will work with the field that is directed parallel to

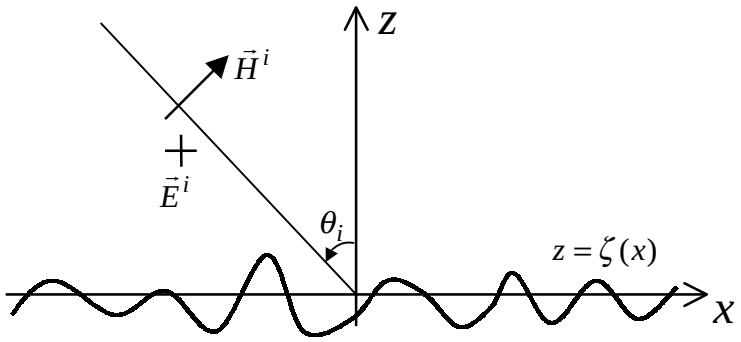

Horizontal polarization (TE case)

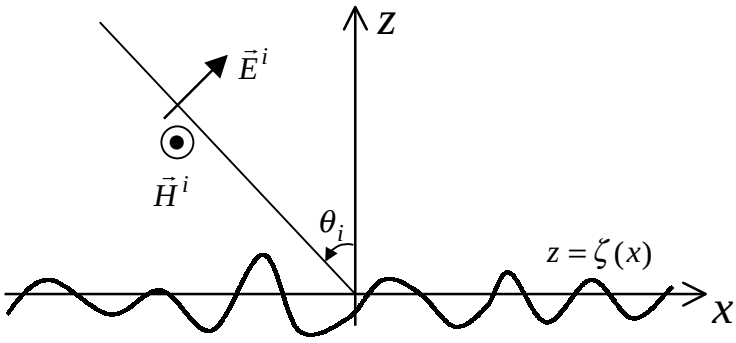

Vertical polarization (TM case)

Figure 2-3. Polarization cases in 2-D situation.

the y-axis; so, in the TE case we choose $\psi \equiv E$. Further, since the surface is assumed to

be a perfect conductor, we require that on the surface $E = 0$, i.e. the field satisfies the Dirichlet boundary condition. Then the Helmholtz formula (2.6) becomes

$$E(\vec{r}) = E^i(\vec{r}) - \int_S dS' G(\vec{r}', \vec{r}) \frac{\partial E(\vec{r}')}{\partial n'} \tag{2.7}$$

In (2.7) we have switched (as compared to (2.6)) $\vec{r}'$ and $\vec{r}$ so that the integration is performed over the primed variables. G is a 2-D free-space Green's function (Green's function of the infinite line source):

$$G(\vec{r}', \vec{r}) = \frac{1}{4j} H_0^{(2)}(k|\vec{r} - \vec{r}'|^2) \tag{2.8}$$

where $H_0^{(2)}$ is the zeroth order Hankel function of the second kind.

For the TM case, we choose $\psi \equiv H$. Now for the PEC surface we have the Neumann boundary condition and the Helmholtz formula (2.6) will yield

$$H(\vec{r}) = H^i(\vec{r}) + \int_S dS' \frac{\partial G(\vec{r}', \vec{r})}{\partial n'} H(\vec{r}') \tag{2.9}$$

In (2.7) and (2.9) the observation point $\vec{r}$ is located in the upper half-space (cf. Fig. 2-2) while the source points $\vec{r}'$ lie on the surface. To develop the integral equation for the surface scattering we bring the observation point to the surface. Since the Green's function in (2.8) and its derivative have a singularity at $\vec{r} = \vec{r}'$, some caution should be exercised.

If we move the observation point to the surface in (2.7) and then use the Dirichlet boundary condition, we obtain

$$E^i(\vec{r}) = \int_S dS' G(\vec{r}', \vec{r}) \frac{\partial E(\vec{r}')}{\partial n'} \ , \tag{2.10}$$

which is an integral equation of the first kind, or the electric field integral equation (EFIE). Note that its kernel has an integrable singularity (sometimes called a "weak singularity" [Thorsos, 1988]) at $\vec{r} = \vec{r}'$. This property can be used when solving the EFIE numerically, as is done, for example, in the banded matrix iterative approach (BMIA) [Donohue *et al*, 1997].

Now we consider (2.9) and again move the observation point $\vec{r}$ to the surface. This time the singularity in the derivative of the Green's function can be removed [e.g. Morita *et al*, 1990] resulting in

$$H(\vec{r}) = 2H^i(\vec{r}) + 2\int_S dS' \frac{\partial G(\vec{r}', \vec{r})}{\partial n'} H(\vec{r}') \ , \tag{2.11}$$

which is the integral equation of the second kind, or the magnetic field integral equation (MFIE).

A similar integral equation of the second kind can be developed in the TE case for the normal derivative of the electric field. By letting the observation point in (2.7) approach the surface and taking the normal derivative, one obtains (cf. for example, [Thorsos, 1988])

$$\frac{\partial E(\vec{r})}{\partial n} = 2\frac{\partial E^i(\vec{r})}{\partial n} - 2\int_S dS' \frac{\partial G(\vec{r}', \vec{r})}{\partial n} \frac{\partial E(\vec{r}')}{\partial n'} \tag{2.12}$$

Since the derivations of (2.11) and (2.12) involve the removal of a singularity, the principal value of the integral should be taken in those expressions. However, in the 2-D case the integrals with such kernels always converge and taking a Cauchy principal value is not necessary [Morita *et al*, 1990, pp. 131-134]. More details on the limiting procedure used to obtain (2.11) and (2.12) can be found in the same reference.

In our studies of the scattering from 1-D, PEC, randomly rough surfaces we will rely solely on the MFIE formulation, both for the TM and the TE polarizations, because of the very efficient solution technique available for the MFIE. This technique, called the method of ordered multiple interactions (MOMI) is described below.

2.2 MFIE for Two-Dimensional Scattering Problem and the MOMI

2.2.1 Details on the MFIE Method for the TE and TM Cases

As was mentioned earlier in Section 2.1.2 and is depicted in Fig. 2-3, it is convenient to introduce a Cartesian coordinate system and choose the horizontal x axis in the mean surface plane. The surface height above the mean surface plane is given by a function $z = \zeta(x)$. For such a PEC surface both (2.11) and (2.12) can be rewritten in the following generic form:

$$J(x) = J^i(x) + \int_X P(x,x')J(x')dx' \tag{2.13}$$

In (2.13) $J(x)$ is the surface current to be determined, $P(x,x')$ is a kernel or propagator, and $J^i(x)$ is a forcing term due to the incident field. The domain over which the integration is performed and where all functions are defined should in principle be infinite. However, if some taper for the incident field is assumed, in practice one can usually choose it to be finite.

Comparing (2.13) to the earlier established equations (2.11) and (2.12) we make the following identifications. For vertical, or TM, polarization (H^i tangential to the surface, cf. Fig 2-3) the quantities involved in (2.13) are:

$$J^i(x) = 2H^i(x,z)\Big|_{z=\zeta(x)} \tag{2.14a}$$

$$P(x,x') \equiv 2\frac{\partial G(x,x')}{\partial n'}\sqrt{1+\zeta_x^2(x')} \tag{2.14b}$$

For horizontal, or TE, polarization (E^i tangential to the surface) we have the following:

$$J^i(x) = 2\frac{\partial E^i(x,z)}{\partial n}\Big|_{z=\zeta(x)} \tag{2.15a}$$

$$P(x,x') \equiv -2\frac{\partial G(x,x')}{\partial n}\sqrt{1+\zeta_x^2(x')} \tag{2.15b}$$

The factor $\sqrt{1+\zeta_x^2(x')}$ included in the propagator results from converting an integration along the surface to integration along the mean surface plane. In the case of vertical polarization the current $J(x)$ is actually the total magnetic field on the surface, while in the case of horizontal polarization $J(x)$ is the normal derivative of the total electric field on the surface. The forcing term $J^i(x)$ is often referred to as the "Kirchhoff current".

The normal derivatives of the Green's function are (also cf. [Kapp, 1995] and [Kapp and Brown, 1996]):

$$\begin{aligned}\frac{\partial G(x,x')}{\partial n'} = \frac{k}{4j}\frac{-\zeta_x(x')(x-x')+\zeta(x)-\zeta(x')}{\sqrt{1+\zeta_x^2(x')}\sqrt{(x-x')^2+(\zeta(x)-\zeta(x'))^2}}\times \\ \times H_1^{(2)}(k\sqrt{(x-x')^2+(\zeta(x)-\zeta(x'))^2}),\end{aligned} \tag{2.16}$$

$$\frac{\partial G(x,x')}{\partial n} = -\frac{k}{4j}\frac{-\zeta_x(x)(x-x')+\zeta(x)-\zeta(x')}{\sqrt{1+\zeta_x^2(x)}\sqrt{(x-x')^2+(\zeta(x)-\zeta(x'))^2}}\times$$
$$\times H_1^{(2)}(k\sqrt{(x-x')^2+(\zeta(x)-\zeta(x'))^2}\ ) \tag{2.17}$$

where $H_1^{(2)}$ is the first-order Hankel function of the second kind and $k = \omega / c$ is a free space electromagnetic wavenumber.

2.2.2 Numerical Solution of the MFIE

In the case of an arbitrarily rough surface no exact analytical solution of the MFIE (2.13) is available, but for each given surface and incident field it can be solved numerically. To do this, the equation (2.13) should be discretized, i.e. put in the vector-matrix form:

$$\boldsymbol{J} = \boldsymbol{J}^i + \boldsymbol{P}\boldsymbol{J} \tag{2.18}$$

In (2.18) $\boldsymbol{J}$ and $\boldsymbol{J}^i$ are vectors and $\boldsymbol{P}$ is a square propagator matrix. For rough surfaces it is common, e.g. [Kapp and Brown, 1996], [Thorsos, 1988], to discretize the MFIE by taking values of the surface height, current and propagator at discrete points $\{x_m\}$ which form a uniform grid with some spacing Δx. That is, the *m*-th element of the surface current vector, the *m*-th element of the Kirchhoff current vector and the (*m*,*n*)-th element of the propagator matrix are respectively :

$$J_m = J(x_m), \quad J_m^i = J^i(x_m) \quad \text{and} \quad P_{mn} = P(x_m, x_n)\Delta x \tag{2.19}$$

The diagonal terms ($m = n$) of the propagator matrix may require separate treatment, as will be described and studied in Chapter 4. Following the discretization, a number of numerical techniques can be applied.

The traditional Method of Moments (MoM) solution to (2.18) would be

$$\boldsymbol{J} = (\boldsymbol{I} - \boldsymbol{P})^{-1}\boldsymbol{J}^i \tag{2.20}$$

Due to the identity matrix which is the result of the extraction of a self-term, the $(\boldsymbol{I} - \boldsymbol{P})$ matrix is likely to be well-conditioned (of course, a number of factors like surface type and sampling interval size can influence this property) but it is not guaranteed. Instead of

resorting to the direct matrix inversion, it is usually more practical to solve a set of linear equations $(\boldsymbol{I}-\boldsymbol{P})\boldsymbol{J}=\boldsymbol{J}^i$.

Another approach is the iterative solution of (2.18). In fact, the MFIE (2.13) or its discretized version (2.18) readily lends itself to iteration in a straightforward manner:

$$\boldsymbol{J}^{(0)}=\boldsymbol{J}^i$$

$$\boldsymbol{J}^{(1)}=\boldsymbol{J}^i+\boldsymbol{P}\boldsymbol{J}^{(0)}=\boldsymbol{J}^i+\boldsymbol{P}\boldsymbol{J}^i$$

$$\boldsymbol{J}^{(2)}=\boldsymbol{J}^i+\boldsymbol{P}\boldsymbol{J}^{(1)}=\boldsymbol{J}^i+\boldsymbol{P}\boldsymbol{J}^i+\boldsymbol{P}(\boldsymbol{P}\boldsymbol{J}^i)$$

$$\cdots$$

or

$$\boldsymbol{J}=\boldsymbol{J}^i+\boldsymbol{P}\boldsymbol{J}^i+\boldsymbol{P}^2\boldsymbol{J}^i+\ldots \qquad (2.21)$$

This formal solution to the MFIE is called the "Neumann series". It turns out that for rough surface scattering problems a significant number of terms in (2.21) may be required to achieve a suitable precision, especially if there is substantial multiple scattering present on the surface. In fact there is no guarantee that the series in (2.21) will always converge, and indeed it sometimes fails to do so [Wingham and Devayya, 1992].

A Neumann series is not the only iterative scheme possible; other techniques can be developed by reformulating (2.18) or (2.13). One such technique is the method of ordered multiple interactions (MOMI) [Kapp, 1995], [Kapp and Brown, 1996] described below. A remarkable feature of this technique is that for rough surface scattering problems it demonstrates extremely rapid convergence. This property stems from the fact that the mathematical formulation follows the physics of the scattering processes taking place on the surface: each next iteration picks up the next order of multiple scattering [Kapp and Brown, 1996]. Also, MOMI eliminates the necessity to store the whole propagator matrix, which significantly relieves computer memory requirements. A similar technique called "forward-backward" has been independently proposed by Holliday, DeRaad and St-Cyr [Holliday *et al*, 1996]

2.2.3 Overview of the MOMI

In MOMI, the propagator matrix $\boldsymbol{P}$ is split in the lower and upper triangular matrices $\boldsymbol{L}$ and $\boldsymbol{U}$:

$$\boldsymbol{P} = \boldsymbol{L} + \boldsymbol{U} \tag{2.22}$$

The lower triangular matrix $\boldsymbol{L}$ represents the contributions of all surface points located to the left of the observation point and the upper triangular matrix $\boldsymbol{U}$ corresponds to the contributions of all surface points to the right. By going through the following consecutive term rearrangements in (2.18) with (2.22)

$$[\boldsymbol{I} - (\boldsymbol{L} + \boldsymbol{U})]\boldsymbol{J} = \boldsymbol{J}^i,$$

$$[(\boldsymbol{I} - \boldsymbol{L})(\boldsymbol{I} - \boldsymbol{U}) - \boldsymbol{L}\boldsymbol{U}]\boldsymbol{J} = \boldsymbol{J}^i,$$

$$(\boldsymbol{I} - \boldsymbol{L})(\boldsymbol{I} - \boldsymbol{U})\boldsymbol{J} = \boldsymbol{J}^i + \boldsymbol{L}\boldsymbol{U}\boldsymbol{J}$$

and multiplying the last result by $(\boldsymbol{I} - \boldsymbol{U})^{-1}(\boldsymbol{I} - \boldsymbol{L})^{-1}$ one obtains

$$\boldsymbol{J} = (\boldsymbol{I} - \boldsymbol{U})^{-1}(\boldsymbol{I} - \boldsymbol{L})^{-1}\boldsymbol{J}^i + (\boldsymbol{I} - \boldsymbol{U})^{-1}(\boldsymbol{I} - \boldsymbol{L})^{-1}\boldsymbol{L}\boldsymbol{U}\,\boldsymbol{J} \tag{2.23}$$

This is the new integral equation that is similar to (2.18) but has a new forcing term (the so-called "new Born term") and a new kernel matrix. It can now be iterated with the new Born term

$$\boldsymbol{J}_B \equiv (\boldsymbol{I} - \boldsymbol{U})^{-1}(\boldsymbol{I} - \boldsymbol{L})^{-1}\boldsymbol{J}^i \tag{2.24}$$

serving as the zeroth-order iterate. The formal iterative solution in the form of a series can be written as

$$\boldsymbol{J} = \sum_{p=0}^{\infty} \left\{(\boldsymbol{I} - \boldsymbol{U})^{-1}(\boldsymbol{I} - \boldsymbol{L})^{-1}\,\boldsymbol{L}\boldsymbol{U}\right\}^p (\boldsymbol{I} - \boldsymbol{U})^{-1}(\boldsymbol{I} - \boldsymbol{L})^{-1}\boldsymbol{J}^i \tag{2.25}$$

Using the fact that for any matrix $\boldsymbol{A}$ the following identity holds:

$$\boldsymbol{A}(\boldsymbol{I} - \boldsymbol{A})^{-1} = (\boldsymbol{I} - (\boldsymbol{I} - \boldsymbol{A}))(\boldsymbol{I} - \boldsymbol{A})^{-1} \equiv (\boldsymbol{I} - \boldsymbol{A})^{-1} - \boldsymbol{I}, \tag{2.26}$$

one can write

$$\begin{aligned} \boldsymbol{U}(\boldsymbol{I} - \boldsymbol{U})^{-1} &= (\boldsymbol{I} - \boldsymbol{U})^{-1} - \boldsymbol{I} \\ \boldsymbol{L}(\boldsymbol{I} - \boldsymbol{L})^{-1} &= (\boldsymbol{I} - \boldsymbol{L})^{-1} - \boldsymbol{I} \end{aligned} \tag{2.27}$$

This allows (2.25) to be cast in the form

$$\boldsymbol{J} = (\boldsymbol{I} - \boldsymbol{U})^{-1} \sum_{p=0}^{\infty} \left\{\left((\boldsymbol{I} - \boldsymbol{L})^{-1} - \boldsymbol{I}\right)\left((\boldsymbol{I} - \boldsymbol{U})^{-1} - \boldsymbol{I}\right)\right\}^p (\boldsymbol{I} - \boldsymbol{L})^{-1}\boldsymbol{J}^i \tag{2.28}$$

that contains only $(\boldsymbol{I}-\boldsymbol{L})^{-1}$ and $(\boldsymbol{I}-\boldsymbol{U})^{-1}$ matrices and no separate $\boldsymbol{L}$ and $\boldsymbol{U}$ matrices as in (2.25). Note that due to the triangular nature of matrices $(\boldsymbol{I}-\boldsymbol{U})$ and $(\boldsymbol{I}-\boldsymbol{L})$ no actual matrix inversion is necessary; forward or back substitution can be used and this eliminates the necessity to store and invert the propagator matrix. In fact, it turns out that very few terms in the sum in (2.28) are needed to achieve sufficient accuracy. For the rough surfaces we worked with, we found that the new Born term (2.24) often gives a reasonable answer and that two iterations above the new Born term are more than adequate. Following the outlined steps, one can develop the equations similar to (2.24), (2.25) and (2.28), with the matrices $\boldsymbol{L}$ and $\boldsymbol{U}$ interchanged. This modified iteration scheme will have same convergence properties and will lead to the same results [Adams, 1998].

2.3 Calculation of the Scattered Field. Normalized Radar Cross Section

Once the MFIE (2.13) is solved and the surface current $J(x)$ is known, the field off the surface can be found from equation (2.7) or (2.9). They are applicable immediately if one recalls that, according to our notation, in the TM case the current J corresponds to the total H field on the surface, and in the TE case the current corresponds to the normal derivative of the total E field on the surface. The scattered field is by definition the total field minus the incident field:

$$\psi^s(\vec{r}) = \psi(\vec{r}) - \psi^i(\vec{r}) \tag{2.29}$$

In our studies we will be interested mostly, if not solely, in the scattered field in the far-field zone. Then, a large-argument approximation can be used for the Hankel functions that appear in G and $\partial G/\partial n'$ in (2.7) and (2.9). The expression for the far-zone scattered field at a distance r from the center of the illuminated part of the surface can be written as

$$\psi^s(\theta_s, r) = \frac{e^{-j\pi/4}}{2\sqrt{2\pi k}} \frac{e^{-jkr}}{\sqrt{r}} \int_X Q(x, \theta_s) J(x) dx \tag{2.30}$$

For the vertical polarization (TM case) we solve for magnetic field, $\psi^s = H^s$, and the integral kernel is

$$Q(x,\theta_s) = jk\left(-\zeta_x(x)\sin\theta_s + \cos\theta_s\right)\exp\left\{jk(x\sin\theta_s + \zeta(x)\cos\theta_s)\right\} \tag{2.31}$$

In the case of horizontal polarization (TE case) we work with electric field, i.e. $\psi^s = E^s$, and

$$Q(x,\theta_s) = -\exp\left\{jk(x\sin\theta_s + \zeta(x)\cos\theta_s)\right\}\sqrt{1+\zeta_x^2(x)} \tag{2.32}$$

Once again, the factor $\sqrt{1+\zeta_x^2(x)}$ associated with the conversion of integration along the surface to integration along the mean surface plane was included in the kernel Q. The scattering angle θ_s appearing in (2.30)-(2.32) is defined with respect to the vertical (z) axis and is assumed to be positive in a clockwise direction. The choice of incident and scattering angles is once again illustrated in Fig. 2-4. Of course, if the discretized

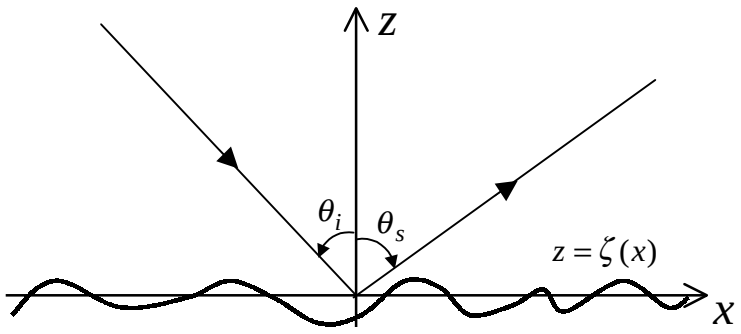

Figure 2-4. The choice of incident and scattered angles positive convention.

numerical solution to the MFIE (2.18) is used, the integral in (2.30) should be replaced by a sum. The appropriate way to do this will be further discussed in Chapter 4.

To describe scattering from a particular irregular surface a bistatic normalized radar cross section (NRCS) $\sigma^0(\theta_i,\theta_s)$ can be introduced:

$$\sigma^0(\theta_i,\theta_s) = \lim_{r\to\infty}\frac{2\pi\, r\,|\psi^s|^2}{\int|\psi^i(x,0)|^2\,dx}, \tag{2.33}$$

where ψ^s is given by (2.30). The backscattered NRCS is

$$\sigma^0_{bsc}(\theta_i) \equiv \sigma^0(\theta_i, \theta_s = -\theta_i) \tag{2.34}$$

For randomly rough surfaces, $\sigma^0(\theta_i, \theta_s)$ can be averaged over an ensemble of several surface realizations to obtain an average NRCS $\langle \sigma^0 \rangle$.

Chapter 3

Statistical Description of Randomly Rough Surfaces and Generating Surface Realizations

In this chapter we consider mathematical aspects of a statistical description of Gaussian randomly rough surfaces and, based on this analysis, present a consistent development of the spectral method for generating realizations of such surfaces. These surface realizations will be used in numerical Monte Carlo simulations of scattering by randomly rough surfaces.

Depending on the statistical model and formulation used for the surface, various surface generation techniques can be considered [Ogilvy, 1991]. For the Gaussian randomly rough surfaces, a so-called spectral technique is usually the preferred one. Probably one of the first uses of this technique for substantial numerical scattering simulations was by E. Thorsos [Thorsos, 1988] (for references to a few earlier works cf. [Ogilvy, 1991]). At present, this technique is used extensively in numerical scattering simulations [Johnson, 1998], [Donohue *et al*, 1998], [Toporkov *et al*, 1998]. Since to our knowledge there has been no detailed description of the development of this method readily available in the literature on numerical scattering simulations (the brief prescription given in [Thorsos, 1988] probably being the most complete and detailed one), it is useful to present such a discussion. For example, there is some lack of understanding as to what extent the generated "model" (inherently finite-extent) surfaces correspond to the "real" (supposedly infinite-extent) surfaces. Also, we will set our discussion in a somewhat general framework showing why the spectral representation for Gaussian surfaces are frequently preferred.

3.1 General Remarks on the Description and Generation of the Randomly Rough Surfaces

In studies of scattering from rough surfaces, it is customary to treat the irregular surfaces in a statistical manner. That is, the surfaces are assumed to be realizations of a random process and then averages of electromagnetic scattering parameters (like NRCS introduced in the previous Chapter) over an ensemble of such surface realizations are considered.

The most common model for randomly rough surfaces is the Gaussian surface, i.e. the surface is treated as a Gaussian random process. It is very attractive for several reasons. First, its analytical simplicity permits many closed form theoretical results (that are developed, for example, within the Kirchhoff theory or the perturbation theory). Second, for a vast class of irregular surfaces of interest to us, namely ocean surfaces, the assumption of Gaussian nature presents a quite reasonable first approximation if one considers the linear theory of wind-generated waves [Longuet-Higgins, 1963]. Recent attempts to formulate a statistical theory of ocean surface waves using a Hamiltonian/Lagrangian form of fluid dynamical equations include for example [Allen and Joseph, 1989, 1990]. Though deviations from the Gaussian statistics are likely to occur for the oceanic surfaces and can appreciably affect the backscatter from such surfaces and their radar imaging (e.g. [Toporkov and Brown, 1996]), here we will limit the scope of our consideration to the surfaces with the Gaussian statistics. Finally, it turns out that realizations of Gaussian surfaces are relatively easy to generate, as will be discussed in this Chapter.

A review of the most commonly used techniques to generate samples of random surfaces (not necessarily Gaussian) can be found in [Ogilvy, 1991]. They include moving average processes, autoregressive processes and the spectral method. All these methods involve generating independent random numbers γ_l (this capability is a standard feature of almost every computational platform) and then applying some transformation to obtain samples of a random surface realization ζ_n. For the moving average processes such a transformation has a generic form of

$$\zeta_n = \sum_{m=0}^{M} a_m \gamma_{n-m} \tag{3.1}$$

(a_m are coefficients and M is a constant that defines the order of the process). For the autoregressive processes the transformation is

$$\zeta_n = \sum_{m=1}^{M} a_m \zeta_{n-m} + \gamma_n \tag{3.2}$$

and M again defines the order of the process. In the case of the spectral method the random numbers γ_m are transformed as

$$\zeta_n = \sum_{m=-M/2}^{M/2-1} a_m e^{-\frac{j2\pi}{M}nm} \gamma_m \tag{3.3}$$

and M in (3.3) is a number of points in the spectral domain. It can be observed that expressions in (3.1) and (3.2) describe an output of the linear system with a random input. In particular, (3.1) corresponds to a system without a feedback and in (3.2) a linear system has a feedback. Therefore methods of analysis and results developed in the area of linear of filtering/spectral estimation of stochastic processes (e.g. [Van Trees, 1968, Ch. 6], [Papoulis, 1991, Ch. 13]) can be readily applied.

The choice of a particular method may depend on several factors, the main consideration probably being what surface statistics is desired. For example, the first-order ($M = 1$) autoregressive process in (3.2) is a linear Markov process [Beckmann and Spizzichino, 1963] and is certainly a choice if Markovian properties of the surface are to be emphasized. In general, autoregressive processes are non-stationary, even when the input γ_l is a stationary random process; however, under certain conditions these methods become asymptotically stationary [Ogilvy, 1991]. Unlike two other methods, (3.2) is very limited as to what correlation function or spectral density can be implemented and is not as much convenient with respect to generating surface derivatives [Thorsos, 1988]. The methods (3.1) and (3.3) in principle have similar capabilities in generating stationary random surfaces with given correlation function or power spectral density and their derivatives, with the spectral method probably being more flexible. The use of the Fast Fourier Transform (FFT) algorithm makes the spectral method very efficient computationally. In contrast, the moving average process, being essentially a

convolution, can be computationally competitive only for low orders M, i.e. for very narrow correlation functions. Indeed, to generate a surface of N points, (3.1) would require $O(NM)$ operations. Evaluation of (3.3) is performed by the FFT; this usually involves setting $M = N$, but the number of operations goes as $O(N \log_2 N)$ (for a radix 2 FFT). Of course, one could consider computing the convolution in (3.1) in the spectral domain with the transfer between domains accomplished by the FFT, but then it might be wiser to choose the spectral method in (3.3) from the very beginning. The moving average process may offer some advantage in "constructing" surfaces with a given height or slope probability density function (pdf); an example of the recent work in this area is [Leskova *et al*, 1998]. Since we will work with surfaces that are traditionally specified in terms of their spectrum (and, besides, have quite broad correlation functions, as shown in Chapter 4), the spectral method is very convenient, efficient and thus emerges as a natural choice.

If the spectral method is used, it is easy to show that no matter what particular probability density functions random numbers γ_n have, the power spectral density and correlation function of the surface generated will remain the same as long as γ_n are uncorrelated and their first two moments do not change. This can be seen, for example, by forming a correlation $\langle \zeta_n \zeta_m \rangle$ from (3.3). However, both marginal (single-point) and joint pdf's of the surface height will depend on the pdf's of γ_n, and may not be easy to determine and control, especially the joint pdf. Yet if γ_n have the Gaussian pdf's it can be shown that the generated surface is Gaussian, which as was mentioned before, will be our goal.

In this Chapter, however, we will present a more general discussion. We consider representing Gaussian, in general non-stationary surface in different bases and find that there exists the basis where this description significantly simplifies. For stationary surfaces such a basis will be composed of complex exponentials suggesting a spectral representation as a convenient analytical tool. This will also explain why the emphasis is usually put on developing analytical models of the surface spectrum rather than surface correlation function (of course, for stationary surfaces the two are related by the Fourier transform, cf. (3.16)-(3.17), but a tractable closed-form expression is usually available

only for one of them). We develop the spectral method of surface generation as a logical extension of this concept. Since our surfaces will be defined exclusively in terms of their spectrum, this method will suit us ideally. In the process we will develop important details regarding the application of this method, i.e. generation of the surface derivatives, representing the surface and its derivatives with a discrete set of values and efficient calculation of the surface samples. It should be pointed out once again that our ability to calculate (3.3) efficiently via the FFT is an important practical factor in deciding to use the spectral method. Indeed, it can be shown that under certain conditions the spectral method for the Gaussain surfaces can be cast in the form (3.1), but as we have discussed this would offer neither convenience in surface description nor computational advantage. The development presented in this Chapter may be useful in devising methods of generating surfaces with controlled deviations from the Gaussian statistics.

The layout of this Chapter is consequently as follows. In Section 3.2 we discuss statistical preliminaries. This includes a review of the concept of probability density functional through which our Gaussian randomly rough surface will be defined, followed by a discussion on a stationary (spatially homogeneous) random surfaces and their description. Section 3.3 presents the development of the spectral method. First we consider a more general case of non-stationary Gaussian random surface and find that its description significantly simplifies if the eigenfunctions of the correlation function $C(x_1, x_2)$ viewed as a kernel are used as the new basis. In this new basis the Gaussian surface will be represented by a discrete set of independent Gaussian random variables. In Section 3.3.3 we turn our attention to a subclass of stationary Gaussian surfaces and find that in this case the basis functions are easily found and turn out to be Fourier exponentials. Up to this point the surface is assumed to be continuous, which allows to consider its derivatives as well (for our simulations we will need first and second surface derivatives – cf. Chapters 2, 4). Sections 3.3.4 and 3.3.5 consider stationary surfaces with band-limited spectra and discuss how they and their derivatives can be represented by a discrete set of values based on the sampling theorem. The outcome of this discussion is essentially the spectral method as given in (3.3) (with γ_n being independent Gaussian random numbers). We cast the derived expressions in a form suitable for application of the FFT and list the steps of a practical algorithm to generate samples of a Gaussian

random surface and its derivatives. The developments in this Chapter also reveal what requirements should be set on certain parameters involved and what the method's limitations are.

3.2 Some Aspects of the Statistical Description of Gaussian Rough Surfaces

3.2.1 A Description of a Continuous Random Surface through a Probability Density Functional

We will define our Gaussian randomly rough surface through a probability density functional. One of the benefits of this description is that it allows to deal with *continuous* functions describing the random surface height. This will permit us to readily consider surface derivatives when necessary. Alternative descriptions of the Gaussian random process can be found, among others, in [Van Trees, 1968] and [Davenport and Root, 1987]. Though probability density functionals are extensively used in many physical and engineering disciplines (radar detection theory, statistical and quantum physics being just a few examples), it is helpful to review this concept. We will refer to the results of this Section in our further developments. More details about probability functionals and related questions can be found for example, in [Feynman and Hibbs, 1965] and [Mandel and Wolf, 1995].

Consider a joint multivariate Gaussian probability density function (pdf) of real random variables $\{\zeta_1, ..., \zeta_N\}$ with zero means

$$\vec{\zeta} \equiv \begin{bmatrix} \zeta_1 \\ \vdots \\ \zeta_N \end{bmatrix} \tag{3.4}$$

and a covariance matrix $\boldsymbol{C}$:

$$\boldsymbol{C} \equiv [C_{ij}] = [\langle \zeta_i \zeta_j \rangle] \tag{3.5}$$

This density has the form

$$\begin{aligned} p(\{\zeta_1,...,\zeta_N\}) &= \frac{1}{\sqrt{(2\pi)^N \det \boldsymbol{C}}} \exp\left(-\frac{1}{2} \vec{\zeta}^T \boldsymbol{\Gamma} \vec{\zeta} \right) \\ &\equiv \frac{1}{\sqrt{(2\pi)^N \det \boldsymbol{C}}} \exp\left(-\frac{1}{2} \sum_{i=1}^{N} \sum_{j=1}^{N} \zeta_i \Gamma_{ij} \zeta_j \right) \end{aligned} \tag{3.6}$$

In (3.6), $\boldsymbol{\Gamma}$ is the inverse covariance matrix:

$$\boldsymbol{\Gamma} = \boldsymbol{C}^{-1}$$

or,

$$\boldsymbol{\Gamma}\boldsymbol{C} = \boldsymbol{I}\,, \tag{3.7}$$

where, as usual, $\boldsymbol{I}$ denotes the identity matrix.

In order to introduce the concept of the probability density functional, it is helpful to consider the situation depicted in Fig. 3-1. Imagine that random variables $\zeta_1, \zeta_2 ..., \zeta_N$

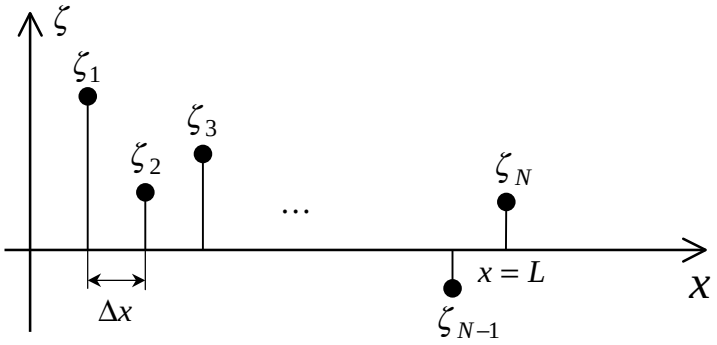

Figure 3-1. Samples of a stochastic (x-dependent) process.

are located along the x-axis with some spacing Δx. Let us increase the number of these variables N and decrease Δx while keeping their product constant:

$$N\Delta x = L \tag{3.8}$$

Regarding ζ_i and ζ_j in (3.6) as values of random process at points with x-coordinates $i\Delta x$ and $j\Delta x$, we replace as $\Delta x \to 0$ discrete indices i and j by continuous variables x_1 and x_2; consequently, the summation in the exponent in (3.6) is replaced by integration:

$$\lim_{\substack{N\to\infty \\ N\Delta x=L}} \sum_{i=1}^{N}\sum_{j=1}^{N} \zeta(i\Delta x)\Gamma_{ij}\zeta(j\Delta x) = \lim_{\substack{N\to\infty \\ N\Delta x=L}} \sum_{i=1}^{N}\Delta x \sum_{j=1}^{N}\Delta x\,\zeta(i\Delta x)\frac{\Gamma_{ij}}{(\Delta x)^2}\zeta(j\Delta x)$$
$$= \int_0^L\int_0^L \zeta(x_1)\Gamma(x_1,x_2)\zeta(x_2)dx_1dx_2, \tag{3.9}$$

For our purposes it is more convenient to define the kernel $\Gamma(x_1,x_2)$ that we formally substituted in (3.9) for the limit of $\Gamma_{ij}/(\Delta x)^2$ as $\Delta x\to 0$ in the way analogous to (3.7). To do this, we rewrite (3.7) as

$$\sum_{j=1}^{N}\frac{\Gamma_{ij}}{(\Delta x)^2}C_{jk}\Delta x = \frac{\delta_{jk}}{\Delta x}$$

(δ_{jk} is a Kronecker delta) and take the limit of both sides as $\Delta x\to 0$ ($N\to\infty$). Note that in the continuous limit the covariance matrix $\boldsymbol{C}$ in (3.5) becomes a correlation function

$$C(x_1,x_2) \equiv \langle \zeta(x_1)\zeta(x_2)\rangle \tag{3.10}$$

and $\delta_{jk}/\Delta x$ is replaced by a δ-function. Thus the equation defining $\Gamma(x_1,x_2)$ is

$$\int_0^L \Gamma(x_1,x_2)C(x_2,x_3)dx_2 = \delta(x_1-x_3) \tag{3.11}$$

In what follows we will have no need to solve (3.11), rather we will find it helpful in establishing certain properties of the eigenfunctions and eigenvalues of the kernel Γ.

With (3.9), in the continuous limit the multivariate joint pdf becomes

$$p(\{\zeta(x)\}) = D\exp\left(-\frac{1}{2}\int_0^L\int_0^L \zeta(x_1)\Gamma(x_1,x_2)\zeta(x_2)dx_1dx_2\right) \tag{3.12}$$

with the normalization factor D being understood again as a limit

$$D = \lim_{\substack{N\to\infty \\ N\Delta x=L}} \frac{1}{\sqrt{(2\pi)^N \det \boldsymbol{C}}} \tag{3.13}$$

As the multivariate pdf in (3.6) contains the most detailed description of statistical properties of N discrete random variables, the functional in (3.12) presents the most

complete description of statistical properties of a continuous random process. We will later find that in a certain basis this description simplifies significantly.

3.2.2 A Stationary Random Process: Its Correlation Function and Spectrum

An important class of random processes is the stationary random processes; for the case of randomly rough surfaces where the surface height is a function of spatial coordinates rather than time, the term "spatially homogeneous random process" may be somewhat more appropriate. The rigorous definition of stationarity can be found, for example, in [Middleton, 1960]. Concisely put, this property implies that *all* probability measures of the process remain unaffected by the change of the coordinate $\vec{r} \to \vec{r} + \vec{r}'$. This is often called a "strict" or "complete" stationarity. A less restrictive form of stationarity is a "wide sense" stationarity when one requires that the correlation function depend only on the coordinate difference, $\vec{r}_2 - \vec{r}_1$. For the 1-D surfaces (interfaces in a 2-D space) that we are considering this means

$$C(x_1, x_2) = C(x_2 - x_1) \tag{3.14}$$

Since the zero mean Gaussian process is entirely defined by its correlation function, it can be easily shown that for such a process the "wide sense" stationarity is equivalent to the "strict" stationarity. Because we are dealing exclusively with Gaussian processes, in the future we will simply use the term "stationary" or "spatially homogeneous" keeping in mind that it means both types of stationarity as noted above. Also, since $C(x_1, x_2)$ in (3.10) should be symmetric [Papoulis, 1991, p.293], $C(x_2 - x_1)$ in (3.14) is even:

$$C(x_2 - x_1) = C(x_1 - x_2) \tag{3.15}$$

For a stationary random process one can introduce a Fourier transform of the correlation function, which is called a power spectral density

$$W(K) = \frac{1}{2\pi} \int_{-\infty}^{\infty} C(x) e^{jKx} dx \tag{3.16}$$

In (3.16) we have used a new variable $x \equiv x_2 - x_1$ in the argument of C and the factor $1/2\pi$ was incorporated to follow [Thorsos, 1988]. Conversely, given the power spectral density one can recover the correlation function as

$$C(x) = \int_{-\infty}^{\infty} W(K) e^{-jKx} dK \tag{3.17}$$

Expressions in (3.16) and (3.17) obviously form a Fourier transform pair. So, if a random process is stationary, one can specify either its correlation function or its power spectral density. It turns out that it is often more convenient to characterize and classify the randomly rough surfaces by their power spectral density (which we sometimes will refer to as the "surface spectrum").

It should be noted that the infinite limits of integration in (3.16) presume that the random process has an infinite support, and this leads to an infinite energy process. Application of the probability density functional in (3.12) when L is infinite requires special care and is likely to be plagued by divergences. However, the assumption of the infinite surface extent has its advantages (one of them, for example, being an analytical simplicity of the Fourier pair (3.16)-(3.17)) and can be viewed as a limiting case of situations where the surfaces have finite supports. For our simulations, we will be generating finite-extent surfaces, so we will eventually have to discuss in what sense and to what extent such are surfaces described by the spectrum $W(K)$ in (3.16).

3.3 Generation of Realizations of Gaussian Rough Surfaces

3.3.1 Preliminary Considerations

If one needs to generate random numbers that are described by a single-variable, zero mean, Gaussian probability density function

$$p(\zeta) = \frac{1}{\sqrt{2\pi\sigma^2}} \exp\left(-\frac{\zeta^2}{2\sigma^2} \right), \tag{3.18}$$

σ^2 being the variance, the task is relatively simple and straightforward. Almost all computers have built-in random number generators and virtually all compilers and libraries provide tools to generate random numbers with the uniform if not the Gaussian pdf. The former can then be transformed into Gaussian random numbers through change of variables and corresponding probability transformations, as is described in the Appendix at the end of this Chapter. Generation of several independent sets of Gaussian random numbers (corresponding to independent random variables) also does not present

a problem. However, if one wants to generate random numbers according to the multivariate pdf in (3.6), the necessity to account for specific correlation properties makes the problem less straightforward.

One possible solution is to find a new basis in which the inverse covariance matrix $\mathbf{\Gamma}$ is diagonal. Then in this new coordinate system the multivariate Gaussian pdf in (3.6) can be factorized in a product of single-point Gaussian pdf's indicating that the new random variables are *independent*. These independent random numbers can be generated using the available tools that we just discussed. They define a random vector with respect to the new basis; we need to find the coordinates of this vector in the old basis (where $\mathbf{\Gamma}$ is not diagonal) and this is accomplished by multiplying this vector by the transition matrix relating the two coordinate systems.

The very same idea can be applied to generating the realizations of the continuous Gaussian random process described by the probability density functional in (3.12).

3.3.2 Factorization of the Gaussian Probability Density Functional

Since the 1-D surfaces that we will use in our simulations will inherently have some finite length L, we will consider the Gaussian random process defined on the finite interval $x \in [-L/2, L/2]$ and described by the probability density functional of the type (3.12):

$$p(\{\zeta(x)\}) = D \exp\left(-\frac{1}{2} \int_{-L/2}^{L/2} \int_{-L/2}^{L/2} \zeta(x_1) \Gamma(x_1, x_2) \zeta(x_2) dx_1 dx_2 \right) \tag{3.19}$$

In contrast to (3.12), in (3.19) we used symmetric limits of integration.

Suppose that we know the eigenfunctions of the correlation function C, i.e. the functions $\varphi_n(x)$ that satisfy the following equation

$$\int_{-L/2}^{L/2} C(x_1, x_2) \varphi_n(x_1) dx_1 = \sigma_n^2 \varphi_n(x_2) \tag{3.20}$$

where σ_n^2 are the corresponding eigenvalues. In principle, there will be an infinite number of the eigenfunctions and eigenvalues. Under certain conditions which the kernel C most often satisfy, namely if the kernel is real, symmetric and positive definite, its

eigenfunctions form a complete orthonormal set for the class of functions square-integrable on $[-L/2, L/2]$ [Middleton, 1960, p.726], cf. also [Courant and Hilbert, 1953]. The corresponding eigenvalues are real and positive, which we underscore by writing them as squares. These functions $\varphi_n(x)$ will be also the eigenfunctions of the kernel Γ. To demonstrate this, let us use the definition (3.11) for Γ, multiply both sides by $\varphi_n(x_3)$ and integrate over x_3:

$$\int_{-L/2}^{L/2}\int_{-L/2}^{L/2}\Gamma(x_1,x_2)C(x_2,x_3)\varphi_n(x_3)dx_2dx_3 = \int_{-L/2}^{L/2}\delta(x_1-x_3)\varphi_n(x_3)dx_3 \qquad (3.21)$$

The integration with the delta-function on the right-hand side yields $\varphi_n(x_1)$; on the left-hand side we use (3.20) (together with the symmetry property of the correlation function) to get

$$\sigma_n^2\int_{-L/2}^{L/2}\Gamma(x_1,x_2)\varphi_n(x_2)dx_2 = \varphi_n(x_1) \qquad (3.22)$$

or, dividing both sides by σ_n^2:

$$\int_{-L/2}^{L/2}\Gamma(x_1,x_2)\varphi_n(x_2)dx_2 = \frac{1}{\sigma_n^2}\varphi_n(x_1) \qquad (3.23)$$

The equation in (3.23) is similar to (3.20) and demonstrates that the kernel Γ has the very same eigenfunctions as the kernel C, with the eigenvalues being the reciprocals of the corresponding eigenvalues of C.

Assuming the completeness of the eigenfunctions set $\{\varphi_n(x)\}$ in the class of square-integrable functions, let us write a realization $\zeta(x)$ of the random process in terms of the $\varphi_n(x)$, i.e.

$$\zeta(x) = \sum_{n=1}^{\infty}\eta_n\varphi_n(x) \qquad (3.24)$$

Series in (3.24) is often referred to as the Karhunen-Loeve expansion [Van Trees, 1968, p.182]. The expansion coefficients $\{\eta_n\}$ as well as the eigenfunctions $\{\varphi_n(x)\}$ can, in principle, be complex. However, to illustrate the idea of factorizing the probability density functional, let us assume that they are real. As we will see in the next Section, the

case when complex eigenfunctions are used to expand the real function requires some additional care.

Consider now the exponential in (3.19). With the use of the expansion (3.24) we can write:

$$\begin{aligned} &\exp\left[-\frac{1}{2}\int_{-L/2}^{L/2}\int_{-L/2}^{L/2}\zeta(x_1)\Gamma(x_1,x_2)\zeta(x_2)dx_1dx_2\right] \\ &=\exp\left[-\frac{1}{2}\int_{-L/2}^{L/2}\int_{-L/2}^{L/2}\left(\sum_{m=1}^{\infty}\eta_m\varphi_m(x_1)\right)\Gamma(x_1,x_2)\left(\sum_{n=1}^{\infty}\eta_n\varphi_n(x_2)\right)dx_1dx_2\right] \end{aligned} \tag{3.25}$$

We further make use of (3.23) to simplify the x_2-integration and recall that the eigenfunctions $\{\varphi_n(x)\}$ are (or can be chosen to be) orthonormal, i.e.

$$\int_{-L/2}^{L/2}\varphi_m(x)\varphi_n(x)dx=\delta_{mn}, \tag{3.26}$$

with δ_{mn} being a Kronecker delta. Then we have for the exponential:

$$\begin{aligned} &\exp\left\{-\frac{1}{2}\int_{-L/2}^{L/2}\int_{-L/2}^{L/2}\zeta(x_1)\Gamma(x_1,x_2)\zeta(x_2)dx_1dx_2\right\} \\ &=\exp\left\{-\frac{1}{2}\sum_{m=1}^{\infty}\sum_{n=1}^{\infty}\frac{1}{\sigma_n^2}\eta_m\eta_n\int_{-L/2}^{L/2}\varphi_m(x_1)\varphi_n(x_1)dx_1\right\} \\ &=\exp\left\{-\frac{1}{2}\sum_{m=1}^{\infty}\sum_{n=1}^{\infty}\frac{1}{\sigma_n^2}\eta_m\eta_n\delta_{mn}\right\}=\exp\left\{-\sum_{n=1}^{\infty}\frac{\eta_n^2}{2\sigma_n^2}\right\} \end{aligned} \tag{3.27}$$

Let us examine the normalizing factor D in front of the exponential in (3.19) as well. In (3.13) we defined it as a limit of the corresponding normalization factor for a discrete multivariate pdf, and that factor contains a determinant of the covariance matrix. Noting the fact that if a $N\times N$ matrix has eigenvalues $\{\lambda_n\}$ then its determinant is equal to the product of these eigenvalues:

$$\det\mathbf{C}=\prod_{n=1}^{N}\lambda_n\ ,$$

we can write

$$D = \lim_{N\to\infty} \frac{1}{\sqrt{(2\pi)^N \det \boldsymbol{C}}} = \lim_{N\to\infty} \frac{1}{\sqrt{(2\pi)^N \prod_{n=1}^{N} \lambda_n}} = \prod_{n=1}^{\infty} \frac{1}{\sqrt{(2\pi)\sigma_n^2}}, \qquad (3.28)$$

where $\{\sigma_n^2\}$ are the eigenvalues of our "infinitely large covariance matrix", i.e. the correlation function.

Combining (3.27) and (3.28) we see that in the new eigenfunction basis set for the of the kernel C the probability density functional in (3.19) assumes the form

$$p(\{\eta_n\}) = \prod_{n=1}^{\infty} \frac{1}{\sqrt{(2\pi)\sigma_n^2}} \exp\left(-\frac{\eta_n^2}{2\sigma_n^2}\right) \qquad (3.29)$$

Actually, in order to write down (3.29), we should also consider (by analogy with the transformations of multivariate pdf's) multiplying the product of (3.27) and (3.28) by the absolute value of the Jacobian of the transformation [Papoulis, 1991, p. 183]. However, because of the orthonormal property (3.26) we are essentially dealing with an orthogonal linear transformation, and the above-mentioned Jacobian will have unity absolute value.

Expression in (3.29) has the form of a product (although an infinite one) of single-point Gaussian probability density functions of random variables η_n, which implies that these variables are independent. This means that we have formally achieved our goal. Now we can generate *independent* random numbers according to single-point pdf's in (3.29) and then use (3.24) to obtain a realization of the random process specified by the probability density functional in (3.19).

Of course, to be able to apply the scheme outlined above we need to know the eigenfunctions of C. Another problem from the practical point of view is that so far we still need to sum an infinite number of terms in (3.24). In the following Section we will address these questions. We will show that for the stationary Gaussian random process such eigenfunctions are easily found and turn out to be the Fourier exponentials, which relates the eigenvalues σ_n^2 to the power spectral density. We will also discuss the use of band-limited spectra, and this will allow us to represent the surface in (3.24) with a finite number of terms.

3.3.3 Generation of Realizations of a Stationary Random Process

Let us consider applying the formalism developed in the previous Section to a *stationary* random process. In order to consider the finite-extent surface and be able to maintain the stationarity property (3.14) let us assume that our random process is periodic with the period L, with the correlation function that is L-periodic, and still depends only on the difference $x \equiv x_2 - x_1$. From the developments that follow it will be clear that such a choice effectively imposes periodic boundary conditions on the surface height and all existing surface derivatives (i.e. if the process has the l-th derivative, it will be continuous across the boundary). We will denote such stationary, L-periodic correlation function as $C_L(x)$.

In the literature the Gaussian stationary surfaces are usually specified on the infinite interval as non-periodic. Namely, $C(x)$, if given explicitly, is defined for $x \in (-\infty, \infty)$ and is non-periodic (nor does it include any finite-amplitude periodic function as one of its terms). A popular form of the correlation function is, for example, a Gaussian correlation function [Thorsos, 1988]:

$$C(x) = h^2 e^{-x^2/l^2} \tag{3.30}$$

with h being a root mean square height and l being a correlation length. Alternatively, if the surface is specified through its spectrum in (3.16), $W(K)$ is usually continuous and does not contain any singularities. For example, the spectrum corresponding to (3.30) is

$$W(K) = \frac{lh^2}{2\sqrt{\pi}} e^{-K^2 l^2/4} \tag{3.31}$$

Another example of the spectrum is given in (4.2). When generating our finite-length (periodically extended) surfaces, we would like to use this information and be able to claim that our surfaces are representative of the given correlation function $C(x)$ or spectrum $W(K)$.

Since the approach described in the previous Section starts from the correlation function, let us consider a way to construct a periodic stationary correlation function $C_L(x)$ from $C(x)$ in (3.17). One condition that we would like this new "constructed"

correlation function to satisfy is that as $L \to \infty$, $C_L(x)$ should become $C(x)$. One possible way to do it is

$$C_L(x_1, x_2) \equiv C_L(x_2 - x_1) = \sum_{k=-\infty}^{\infty} C(x_2 - x_1 - kL) \tag{3.32}$$

The reason we have chosen such a form is that it will lead to an especially simple relation between the eigenvalues of C_L and the spectrum $W(K)$ in (3.16). As we discussed, $C(x)$ is non-periodic and for all cases of interest to us goes to zero as $|x| \to \infty$. In fact, when a spectrum $W(x)$ is non-singular, the decaying behavior of the correlation function follows from the properties of the Fourier transform [Bracewell, 1965, p. 147]. As $L \to \infty$, all shifted replicas of the correlation function C in (3.32) move to plus or minus infinity, and we have that in this limit $C_L(x) \to C(x)$. Also, if L is chosen large enough compared to the correlation length, the tails of the shifted replicas of C will not cause too much interference so that on the interval $x \in [-L/2, L/2]$ functions $C(x)$ and $C_L(x)$ will differ only slightly.

A possibility that we would like to mention is when $C(x)$ is non-periodic, but contains a finite-amplitude periodic (with a period L_p) component $C_p(x)$:

$$C(x) = C_p(x) + C_n(x) \tag{3.33}$$

(C_n denotes a residual non-periodic part). This means, in particular, that $C(x)$ does not go to zero as x goes to infinity. The spectrum $W(K)$ in this case will contain singularities (delta-functions). Such a situation can occur for example when one considers a sinusoidal surface with a roughness on it. In this case C_L should be constructed as follows:

$$C_L(x_2 - x_1) = C_p(x_2 - x_1) + \sum_{k=-\infty}^{\infty} C_n(x_2 - x_1 - kL) \tag{3.34}$$

with L now being a multiple of the period L_p. However, if several periodic finite-amplitude components C_{p1}, C_{p2}, etc. with arbitrary periods are involved in (3.33), it may be impossible to find L that is a multiple of each period. In this case one might want

to reconsider the model (3.32) for C_L to include some windowing (tapering) function $T_L(x)$ which broadens as L increases:

$$C_L(x_2 - x_1) = \sum_{k=-\infty}^{\infty} T_L(x_2 - x_1 - kL) C(x_2 - x_1 - kL) \tag{3.35}$$

In general, from what follows we will see that the problems with (3.32) might arise only if the spectrum $W(K)$ has singularities (cf. (3.52)). The solution to this complication is then either to adjust L to "hit" all of these singularities exactly or spread them out by tapering $C(x)$. In what follows we will assume that $W(K)$ is non-singular and proceed with (3.32); the results can be generalized without any problem for the case in (3.34); however for the model in (3.35) some modifications to the analysis presented would have to be considered.

Let us now consider the probability density functional (3.19) with the kernel $\Gamma_L(x_1, x_2)$ corresponding, through (3.11), to a stationary L-periodic correlation function $C_L(x_1, x_2) \equiv C_L(x_2 - x_1)$. So far we will not make use of a specific form of C_L suggested in (3.32). As the first and the major step, we need to find the eigenfunctions of the C_L. It turns out that for a stationary periodic kernel these functions can be readily guessed based on the properties of complex exponentials:

$$\varphi_n(x) = \frac{1}{\sqrt{L}} e^{-j\frac{2\pi n}{L}x}, \quad n = -\infty, ..., \infty \tag{3.36}$$

Indeed, let us consider the equation (3.17). On the left-hand side we will have:

$$\begin{aligned} \int_{-L/2}^{L/2} C_L(x_1, x_2)\varphi_n(x_1)dx_1 &\equiv \frac{1}{\sqrt{L}} \int_{-L/2}^{L/2} C_L(x_2 - x_1) e^{-j\frac{2\pi n}{L}x_1} dx_1 \\ &= \frac{1}{\sqrt{L}} e^{-j\frac{2\pi n}{L}x_2} \int_{-L/2}^{L/2} C_L(x) e^{j\frac{2\pi n}{L}x} dx \end{aligned} \tag{3.37}$$

To obtain the last expression in (3.37) we performed the change of integration variable $x_1 = x_2 - x_1$ and used the fact that both functions in the integrand are L-periodic. Comparing (3.37) to (3.20) we see that (3.36) are indeed the eigenfunctions of C_L with the eigenvalues being

$$\sigma_n^2 = \int_{-L/2}^{L/2} C_L(x) e^{j\frac{2\pi n}{L}x} dx \tag{3.38}$$

We will see that that the kernel $C(x_2 - x_1)$ being positive definite (or non-negative definite) assures that all $\sigma_n^2 > 0$ (or $\sigma_n^2 \geq 0$). It is well known [e.g. Arfken and Weber, 1995] that the complex exponentials in (3.36) form a complete orthonormal set, with the orthogonality relation being

$$\int_{-L/2}^{L/2} \varphi_m^*(x)\varphi_n(x)dx = \delta_{mn} \tag{3.39}$$

Since now we deal with complex functions, the scalar product has been appropriately modified to include a complex conjugate; (3.39) is clearly an extension of (3.26) that was formulated for real functions.

As the next step, we write the expansion in (3.24) for a realization of a randomly rough surface:

$$\zeta(x) = \frac{1}{\sqrt{L}} \sum_{n=-\infty}^{\infty} \eta_n e^{-j\frac{2\pi n}{L}x} \tag{3.40}$$

Now we can follow the procedure discussed in Section 3.3.2, albeit with some modifications due to the fact that now the eigenfunctions and the expansion coefficients in (3.40) are complex. Let us notice that since $\zeta(x)$ is real we can write

$$\zeta(x) \equiv \zeta^*(x) = \frac{1}{\sqrt{L}} \sum_{n=-\infty}^{\infty} \eta_n^* e^{j\frac{2\pi n}{L}x} \tag{3.41}$$

Then in (3.27) we use (3.24) for $\zeta(x_2)$ and (3.41) for $\zeta(x_1)$, so the probability density functional expressed in the new basis becomes

$$p(\{\eta_n\}) = D' \exp\left\{-\frac{1}{2} \sum_{n=-\infty}^{\infty} \frac{|\eta_n|^2}{\sigma_n^2}\right\} \tag{3.42}$$

Let us now examine the additional constraints on the coefficients $\{\eta_n\}$ resulting from the fact that the surface $\zeta(x)$ is real. Consider (3.41) and change the summation index as $n \to -n$. This results in

$$\zeta(x) = \frac{1}{\sqrt{L}} \sum_{n=-\infty}^{\infty} \eta_{-n}^{*} e^{-j\frac{2\pi n}{L}x} \tag{3.43}$$

Comparing (3.43) to (3.40), we conclude that the following should hold:

$$\eta_0 = \eta_0^{*} \tag{3.44a}$$

$$\eta_n = \eta_{-n}^{*} \tag{3.44b}$$

We can also show that

$$\sigma_n^2 = \sigma_{-n}^2 \tag{3.45}$$

This comes from considering (3.38) and the fact that $C_L(x)$ is even (cf. (3.15) and (3.32)):

$$\sigma_{-n}^2 = \int_{-L/2}^{L/2} C_L(x) e^{-j\frac{2\pi n}{L}x} dx \underset{x\to -x}{=} \int_{-L/2}^{L/2} C_L(-x) e^{j\frac{2\pi n}{L}x} dx = \int_{-L/2}^{L/2} C_L(x) e^{j\frac{2\pi n}{L}x} dx \equiv \sigma_n^2 \tag{3.46}$$

Let us consider the exponential in (3.42). Because of (3.44) and (3.45) it can be rewritten as

$$\begin{aligned} \exp\left\{-\frac{1}{2}\sum_{n=-\infty}^{\infty}\frac{|\eta_n|^2}{\sigma_n^2}\right\} &= \exp\left\{-\frac{\eta_0^2}{2\sigma_0^2} - \frac{1}{2}\sum_{n=1}^{\infty} 2\frac{\eta_{Rn}^2 + \eta_{In}^2}{\sigma_n^2}\right\} \\ &= \exp\left\{-\frac{\eta_0^2}{2\sigma_0^2} - \frac{1}{2}\sum_{n=1}^{\infty}\frac{\eta_{Rn}^2 + \eta_{In}^2}{(\sigma_n^2/2)}\right\} \end{aligned} \tag{3.47}$$

where η_{Rn} and η_{In} are the real and imaginary parts of η_n respectively, and η_0 is real as follows from (3.44a). From (3.47) we conclude that:

- all η_{Rn}'s, η_{In}'s and η_0 are independent Gaussian variables;
- η_0 has a variance σ_0^2, while η_{Rn} and η_{In} have variances $\sigma_n^2/2$.

In fact, one can show in a manner similar to (3.28) that the normalization coefficient D' in (3.42) is consistent with these variances, i.e. is equal to

$$D' = \frac{1}{\sqrt{(2\pi)\sigma_0^2}} \prod_{n=1}^{\infty} \frac{1}{\pi\sigma_n^2} \tag{3.48}$$

This time there will be some contribution from the transformation Jacobian that will not be equal to 1.

Now let us take a closer look at the eigenvalues $\{\sigma_n^2\}$. At this point we will use the specific form of $C_L(x)$ given in (3.32). Before using (3.38) to calculate σ_n^2 let us consider the following. We can rewrite (3.32) as a convolution of $C(x)$ with a comb of δ-functions:

$$C_L(x) = \sum_{k=-\infty}^{\infty} C(x-kL) = \sum_{k=-\infty}^{\infty} \int_{-\infty}^{\infty} C(x')\delta(x-x'-kL)dx' = \int_{-\infty}^{\infty} C(x') \sum_{k=-\infty}^{\infty} \delta(x-x'-kL)dx' \tag{3.49}$$

and recall the Poisson summation formula [Papoulis, 1991, p. 395]

$$\sum_{k=-\infty}^{\infty} \delta(x-kL) = \frac{1}{L} \sum_{p=-\infty}^{\infty} e^{-j\frac{2\pi p}{L}x} \tag{3.50}$$

Then, plugging (3.50) in (3.49) and invoking (3.16) we get

$$\begin{aligned} C_L(x) &= \frac{1}{L} \int_{-\infty}^{\infty} C(x') \sum_{p=-\infty}^{\infty} e^{-j\frac{2\pi p}{L}(x-x')}dx' = \frac{1}{L} \sum_{p=-\infty}^{\infty} e^{-j\frac{2\pi p}{L}x} \int_{-\infty}^{\infty} C(x')e^{j\frac{2\pi p}{L}x'}dx' \\ &= \frac{2\pi}{L} \sum_{p=-\infty}^{\infty} e^{-j\frac{2\pi p}{L}x} W\left(\frac{2\pi p}{L}\right) \end{aligned} \tag{3.51}$$

Now we can substitute (3.51) in (3.38) and use the orthogonality property (3.39) of the complex exponentials to get

$$\begin{aligned} \sigma_n^2 = \int_{-L/2}^{L/2} C_L(x)e^{j\frac{2\pi n}{L}x}dx &= 2\pi \sum_{p=-\infty}^{\infty} W\left(\frac{2\pi p}{L}\right) \int_{-L/2}^{L/2} \left(\frac{1}{\sqrt{L}} e^{-j\frac{2\pi p}{L}x}\right)\left(\frac{1}{\sqrt{L}} e^{j\frac{2\pi n}{L}x}\right)dx \\ &= 2\pi \sum_{p=-\infty}^{\infty} W\left(\frac{2\pi p}{L}\right)\delta_{np} = 2\pi W\left(\frac{2\pi n}{L}\right) \equiv 2\pi W(n\Delta K), \end{aligned} \tag{3.52}$$

where we have introduced for convenience

$$\Delta K = \frac{2\pi}{L} \tag{3.53}$$

The expression in (3.52) shows that once a particular model (3.32) for an L-periodic correlation function C_L is chosen, the variances of the independent variables in the new

basis system will be (up to a constant) just samples of the power spectral density (3.16) defined for the infinite-extent non-periodic surface. The result (3.52) can be interpreted the other way around as well: if we decided to generate our finite-extent random surfaces using samples of the surface spectrum $W(K)$, the resulting ensemble would have the correlation function (3.32) rather than (3.17). Let us note that the power spectral density $W(K)$ as defined in (3.16) is an even function (because the correlation function is even, cf. (3.14)) so that (5.52) does not contradict the property (3.45) we have established for $\{\sigma_n^2\}$. Also, $W(K)$ is a non-negative function [Papoulis, 1991] (as in fact it should be if $C(x_2 - x_1)$ is specified as a non-negative definite kernel; this can be shown directly from the definition of the definiteness property [Courant and Hilbert, 1953, p. 123]) which assures that $\sigma_n^2 \geq 0$.

We can now combine (3.42), (3.47), (3.48) and (3.52) to yield

$$p(\{\eta_n\}) = \frac{1}{\sqrt{2\pi(2\pi W(0))}} \exp\left\{-\frac{\eta_0^2}{2(2\pi W(0))}\right\} \times \prod_{n=1}^{\infty} \frac{1}{\pi(2\pi W(n\Delta K))} \exp\left\{-\frac{1}{2}\sum_{n=1}^{\infty} \frac{\eta_{Rn}^2 + \eta_{In}^2}{(\pi W(n\Delta K))}\right\} \tag{3.54}$$

This expression suggests the following steps to "construct" a realization of the randomly rough Gaussian surface provided that we know the spectrum $W(K)$:

- generate a Gaussian random number η_0 with the variance $2\pi W(0)$;
- generate independent pairs of Gaussian random numbers η_{Rn} and η_{In} ($n > 0$) with variances $\pi W(2\pi n / L)$ (in principle, an infinite number of such pairs is necessary);
- combine η_{Rn} and η_{In} in $\eta_n = \eta_{Rn} + j\eta_{In}$ for $n > 0$ and use (3.44b) to get η_n for $n < 0$;
- calculate a realization of the randomly rough surface according to (3.40).

The choice of the surface length L will be dictated, in general, by a particular scattering problem, but as we have already pointed out it should be larger than the surface correlation length, i.e. the width of $C(x)$.

3.3.4 Surfaces with Band-Limited Spectra and Further Practical Considerations

In the previous Section we developed an approach which is capable of generating realizations of a zero mean, Gaussian, rough surfaces. However, so far it is of little practical use as we are faced with the necessity to deal with an infinite set of random numbers, which is not feasible in applied computer simulations. Also, a surface realization calculated in accordance with (3.40) is continuous while for computer simulation purposes we need to represent it by a finite number of points. Both these problems can be resolved if the spectrum $W(K)$ is band-limited i.e. vanishes outside some cutoff wavenumber K_c. As will be discussed in Chapter 4, for the ocean-like surfaces such a cutoff occurs naturally and it is also possible to consider an artificial cutoff for simulation purposes. In any case, let us consider $W(K)$ that has a property of being identically zero for all $|K| > K_c$.

For a band-limited spectrum, we will have a finite number of non-zero eigenvalues σ_n^2 of C_L in (3.32), as is evident from (3.52). The largest value of index n for which σ_n^2 is still not identically zero is from (3.46)

$$M = \left[\frac{K_c L}{2\pi} \right] \tag{3.55}$$

where "[ ]" denotes a truncation operation (taking an integer part). Let us now write (3.54) as follows:

$$\begin{aligned} p(\{\eta_n\}) &= \frac{1}{\sqrt{2\pi(2\pi W(0))}} \exp\left\{ -\frac{\eta_0^2}{2(2\pi W(0))} \right\} \\ &\times \prod_{m=1}^{M} \left(\frac{1}{\pi(2\pi W(m\Delta K))} \exp\left\{ -\frac{1}{2} \frac{\eta_{Rm}^2 + \eta_{Im}^2}{(\pi W(m\Delta K))} \right\} \right) \\ &\times \prod_{m=M+1}^{\infty} \left(\frac{1}{\pi\sigma_m^2} \exp\left\{ -\frac{1}{2} \frac{\eta_{Rm}^2 + \eta_{Im}^2}{(\sigma_m^2/2)} \right\} \right) \end{aligned} \tag{3.56}$$

In the above expression all σ_m^2 in the second product are identically zero. Let us recall the following definition of the δ-function [e.g. Arfken and Weber, 1995]:

$$\lim_{\alpha\to 0}\frac{1}{\sqrt{\pi}\alpha}\exp\left\{-\frac{x^2}{\alpha^2}\right\}=\delta(x) \tag{3.57}$$

In fact, (3.57) can be extended for more than one variable in the exponential [Jackson, 1975, p. 50]:

$$\lim_{\alpha\to 0}\frac{1}{\pi\alpha^2}\exp\left\{-\frac{x^2+y^2}{\alpha^2}\right\}=\delta(x)\delta(y), \tag{3.58}$$

which is more applicable in our case. Considering the terms in the second product in (3.59) in the sense of $\lim_{\sigma_m^2\to\infty}$ one can use (3.58) to rewrite (3.56) as

$$\begin{aligned} p(\{\eta_m\}) &= \frac{1}{\sqrt{2\pi(2\pi W(0))}}\exp\left\{-\frac{\eta_0^2}{2(2\pi W(0))}\right\} \\ &\times\prod_{m=1}^{M}\left(\frac{1}{\pi(2\pi W(m\Delta K))}\exp\left\{-\frac{\eta_{Rm}^2+\eta_{Im}^2}{2(\pi W(m\Delta K))}\right\}\right)\prod_{m=M+1}^{\infty}(\delta(\eta_{Rm})\delta(\eta_{Im})) \end{aligned} \tag{3.59}$$

It is clear now that (3.53) contains only $2M+1$ *random* variables η_0, η_{R1}, η_{I1}, ..., η_{RM}, η_{IM}; due to δ-functions all other variables are *deterministic*, each having a value of zero. Thus, (3.40) contains only *a finite* number of terms:

$$\zeta(x)=\frac{1}{\sqrt{L}}\sum_{m=-M}^{M}\eta_m e^{-j\frac{2\pi m}{L}x} \tag{3.60}$$

Of course, it should be remembered that η_n's in (3.60) are complex numbers and those with negative indices are constructed according to (3.44). Furthermore, (3.60) shows that realizations $\zeta(x)$ of the random process do not contain harmonics with spatial frequencies higher than

$$K_c' = 2\pi M / L \tag{3.61}$$

This means that each realization is band-limited, which is probably not very surprising and could be intuitively expected given the band-limited nature of $W(K)$.

Note that K_c' is in principle slightly different from K_c that we defined as a cutoff of a continuous spectrum $W(K)$, note a truncation operation in (3.55). From (3.61) and (3.55) they are related as

$$K_c' = \Delta K \left[\frac{K_c}{\Delta K} \right] \tag{3.62}$$

with ΔK defined in (3.53). Once again, square brackets in (3.62) indicate taking an integer part. Of course, if one specifies K_c as a multiple of ΔK, as is often the case when the cutoff is artificially introduced in numerical simulations, K_c and K_c' are equal. For what follows we will need K_c' in (3.61). However, the difference between K_c and K_c', if any, is quite minute (not more than $\Delta K = 2\pi / L$) and for almost all practical purposes can be disregarded.

We can now use the band-limited property along with the sampling theorem to represent our random surface realizations by a finite number of discrete points in the spatial domain as well. However, we should point out the following. *So far we based our derivations only on the statistical properties of the randomly rough surfaces; at no time were we concerned about any specifics of the scattering problem that we ultimately need to solve. Any further simplifications of* (3.60) *involving discretization of the continuous surface height* $\zeta(x)$ *should be based on the requirements posed by the electromagnetic problem.* Here we will use the sampling theorem as a guideline in determining the largest allowable discretization interval for $\zeta(x)$ in (3.60); however we will formulate the technique that is not limited to that particular interval but enables generating surface samples with smaller intervals Δx if necessary.

The sampling theorem states that if a function $f(x)$ is band-limited with respect to some wavenumber K_{up}, i.e. its Fourier spectrum is identically zero outside the interval $[-K_{up}, K_{up}]$, it can be represented as [e.g. Brigham, 1974, p. 83]

$$f(x) = \sum_{n=-\infty}^{\infty} f(n\Delta x) \frac{\sin \pi (x/\Delta x - n)}{\pi (x/\Delta x - n)} \tag{3.63}$$

provided that the sampling interval Δx is chosen as

$$\Delta x \le \frac{\pi}{K_{up}} \tag{3.64}$$

It is important to realize that while for such band-limited function its samples $\{f(n\Delta x)\}$ contain all the information about this function, the function *itself* still has to be "assembled" from these samples using (3.63).

While (3.64) provides an upper limit on Δx, the actual choice of this sampling interval will be studied in Chapter 4 based on the analysis of the MFIE. Right now this point can be illustrated as follows. When dealing with the scattering problem, we will have functions that, for example, depend on the surface height as follows:

$$b(x) \equiv B(\zeta(x), x)$$

(this is the case of dependence in the Kirchhoff current in the vertical case). Following the analysis, we will determine that $b(x)$ should be sampled at some interval Δx_b, i.e. we will need its values at points $x = n\Delta x_b$:

$$b(n\Delta x_b) = B(\zeta(n\Delta x_b), n\Delta x_b)$$

The above expression means that we will need to know the samples of the surface $\zeta(x)$ taken at the interval Δx_b, while from (3.64) one might conclude, for example, that a larger interval Δx_ζ would suffice to properly represent $\zeta(x)$. To avoid a cumbersome re-sampling procedure (i.e. representing the surface sampled at Δx_ζ by a series in (3.63) and then calculating new samples at Δx_b spacing) it is desirable to generate surface samples at the interval Δx_b from the beginning.

Let us consider applying the sampling theorem to surface realizations $\zeta(x)$ in (3.60). The Fourier spectrum of $\zeta(x)$ is, using (3.60):

$$S_\zeta(K) \equiv \int_{-\infty}^{\infty} \zeta(x) e^{jKx} dx = \frac{2\pi}{\sqrt{L}} \sum_{m=-M}^{M} \eta_m \delta(K - 2\pi m / L) \tag{3.65}$$

As we noted in (3.61) and as (3.65) confirms, $\zeta(x)$ is bandlimited with all spectral components outside $\pm 2\pi M / L \equiv \pm K_c'$ being zero. So, to apply (3.63)-(3.64), we use

$$K_{up} = K_c' \tag{3.66}$$

The sampling interval corresponding to the equality sign in (3.64) is sometimes called the critical sampling interval:

$$\Delta x_0 = \frac{\pi}{K_c'} \tag{3.67}$$

Because of the fact that the Fourier spectrum (3.65) of our function has impulsive behavior at $\pm K_c'$, the exact recovery of $\zeta(x)$ sampled at the critical interval (3.67) is not possible unless some additional constraints are enacted (namely, η_M should be real) [Bracewell, 1965]. Because of this we will avoid using the critical sampling interval. When necessary, a slightly smaller interval can be used, as will be discussed.

The samples of $\zeta(x)$ in (3.60) evaluated at $x = n\Delta x$ ($n = 0, \pm 1, \pm 2, \ldots$) are

$$\zeta(n\Delta x) = \frac{1}{\sqrt{L}} \sum_{m=-M}^{M} \eta_m e^{-j\frac{2\pi\Delta x}{L}nm} \tag{3.68}$$

As has been assumed and as is evident from (3.60), $\zeta(x)$ is L-periodic. It is desirable to choose

$$L = N\Delta x, \tag{3.69}$$

where N is an integer (we will discover later that if we want to use the radix 2 Fast Fourier Transform (FFT), N should be a power of 2) . Then (3.68) is rewritten as

$$\zeta(n\Delta x) = \frac{1}{\sqrt{L}} \sum_{m=-M}^{M} \eta_m e^{-j\frac{2\pi}{N}nm} \tag{3.70}$$

and the sequence $\{\zeta(n\Delta x)\}$ is also periodic with the period. Note that (3.70) together with (3.64) and (3.66) means that the following should hold (we use only the inequality sign to avoid the problems with the critical sampling interval mentioned above):

$$N > 2K_c'\left(\frac{L}{2\pi}\right) = \frac{2K_c'}{\Delta K} \tag{3.71}$$

Recalling (3.61) we get

$$N > 2M \tag{3.72}$$

We can now determine the largest allowed value of the sampling interval that still does not exceed the critical interval Δx_0 in (3.67). Setting $N = 2M + 2$ (we add 2 and not 1 to keep N even, a property that we will eventually need) and using (3.69), (3.53) and (3.61), we find:

$$\Delta x_0' = \frac{L}{2M+2} = \frac{\pi}{(2\pi/L)(M+1)} = \frac{\pi}{\Delta K(M+1)} = \frac{\pi}{(K_c' + \Delta K)} \tag{3.73}$$

Though a straightforward computation of (3.68) or (3.70) is possible, it is rather expensive computationally, especially when N and M are large. This problem could be alleviated considerably if we were able to apply the FFT technique. To do this, we need to reformulate (3.70) as the Discrete Fourier Transform (DFT) type sum [Brigham, 1974].

Keeping in mind (3.72) let us extend the limits of summation in (3.70) to $\pm(N-1)$. This can be done because for $|m| > M$ all η_m's should be zero as we discussed following (3.59). We get:

$$\zeta(n\Delta x) = \frac{1}{\sqrt{L}} \sum_{m=-(N-1)}^{N-1} \eta_m e^{-j\frac{2\pi}{N}nm} \tag{3.74}$$

Fig. 3-2 illustrates how this extension of the limits is performed. As we mentioned earlier, the sequence $\{\zeta(n\Delta x)\}$ is periodic. We will confine our interest to the samples

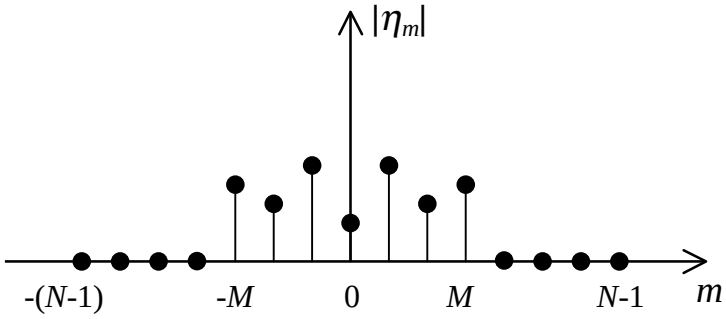

Figure 3-2. Illustration of the extension of the summation limits in (3.70) for the case of $M = 3$ and $N = 8$.

with $n\Delta x \in [-L/2; L/2]$. Assuming that N is *even*, this means that the index n varies from $-N/2$ to $N/2$. Also, due to the periodicity,

$$\zeta\left(-(N/2)\Delta x\right) = \zeta\left((N/2)\Delta x\right) \tag{3.75}$$

So, we need to consider only N samples, say $\zeta\left(-(N/2)\Delta x\right),\ldots,\zeta\left((N/2-1)\Delta x\right)$. This situation is illustrated in Fig. 3-3. The index n in (3.74) now assumes the values

$$n=-N/2,\ldots,N/2-1 \tag{3.76}$$

Further, in order to cast (3.74) in the DFT form, it is convenient to turn to an index that

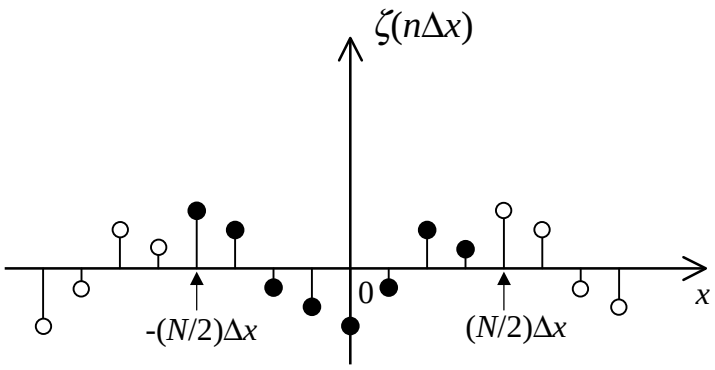

Figure 3-3. Periodic sequence of samples of a random surface realization. We will consider only N samples shown with solid circles. In this example, $N=8$.

runs from 0 to $N-1$:

$$p=n+N/2 \tag{3.77}$$

Then, on the left-hand side of (3.74) we will have

$$\zeta\left(n\Delta x\right)=\zeta\left((p-N/2)\Delta x\right)\equiv\hat{\zeta}_p \tag{3.78}$$

where we have defined the new sequence $\{\hat{\zeta}_p\}$. For example, from (3.78) one can see that $\hat{\zeta}_0$ corresponds to $\zeta\left((-N/2)\Delta x\right)=\zeta\left(-L/2\right)$. Now (3.74) can be rewritten as

$$\hat{\zeta}_p=\frac{1}{\sqrt{L}}\sum_{m=-(N-1)}^{N-1}\eta_m e^{-j\frac{2\pi}{N}(p-N/2)m}\equiv\sum_{m=-(N-1)}^{N-1}\hat{\eta}_m e^{-j\frac{2\pi}{N}pm} \tag{3.79}$$

where we have defined

$$\hat{\eta}_m = \frac{\eta_m e^{j\pi m}}{\sqrt{L}} = \frac{(-1)^m}{\sqrt{L}}\eta_m \tag{3.80}$$

(at this point the factor $1/\sqrt{L}$ was also absorbed in $\hat{\eta}_m$ for convenience). We point out that since each of these new $\hat{\eta}_m$'s differs from the corresponding η_m by a *real* factor, they still satisfy the same complex conjugate relationships that we had in (3.44) for η_m's. In particular, $\hat{\eta}_0$ is real. Let us now write (3.79) as follows:

$$\begin{aligned}\hat{\zeta}_p &= \left(\hat{\eta}_0 + \sum_{m=1}^{N-1} \hat{\eta}_m e^{-j\frac{2\pi}{N}pm} + \sum_{m=-(N-1)}^{-1} \hat{\eta}_m e^{-j\frac{2\pi}{N}pm} \right) \\ &= \left(\hat{\eta}_0 + \sum_{m=1}^{N-1} \left\{ \hat{\eta}_m e^{-j\frac{2\pi}{N}pm} + \hat{\eta}_{-m} e^{j\frac{2\pi}{N}pm} \right\} \right)\end{aligned} \tag{3.81}$$

Using (3.44b) that holds for $\hat{\eta}_m$'s as well, we continue with (3.81):

$$\begin{aligned}\hat{\zeta}_p &= \left(\hat{\eta}_0 + \sum_{m=1}^{N-1} \left\{ \hat{\eta}_m e^{-j\frac{2\pi}{N}pm} + \hat{\eta}_m^* \left(e^{-j\frac{2\pi}{N}pm} \right)^* \right\} \right) \\ &= \left(\hat{\eta}_0 + 2\,\mathrm{Re}\left\{ \sum_{m=1}^{N-1} \hat{\eta}_m e^{-j\frac{2\pi}{N}pm} \right\} \right) = 2\,\mathrm{Re}\left\{ \sum_{m=0}^{N-1} \hat{\eta}'_m e^{-j\frac{2\pi}{N}pm} \right\}\end{aligned} \tag{3.82}$$

where we have introduced yet another definition

$$\hat{\eta}'_m \equiv \begin{cases} \hat{\eta}_0 / 2, & m = 0 \\ \hat{\eta}_m & \text{otherwise} \end{cases} \tag{3.83}$$

Now within the rightmost curly bracket in (3.82) *we have a DFT-type sum*, with both indices (p and m) running from 0 to $N-1$. It can be calculated (for all values of p simultaneously) very efficiently using FFT algorithms. In particular, if N is a power of 2, a rather simple and commonly used radix 2 FFT can be applied. This was the major reason why we sought to recast (3.68) into the form in (3.82).

Now we can recall the intermediate steps and auxiliary definitions we have made to arrive at (3.82) and summarize the procedure to generate the samples of the random surface realizations.

1. Decide on the surface length L and the sampling interval Δx. L should be larger than the surface correlation length; other requirements can and will arise from considering the electromagnetic problem. Δx is determined from the electromagnetic problem and should be subject to the constraint in (3.64). Also, L and Δx should be chosen so that N in (3.69) is a power of 2.
2. Generate a Gaussian random number η_0 with the variance $2\pi W(0)$. Generate M pairs of independent Gaussian random numbers η_{Rm} and η_{Im} with variances $\pi W(2\pi m / L)$. The number M is determined from (3.55).
3. Combine η_{Rm}'s and η_{Im}'s into M complex numbers $\eta_m = \eta_{Rm} + j\eta_{Im}$, $m = 1, ..., M$.
4. Complete this sequence with $N - M - 1$ zero terms: $\eta_m = 0$, $m = M + 1, ..., N - 1$.
5. Calculate $\hat{\eta}'_m$'s (cf. (3.80) and (3.83)):

$$\hat{\eta}'_m \equiv \begin{cases} \dfrac{\eta_0}{2\sqrt{L}}, & m = 0 \\ \dfrac{(-1)^m \eta_m}{\sqrt{L}}, & m = 1, ..., N-1 \end{cases}$$

6. Calculate N (complex) numbers $\hat{\xi}'_p$, $p = 0, ..., N$:

$$\hat{\xi}'_p = \sum_{m=0}^{N-1} \hat{\eta}'_m e^{-j\frac{2\pi}{N}pm}$$

   (cf. (3.82)) using the FFT.

7. Take the real part of each $\hat{\xi}'_p$ and multiply results by 2 (again, cf. (3.82)):

$$\hat{\xi}_p = 2\,\mathrm{Re}\{\hat{\xi}'_p\}, \quad p = 0, ..., N$$

8. Associate $\hat{\xi}_p$'s with the surface samples (from (3.78)):

$$\zeta(n\Delta x) = \hat{\xi}_{n+N/2}, \quad n = -N/2, ..., N/2 - 1$$

The outlined algorithm contains a number of multiplication operations that occur at different steps. These operations can be aggregated to make the algorithm more efficient. Another useful point to recall is that if one has several *independent* Gaussian random variables $\{\gamma_i\}$ with *unit* variances, the random variables obtained by multiplying each γ_i by some σ_i will also be *independent* Gaussian random variables each having a variance of σ_i^2. This can be confirmed, for example, from the multiplicative probability transformation [Papoulis, 1991]. In fact, since each single-variable Gaussian pdf is even, factors σ_i can be negative as well. We will use these considerations in the next Section where the problem of generating surface derivatives will be discussed and the algorithm for calculating both surface height and two first surface derivatives will be outlined.

3.3.5 Calculation of the Surface Slope and Higher Surface Derivatives

In Chapter 2 we noted that currents and propagators in the MFIE depend not only on the surface height but also on the surface slope. In fact, as we will discuss in Chapter 4, the MFIE propagator matrix will contain so-called "curvature" terms that are proportional to the second surface derivative. So we need to address the question of how to generate derivatives of realizations of randomly rough surface.

Let us start with expression for a surface realization in (3.60). The l-th derivative of $\zeta(x)$ will be:

$$\zeta^{(l)}(x) \equiv \frac{d^l \zeta(x)}{dx^l} = \frac{1}{\sqrt{L}} \sum_{m=-M}^{M} \left(-j\frac{2\pi m}{L} \right)^l \eta_m e^{-j\frac{2\pi m}{L}x} = \frac{1}{\sqrt{L}} \sum_{m=-M}^{M} (-j\Delta K m)^l \eta_m e^{-j\Delta K m x} \tag{3.84}$$

From (3.84) it is obvious that derivatives are also band-limited functions, with the same cutoff K_c' as in (3.61). This means that the sampling theorem (3.63)-(3.64) can be applied to the derivatives in (3.84) in the very same manner that we did to $\zeta(x)$ itself. The derivatives $\zeta^{(l)}(x)$ can be reconstructed according to (3.63) from their samples calculated as (compare to (3.68))

$$\zeta^{(l)}(n\Delta x) = \frac{1}{\sqrt{L}} \sum_{m=-M}^{M} (-j\Delta K m)^l \eta_m e^{-j\frac{2\pi\Delta x}{L}nm} \tag{3.85}$$

Because the cutoff wavenumber remains the same, the sampling interval Δx that is sufficient for reconstruction of $\zeta(x)$ will be equally sufficient for all derivatives. *So, the same* Δx *can be simultaneously used both in* (3.68) *and* (3.85). In fact, (3.68) can be viewed as special case of (3.78) when $l = 0$. It should be remembered that the actual requirement on Δx comes from the electromagnetic problem.

Of course, some caution should be used when deciding if the original surface spectrum $W(K)$ can be treated as band-limited when surface derivatives are of interest. This is because the higher the derivative, the more the spectral components with high wavenumbers are emphasized, as can be seen in (3.84). So even though some spectral components are considered negligible in the representation of the surface height, they may be important for higher derivatives. In our studies we will need the surface derivatives of order no higher than 2 and will assume that the same spectral cutoff holds for all of them.

We can recast (3.85) into the DFT-type sum, just as we did with (3.68). This will allow us to apply the FFT technique. Following exactly the same steps that led to (3.82) we obtain

$$\hat{\zeta}_p^{(l)} = 2\,\mathrm{Re}\left\{\sum_{m=0}^{N-1} \hat{\eta}'_m (-j\Delta K m)^l \, e^{-j\frac{2\pi}{N}pm}\right\}. \tag{3.86}$$

The $\hat{\eta}'_m$'s that appear in (3.86) are defined in (3.83). It should be stressed that the same set $\{\hat{\eta}'_m\}$ should be used while generating samples of the surface height and its derivatives for any particular surface realization. The sequence $\{\zeta_p^{(l)}\}$, $p = 0, ..., N-1$ can be associated with the samples of the l-th surface derivative in the manner similar to (3.78):

$$\zeta^{(l)}(n\Delta x) = \zeta^{(l)}((p - N/2)\Delta x) \equiv \hat{\zeta}_p^{(l)} \tag{3.87}$$

Finally, we can rewrite (3.86) for the cases of the first and the second derivatives that we will be interested in:

$$\hat{\zeta}_p^{(1)} = 2\,\mathrm{Re}\left\{\sum_{m=0}^{N-1} \hat{\eta}'_m (-j\Delta K m) e^{-j\frac{2\pi}{N}pm}\right\} = 2\,\mathrm{Im}\left\{\sum_{m=0}^{N-1} \hat{\eta}'_m \Delta K m \, e^{-j\frac{2\pi}{N}pm}\right\} \tag{3.88}$$

$$\hat{\zeta}_p^{(2)} = 2\,\mathrm{Re}\left\{\sum_{m=0}^{N-1}\hat{\eta}'_m(-j\Delta Km)^2 e^{-j\frac{2\pi}{N}pm}\right\} = -2\,\mathrm{Re}\left\{\sum_{m=0}^{N-1}\hat{\eta}'_m(\Delta Km)^2 e^{-j\frac{2\pi}{N}pm}\right\} \quad (3.89)$$

The algorithm for generating surface realization and its first and second derivatives could then be as follows. It resembles very much the procedure outlined in the previous Section; we also implemented some changes (like combining most of multiplications at a single step) discussed at the end of that Section.

1. Decide on the surface length L and the sampling interval Δx. L should be larger than the surface correlation length; other requirements can and will arise from considering the electromagnetic problem. Δx is determined from the electromagnetic problem and should be subject to the constraint in (3.64). Also, L and Δx should be chosen so that N in (3.69) is a power of 2.
2. Generate $2M+1$ independent Gaussian random numbers γ_i with unit variances, $i = 1, ..., 2M+1$.
3. Combine them in the $M+1$ complex numbers $\hat{\gamma}_m$ as follows:

$$\hat{\gamma}_0 = \gamma_1 + j0$$

$$\hat{\gamma}_m = \gamma_{2m} + j\gamma_{2m+1},\ m = 1, ..., M$$

4. Calculate

$$\hat{\eta}'_m \equiv \begin{cases} \sqrt{\dfrac{\pi \mathrm{W}(0)}{2L}}\hat{\gamma}_0, & m = 0 \\ \sqrt{\dfrac{\pi \mathrm{W}(2\pi m/L)}{L}}\hat{\gamma}_m, & m = 1, ..., M \end{cases}$$

5. Complete this sequence with $N-M-1$ zero terms: $\hat{\eta}'_m = 0$, $m = M+1, ..., N-1$.
6. Calculate N complex numbers $\hat{\zeta}'_p$, $p = 0, ..., N$:

$$\hat{\zeta}'_p = \sum_{m=0}^{N-1}\hat{\eta}'_m e^{-j\frac{2\pi}{N}pm}$$

using the FFT.

7. Multiply each $\hat{\eta}'_m$'s by ΔKm, $m = 0, ..., M$ and calculate N complex numbers $\hat{\zeta}'^{(1)}_p$, $p = 0, ..., N$:

$$\hat{\zeta}'^{(1)}_p = \sum_{m=0}^{N-1} \hat{\eta}'_m \Delta K m \, e^{-j\frac{2\pi}{N}pm}$$

using the FFT.

8. Multiply each $\hat{\eta}'_m$'s by $(\Delta K m)^2$, $m = 0, ..., M$ and calculate N complex numbers $\hat{\zeta}'^{(2)}_p$, $p = 0, ..., N$:

$$\hat{\zeta}'^{(2)}_p = \sum_{m=0}^{N-1} \hat{\eta}'_m (\Delta K m)^2 e^{-j\frac{2\pi}{N}pm}$$

using the FFT.

9. Take the real part of each $\hat{\zeta}'_p$ and multiply results by 2:

$$\hat{\zeta}_p = 2\,\mathrm{Re}\left\{\hat{\zeta}'_p\right\},\ p = 0, ..., N$$

10. Take the imaginary part of each $\hat{\zeta}'^{(1)}_p$ and multiply results by 2:

$$\hat{\zeta}^{(1)}_p = 2\,\mathrm{Im}\left\{\hat{\zeta}'^{(1)}_p\right\},\ p = 0, ..., N$$

11. Take the real part of each $\hat{\zeta}'^{(1)}_p$ and multiply results by -2:

$$\hat{\zeta}^{(2)}_p = -2\,\mathrm{Re}\left\{\hat{\zeta}'^{(2)}_p\right\},\ p = 0, ..., N$$

12. Associate $\hat{\zeta}_p$'s, $\hat{\zeta}^{(1)}_p$'s and $\hat{\zeta}^{(2)}_p$'s with the samples of the surface height, first and second derivative according to (3.78) and (3.87):

$$\zeta(n\Delta x) = \hat{\zeta}_{n+N/2},\ \zeta^{(1)}(n\Delta x) = \hat{\zeta}^{(1)}_{n+N/2},\ \zeta^{(2)}(n\Delta x) = \hat{\zeta}^{(2)}_{n+N/2},$$
$$n = -N/2, ..., N/2 - 1$$

As we mentioned, the factors $(-1)^m$ were dropped (or "absorbed" in the random numbers $\hat{\gamma}_m$) since the corresponding probability transformation will still lead to independent Gaussian variables.

Appendix 3.A Generating Random Numbers Having a Gaussian PDF from Uniformly Distributed Random Numbers

We will assume that a computer can generate random numbers that are uniformly distributed on the interval [0,1]. Virtually all computer platforms and programming language compilers provide such a tool.

Consider a random variable α with the pdf

$$p_\alpha(\alpha) = \begin{cases} 1, & 0 \le \alpha \le 1 \\ 0 & \text{elswhere} \end{cases} \tag{3.A.1}$$

Our goal is to obtain a random variable β with the Gaussian pdf:

$$p_\beta(\beta) = \frac{1}{\sqrt{2\pi}\sigma} \exp\left(-\frac{\beta^2}{2\sigma^2} \right) \tag{3.A.2}$$

There are several ways to achieve this, one being the transformation of a random variable. Suppose we have a random variable *x* with the pdf $p_x(x)$ and form the new variable *y* through a transformation

$$y = f(x) \tag{3.A.3}$$

Let $f(x)$ be a monotone function so that the inverse function $x = f^{-1}(y)$ exists. Consider the normalization relation:

$$1 = \int_a^b p_x(x)dx = \int_A^B p_x(f^{-1}(y)) \frac{df^{-1}(y)}{dy} dy = \int_{\min(A,B)}^{\max(A,B)} p(y)dy \tag{3.A.4}$$

Note that if f^{-1} is decreasing, then the derivative is negative. But then, also, $B<A$ (we have assumed $b>a$) and we should switch the limits of integration, which would result in another minus sign and the overall result will again be positive. So, the pdf of the random variable *y* is then

$$p_y(y) = \left| \frac{df^{-1}(y)}{dy} \right| p_x\left(f^{-1}(y)\right) \tag{3.A.5}$$

We would like to attempt to find a transformation $\beta = f(\alpha)$ to transform the uniformly distributed α into the normally distributed β. A straightforward approach would suggest that since $p_x(x) \equiv p_\alpha(\alpha) = 1$, it is desirable to have an f that satisfies the following equation (from (3.A.5))

$$\frac{\mathrm{d}f^{-1}(\beta)}{\mathrm{d}\beta} = \frac{1}{\sqrt{2\pi}\sigma}\exp\left(-\frac{\beta^2}{2\sigma^2}\right)$$

However, the solution for $f^{-1}(\beta)$ will be in terms of the error function $\mathrm{erf}(\beta)$ and this would further complicate finding the inverse function. So, a direct application of (3.A.5) apparently does not lead to any simple algorithm. However, let us use it to obtain a helpful result. Consider the following inverse transformation:

$$f^{-1}(y) = \exp\left(-\frac{y^2}{2\sigma^2}\right), \qquad y > 0 \tag{3.A.6}$$

Then, from (3.A.5) with $p_x \equiv p_\alpha$ as in (3.A.1), we have:

$$p_y(y) = 1\left|\frac{df^{-1}(y)}{dy}\right| = \frac{y}{\sigma^2}\exp\left(-\frac{y^2}{2\sigma^2}\right), \tag{3.A.7}$$

which is the Rayleigh pdf. So, the transformation (from (3.A.6))

$$y = f(x) = \sigma\sqrt{-2\ln x} \tag{3.A.8}$$

applied to the uniformly distributed random variable α in (3.A.1) gives the random variable with the Rayleigh pdf.

Let us now take a different approach. Consider *two* independent Gaussian random variables, β_1 and β_2 with the same variance σ^2 and the pdf

$$p_{12}(\beta_1, \beta_2) = p_1(\beta_1)\,p_2(\beta_2) = \frac{1}{2\pi\sigma^2}\exp\left(-\frac{\beta_1^2 + \beta_2^2}{2\sigma^2}\right) \tag{3.A.9}$$

Consider this pdf in polar coordinates (ρ, φ):

$$\beta_1 = \rho\cos\varphi, \qquad \beta_2 = \rho\sin\varphi \tag{3.A.10}$$

with $0 \le \rho < \infty$ and $0 \le \varphi < \pi$. To get the expression for the pdf in the polar coordinates let us again write the normalization condition in both coordinate systems, noting that $\beta_1^2 + \beta_2^2 = \rho^2$ and $d\beta_1 d\beta_2 = \rho\, d\rho\, d\varphi$:

$$1 = \int_{-\infty}^{\infty}\int_{-\infty}^{\infty}\frac{1}{2\pi\sigma^2}\exp\left(-\frac{\beta_1^2 + \beta_2^2}{2\sigma^2}\right)d\beta_1 d\beta_2 = \int_0^{2\pi}\int_0^{\infty}\frac{1}{2\pi\sigma^2}\exp\left(-\frac{\rho^2}{2\sigma^2}\right)\rho\, d\rho\, d\varphi \tag{3.A.11}$$

The integrand on the right-hand side represents $p_{\rho\varphi}(\rho, \varphi)$. Clearly, it can be written as

$$p_{\rho\varphi}(\rho,\varphi) = p_{\rho}(\rho)p_{\varphi}(\varphi), \tag{3.A.12}$$

which means that ρ and φ are independent random variables with

$$p_{\varphi}(\varphi) = \begin{cases} 1/2\pi, & 0 \le \varphi < 2\pi \\ 0 & \text{elswhere} \end{cases} \tag{3.A.13}$$

and

$$p_{\rho}(\rho) = \frac{\rho}{\sigma^2}\exp\left(-\frac{\rho^2}{2\sigma^2}\right), \ \rho \ge 0 \tag{3.A.14}$$

One can see:

- $p_{\varphi}(\varphi)$ is the uniform distribution that is very similar to $p_{\alpha}(\alpha)$; one can use the transformation $\varphi = 2\pi\alpha$ to get $p_{\varphi}(\varphi)$ from $p_{\alpha}(\alpha)$;
- $p_{\rho}(\rho)$ is the Rayleigh pdf that can be obtained from $p_{\alpha}(\alpha)$ using (3.A.8).

So, assuming that we can generate two independent sequences of the uniformly distributed random numbers corresponding to random variables α_1 and α_2, the algorithm for generating the Gaussian random numbers is as follows:

1) generate two independent random numbers α_1 and α_2 with the pdf in (3.A.1);

2) form $\varphi = 2\pi\alpha_1$;

3) form $\rho = \sigma\sqrt{-2\ln\alpha_2}$;

4) calculate $\beta_1 = \rho\cos\varphi$, and $\beta_2 = \rho\sin\varphi$, which are two independent Gaussian random numbers with variance σ.

More discussion on this and other methods to generate Gaussian random numbers can be found in [Papoulis, 1991].

Chapter 4

Discretization of the Integral Equation Describing Scattering by Rough Conducting Surfaces

In this chapter we present the results of numerical simulations of scattering from one-dimensional randomly rough surfaces with an ocean-like Pierson-Moskowitz (P-M) spectrum. The simulations were based on a recently proposed numerical technique, the method of ordered multiple interactions (MOMI) described in Chapter 2. Extensive simulations including the low grazing regime that was not quite feasible with previous less efficient techniques have been completed. However, the results appeared to show an unexpected sensitivity to the choice of the sampling interval, especially at low grazing angles. Further numerical studies showed that the problem was not with the numerical technique but rather with the way that the magnetic field integral equation (MFIE) was discretized. In a sense MOMI, due to its efficiency, allowed us to check the results using much smaller sampling intervals than are normally used (the smaller intervals result in larger matrices which can be handled by MOMI but are prohibitive for other methods) to isolate the problem. With regards to the MFIE, we demonstrate that the inclusion of so-called "curvature terms" (terms proportional to the second derivative of the surface height) in the diagonal of the propagator matrix completely eliminates this problem. Previously, there had been different views on the role of these terms, with some authors regarding them as an additional correction (e.g. [Kapp and Brown, 1996]) and some ignoring them altogether [Tran and Elson, 1997]. Also, it was noted [Kapp, 1995] that at least for surfaces with the Gaussian spectrum inclusion or exclusion of these terms does not make any difference. We settle these diverse issues with our results.

Having found numerically that for P-M surfaces the curvature terms are important, we examine the discretization procedure for the MFIE analytically and demonstrate that the "curvature terms" should be included in the propagator matrix. We also formulate a criterion for choosing the sampling interval as a function of

electromagnetic wavelength and the surface spectral cutoff. Finally, the choice of the surface spectral cutoff for the scattering simulation purposes is studied numerically.

4.1 Introduction and Preview of the Results

Before any numerical technique can be applied to solve the integral equation, it must be discretized, i.e. recast in a matrix form. Clearly, the discretization can affect the accuracy of the computed solutions. When studying scattering from one-dimensional random surfaces with an ocean-like Pierson-Moskowitz (P-M) type spectrum, we found that questions regarding the stability of the solution with respect to sampling interval needed to be addressed and that these questions are tied to an understanding of a role of the so-called "curvature term" in the propagator.

In regards to the MFIE, there has been some discussion [Kapp, 1995], [Brown and Kapp, 1996] on whether the curvature term (a term which is proportional to the surface curvature[1]) should be included in the diagonal of the propagator matrix in the discretized equation and how this term affects both the traditional Method of Moments (MoM) and MOMI solutions. For P-M surfaces, we observed that using a propagator matrix without the curvature term can result in a significant sensitivity in the calculated field to changes in the sampling interval - an effect that is not present for surfaces with Gaussian spectrum. This effect is pronounced in the case of horizontal polarization for backscattering at low grazing angles and is not very evident for vertical polarization. It appears to be tied to the small-scale (high-frequency) surface curvature which is characteristic of the P-M spectrum. A stable result can eventually be achieved by decreasing the sampling interval, which, of course, increases the matrix dimension and computational expense of the algorithm. If, however, the curvature terms are included in the diagonal of the propagator matrix, the stable result is obtained at much larger sampling intervals and no drastic increase in a sampling rate is necessary.

This finding prompted us to take a more in-depth look at how the discretization of MFIE is performed, what the role of the curvature term is, and if it should appear in the propagator matrix as a result of discretization. The behavior of the spectra for the currents

[1] For 1-dimensional surfaces curvature is classically defined as $\zeta_{xx}/(1+\zeta_x^2)^{3/2}$; however, as used herein, the term "curvature" will refer to the second surface derivative, ζ_{xx}.

and the propagator entering the MFIE for P-M surfaces suggest that they can be treated as band-limited functions, with the upper wavenumber (or spatial frequency) beyond which the spectra are assumed to effectively vanish being related to the cutoff in P-M spectrum. Consequently, the sampling theorem can be applied to discretize the MFIE. This consideration suggests choosing the sampling interval based in general on *both* the electromagnetic wavelength and the surface spectral cutoff. Also, it shows that the curvature term, in fact, should appear in the diagonal of the propagator matrix that results from its discretization by sampling and that no higher-order corrections should be included in either the off-diagonal or diagonal terms. It should be stressed that although we used MOMI as the core of our numerical algorithm, the discussion of discretization refers to the original MFIE before it is reformulated into MOMI. *That is why we fully expect that similar problems with sampling stability, when the curvature terms are left out of the diagonal of the propagator matrix, will be observed no matter what numerical method is used to solve the discretized MFIE.*

Our result relates the sampling interval to electromagnetic wavelength and the surface spectral cutoff. In Chapter 3 we briefly discussed that in natural ocean surfaces such a cutoff occurs due to viscous damping mechanisms and can vary if, for example, pollutants or surfactants are present. However, one can expect that the surface spectral components with the wavenumbers much larger than the electromagnetic wavenumber may have little or no effect on the surface back scattering, and for scattering simulation purposes a lower, an artificial surface spectral cutoff can be introduced. We study how the spectral cutoff affects the NRCS at different angles of incidence and give the recommendation for a choice of such artificial cutoff.

4.2 Scattering Simulations for 1-D Pierson-Moskowitz Surfaces

4.2.1 The Discretized MFIE and the "Curvature Term"

The development of the integral equation for rough surface scattering and its numerical solution were discussed in Chapter 2. There we wrote down the MFIE in its discretized form (2.18)-(2.19). The discretization of the MFIE can affect the accuracy of its solution and the calculated scattered field. One parameter that can obviously have an impact and whose choice should be addressed is the sampling interval Δx. Also, there

have been different treatments of the diagonal elements of the propagator matrix in (2.19). In the original version of MOMI [Kapp and Brown, 1996] the diagonal elements of the propagator matrix P_{mm} were set to be zero. Other authors [Thorsos, 1988] include in the diagonal a term that is proportional to the second derivative of the surface height and is often referred to as the "curvature term":

$$P_{mm} = \pm \frac{\zeta_{xx}(x_m)}{2\pi(1+\zeta_x^2(x_m))}\Delta x \tag{4.1}$$

In (4.1) the upper sign corresponds to the case of vertical polarization and the lower to the horizontal polarization. [Kapp and Brown, 1996] argued that this term can be neglected if it is small compared to one, which can always be achieved by choosing Δx sufficiently small. The question about the inclusion of this term was also addressed in [Kapp, 1995] and [Brown and Kapp, 1996]. One of the conclusions was that the curvature term does not affect the rate of MOMI convergence. It was also reported that for one sample sinusoidal surface with high curvature and the field incident at 45° with respect to the normal, the inclusion of the curvature term did permit an increase in the sampling interval resulting in the same scattered field as would be obtained without the curvature term but with tighter sampling. Nevertheless, for a randomly rough surface with Gaussian spectrum and root mean square (rms) slopes as high as 45° illuminated at the incident angle of 85°, no effects related to inclusion or exclusion of the curvature term were observed. The study in [Kapp, 1995] regarded the curvature term as an additional correction to the already extracted self-term and pointed out that it may be inconsistent to include this correction on the diagonal of the propagator matrix and not include similar corrections proportional to higher surface derivatives in off-diagonal terms.

In the subsequent sections we present the results of numerical calculations of scattering from randomly rough surfaces with P-M spectra and these results suggest that for such surfaces the curvature term can play an important role and should be included in the diagonal of the propagator matrix. In Section 4.3 we discuss the procedure that leads to the discretized MFIE (2.18)-(2.19) and suggest a choice of the sampling interval for P-M surfaces. It will be shown that *once the proper sampling interval is chosen, the*

curvature term in (4.1) *must appear on the diagonal of the propagator matrix, the off-diagonal terms should be samples of the propagator as given by* (2.19), *and there is no need for any higher-order corrections to either the diagonal or the off-diagonal terms.*

4.2.2 "Pierson-Moskowitz" Randomly Rough Surfaces

We used MOMI to calculate the scattering from ocean-like randomly rough perfectly conducting surfaces described by a P-M spectrum. For the 1-D surfaces we used a one-dimensional version of the P-M spectrum proposed by E. Thorsos [Thorsos, 1990]:

$$W(K) = \frac{\alpha}{4|K|^3} \exp\left\{ -\frac{\beta g^2}{K^2 U^4} \right\} \tag{4.2}$$

In (4.2) K is the spatial wavenumber (which can be both positive and negative), U is the windspeed at a height of 19.5 m, $g = 9.81\,\mathrm{m/s^2}$ is gravity acceleration and other constants are $\alpha = 8.10 \times 10^{-3}$ and $\beta = 0.74$. The spectrum in (4.2) is shown in Fig. 4-1 for several windspeeds. The spectrum (4.2) has a peak at the wavenumber

$$K_p = \sqrt{\frac{2\beta}{3}} \frac{g}{U^2} \tag{4.3}$$

which can be interpreted as corresponding to the dominant wave having the wavelength

$$\Lambda_p = \frac{2\pi}{K_p} = \pi \sqrt{\frac{6}{\beta}} \frac{U^2}{g} \tag{4.4}$$

This dominant surface wavelength turns out to be closely related to the surface correlation length L_c. Indeed, if L_c is defined as

$$L_c = \frac{1}{C^2(0)} \int_{-\infty}^{\infty} C^2(x)\,dx \tag{4.5}$$

the correlation length turns out to be directly proportional to Λ_p:

$$L_c = \frac{3\pi}{8} \sqrt{\frac{\pi}{2\beta}} \frac{U^2}{g} = \frac{\sqrt{3\pi}}{16} \Lambda_p \tag{4.6}$$

Details regarding the definition in (4.5) and the calculation of L_c in (4.6) are given in Appendix 4.A at the end of this Chapter. An alternative to the definition in (4.5) is also considered there. The mean square surface height is

$$\langle \zeta^2 \rangle = C(0) = \int_{-\infty}^{\infty} W(K)dK = \frac{\alpha U^4}{4\beta g^2} \tag{4.7}$$

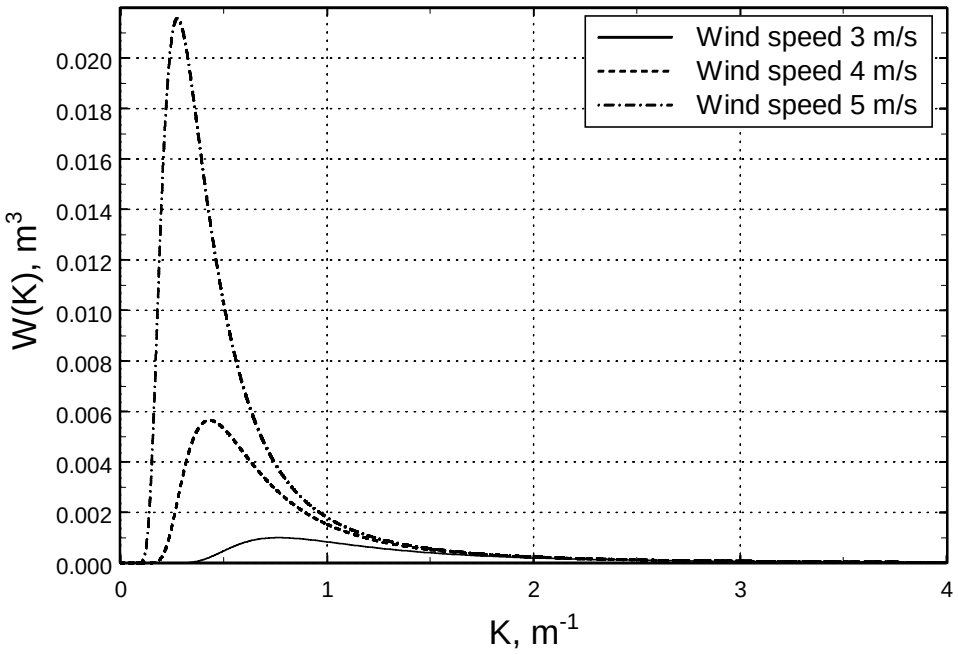

Figure 4-1. 1-D Pierson-Moskowitz spectrum in (4.2) for several values of the wind speed.

The P-M spectrum (4.2) has only one variable parameter, the windspeed *U*, which controls both the mean-square surface height and the dominant surface wavelength as can be seen from (4.4) and (4.7). The surface correlation function $C(x)$, which is related to the surface spectrum as in (3.17), is shown in Fig. 4-2 for a windspeed $U = 5\,\text{m/s}$. It is instructive to examine how well the correlation length L_c and the related dominant wavelength Λ_p describe the width of the correlation function. For $U = 5\,\text{m/s}$, Λ_p is $22.8\,\text{m}$. We can see from Fig. 4-2 that outside $x = \pm 2\Lambda_p$ the correlation function is essentially zero. L_c for this windspeed is 4.3 m and is smaller than Λ_p. It may serve as a

good indicator of the width of the main peak in Fig. 4-2. However, Λ_p is obviously more handy in determining when the correlation function drops to a negligible level.

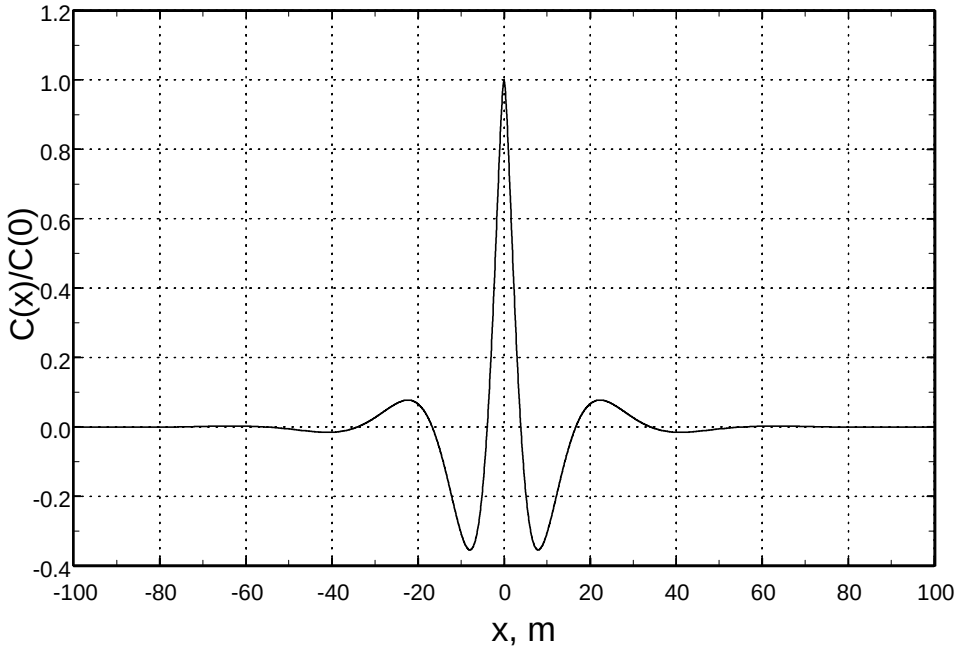

Figure 4-2. Normalized correlation function for a P-M surface. Windspeed $U = 5\,\text{m/s}$.

A characteristic feature of the P-M spectrum in (4.2) is its power-law behavior at large surface wavenumbers K (as $|K|^{-3}$). In fact, due to this behavior integrals of the type

$$\left\langle \left(\frac{d^l \zeta}{dx^l} \right)^2 \right\rangle = \int_{-\infty}^{\infty} K^{2l} W(K) dK \tag{4.8}$$

describing the mean-square slope ($l = 1$), mean-square curvature ($l = 2$) and all higher derivatives (cf. [Middleton, 1960, p. 153]) will be divergent unless some cutoff wavenumber K_c is chosen, i.e. the spectrum becomes:

$$W_1(K) = \begin{cases} W(K), & |K| < K_c \\ 0 & \text{otherwise} \end{cases} \tag{4.9}$$

This means that for Pierson-Moskowitz surfaces the short-wave surface structure is the major contributor to the mean-square surface slope and higher derivative statistics. In

most of our simulations we fixed the cutoff to be five times the electromagnetic wavenumber, i.e.

$$K_c = 5k\,, \tag{4.10}$$

which definitely includes all potential Bragg scatterers. Later we will study the influence of this choice on the scattering simulation results.

4.2.3 Other Simulation Details

The electromagnetic wavelength we used in these calculations is $\lambda = 23\,\text{cm}$. We also chose to work with surfaces corresponding to the windspeed $U = 5$ m/s. The dominant surface wavelength, calculated earlier to be 22.8 m, is given in terms of λ by;

$$\Lambda_p = 99.1\,\lambda \tag{4.11}$$

We use surfaces with sizes that include several dominant wavelengths, as will be discussed later in this Section. It should be pointed out that as one moves towards grazing, other considerations come into play and require increasingly larger surfaces to be used in the simulations. The rms surface height corresponding to the 5 m/s windspeed is (from (4.7)) $\langle \zeta^2 \rangle^{1/2} = 0.133\,\text{m}$, or $0.58\,\lambda$ and $k\langle \zeta^2 \rangle^{1/2} = 3.6$.

The incident field is taken to be a plane wave with a modified Gaussian taper suggested in [Thorsos, 1988]:

$$\psi^i(x,z) = \exp\{-jk(x\sin\theta_i - z\cos\theta_i)(1+w(x,z))\}\exp\left\{-\frac{(x+z\tan\theta_i)^2}{\text{g}^2}\right\} \tag{4.12}$$

where, again, ψ is either the *E* or *H* field, depending on the polarization considered. The incident angle θ_i is defined in Fig. 2-4; g is the parameter that controls the tapering (not to be confused with gravity acceleration in (4.2)), and

$$w(x,z) = \{2(x+z\tan\theta_i)^2/\text{g}^2 - 1\}/(k\text{g}\cos\theta_i)^2\,.$$

The choice of $\text{g} = L/6$ ($L =$ finite surface length) gives an acceptable tapering of the incident field at the edges. Further considerations regarding the use of the incident field (4.12) can be found in Chapter 5 where the applicability of Thorsos/Gaussian taper is studied. In the case of horizontal polarization a normal derivative of (4.12) is needed to

calculate the Kirchhoff current J^i; an analytical expression for the derivative can be easily obtained from (4.12).

Scattering from each surface realization will be described by either bistatic or backscattered NRCS that have been introduced in (2.33)-(2-34).

Surface realizations were generated using the spectral technique developed in Chapter 3. Here we briefly recall the procedure. First we need to decide on what sampling interval and the surface length to use. The critical (maximum) sampling interval for the cutoff K_c in (4.10) is, from (3.64),

$$\Delta x_0 = \pi/(5k) = \lambda/10 \tag{4.13}$$

In the simulations reported in this Chapter we chose Δx_0 to be the basic sampling interval; if smaller intervals were needed, they differed from Δx_0 by a factor of 2^i ($i =$ some positive integer) as will be explained below. To avoid the problem with sampling at exactly the critical interval discussed in Section 3.3.4, in practice Δx_0 should be chosen slightly larger or, conversely, the spectral cutoff may be chosen slightly smaller. Since it was appealing to use the basic sampling interval that is exactly a one-tenth of the electromagnetic wavelength, the actual value of the surface cutoff used was $K_c = 4.99k$. For all other practical purposes we will use the expression in (4.10).

The surface length L is a multiple of the sampling interval. In particular, for the interval Δx_0 from (4.13) we have:

$$L = N_0 \Delta x_0 \tag{4.14}$$

As discussed in Chapter 3, N_0 in (4.14) should be a power of 2 since we use a radix 2 FFT in our surface generating technique. The choice of $N_0 = 8192 = 2^{13}$ provides a surface length $L = 819.2\,\lambda$. This surface length was deemed to be acceptable for our study for various reasons but primarily because it contained several dominant surface wavelengths. Referring to (4.11) we see that such a choice yields $L = 8.26\Lambda_p$. From the discussion following Fig. 4-2 we concluded that $C(x)$ is essentially zero for $|x| > 2\Lambda_p$. This means that if we choose $L > 4\Lambda_p$, the shifted replicas of $C(x)$ in (3.32) do not interfere with each other, which was specified in Chapter 3 as one of the considerations in

choosing L. Another reason to make the surface length to be at least several dominant wavelengths is as follows. The P-M spectrum in (4.2) has a peak at K_p which moves closer to zero and becomes sharper as the windspeed U increases. One would like to choose the increment in the spectral domain, $\Delta K = 2\pi / L$, small enough to represent this peak adequately and certainly not to miss it altogether. This means choosing $\Delta K << K_p$ or, equivalently, $L >> \Lambda_p$. Finally, this surface length permitted use of the tapering parameter value $g = L/6 = 136.5\,\lambda$ which is sufficiently large to use the tapered incident field in (4.12) safely for incident angles up to 83-84°. Should we decide to study scattering at incident angles closer to grazing, the required beam waist must be larger (as discussed in Chapter 5) and we would require a larger surface.

Having decided on the surface length, sampling interval and the number of surface samples, we apply the algorithm stipulated in Section 3.3.5. Briefly put, it consists of generating independent Gaussian random numbers $\{\hat{\eta}'_m\}$ with variances proportional to the samples of the surface spectrum $W(K)$ in (4.9) taken at discreet points K_m with a step $\Delta K = 2\pi / L$. These random numbers $\{\hat{\eta}'_m\}$ represent a Fourier spectrum of a particular surface realization. Spectra of first and second surface derivatives can be obtained by multiplying the $\hat{\eta}'_m$'s by $(-jK_m)$ and $(-jK_m)^2$ respectively. FFT is then applied to obtain the samples of the surface realization and its derivatives. If a smaller sampling interval was needed, we retained the random spectral values $\{\hat{\eta}'_m\}$ already generated (cf. Section 3.3.5), added zeros to this sequence so that it contained a new, larger number N of terms and then took the FFT of this newly constructed sequence. This resulted in the generation of the same (but tighter sampled) surface realization (the details are given in Chapter 3; in particular, we have seen that a *continuous* band-limited surface realization is completely defined in a spectral domain by a finite set of random numbers). Again, due to the radix 2 FFT used it was convenient to decrease Δx each time by a factor of 2 so that the total number of surface points N remained a power of 2.

The result of the surface generation procedure are sample values of the surface height $\{\zeta(x_m)\}$, slope $\{\zeta_x(x_m)\}$ and second derivative $\{\zeta_{xx}(x_m)\}$ at discrete values of

x, $x_m = (m - N/2)\,\Delta x$, $m = 0, 1, ..., N-1$. By substituting these values in expressions (2.14) and (2.15) (and using (2.16), (2.17) and (4.12)) we get discretized values of the current and propagator shown in (2.19). To calculate a scattered field from (2.30), we also take the values of a kernel Q only at points $\{x_m\}$, so the integral in (2.30) is also replaced by a discrete sum.

An example of a P-M surface realization for a windspeed of 5 m/s is given in Fig. 4-3 (note the difference in horizontal and vertical scales), together with the superimposed absolute value of the incident field in (4.12) with $g = 136.5\,\lambda$ (as can be seen from (4.12), $|\psi^i(x,0)|$ does not depend on the incidence angle).

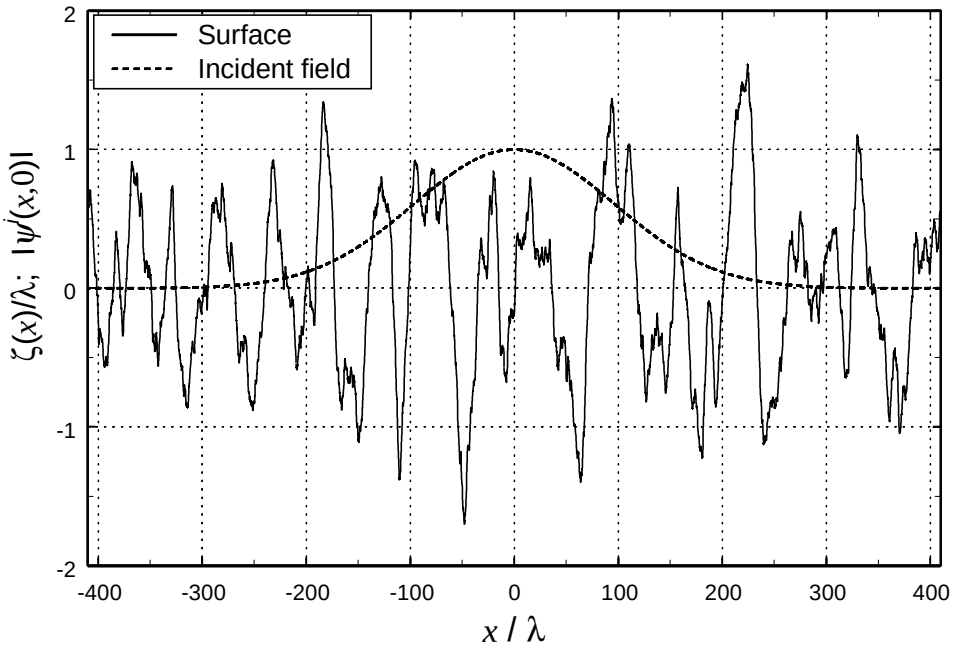

Figure 4-3. A sample P-M surface, $U = 5$ m/s. Also shown is the absolute value of the tapered incident field in (4.12).

4.2.4 Simulation results

We started by applying MOMI with its propagator matrix containing zeros on its diagonal. Fig. 4-4 shows the calculated backscattered cross section for one surface

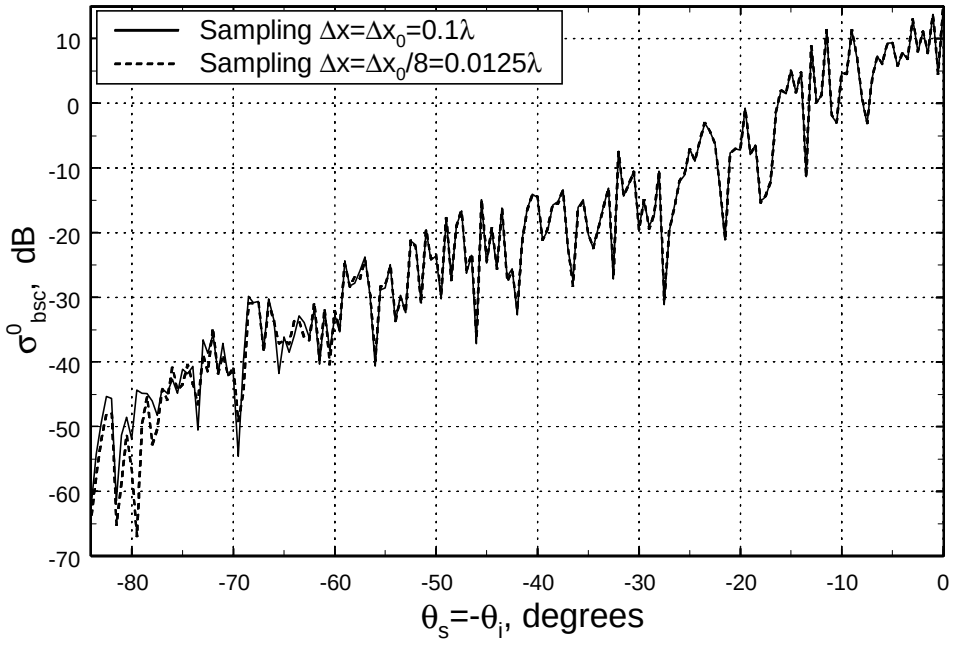

Figure 4-4. Normalized radar cross section in the backscattered direction (for a single realization of a P-M surface). Horizontal (TE) polarization, one MOMI iteration, curvature term not included.

realization for horizontal polarization. One curve on the graph corresponds to the sampling interval $\Delta x_0 = \lambda/10$ and another to the interval eight times smaller: $\Delta x = \Delta x_0/8$ (the spectral cutoff wavenumber is given by (4.10)). It can be seen that at moderate incident angles the two curves are on top of each other, but as one moves towards grazing, the calculated NRCS's start showing significant differences. The same effect can be seen for the bistatic cross section as shown in Fig. 4-5 for a horizontally polarized field incident at 80° (only negative scattering angles corresponding to backward scattering are shown). It can be observed that cross sections calculated for intervals Δx_0 and $\Delta x_0/8$ start showing some differences even at moderate scattering

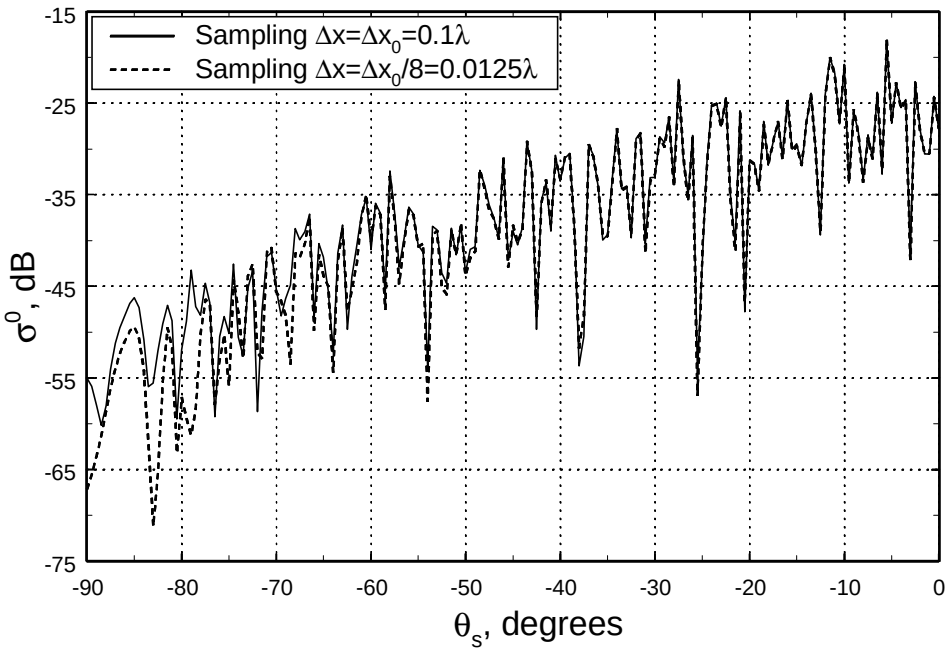

Figure 4-5. Bistatic normalized radar cross section (for a single realization of a P-M surface). Horizontal (TE) polarization, $\theta_i = 80^\circ$, two MOMI iterations, curvature term not included.

angles and as the observation direction moves towards grazing these differences become more pronounced. Similar behavior is observed for bistatic cross sections corresponding to smaller incident angles, although the differences in dB are in general smaller.

A typical behavior of the backscattered field as the sampling interval changes is shown in Figs. 4-6 and 4-7 ($\theta_i = 80^\circ$). Fig. 4-6 shows the NRCS which is proportional to the square of field magnitude and Fig. 4-7 shows the phase of the scattered field with the factor e^{-jkr} that is present in (2.30) ignored. Each figure displays results calculated using 0, 1 and 2 iterations of MOMI above the new Born term. One can see that points corresponding to 1 and 2 iterations of MOMI practically coincide, so *MOMI does converge no matter what sampling interval is chosen, but for different sampling intervals it converges to different values*. Fig. 4-7 suggests that even for the sampling interval of $\Delta x = \Delta x_0/16 = \lambda_0/160$ the phase of the scattered field still has not reached its final value and would change if we reduced the sampling interval further.

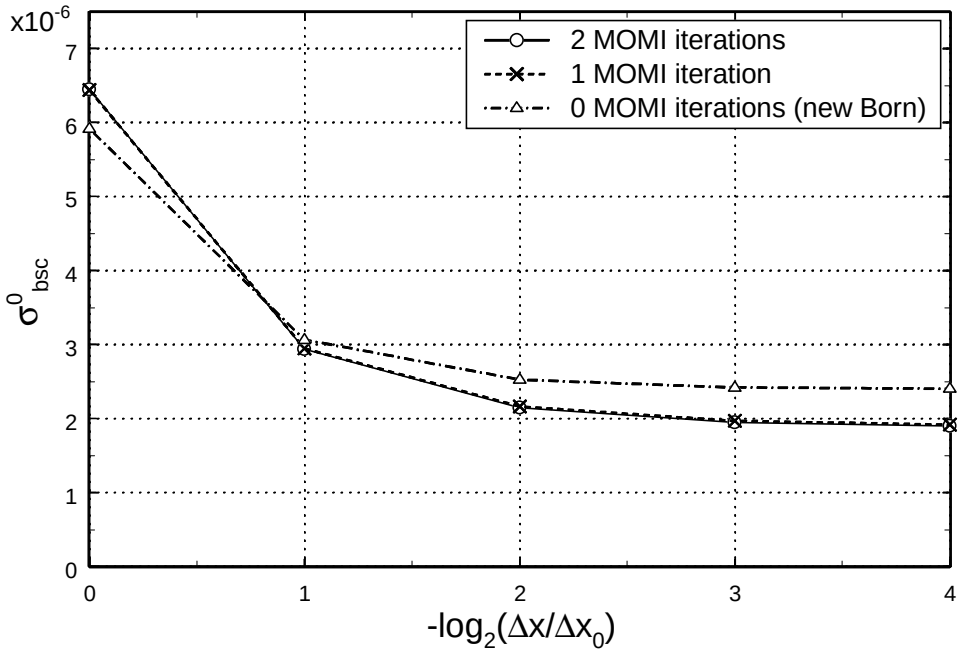

Figure 4-6. Normalized radar cross section in the backscattered direction ($\theta_i = 80^\circ$, single realization of a P-M surface) vs. sampling interval. Horizontal (TE) polarization, curvature term not included.

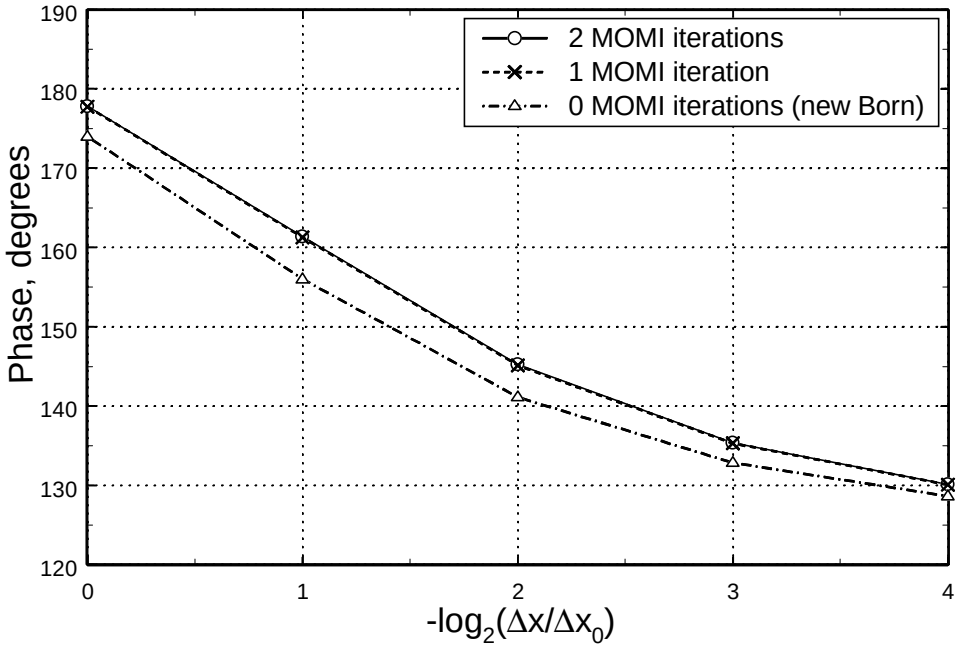

Figure 4-7. Phase of the backscattered field ($\theta_i = 80^\circ$, single realization of a P-M surface) vs. sampling interval. Horizontal (TE) polarization, curvature term not included.

This dependence of the calculated NRCS on the sampling interval appears to be tied to the short wave structure on the surface. Fig. 4-8 presents bistatic cross sections for horizontal polarization calculated with sampling intervals Δx_0 and $\Delta x_0/8$ for a surface with a spectral cutoff wavenumber $K_{c1} = k$ which is five times smaller than the cutoff K_c used in previous simulations. This Figure should be compared to Fig. 4-5 and one can see almost no differences except for a few nulls near grazing where some discrepancy is not surprising given the extremely low levels. This apparent cause and effect relation between the observed changes in calculated NRCS with the sampling interval and the short-wave components suggests that the effect should not be seen if a surface with Gaussian spectrum is used because it effectively contains no short-wave components since they are exponentially suppressed.

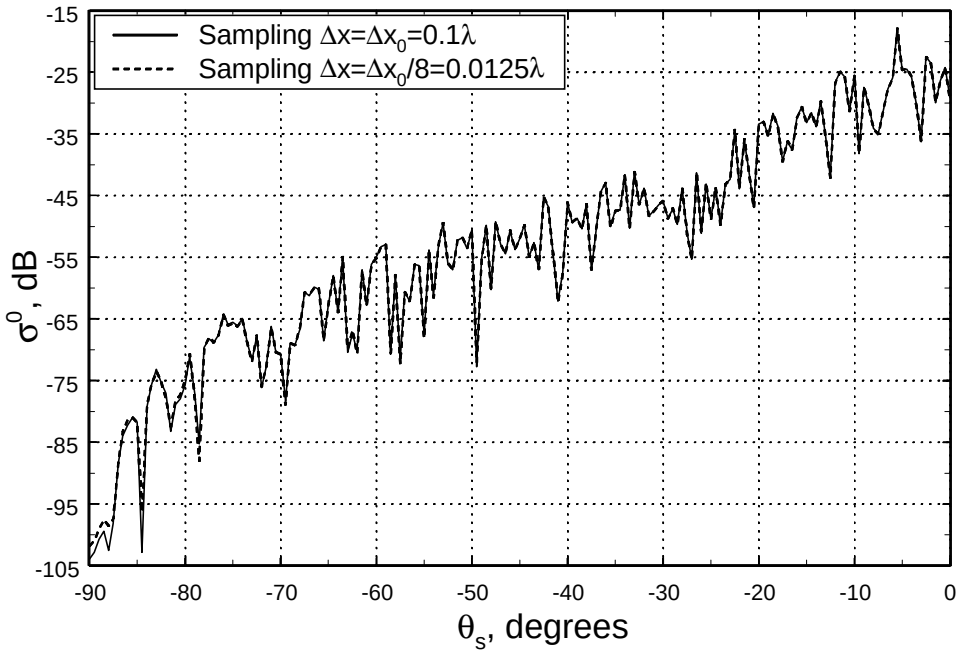

Figure 4-8. Bistatic normalized radar cross section (for a single realization of a P-M surface with spectral cutoff wavenumber reduced to $k = 2\pi/\lambda$). Horizontal (TE) polarization, $\theta_i = 80^\circ$, two MOMI iterations, curvature term not included.

As has been mentioned, it is the short-wave components that are the main contributors to the rms slope and especially the rms curvature of the P-M surface. Consequently, including the curvature terms (4.1) in the diagonal of the propagator matrix may be one possible remedy to the problem. NRCS calculations with the curvature term included are shown in Fig. 4-9. The surface is the same as was used for calculations in Figs. 4-4 – 4-7; its spectral cutoff is given by (4.10). These new results show that the bistatic NRCS calculated with the sampling interval Δx_0 is virtually the same as the NRCS obtained from calculations with a much smaller interval of $\Delta x_0/8$. This presents

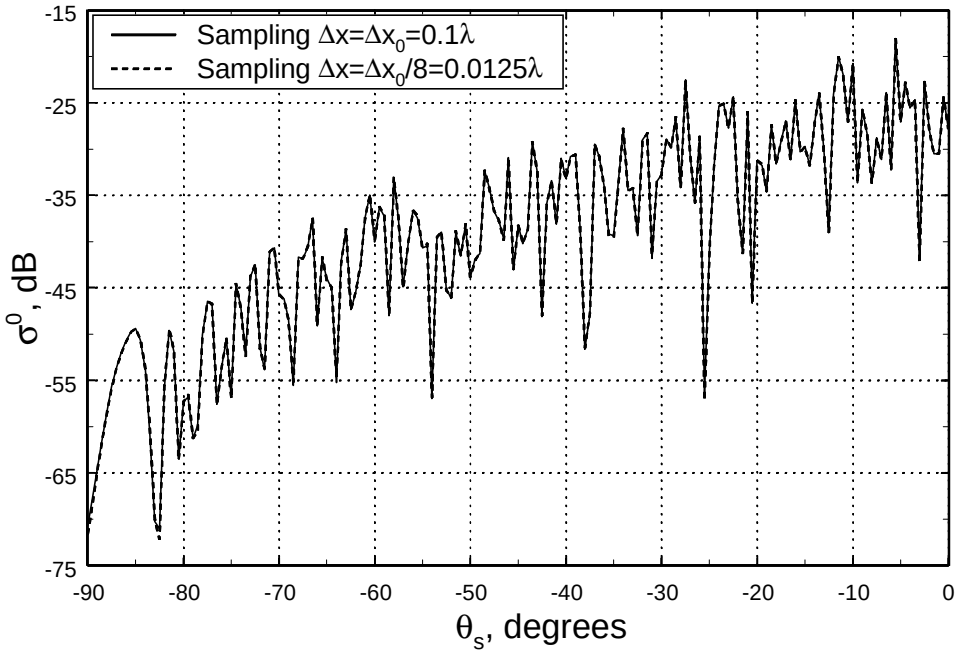

Figure 4-9. Bistatic normalized radar cross section (for a single realization of a P-M surface). Horizontal (TE) polarization, $\theta_i = 80^\circ$, two MOMI iterations, curvature term included.

quite a different picture from the situation shown in Fig. 4-5. The behavior of the scattered field versus the sampling interval is again examined in Figs. 4-10 and 4-11 for backscattering at 80°. Fig. 4-10 shows that once the curvature term is included, there is

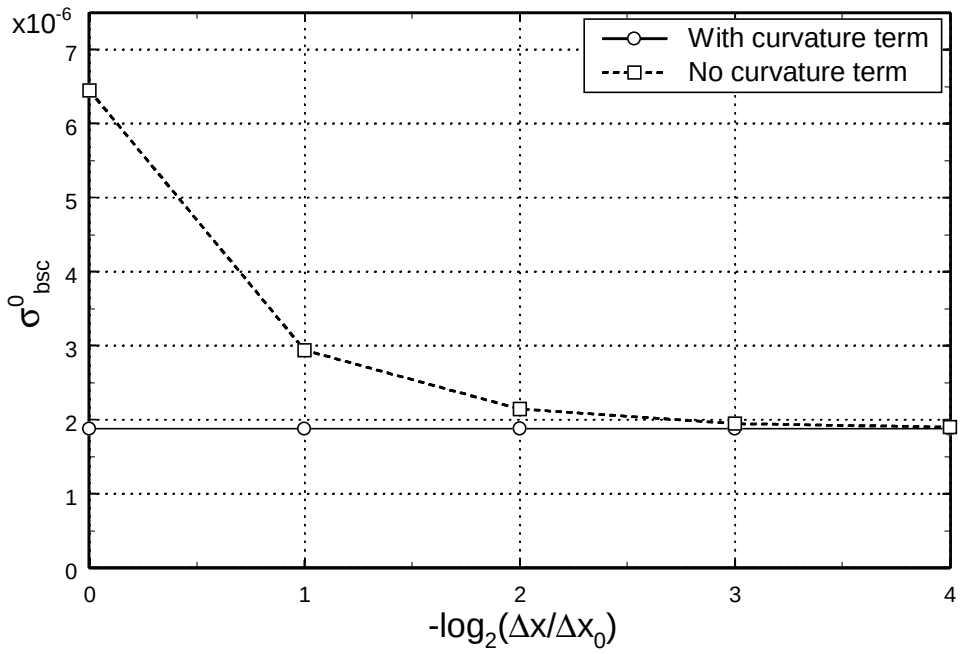

Figure 4-10. Normalized radar cross section in the backscattered direction ($\theta_i = 80^\circ$, single realization of a P-M surface) vs. sampling interval. Horizontal (TE) polarization.

no noticeable change in the NRCS. In Fig. 4-11 a slight change in the phase of the calculated backscattered field can be noticed as one moves from the sampling interval of Δx_0 to $\Delta x_0/2$, but after that its value remains constant. As the sampling interval is decreased both the NRCS and phase of the scattered field calculated without curvature eventually converge to their counterparts calculated with the curvature term. Note that the phase of the field calculated without curvature term does not reach this stable value even at a sampling interval as small as $\Delta x_0/16$. *This demonstrates that with the inclusion of the curvature term one indeed achieves stability with respect to the sampling interval and obtains the correct values of the scattered field without resorting to the heavy oversampling that would have been necessary otherwise.*

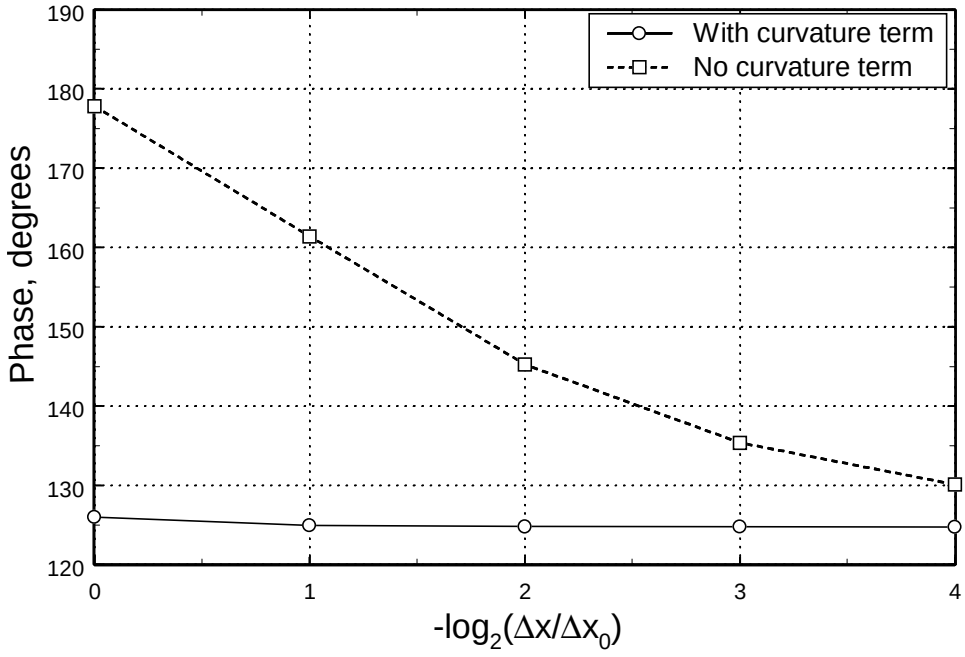

Figure 4-11. Phase of the backscattered field ($\theta_i = 80^\circ$, single realization of a P-M surface) vs. sampling interval. Horizontal (TE) polarization.

So far we addressed only the case of horizontal polarization. For vertical polarization, we found that when the propagator matrix without the curvature terms is used, the calculated NRCS does not appear to possess the same degree of sensitivity to the size of the sampling interval that was observed in the case of horizontal polarization. This fact is demonstrated in Fig. 4-12, where calculations of the bistatic NRCS for vertical polarization and an incident angle of 80° are presented for two different sampling intervals.

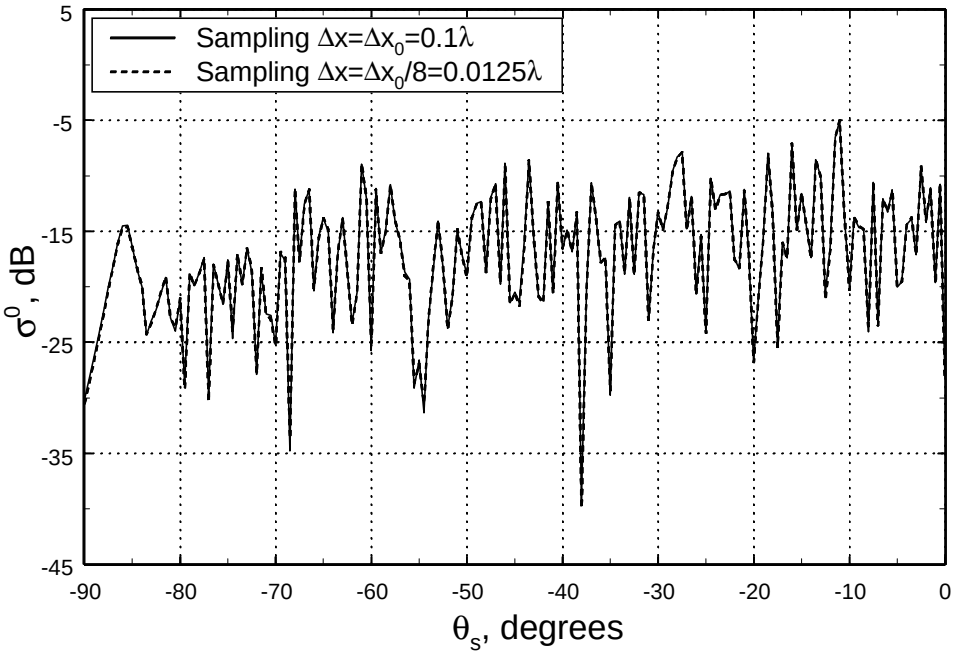

Figure 4-12. Bistatic normalized radar cross section (for a single realization of a P-M surface). Vertical polarization, $\theta_i = 80^\circ$, two MOMI iterations, curvature term not included.

However, if one examines the *absolute difference* in the scattered field calculated without the curvature term at two different sampling intervals, this difference is usually larger for vertical polarization than for horizontal polarization. Such an absolute difference in the scattered field calculated with sampling intervals Δx_0 and $\Delta x_0 / 16$ is shown in Fig. 4-13 for both TE and TM polarizations and $\theta_i = 80^\circ$. Again, only one surface realization is considered; the field is calculated according to (2.30) with the factor $e^{-jkr} / \sqrt{r}$ disregarded. One can see that for the TM-polarized field this difference exceeds the similar measure for the TE-polarized field for almost all scattered angles.

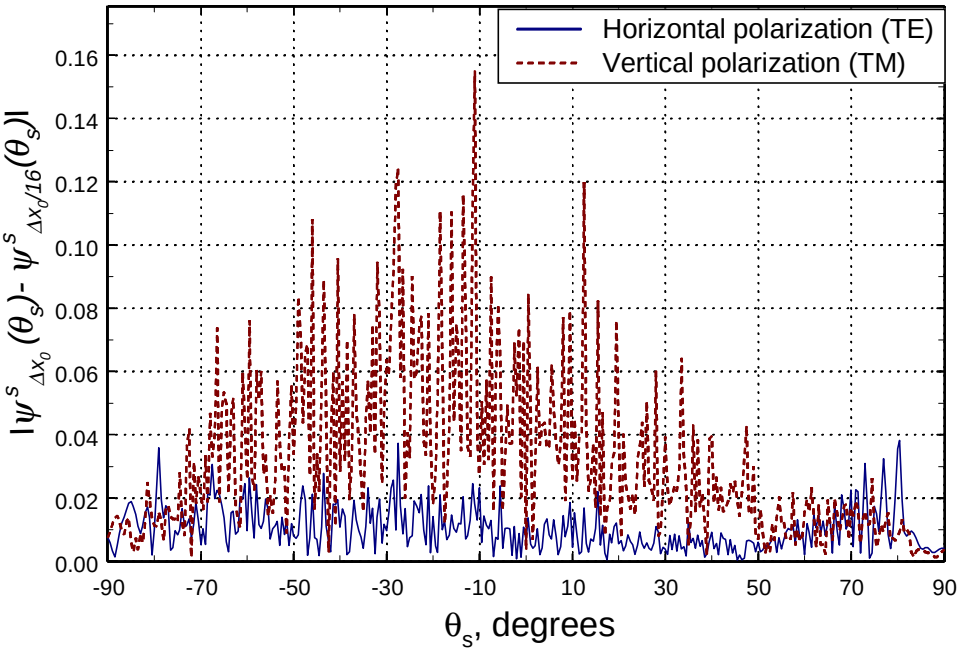

Figure 4-13. Absolute difference in the scattered field calculated with intervals Δx_0 and $\Delta x_0 / 16$ ($\theta_i = 80^\circ$, single realization of a P-M surface). Two MOMI iterations, curvature term not included.

However, since the magnitude of the field scattered in the backward directions is significantly larger in the case of vertical polarization, the *relative* changes in the field

(and, therefore, NRCS) are negligibly small compared to what was observed for the horizontal polarization. Inclusion of the curvature terms in the diagonal of the propagator matrix in the case of vertical polarization also significantly reduces variation in the calculated field and the NRCS as one changes the sampling interval but, again, this variation is relatively small from the beginning.

It is interesting to look at the behavior of the relative mean-square error in the current vs. sampling interval. Assuming the current calculated at the smallest sampling interval of $\Delta x_0/16$ with the curvature term included to be the "exact" current J_0, we define the relative mean square error in the current calculated with some sampling interval Δx as

$$\varepsilon(\Delta x) = \frac{1}{\|J_0\|}\left(\frac{1}{N}\sum_{n=1}^{N}\left|J_{\Delta x}(x_n) - J_0(x_n)\right|^2\right) \tag{4.15}$$

In (4.15) the values $\{x_n\}$ are taken with the sampling interval Δx, $J_{\Delta x}$ denotes the current calculated with this sampling interval (with or without the curvature term) and

$$\|J_0\| = \frac{1}{M}\sum_{l=1}^{M}\left|J_0(x_l)\right|^2 \tag{4.16}$$

where $M = N_0 \times 16 = 2^{17}$ and $\{x_l\}$ are taken with the sampling interval $\Delta x_0/16$. Only one surface realization is considered. Fig. 4-14 shows $\varepsilon(\Delta x)$ for the current calculated with and without the curvature term for both horizontal and vertical polarizations and $\theta_i = 80^\circ$. When the curvature term is not included, the relative mean square error in the current is essentially the same for horizontal and vertical polarizations. Yet, as we have seen, in the case of horizontal polarization this error does produce significant relative variations in NRCS while for vertical polarization these variations are negligible. This once more confirms the well-known fact that an error in the current does not necessarily translate into a significant error in the scattered field. Each time the sampling interval is divided in half, $\varepsilon(\Delta x)$ for the current without curvature term decreases by approximately 6 dB, which means that root mean square error in the current decreases by a factor of 2. When the curvature term is included, $\varepsilon(\Delta x)$ is reduced dramatically, with the relative mean square error for horizontal polarization being smaller than that for vertical

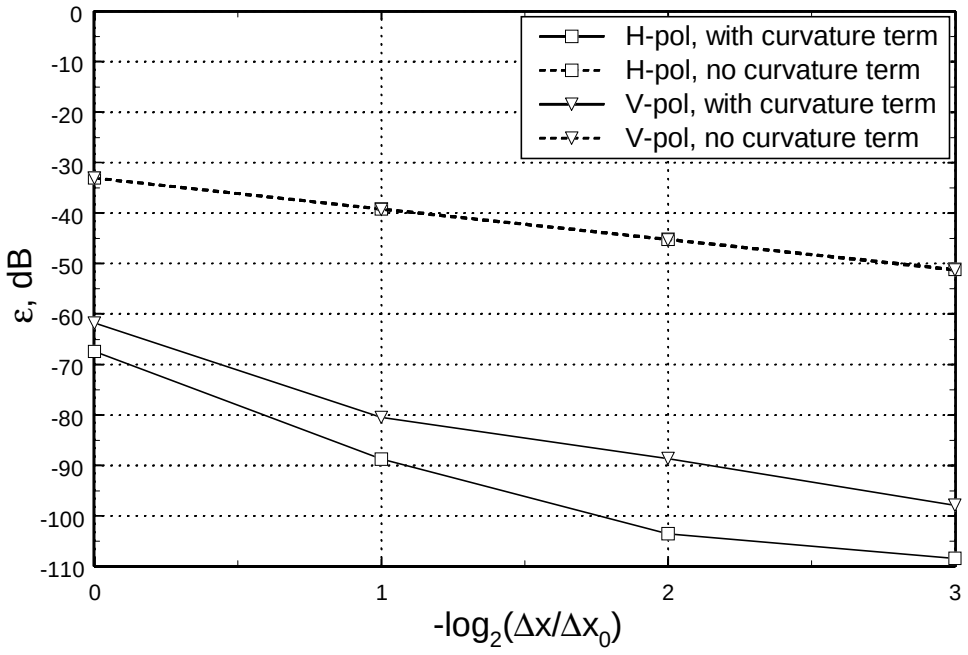

Figure 4-14. Relative mean square error in the calculated surface current vs. sampling interval. $\theta_i = 80^\circ$, single realization of a P-M surface.

polarization. Note that $\varepsilon(\Delta x_0)$ for the currents with curvature is well below $\varepsilon(\Delta x_0/8)$ for the currents without curvature.

Finally, let us address the question of how the inclusion or omission of the curvature term affects the average NRCS. Fig. 4-15 displays the average bistatic NRCS (the average is taken over 100 surfaces) for horizontal polarization and an incident angle of 80° that was calculated with and without curvature term; the mean field was not extracted, so it shows up in the specular direction. The sampling interval of $\Delta x_0/2$ was used. For most of the scattering angles the two curves run on top of each other but as the scattering angle approaches -90°, the differences start showing up, with the NRCS calculated without the curvature term having larger values. Around the grazing scattering

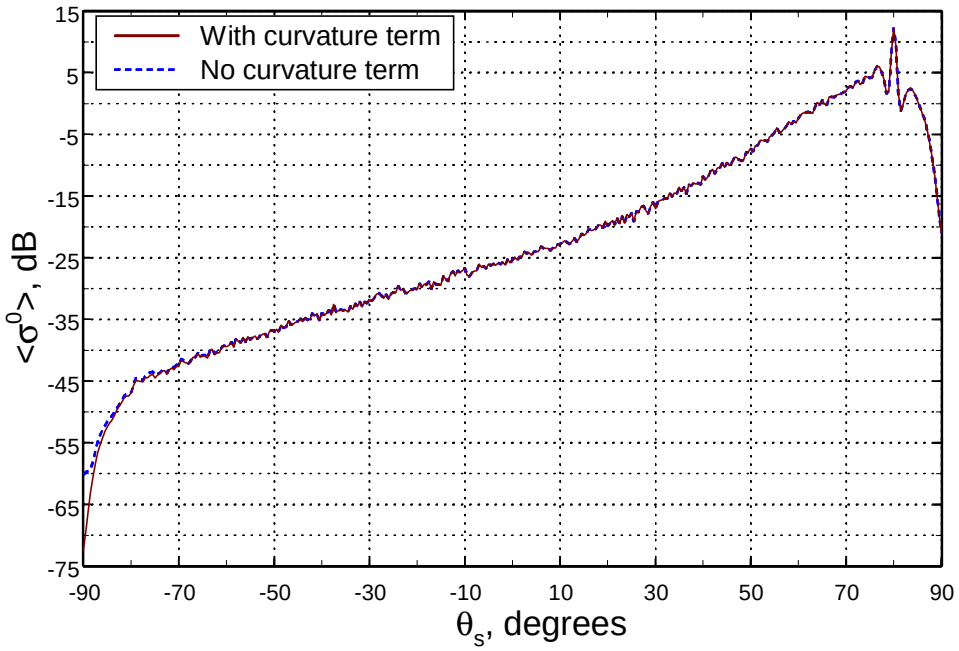

Figure 4-15. Average bistatic normalized radar cross section (average over 100 surfaces with P-M spectrum). Horizontal (TE) polarization, $\theta_i = 80^\circ$, two MOMI iterations, $\Delta x = \Delta x_0/2 = \lambda/20$.

angle of -90° calculations without the curvature term result in an overestimation of average NRCS by more than 10 dB. Fig. 4-16 shows the ratio of the average NRCS calculated without the curvature term to the average NRCS with this term. Expressed in dB, this ratio corresponds to the distance between the curves shown in Fig. 4-15. For comparison, the similar ratio is plotted in Fig. 4-16 for only one surface realization. One can see that, in general, the average NRCS shows much less sensitivity to the inclusion or exclusion of the curvature term than the NRCS for a single surface realization. Still, at scattering angles near grazing even the average NRCS is very sensitive to the presence or absence of the curvature term.

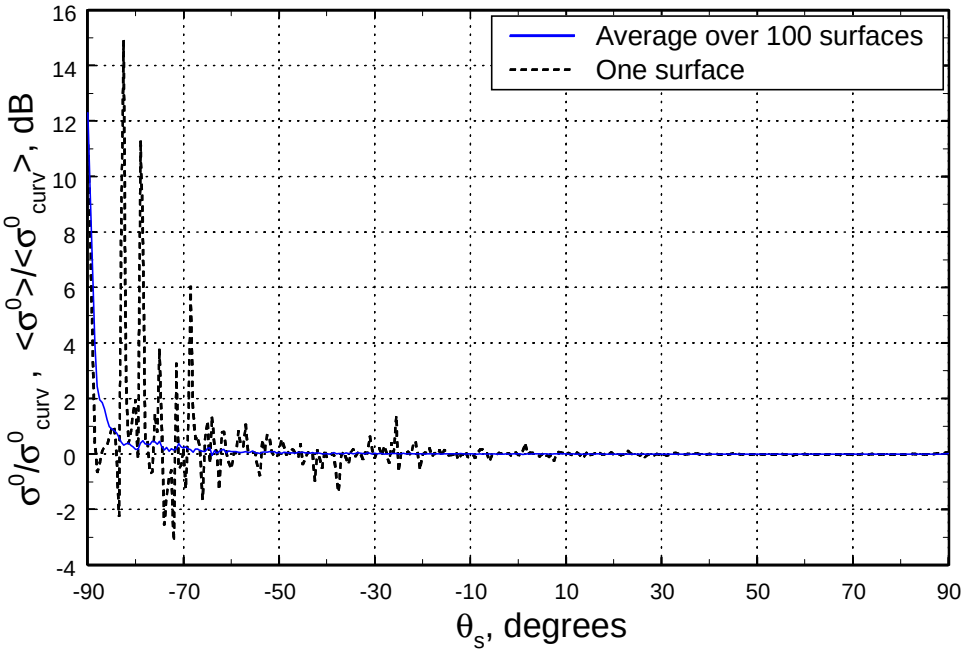

Figure 4-16. Ratio (expressed in dB) of average bistatic normalized radar cross sections calculated without and with the curvature term (average over 100 surfaces with P-M spectrum). Also shown is a similar ratio of normalized radar cross sections corresponding to one P-M surface. Horizontal (TE) polarization, $\theta_i = 80^\circ$, two MOMI iterations, $\Delta x = \Delta x_0/2 = \lambda/20$.

4.3 Discretization of the MFIE: the Necessity of the Curvature Term and the Choice of the Sampling Interval

In the previous section it was shown that when the MFIE is solved for P-M surfaces with the diagonal of the propagator matrix set to zero, in some cases very tight sampling is required to obtain a stable value for the scattered field. However, inclusion of the curvature terms in the diagonal appears to remedy this problem. We now examine the details of discretization to find out why curvature terms should be included in the diagonal of the propagator matrix and whether there should be any higher-order corrections, as well as to develop some recommendations for choosing the sampling interval when discretizing the MFIE for P-M surfaces.

4.3.1 Method of Moments Formalism and Its Application to the MFIE

In Chapter 2 we derived the MFIE (2.13) and wrote down its discretized form in, (2.18)-(2-19), that is usually used. Here we reexamine in detail how this discrete representation can be obtained from the continuous MFIE and what assumptions are involved. The classical Method of Moments approach described in [Harrington, 1993] can be applied to discretize the MFIE in (2.13). Two sets of linearly independent functions, $\{e_n(x)\}$ and $\{t_m(x)\}$ (called expansion and testing functions, respectively) and a scalar product $\langle \cdot, \cdot \rangle$ are introduced. The reasonable scalar product of two possibly complex-valued functions f and g can be defined as

$$\langle f(x), g(x) \rangle = \int_X f^*(x)\, g(x)\, dx\,, \tag{4.17}$$

with the asterisk denoting the complex conjugate. Assuming that the set $\{e_n(x)\}$ is complete for the class of functions that the unknown current $J(x)$ belongs to, one can write

$$J(x) = \sum_n J_n\, e_n(x) \tag{4.18}$$

where $\{J_n\}$ are the expansion coefficients. This expression is substituted in (2.18), and a scalar product is taken of both sides of this equation with each of the testing functions:

$$\sum_n J_n \langle t_m(x), e_n(x) \rangle = \langle t_m(x), J^i(x) \rangle + \sum_n J_n \int_X \langle t_m(x), P(x,x') \rangle e_n(x')\, dx' \qquad (4.19)$$

It can be seen that in order for (4.19) to assume the matrix form (2.18) with $\boldsymbol{J} = [J_n]$ from (4.18), an additional multiplication of both sides of (4.19) by the matrix inverse $[\langle t_m(x), e_n(x) \rangle]^{-1}$ is, in general, necessary. However, if we require that

$$\langle t_m(x), e_n(x) \rangle = a_m \delta_{mn} \qquad (4.20)$$

(a_m are some positive constants and δ_{mn} is a Kronecker delta), i.e. testing and expansion functions should be mutually orthogonal, the goal is readily achieved with the quantities appearing in (2.19) being:

$$\begin{aligned} \boldsymbol{J} &= [J_n], \qquad \boldsymbol{J^i} = \left[\frac{1}{a_m} \langle t_m(x), J^i(x) \rangle \right] \text{ and} \\ \boldsymbol{P} &\equiv [P_{mn}] = \left[\frac{1}{a_m} \int_X \langle t_m(x), P(x,x') \rangle e_n(x') dx' \right] \end{aligned} \qquad (4.21)$$

Furthermore, if the expansion functions $\{e_n(x)\}$ are chosen to be orthogonal and $\{t_m(x)\}$ are chosen to belong to the same class of functions then the completeness of $\{e_n(x)\}$ for this class together with (4.20) means that $t_n(x) = c_n e_n(x)$ where c_n are non-zero constants so the expansion and testing functions are essentially the same. If the testing functions are chosen outside the class that $\{e_n(x)\}$ belong to (one can use δ-functions as an example), this, of course, is not true.

Our goal is to apply the formalism described above to see how and under what conditions a simple discretization such as (2.19) is possible. It is tempting to use δ-functions as expansion and testing functions because this would immediately formally give the discretized equation (2.18) with sampled quantities (2.19). However, in this case one cannot write an expansion (4.18) for any reasonable continuous or square-integrable function such as we expect $J(x)$ to be. Another choice, which we will review in the following Section is to use δ-functions as testing functions together with rectangular pulse expansion functions (in this case, for example, (4.20) can be satisfied). This approach was shown to yield the curvature terms in the diagonal of the propagator matrix [Kapp, 1995]; however a correct interpretation of this result is needed. Then, in Section

4.3.3 we consider the use of *sinc*-type sampling functions and show that such an approach leads naturally to recovering the curvature terms *and* allows for determining the sampling interval Δx.

4.3.2 Rectangular (Pulse) Expansion and Delta Testing Functions

Consider the following choice for expansion and testing functions:

$$\begin{aligned} e_n(x) &= rect\left(x/\Delta x - n\right) \\ t_m(x) &= \delta\left(x - m\Delta x\right) \end{aligned} \tag{4.22}$$

In (4.22), the rectangular functions are defined as

$$rect(x) = \begin{cases} 1, & |x| \leq 1/2 \\ 0, & |x| > 1/2 \end{cases} \tag{4.23}$$

This approach was pursued in [Kapp, 1995]; however, it seems to have its own deficiencies. For example, rectangle pulse functions do not form a complete set for the class of continuous functions, so (4.18) cannot be exact and (2.18) will involve some error from the start. Further, elements of the discretized propagator will contain integration over the pulse width in x'-coordinate:

$$P_{mn} = \int_{x_n - \Delta x/2}^{x_n + \Delta x/2} P(x_m, x')\, dx'; \tag{4.24}$$

to obtain a simplified form as given by (2.19) some additional approximations of these integrals will be necessary. For the off-diagonal terms, integrals in (4.24) can be calculated by expanding the propagator in a Taylor series around x_n and integrating them term by term as follows

$$\begin{aligned} P_{mn} &= \int_{x_n - \Delta x/2}^{x_n + \Delta x/2} P(x_m, x')\, dx' = \int_{x_n - \Delta x/2}^{x_n + \Delta x/2} \left\{ \sum_{l=0}^{\infty} \left. \frac{\partial^l P(x_m, x')}{\partial x'^l} \right|_{x'=x_n} \frac{(x' - x_n)^l}{l!} \right\} dx' = \\ &= \sum_{q=0}^{\infty} \left\{ \left. \frac{\partial^{2q} P(x_m, x')}{\partial x'^{2q}} \right|_{x'=x_n} \frac{(\Delta x)^{2q+1}}{2^{2q}(2q+1)!} \right\} \end{aligned} \tag{4.25}$$

The assumption in (4.25) is that the series converges, which may in fact depend on Δx; in principle this question can be investigated closer using the expressions for the

propagator in (2.14)-(2.17). For practical purposes, only the few first terms in (4.25) are retained. If only the first term corresponding to $q = 0$ is used, we have

$$P_{mn} \approx P(x_m, x_n)\Delta x \tag{4.26}$$

This is exactly the expression for the propagator matrix elements in (2.19). For the diagonal ($m = n$) terms, however, extra caution should be taken since the propagator contains a Hankel function $H_1^{(2)}$ (cf. (2-16)-(2-17)) which is singular at $x_m = x_n$. While it can be readily shown that the limit of $P(x, x')$ as $x' \to x$ exists and is finite (see below), one will need to examine similar limits for all higher derivatives involved in (4.25) as well.

Kapp [Kapp, 1995] chose a different way of looking at the diagonal terms. He expanded all functions in the numerator and denominator of the propagator $P(x, x')$ (cf. (2.14)-(2.17)) in Taylor series and used a small argument approximation for the Hankel function. He was able to recover the leading term of this expansion that did not depend on x'; upon the integrating of this leading term as in (4.24), he got the expression in (4.1), i.e. the curvature term for the diagonal matrix elements. In a sense, Kapp has shown that

$$\lim_{x' \to x} P(x, x') = \pm \frac{\zeta_{xx}(x)}{2\pi(1 + \zeta_x^2(x))} \tag{4.27}$$

with the plus sign corresponding to the TM and the minus sign to the TE polarization. Mathematical details on the derivation of (4.27) are given in Appendix 4.B at the end of this Chapter. Referring to the discretized MFIE in the form

$$\boldsymbol{J} = (\boldsymbol{I} - \boldsymbol{P})^{-1} \boldsymbol{J}^{\boldsymbol{i}}$$

(cf. (2.20)) the curvature term was then interpreted by Kapp as an additional correction to the already extracted self-term represented by the identity matrix $\boldsymbol{I}$. It was then argued that it is not consistent to account for this correction for the diagonal terms and not to account for the higher order corrections to the off-diagonal terms (4.26) that arise from (4.25). However, careful comparison of (4.1) to (4.26) reveals that both curvature terms and the leading terms for off-diagonal entries into the propagator matrix *are of the same order in* Δx *(our small parameter)* in the series expansions reviewed. This means that the

curvature terms in (4.1) have the "same right" to be in the propagator matrix $\boldsymbol{P}$ as the off-diagonal terms in (4.26), as has been also verified by our simulation results.

Although we will not pursue this matter any further, we would like to note the following. If the approach used by Kapp to recover the "curvature terms" is extended to find the higher-order corrections for the diagonal elements of $\boldsymbol{P}$, one may well find that, unlike the off-diagonal elements, this expansion will not result in terms involving only integer powers of Δx. Consider a series expansion for the Hankel function that is a part of the propagator $P(x, x')$ [Gradshtein and Ryzhik, 1994]:

$$H_1^{(2)}(z) = J_1(z)\left[1 - \frac{2j}{\pi}\left(\ln\frac{z}{2} + C\right)\right] + \frac{2j}{\pi z} + \frac{j}{\pi}\sum_{n=1}^{\infty}\frac{(-1)^{n+1}(z/2)^{2n-1}}{n!(n-1)!}\left\{\frac{1}{n} + 2\sum_{m=1}^{n-1}\frac{1}{m}\right\} \quad (4.28)$$

In the above expression

$$J_1(z) = \frac{z}{2}\sum_{n=0}^{\infty}\frac{(-1)^n z^{2n}}{2^{2n} n!(n+1)!}$$

is a first-order Bessel function and $C = 0.577215...$ is the Euler constant. As $z \to 0$, the leading term in the expansion (4.28) is, of course, $2j/(\pi z)$ and it was used to obtain (4.27) and (4.1); however if one investigates higher-order corrections to P_{mm}, other terms in (4.28) should be considered as well, and the logarithmic terms are likely to appear in the result. Finally, when considering including the corrections beyond the leading terms (4.26) or (4.1), it is important to realize that even if the integrals (4.24) are evaluated *exactly* (or, equivalently, *all* terms in the series expansion of the propagator are accounted for), there will still be some error in the solution due to the poor approximation of the continuous current $J(x)$ by rectangular pulses.

4.3.3 Sampling Functions as Basis Functions

In our approach we will use the sampling theorem and the concepts related to it. The P-M surfaces that we will work with have a distinct spectral cutoff as stated in (4.9). This leads to the suspicion that the current and propagator, being functionally dependent on the surface height, might also have their spectra located predominantly within some finite range of wavenumbers and can therefore be reasonably regarded as belonging to the class of band-limited functions. Let us also note the following; for well-behaved

surfaces the limit in (4.27) exists (cf. also Appendix B) so the functions in (2.14b) and (2.15b) can be defined at $x = x'$ to be equal to this limit and thus the propagator in (2.13) is a continuous function.

It is known that for band-limited functions that have zero spectral content beyond some wavenumber K_u, the functions

$$s_n(x) = \frac{\sin \pi(x/\Delta x - n)}{\pi(x/\Delta x - n)}, \quad \Delta x = \pi/K_u \tag{4.29}$$

form a complete set (cf., for example, [Middleton,1960, pp.210-212]). These functions are orthogonal with respect to the scalar product in (4.17) where $\mathrm{X} = (-\infty; \infty)$:

$$\langle s_m(x), s_n(x) \rangle = \Delta x \delta_{mn} \tag{4.30}$$

Any function f of this class of band-limited functions can be expanded in this basis,

$$f(x) = \sum_n f_n \, s_n(x) \tag{4.31}$$

with the expansion coefficients

$$f_n \equiv \frac{1}{\Delta x} \langle s_n(x), f(x) \rangle = f(n\Delta x) \tag{4.32}$$

The previous two equations are essentially the main result of the sampling theorem indicating that a band-limited function can be reconstructed from properly taken samples using *sinc*-type basis functions.

The spectra of $J^i(x)$, $J(x)$ and $P(x, x')$ have a characteristic shape that can be regarded as band-limited and suggests the choice of the wavenumber K_u beyond which the spectra of all these functions are essentially zero.

Fig. 4-17 shows a two-dimensional Fourier spectrum of the propagator $P(x, x')$ as given by (2.15b) for horizontal polarization and one random surface realization. The spectral cutoff of the surface in this particular case was chosen to be $K_c = 2.5k$. Fig. 4-18 displays the spectrum of the propagator given in (2.14b) for vertical polarization and the same surface. The spectrum of the propagator consists of two narrow “blades”, each

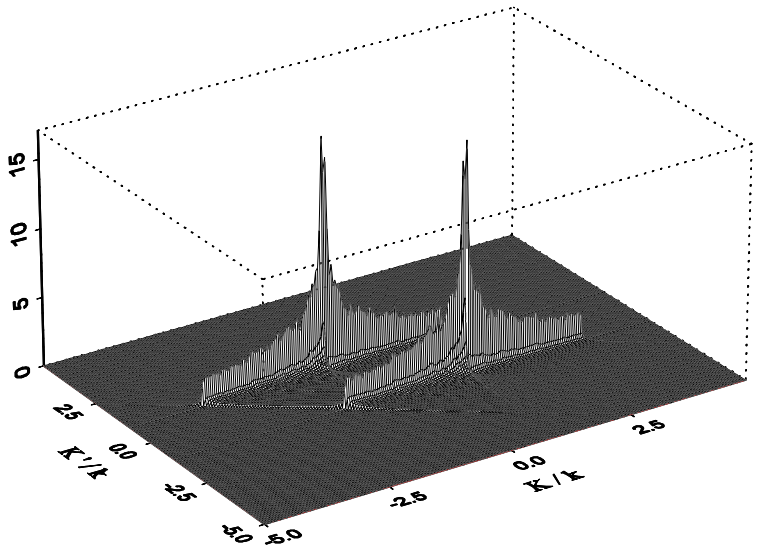

Figure 4-17. Two-dimensional Fourier spectrum of the propagator $P(x, x')$ (linear scale, single realization of a P-M surface, horizontal (TE) polarization, surface spectral cutoff is $2.5k$).

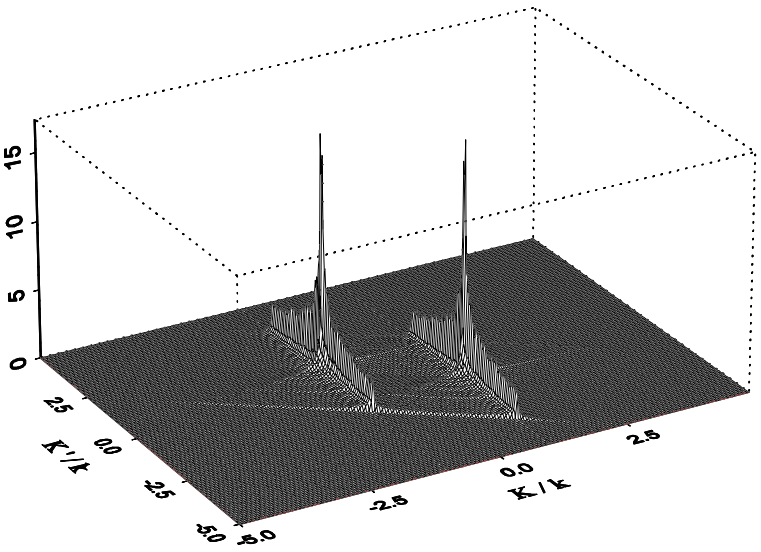

Figure 4-18. Two-dimensional Fourier spectrum of the propagator $P(x, x')$ (linear scale, single realization of a P-M surface, vertical (TM) polarization, surface spectral cutoff is $2.5k$).

having a half-length of K_c, that are centered at $(-k,k)$ and at $(k,-k)$. In the case of horizontal polarization (Fig. 4-17) these two blades are oriented along the K-axis which is the dual to the *x*-coordinate. This is also obvious from Fig. 4-19 which is a contour plot of the propagator spectrum in Fig. 4-17. Clearly, the spectrum is essentially non-zero only in the rectangular domain with K varying within $\pm(k+K_c)$ and K' varying within the range somewhat larger than $\pm k$ (by the thickness of the "blades"). Certainly the spectrum can be considered band-limited within a larger, square domain (which is more convenient for our consideration) defined by $-K_u \le K \le K_u$, $-K_u \le K' \le K_u$ and

$$K_u = k + K_c. \tag{4.33}$$

The same discussion applies to the vertical polarization propagator with the same result (4.33) for the wavenumber domain upper limit K_u.

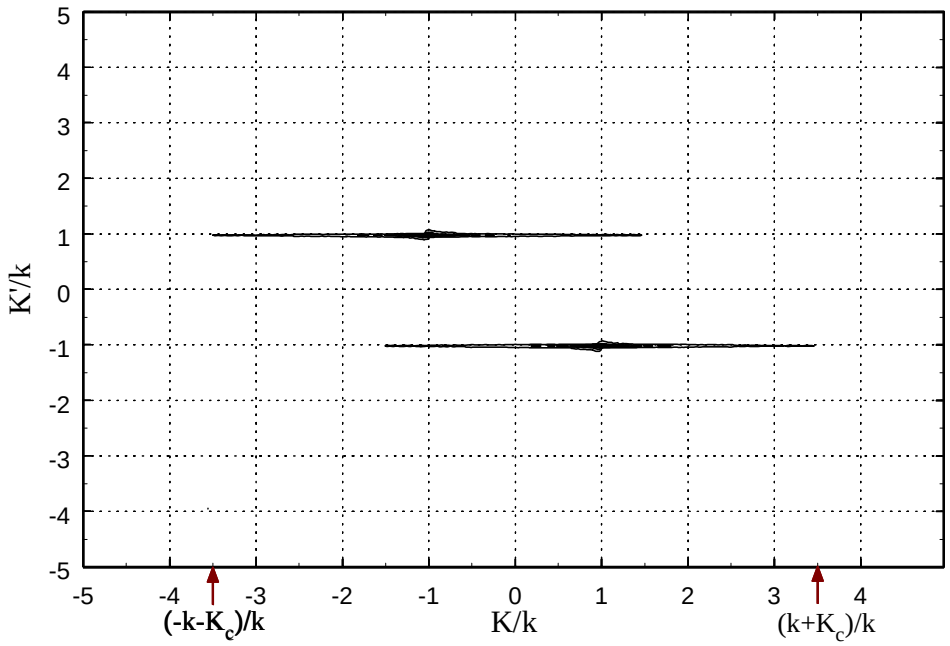

Figure 4-19. Contour plot of the two-dimensional Fourier spectrum of the TE propagator shown in Fig. 4-17.

Fourier spectra of Kirchhoff currents $J^i(x)$ calculated according to (2.14a) or (2.15a) and (4.12) in general have a peak at $K = k\sin\theta_i$ accompanied by a "pedestal" that is centered at the same wavenumber and has the half-width K_c. Examples of such spectra (normalized to their peaks) are shown using a logarithmic scale in Figs. 4-20 and

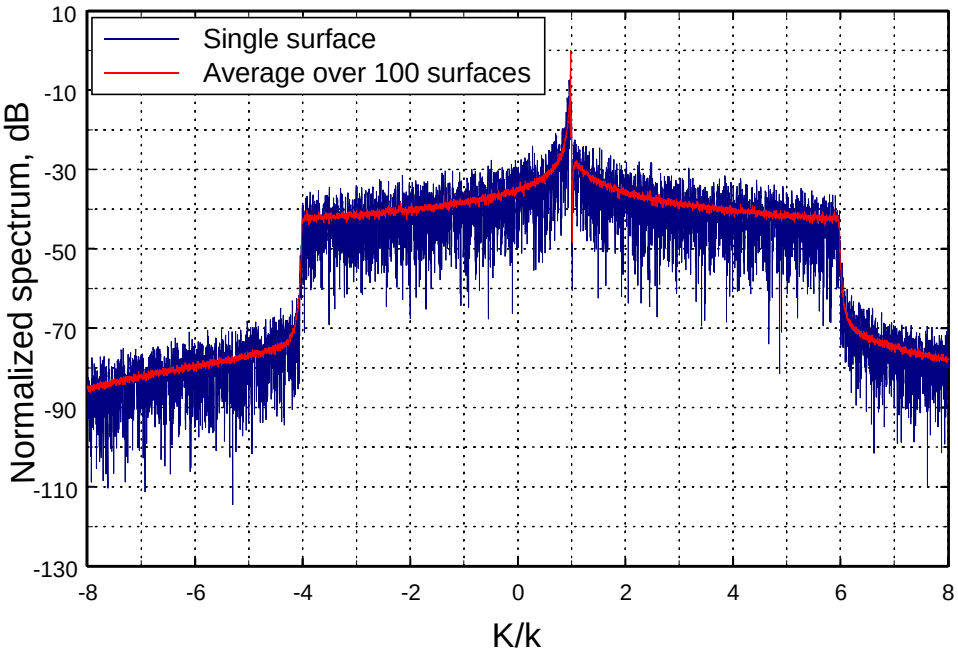

Figure 4-20. Example of the Fourier spectrum of the Kirchhoff current (horizontal (TE) polarization, $\theta_i = 80^\circ$, surface spectral cutoff is $5k$).

4-21 for horizontal and vertical polarizations, respectively, and $\theta_i = 80^\circ$. In these examples surface realizations with the "usual" spectral cutoff of $5k$ were used. Averages $\langle|\tilde{J}^i(K)|^2\rangle$ ($\tilde{J}^i$ is a Fourier transform of a Kirchhoff current for a particular surface) calculated from 100 surface realizations are shown also. The level of the pedestal can be different depending on the incident angle and polarization. In the case of horizontal

polarization it is higher because a derivative is involved in $J^i(x)$ in (2.15a) and as one moves towards grazing, this pedestal can contain an appreciable fraction of the spectral energy. The pedestal is contained within the wavenumber range between $k\sin\theta_i \pm K_c$. So if we want to treat $J^i(x)$ as a band-limited function, (4.33) is also a reasonable choice for all incident angles.

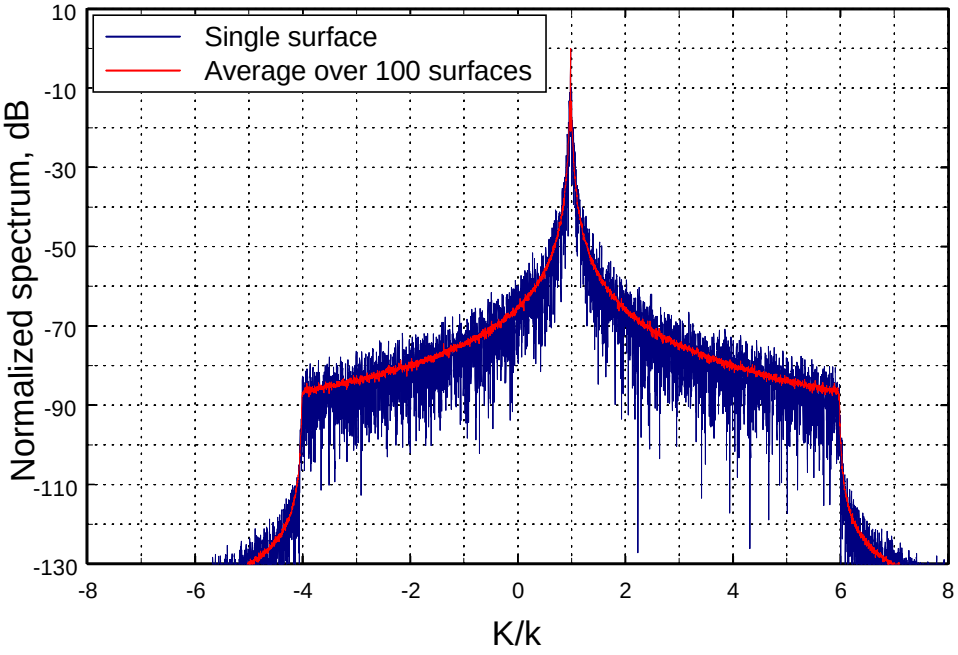

Figure 4-21. Example of the Fourier spectrum of the Kirchhoff current (vertical (TM) polarization, $\theta_i = 80^\circ$, surface spectral cutoff is $5k$).

Spectra of the "exact" currents $J(x)$ (solutions to the MFIE) for horizontal and vertical polarizations are shown in Figs. 4-22 and 4-23, again for $\theta_i = 80^\circ$. These currents also exhibit the pedestal mentioned above and can be considered band-limited functions with K_u given by (4.33). Examination of the 100-surface averages $\langle|\tilde{J}(K)|^2\rangle$ also

support this conclusion. In fact, the MFIE in (2.13) can be rewritten in the spectral domain as (symbols with tilde sign denote spectra of the corresponding quantities)

$$\tilde{J}(K) = \tilde{J}^{i}(K) + \frac{1}{2\pi}\int_{-\infty}^{\infty} \tilde{P}(K,-K')\tilde{J}(K')dK' \tag{4.34}$$

which indicates that if $P(x,x')$ and $J^{i}(x)$ are band-limited, $J(x)$ must also be a band-limited function since the right-hand side in (4.34) is then zero for $K > K_u$.

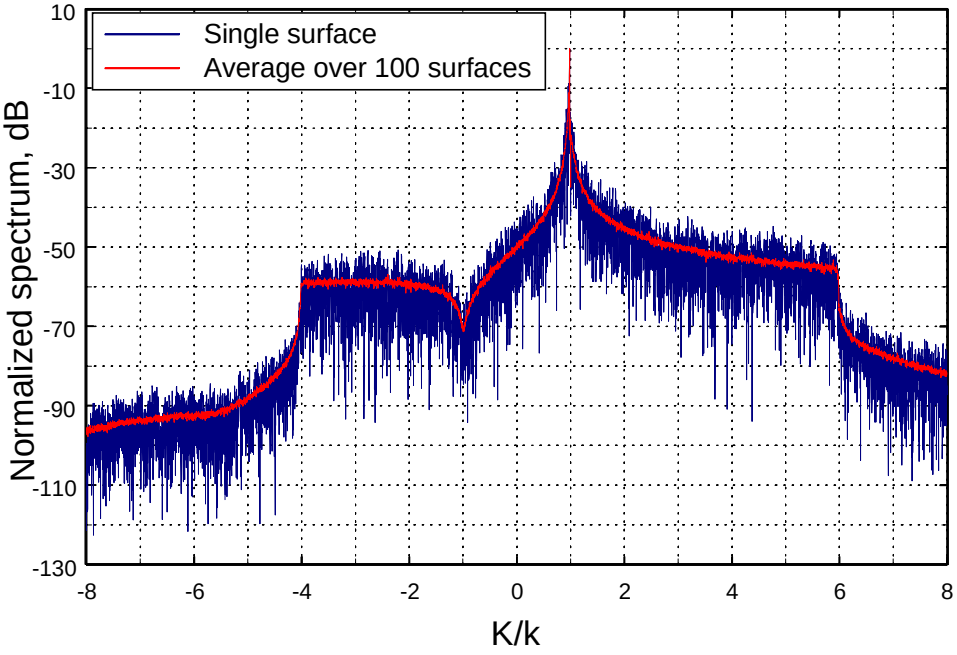

Figure 4-22. Example of the Fourier spectrum of the surface current (horizontal (TE) polarization, $\theta_i = 80^\circ$, two MOMI iterations, surface spectral cutoff is $5k$).

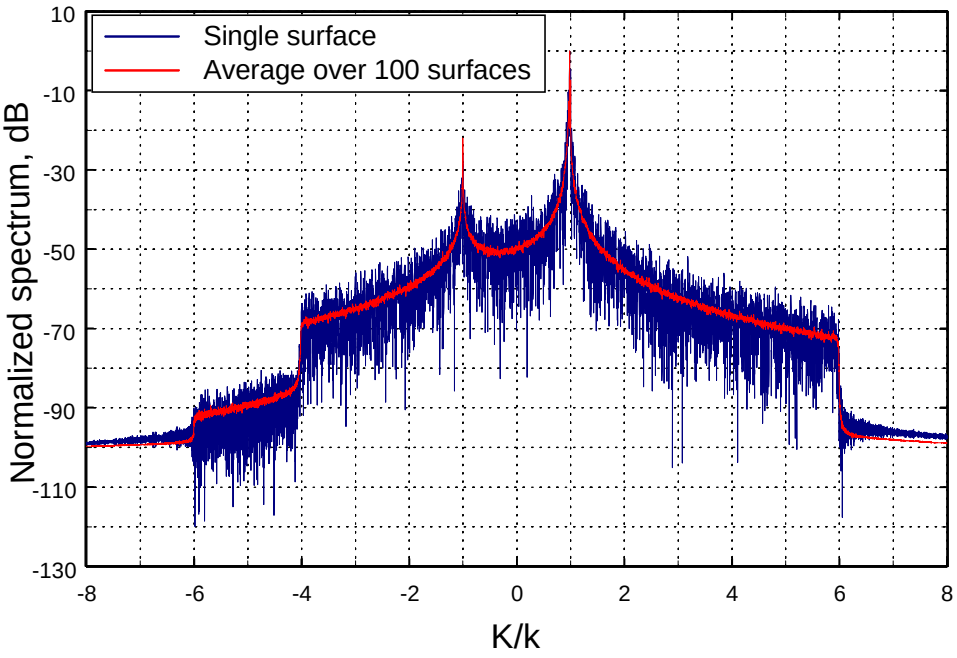

Figure 4-23. Example of the Fourier spectrum of the surface current (vertical (TM) polarization, $\theta_i = 80^\circ$, two MOMI iterations, surface spectral cutoff is $5k$).

Let us point out once again that at moderate incident angles away from grazing the pedestal described above is still observed in the spectra of both $J^i(x)$ and $J(x)$, although this pedestal may now contain a lesser fraction of energy compared to the main peak at $k\sin\theta_i$. In any case, these spectra may indeed be regarded as band-limited with the choice of the upper spectral limit K_u from (4.33) being adequate or even more than adequate for all incident angles.

Once $P(x,x')$, $J^i(x)$ and $J(x)$ are treated as band-limited functions, a moment method approach described at the beginning of this section can be applied with $\{s_n(x)\}$ from (4.29) serving as both the expansion and testing functions. K_u is taken from (4.33) and this in turn determines an appropriate sampling interval Δx in (4.29) as

$$\Delta x = \frac{\pi}{k + K_c} = \frac{\lambda}{2(1 + K_c/k)} \tag{4.35}$$

Elements of vectors and matrix in (4.21) can be rewritten using (4.32) (with $a_m = \Delta x$, as can be seen comparing (4.20) to (4.30)). The expression for P_{mn} in (4.21) involves a two-dimensional scalar product defined similarly to (4.17) as

$$\langle f(x,x'), g(x,x') \rangle = \int_X \int_X f^*(x,x') g(x,x')\, dx dx',$$

and it then can be related to the samples of $P(x,x')$ through a two-dimensional version of (4.32), namely $\langle s_m(x) s_n(x'),\, f(x,x') \rangle \big/ (\Delta x)^2 = f(m\Delta x, n\Delta x)$:

$$P_{mn} = \frac{1}{a_m} \int_X \langle t_m(x), P(x,x') \rangle\, e_n(x') dx' \equiv \frac{1}{\Delta x} \int_X \int_X s_m(x) P(x,x') s_n(x') dx dx'$$

$$= \frac{1}{\Delta x} \langle s_m(x) s_n(x'), P(x,x') \rangle = P(m\Delta x, n\Delta x)\Delta x$$

Thus we finally do arrive at the discretization shown in (2.19).

Note that this approach clearly requires that the diagonal terms of the propagator should be just the samples of the propagator taken at the same point, i.e. $x = x' = m\Delta x$: $P_{mm} = P(m\Delta x, m\Delta x)\Delta x$. As was mentioned, though the value of $P(x,x')$ from (2.14b), (2.16) or (2.15b), (2.17) at such points is indeterminate (behaving as 0/0), the limit does exist and is given by (4.27). Upon multiplying (4.27) by Δx and substituting $x = m\Delta x \equiv x_m$ we obtain (for the diagonal elements of the propagator matrix) exactly the "curvature term" given in (4.1). So, another important conclusion of the sampling approach outlined above *is that the curvature term should appear on the diagonal of the propagator matrix and it is not an additional correction*. When we leave the curvature terms out, we in fact solve the MFIE with an altered kernel, and this is bound to produce the kind of differing results we noted in Section 4.2.4 no matter what particular numerical technique is applied to solve the MFIE. Indeed, we saw (cf. Figs. 4.6 and 4.7) that if the curvature term is not included, MOMI still converges rapidly but it converges to different answers. This means that for each different sampling interval MOMI finds the solution to the MFIE *with a perturbed propagator*. Another important conclusion is that the off-diagonal terms should be just samples of the propagator with no additional curvature

correction being necessary. That is, once the proper sampling interval such as given in (4.35) is chosen, there is no reason to include any additional correction terms like ones that may arise from the evaluation of (4.24) by expansion of the integrand in a Taylor series or to expect that these higher-order terms will improve the accuracy of the solution.

It should be pointed out that the inclusion of the surface curvature in the numerical algorithm is almost trivial since the values for surface curvature can be easily generated together with surface heights and slopes using the spectral technique described in Chapter 3.

Let us finally address a question of calculating the scattered field. The far-field propagators Q (given by (2.31) and (2.32)) also can be treated as band-limited functions with a spectrum concentrated within the limits of $\pm K_u$ as given in (4.33). Their Fourier spectra

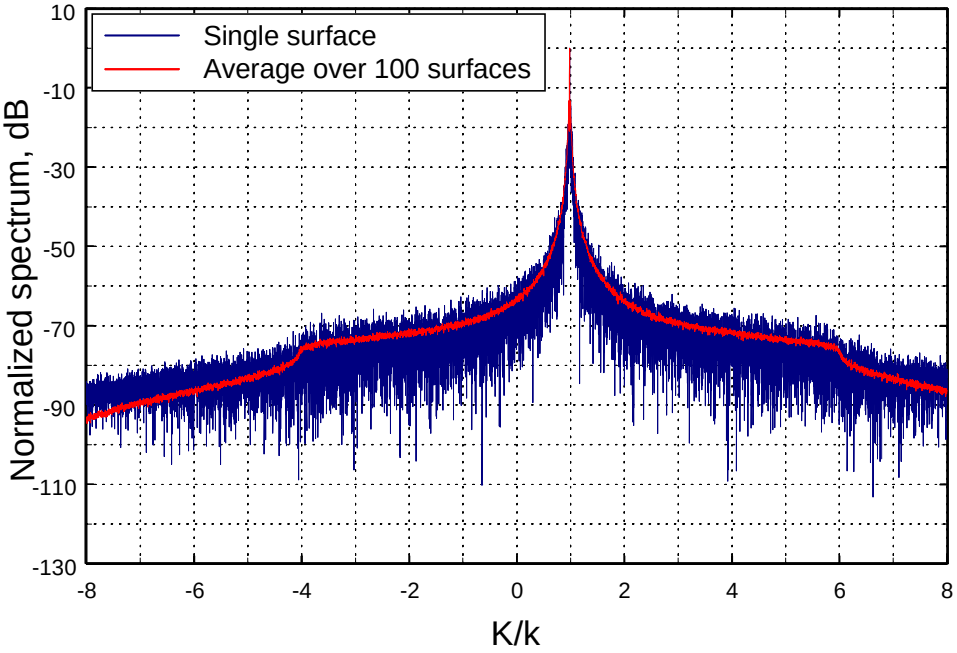

Figure 4-24. Example of the Fourier spectrum of the far-field propagator Q in (2.32) (horizontal (TE) polarization, $\theta_s = -80^\circ$, surface spectral cutoff is $5k$).

$$\tilde{Q}(K,\theta_s) = \int_{-\infty}^{\infty} Q(x,\theta_s) e^{jKx} dx$$

for $\theta_s = -80^\circ$ are shown in Figs. 4-24 and 4-25. Note that although the "pedestal" in Fig. 4-24 is not as much pronounced as in other examples within this Section, the spectrum in this figure has a relatively broad central peak (compare to Fig. 4-25) that contains the

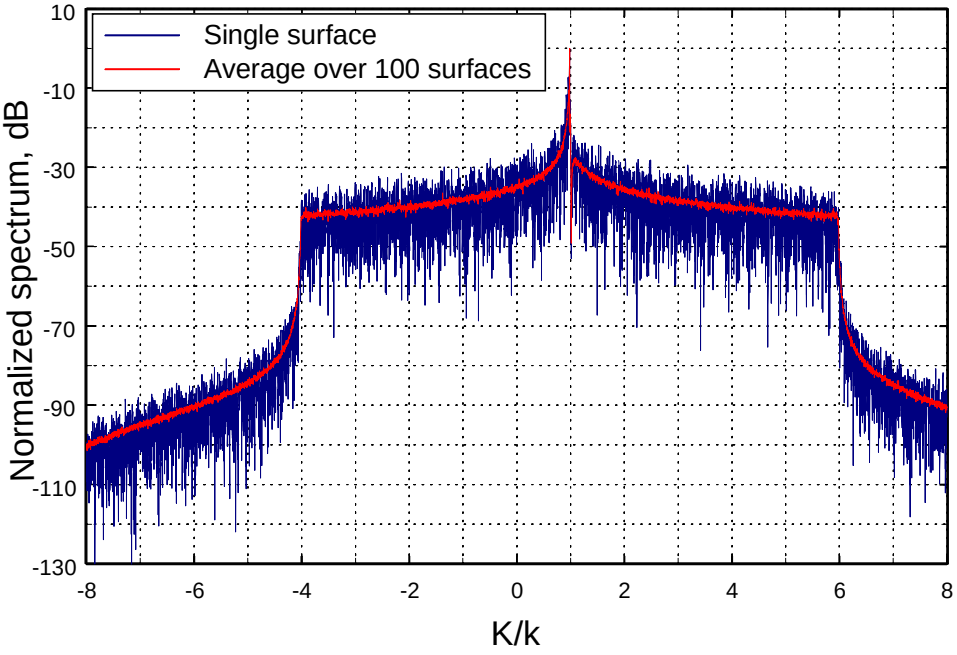

Figure 4-25. Example of the Fourier spectrum of the far-field propagator Q in (2.31) (vertical (TM) polarization, $\theta_s = -80^\circ$, surface spectral cutoff is $5k$).

bulk of its spectral energy. Upon substitution of the expansion (4.18) for $J(x)$ and applying (4.32), the integral in (2.30) can be written as a discrete sum:

$$\int_X Q(x,\theta_s) J(x) dx = \sum_n J_n \int_X s_n(x)\, Q(x,\theta_s) dx = \Delta x \sum_n J_n\, Q(n\Delta x, \theta_s) \qquad (4.36)$$

So, the scattered field can be calculated from the sampled surface current and the similarly sampled far-field propagator Q.

We can compare the sampling interval suggested in (4.35) to that used in Section 4.2. The largest sampling interval there was, from (4.13), $\Delta x_0 = \lambda/10$, while for $K_c = 5k$ (4.35) gives a smaller value of $\Delta x = \lambda/12$. Indeed, in Fig. 4-11 we noticed a slight change in the phase of the calculated field (with the included curvature term) as the sampling interval decreased from $\lambda/10$ to $\lambda/20$ (which is less than $\lambda/12$). Still, the change is very small and this suggests that quite accurate results may be possible with somewhat larger sampling intervals than given by (4.35). Indeed, from Fig. 4-14 we saw that relative mean square error in the current at $\Delta x_0 = \lambda/10$ for the surface with a cutoff given by $K_c = 5k$ is still below -60 dB. However, we believe that the sampling interval should not be larger than π/K_c ($= \lambda/10$ for $K_c = 5k$) since otherwise the surface structure will not be represented correctly (due to spectral aliasing effects). Also, we would like to point out that (4.35) should not be applied to surfaces with spectral cutoffs below $2k$ especially if the backscattered field at low grazing angles is of interest. This is because for such low cutoffs it will be mainly the spectral components of the current outside the pedestal, which becomes narrower due to the small cutoff, that are responsible for the low grazing scattered field, and these components will be sensitive to the spectral aliasing due to their extremely small amplitude. In fact, some differences in NRCS that were observed in Fig. 4-8 are probably due to these effects. In a sense, these "low-cutoff" surfaces might prove to be "tougher" for low grazing backscattering calculations and require even tighter sampling than P-M surfaces with high cutoffs such as $K_c = 5k$.

Our recommendation for the choice of the sampling interval given in (4.35) is based on examining the shapes of the spectra in Figs. 4-17 - 4-23. As noted, these plots correspond to a $23\,\text{cm}$ electromagnetic wavelength and P-M surfaces with the windspeed of 5 m/s. A legitimate question is whether these plots retain their shape in the case of a smaller wavelength and/or larger windspeed and, consequently, if (4.35) remains valid. Our simulations with a shorter wavelength ($\lambda = 10\,\text{cm}$) and windspeeds as large as $U = 10\,\text{m/s}$ show exactly the same spectral patterns; we are confident that our recommendation for Δx is robust for other wavelengths as well provided that the spectral cutoff is still chosen to be several times the *new* electromagnetic wavenumber.

The discretization of the propagator considered in this Section gives the same result that would be obtained if only the leading terms were retained in the expansion (4.25) in the case of rectangular expansion functions. One might wonder if there could be any advantage in accounting for the higher-order terms in (4.25), for example, if one could afford a sampling interval larger than that given by (4.35). We tried to include the expansion terms beyond the "curvature term" in the diagonal of the propagator matrix (while leaving the off-diagonal terms the same as in (4.26)). This was done for the sampling interval of $\Delta x = \lambda/10$ and the error was calculated from a comparison to the results with a much tighter sampling ($\Delta x = \lambda/160$) considered as "exact" (the propagator matrix elements in the latter case were as given by (4.1) and (4.26)). It was found that the error in both the scattered field and the surface current actually *increased* as compared to the case when the sampling interval was also $\Delta x = \lambda/10$ but only the curvature terms were used in the diagonal. It can probably be argued that the higher-order corrections should be included in the diagonal and off-diagonal terms simultaneously. However, the results of this Section suggest that even if the integrals in (4.24) are calculated exactly (*all* terms in the expansion (4.25) are accounted for), the error may still be larger than when only the samples of the propagator are used. Indeed, calculating the integrals like (4.24), e.g.

$$f_n = \int_{x_n - \Delta x/2}^{x_n + \Delta x/2} f(x')dx'$$

is equivalent to convolving $f(x)$ with $rect(x)$ (cf. 4.23)),

$$g(x) = \int_{-\infty}^{\infty} f(x')rect\big((x - x')/\Delta x\big)dx'$$

and taking samples of the resulting function $g(x)$:

$$f_n = g(x_n).$$

Because of the convolution, the spectrum of $g(x)$ will be a product of the Fourier spectra of $f(x)$ and $rect(x)$, the latter of course being a *sinc* function (cf., for example, [Bracewell, 1965]). On one hand, such a multiplication suppresses spectral components with large wavenumbers and reduces the errors due to spectral aliasing when the function

g is discretized. However, we found that for the P-M surfaces the spectra of the currents and the propagator are manifestly band-limited, so these aliasing effects are probably not a significant factor. On the other hand, the multiplication by a *sinc* function alters the spectrum of $f(x)$ at other, smaller wavenumbers as well. So, we essentially end up with solving the MFIE with an altered kernel, which may lead to some error. We believe that for P-M surfaces, it is advisable to use the leading expansion terms (4.26) and (4.1) (that are just the samples of the propagator) *and* the correct sampling interval in (4.35), rather than to account for the higher-order expansion terms in (4.25) or even to evaluate the integrals in (4.24) exactly.

4.4 A Choice of the Cutoff in the P-M Spectrum for Scattering Simulations

In the previous section we developed a criterion (4.35) for sampling the MFIE currents and propagators for P-M surfaces; it suggests that the sampling interval Δx should be chosen based on both the electromagnetic wavelength and the surface spectral cutoff. This choice assures that we obtain correct results for the scattered field for a given cutoff even at low grazing angles where the tolerance to any error is especially small. Usually the natural spectral cutoff for the ocean-like surfaces is very high. With no surfactants, the molecular dissipation mechanism sets this cutoff at about $K_{cd} \cong 6.3 \cdot 10^3 \text{ m}^{-1}$ [Apel, 1994]. For an electromagnetic wavelength of 23 cm used in our simulations, this amounts to $K_{cd} \cong 231k$, which is about 46 times larger than the cutoff in (4.10). Retaining such a large cutoff K_{cd} would in accordance with (4.35) require extremely fine sampling and, as a consequence, matrices and vectors of enormous sizes. However, there is good reason to expect that surface wave components much smaller than electromagnetic wavelength will not have any significant impact on the scattered field. Indeed, approximate theories like first order perturbation theory predict that the cross section will be affected mostly if not solely by the spectral components around the Bragg wavenumber $k_b = 2k \sin\theta_i$ [Ogilvy, 1991].

In this Section we study how an artificially introduced cutoff in the P-M spectrum (4.9) affects our scattering calculation results. We again use $\lambda = 23\,\text{cm}$ and $U = 5\,\text{m/s}$. Unless otherwise specified, all other simulation details are the same as used in Section

4.2.3. The highest spectral cutoff used is $K_c = 5k$; to obtain surface realizations with a lower cutoff, we used a higher cutoff realization and filtered out high-frequency Fourier components while keeping the lower-frequency Fourier components the same. This was especially easy to accomplish since we used the spectral method of surface generation (Chapter 3). Such a procedure allowed meaningful comparisons of the NRCS vs. spectral cutoff on realization-per-realization basis. It was convenient to use the same sampling interval for all spectral cutoffs studied. In order to use some of the results from the previous Sections, we fixed this interval at $\Delta x_0 / 2 = \lambda / 20$ (cf. (4.13)).

Fig. 4-26 shows a general behavior of the average backscattered NRCS for P-M surface with a spectral cutoff equal to $5k$. In what follows we will examine how a few

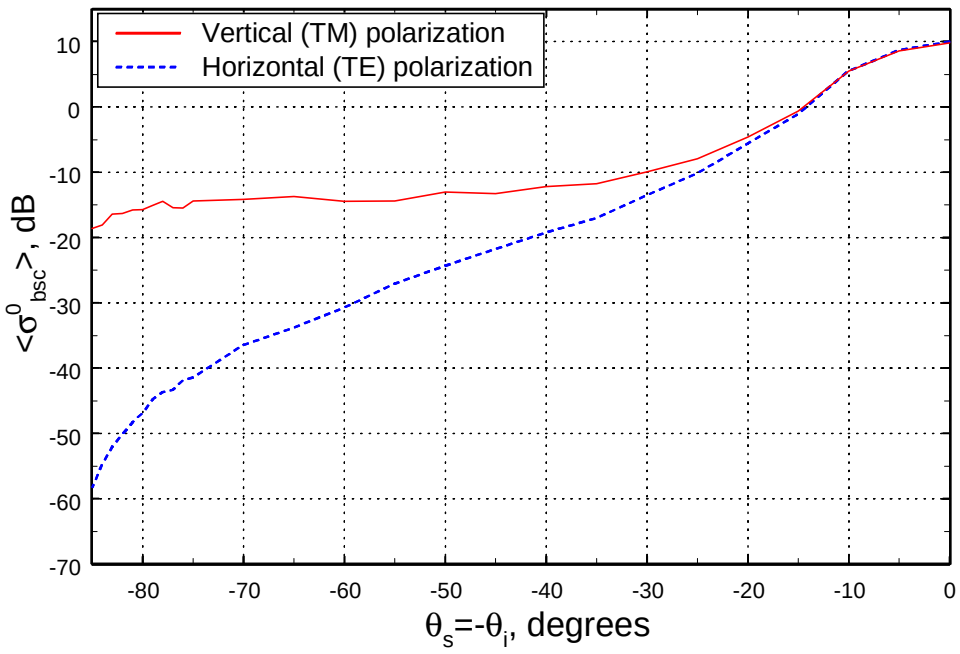

Figure 4-26. Average backscattered NRCS. The average is taken over 100 P-M surfaces with a spectral cutoff of $5k$.

selected points on this graph, corresponding to certain incident angles, behave as the spectral cutoff changes. The dependence of the average backscattered NRCS on the

spectral cutoff for several incident angles ranging from normal incidence to near grazing is shown in Figs. 4-27 and 4-28 for horizontal and vertical polarizations respectively. One can see that the average NRCS ($=\langle\sigma^0_{bsc}\rangle$) corresponding to $\theta_i = 0^\circ$ and $\theta_i = 30^\circ$ are not sensitive to the cutoff wavenumber within the range shown, for both horizontal and vertical polarizations. For $\theta_i = 60^\circ$, the NRCS starts showing change at cutoffs below $K_c \approx 1.8k$ in the horizontal case and at cutoffs below $K_c \approx 1.9k$ in the vertical case. For reference, the Bragg number for backscattering at $\theta_i = 60^\circ$ is $k_b = 2k\sin 60^\circ \cong 1.73k$. The horizontal and vertical NRCS values corresponding to $\theta_i = 80^\circ$ and $\theta_i = 85^\circ$ experience an abrupt drop at $K_c \approx 2.0k$ while staying essentially constant for larger wavenumbers. For $\theta_i = 85^\circ$, slight changes can be noticed as early as $K_c \approx 2.2k$. Again, as a reference we note that the Bragg numbers for backscattering at these angles are very close to $2k$: for $\theta_i = 80^\circ$ one has $k_b \cong 1.97k$ and for $\theta_i = 85^\circ$, $k_b \cong 1.99k$.

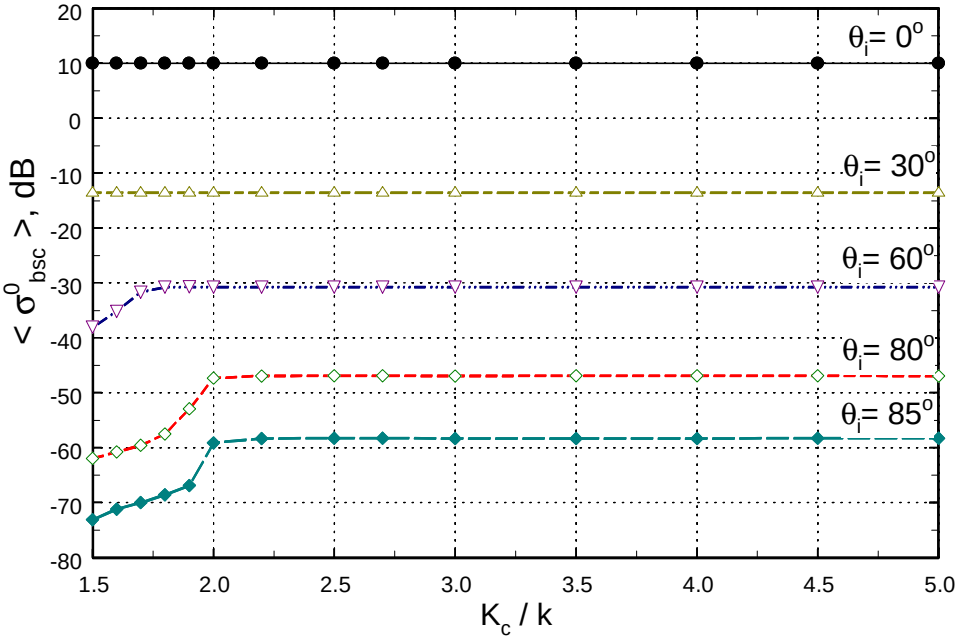

Figure 4-27. Average backscattered NRCS as a function of the surface spectral cutoff (horizontal (TE) polarization, average is taken over 100 P-M surfaces).

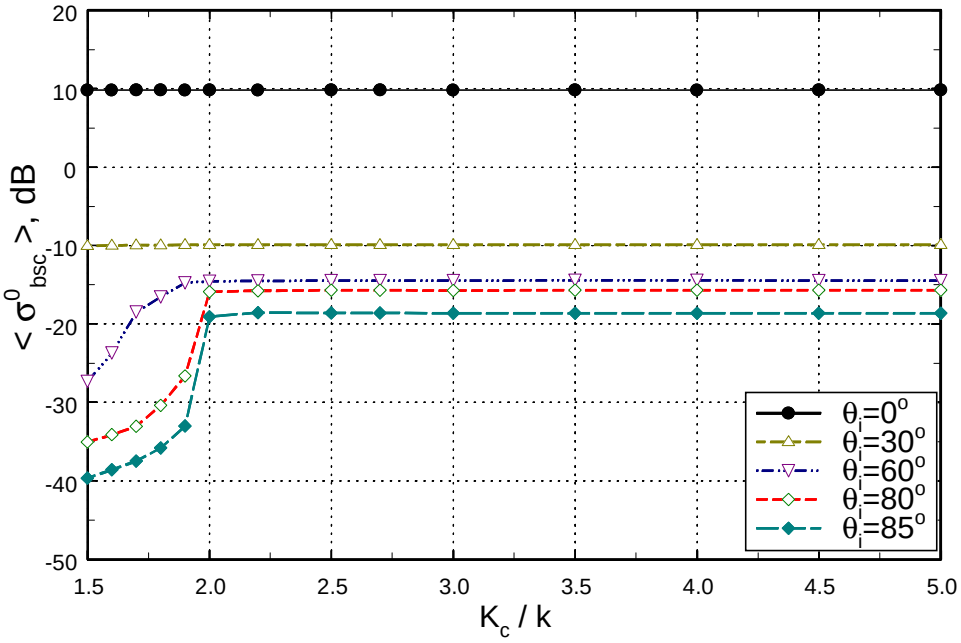

Figure 4-28. Average backscattered NRCS as a function of the surface spectral cutoff (vertical (TM) polarization, average is taken over 100 P-M surfaces).

Figs. 4.29 and 4.30 are similar to Figs. 4.27 and 4.28 and concentrate on the behavior of the average backscattered NRCS with the cutoff at incident angles close to grazing, for horizontal and vertical polarizations respectively. One can see that the average NRCS for large cutoffs remain fairly constant and start showing some changes

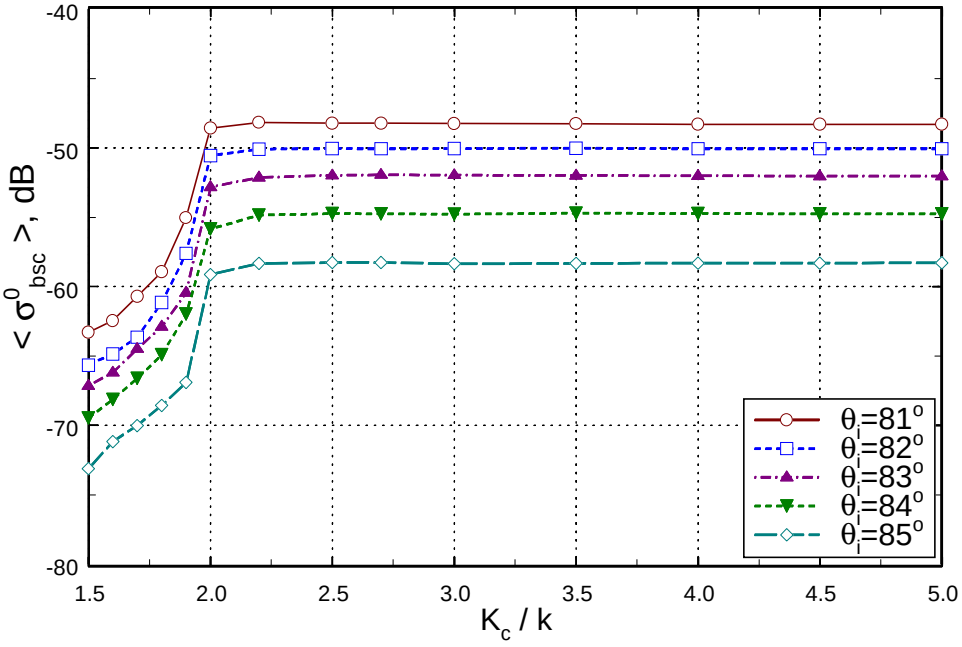

Figure 4-29. Average backscattered NRCS vs. surface spectral cutoff: low grazing angles (horizontal (TE) polarization, average is taken over 100 P-M surfaces).

at $K_c < 2.2k$; this change seems to become somewhat more pronounced as the incident angle increases but not by much. All NRCS's in these Figures experience a significant drop at $K_c \approx 2k$. This observation suggests that cutoff values of $K_c = 2.5k$ or even as low as $K_c = 2.2k$ should suffice as long as the moments of the scattered field (like average NRCS) are of interest. It remains to be seen if this conclusion holds for lower grazing angles (the extensive Monte Carlo simulations for larger incident angles required significantly larger beam waist and surface size). However, the fact that the point where

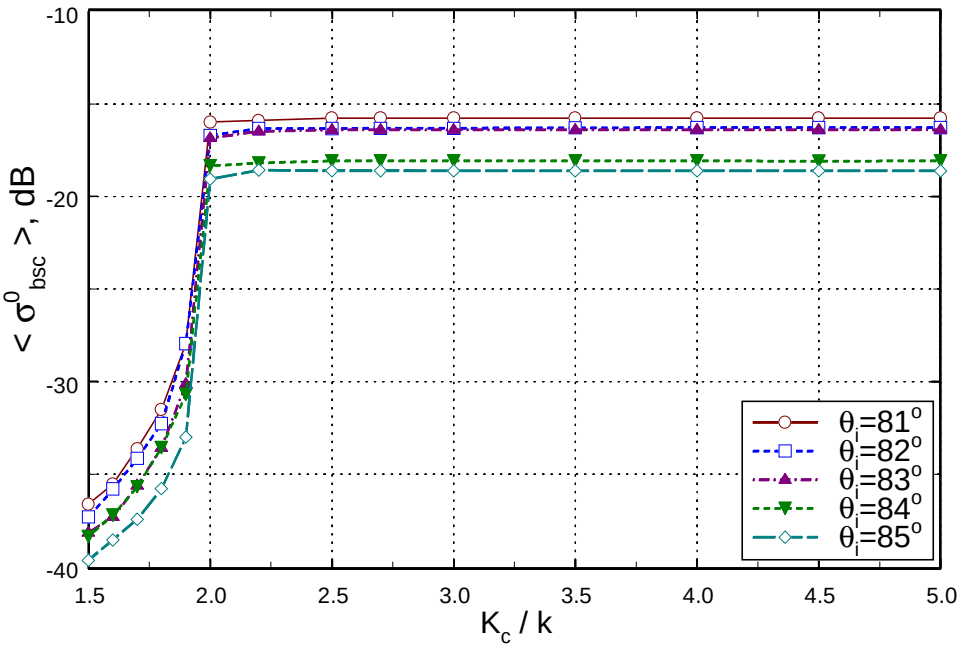

Figure 4-30. Average backscattered NRCS vs. surface spectral cutoff: low grazing angles (vertical (TM) polarization, average is taken over 100 P-M surfaces).

the NRCS starts varying with K_c (which we determined to be around $2.2k$) does not noticeably depend on θ_i seems encouraging. Fig. 4-31 compares the average bistatic cross sections for $\theta_i = 85^\circ$ obtained with the surfaces with the spectral cutoff of $5k$ and $2.5k$ for the horizontal case. The cross sections for vertical polarizations are compared in Fig. 4-32. In both figures, the plots corresponding to different cutoffs virtually coincide once again confirming our speculation that $K_c = 2.5k$ in (4.9) is sufficient for average NRCS calculations even at low grazing angles.

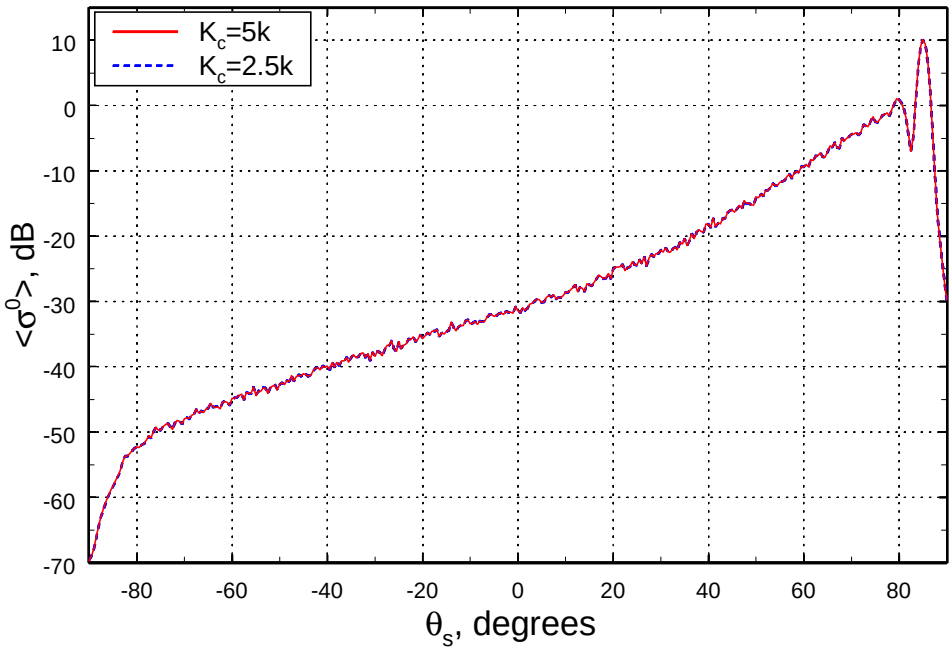

Figure 4-31. Average bistatic NRCS for two different surface spectral cutoffs, (horizontal (TE) polarization, $\theta_i = 85^\circ$, average is taken over 100 P-M surfaces).

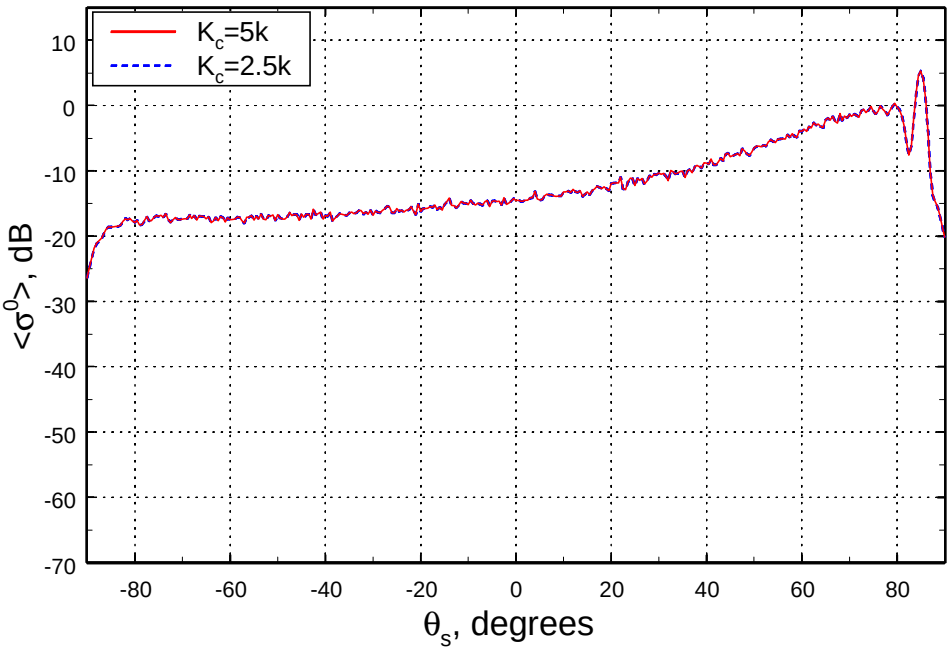

Figure 4-32. Average bistatic NRCS for two different surface spectral cutoffs (vertical (TM) polarization, $\theta_i = 85^\circ$, average is taken over 100 P-M surfaces).

Let us finally investigate how the NRCS of a single realization behaves as we filter out the high-frequency components of the surface. This dependence is analyzed in Figs. 4-33 and 4-34 for horizontal and vertical polarizations. These Figures are similar to

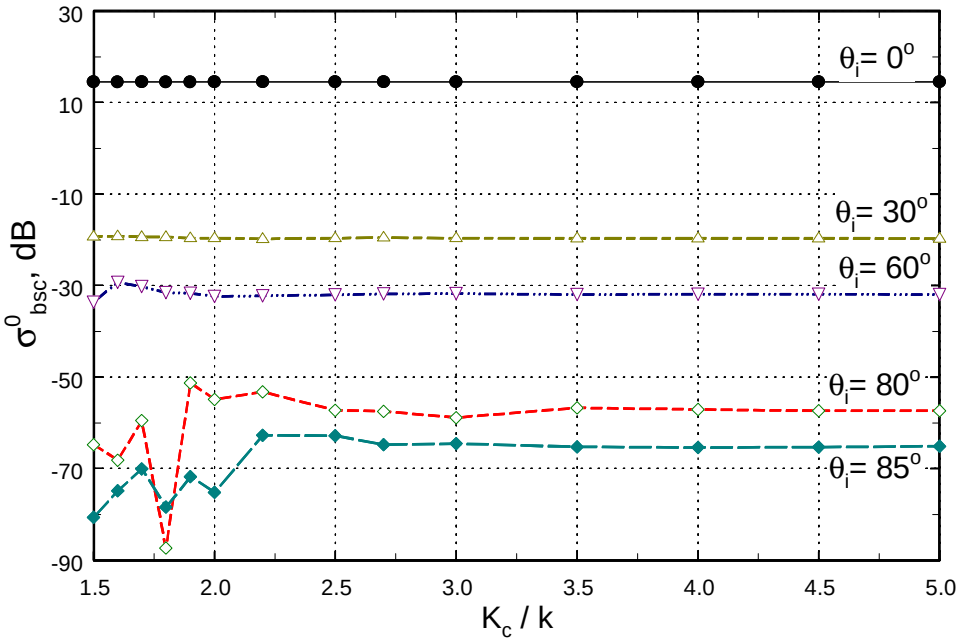

Figure 4-33. Backscattered NRCS as a function of the surface spectral cutoff (horizontal (TE) polarization, single realization of a P-M surface).

Figs. 4-27 and 4-28 except that now no average is taken and just one surface realization is considered. These are typical results and we observed a similar behavior for all realizations that we computed. In general, these figures confirm the conclusions drawn from analyzing the averages in Figs. 4-27 and 4-28. For moderate incident angles there is no significant variation in NRCS. For $\theta_i = 0^\circ$ there is no variation at all; for $\theta_i = 30^\circ$ there is a minute variation below $K_c = 2k$; for $\theta_i = 60^\circ$ there is somewhat larger variation as K_c moves below $2k$. For larger spectral cutoffs the NRCS value remains stable. For the angles closer to grazing ($\theta_i = 80^\circ$, 85°) the variations become larger and,

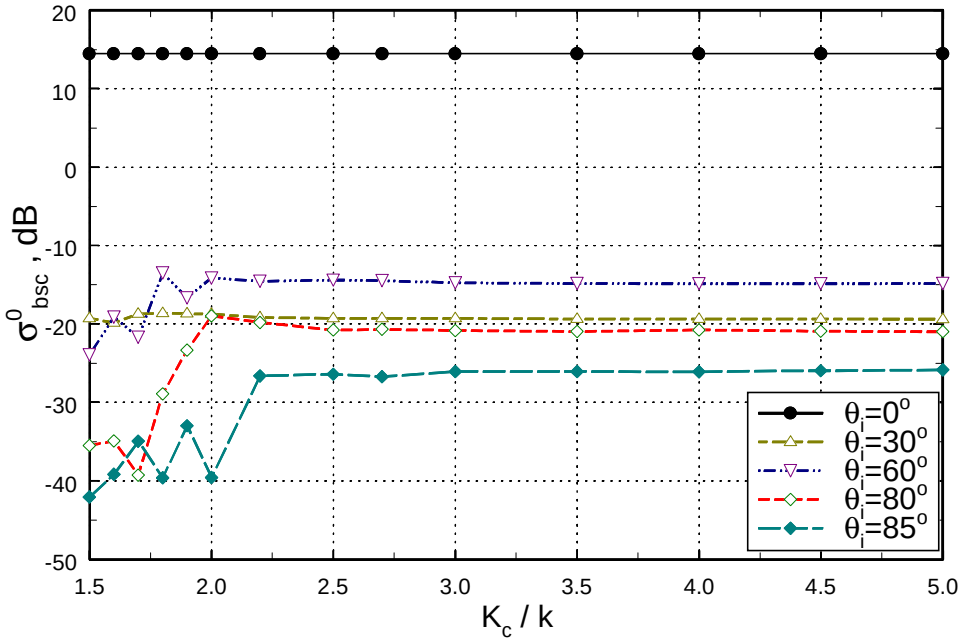

Figure 4-34. Backscattered NRCS as a function of the surface spectral cutoff (vertical (TM) polarization, single realization of a P-M surface).

in contrast to what we observed for the average NRCS, are now visible even at the cutoff wavenumbers as high as $2k$.

Figs. 4-35 and 4-36 examine the NRCS at low grazing incidence angles for both polarizations; they can be regarded as counterparts of Figs. 4-29 and 4-30 for a single surface realization. A general conclusion (based also on similar plots for other surface realizations studied) is that at large incident angles the single surface NRCS is sensitive to the surface spectral cutoff for values as large as $K_c = 3.5k - 4k$, and apparently there is only a weak tendency for this no-variability threshold to increase as one moves down to grazing. This means that if the calculated field or cross section for a single surface realization is of interest or simulation results are used to calculate more intricate statistical moments of the scattered field (or, for example, its pdf), one might want to consider using a cutoff as high as $K_c = 4k$. Our choice in (4.10) seems to be more than sufficient for the range of incident angles considered.

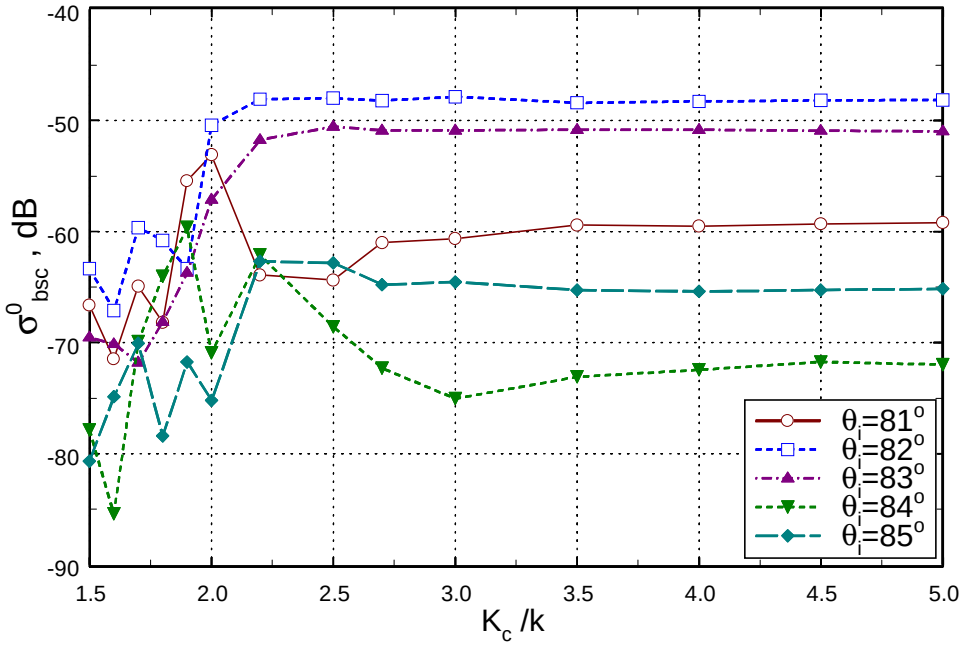

Figure 4-35. Backscattered NRCS vs. surface spectral cutoff: low grazing angles (horizontal (TE) polarization, single realization of a P-M surface).

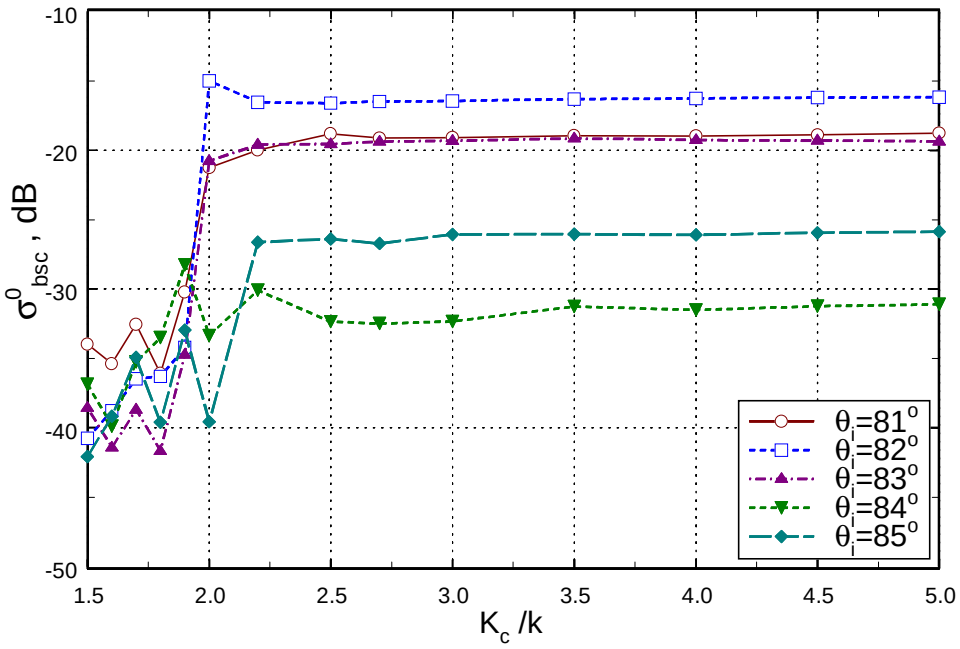

Figure 4-36. Backscattered NRCS vs. surface spectral cutoff: low grazing angles (vertical (TM) polarization, single realization of a P-M surface).

To investigate this issue further, let us examine a relative root mean square error in the field defined as follows. We assume that for each surface realization the scattered field ψ^s calculated with the highest spectral cutoff $K_c = 5k$ represents the "true" or "exact" value of the scattered field that we will denote as ψ_0^s. The rms relative error in the field incurred due to an insufficiently high spectral cutoff is defined as

$$\varepsilon_\psi(K_c) = \left(\frac{\langle |\psi_{K_c}^s - \psi_0^s|^2 \rangle}{\langle |\psi_0^s|^2 \rangle} \right)^{1/2} \tag{4.37}$$

where $\psi_{K_c}^s$ refers to a scattered field corresponding to the same surface with a lower than $K_c = 5k$ cutoff. As usual, the average is taken over an ensemble of surfaces. The ψ^s that is calculated according to (2.30) is a function of a scattering angle θ_s and we will consider only the backscattering, $\theta_s = -\theta_i$. The relative rms error (4.37) for backscattering at low grazing angles is plotted in Figs. 4-37 (horizontal case) and 4-38 (vertical case). Only the region of K_c larger than $2k$ is shown; for smaller cutoffs the relative rms error rapidly becomes substantially greater than one, as could be expected from the previous figures. We observe that both in horizontal and vertical cases the curves corresponding to different θ_i group together and there is no dramatic increase in ε_ψ as we go from $\theta_i = 81^\circ$ to $\theta_i = 85^\circ$, especially for high K_c. At $K_c = 2.5k$ the relative rms error is about 0.10 - 0.15 for the horizontal polarization and about 0.06 for the vertical polarization. For $K_c = 4k$, ε_ψ decreases to approximately 0.02 - 0.03 for the horizontal case and 0.01 for the vertical case, with the values corresponding to different θ_i grouping closer to each other than in the $K_c = 2.5k$ case. Thus, the choice of $K_c = 4k$ in (4.9) will result on the average in 3% error in the field for horizontal polarization and 1% error for vertical polarization for the incident angles as low as 85°. From the behavior of the plots we do not expect that these values will increase significantly for the larger incident angles. Figs. 4-37 and 4-38 provide a guideline for the choice of the spectral cutoff depending on the degree of precision required in the

scattered *field*. We feel that the choice of $K_c = 4k$ should be adequate for all but the most critical purposes.

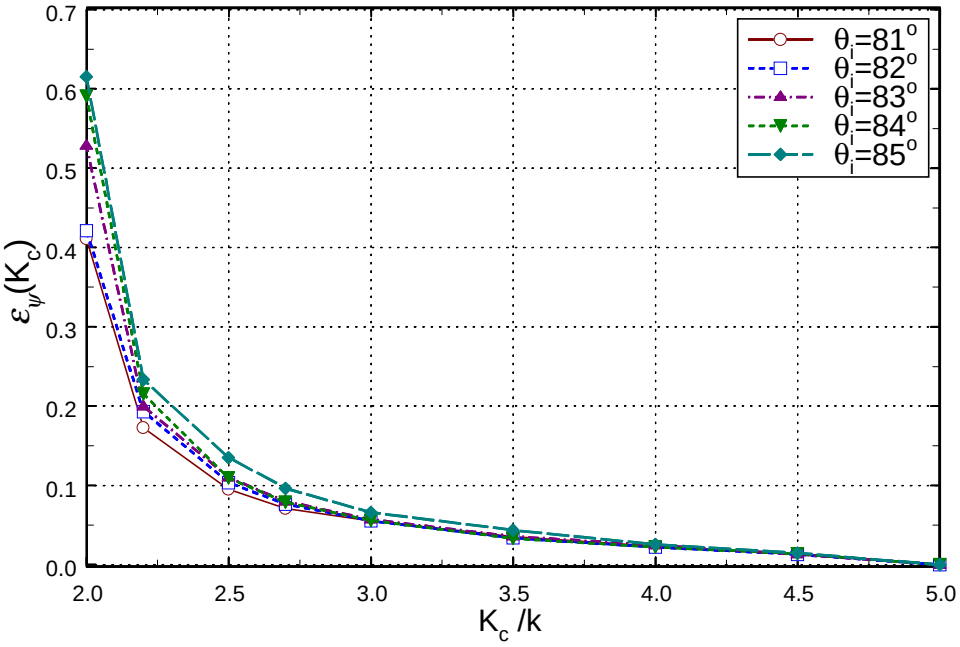

Figure 4-37. Relative rms error in the backscattered field vs. surface spectral cutoff (low grazing angles, horizontal (TE) polarization, average is taken over 100 P-M surfaces).

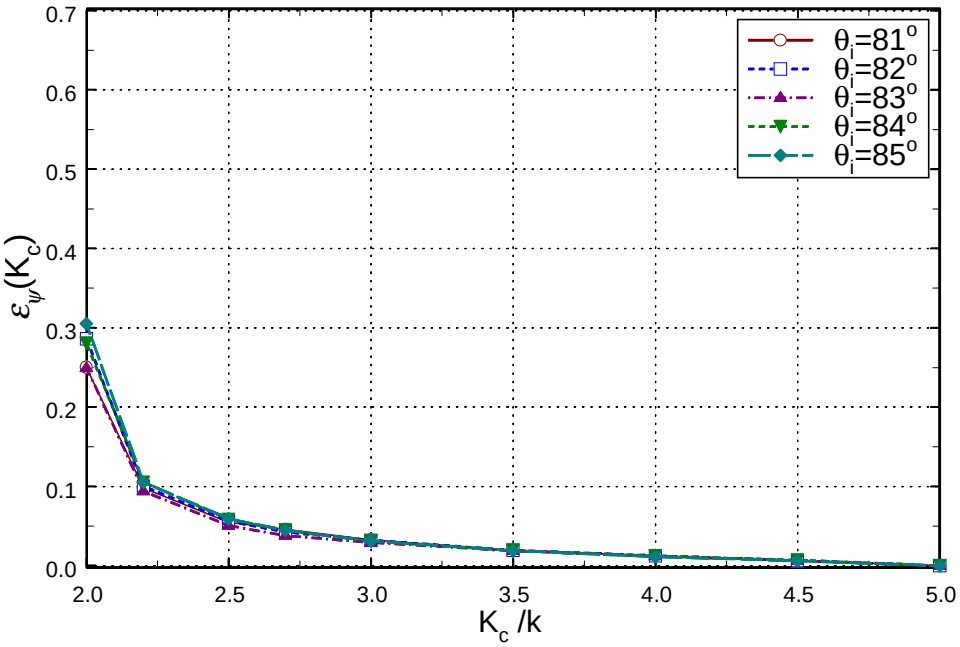

Figure 4-38. Relative rms error in the backscattered field vs. surface spectral cutoff (low grazing angles, vertical (TM) polarization, average is taken over 100 P-M surfaces).

4.5 Conclusion

A brief summary of the new results reported in this Chapter is as follows. Numerical simulations of scattering from Pierson-Moskowitz surfaces show that if the curvature term is not included in the diagonal of the propagator in the discretized MFIE, the results can exhibit excessive sensitivity to the sampling interval and may require very tight sampling to reach a stable value. This effect is especially significant for the scattering at low grazing angles in the case of horizontal polarization and has an impact on average quantities such as the average normalized radar cross section. However, when the curvature terms are included in the diagonal of the propagator matrix, the calculated scattered field reaches a stable value using a much larger sampling interval. Careful consideration of the discretization of MFIE shows that curvature terms indeed must be included in the diagonal of the propagator, being simply the sampled values of the propagator, just as the off-diagonal elements; there is no need for additional correction terms once a proper sampling interval is chosen. The recommendation for choosing such an interval when calculating scattering from Pierson-Moskowitz surfaces is given and is based on the electromagnetic wavelength and the surface spectral cutoff. Subsequent analysis of the influence of the cutoff in the Pierson-Moskowitz spectrum on the scattering simulation results reveals that for the average NRCS calculations this cutoff can be chosen as low as 2.5 times the electromagnetic wavenumber. If the field or NRCS from individual realizations is of interest, a cutoff of 4 times the electromagnetic wavenumber seems sufficient for incident angles down to 85°.

Appendix 4.A Surface Correlation Length

The surface correlation length L_c, which is a measure of the "width" of the surface correlation function $C(x)$, can be defined in a number of ways. One possible definition is

$$L_{c1} = \frac{1}{C^2(0)} \int_{-\infty}^{\infty} C^2(x)dx \tag{4.A.1}$$

which is the definition that we considered in (4.5). The reason for using the square of the correlation function rather than $C(x)$ itself is that the latter can assume negative values, as can be seen in Fig. 4-2. Another possible definition is

$$L_{c2} = \left(\frac{\int_{-\infty}^{\infty} x^2 C^2(x)dx}{\int_{-\infty}^{\infty} C^2(x)dx} \right)^{1/2} \tag{4.A.2}$$

We will evaluate L_{c1} and L_{c2} for the surface with the P-M spectrum in (4-2) and will show that they both are proportional to the dominant surface wavelength Λ_p in (4.4). In the developments that follow our goal will be to calculate all integrals in (4.A.1) and (4.A.2) in K-space (where we know the expression (4.2) for $W(K)$) rather than in x-space (where we do not have an explicit analytical expression for $C(x)$).

Consider L_{c1} first. We recognize that $C^2(0) = \langle \zeta^2 \rangle^2$ and from (4.7) have

$$C^2(0) = \frac{\alpha^2 U^8}{16\beta^2 g^4} \tag{4.A.3}$$

Let us turn our attention to the integral in (4.A.1) which we will denote for brevity as

$$I \equiv \int_{-\infty}^{\infty} C^2(x)dx \tag{4.A.4}$$

Using (3.17) to relate the surface correlation function to the surface spectrum $W(K)$ we can write

$$I = \int_{-\infty}^{\infty} dx \left(\int_{-\infty}^{\infty} dK\, W(K) e^{-jKx} \right)^2 = \int_{-\infty}^{\infty} dx \int_{-\infty}^{\infty} \int_{-\infty}^{\infty} dK dK' W(K) W(K') e^{-j(K+K')x} \quad (4.A.5)$$

Interchanging integrations over x and K's and using the relation (e.g. [Arfken and Weber, 1995, p.852])

$$\int_{-\infty}^{\infty} e^{-jKx} dx = 2\pi\delta(K), \quad (4.A.6)$$

we obtain in (4.A.5):

$$I = 2\pi \int_{-\infty}^{\infty} \int_{-\infty}^{\infty} dK dK' W(K) W(K') \delta(K + K') = 2\pi \int_{-\infty}^{\infty} dK\, W(K) W(-K) \quad (4.A.7)$$

In Section 3.3.3 we mentioned that in general $W(K)$ should be an even function. This follows immediately from the fact that $C(x)$ is even and from the properties of the Fourier transform (e.g. [Brigham, 1974, p.40]) since C and W form a Fourier pair (3.16)-(3.17). Of course, one can verify by inspection that the P-M spectrum in (4-2) is indeed even, so we can further rewrite (4.A.7) as

$$I = 4\pi \int_{0}^{\infty} dK\, W^2(K) \quad (4.A.8)$$

Let us now substitute the expression (4.2) for the P-M spectrum in (4.A.8). We obtain

$$I = \frac{\pi\alpha^2}{4} \int_{0}^{\infty} dK\, e^{-\mu / K^2} K^{-6} \quad (4.A.9)$$

where we have defined

$$\mu = \frac{2g^2\beta}{U^4} \quad (4.A.10)$$

(the quantities α, β, g and U that appear in (4.A.9)-(4.A.10) are defined just after equation (4-2)). With the change of variable $s = 1/K$ (4.A.9) becomes

$$I = \frac{\pi\alpha^2}{4} \int_{0}^{\infty} ds\, e^{-\mu s^2} s^4 \quad (4.A.11)$$

Integrals of this type are well known [Gradshteyn, Ryzhik, 1994, p.382] and

$$\int_0^\infty ds\, e^{-\mu s^2} s^{2n} = \frac{(2n-1)!!}{2(2\mu)^n}\sqrt{\frac{\pi}{\mu}} \tag{4.A.12}$$

Using (4.A.12) for the case of $n = 2$ we obtain

$$I = \frac{3\pi\alpha^2}{32}\sqrt{\frac{\pi}{\mu^5}} \tag{4.A.13}$$

or, recalling the definition for μ in (4.A.10)

$$I = \frac{3\pi\alpha^2}{128}\frac{U^{10}}{g^5\beta^2}\sqrt{\frac{\pi}{2\beta}} \tag{4.A.14}$$

Substitution of (4.A.14) (by virtue of (4.A.4)) and (4.A.3) in (4.A.1) leads to

$$L_{c1} = \frac{3\pi}{8}\sqrt{\frac{\pi}{2\beta}}\frac{U^2}{g}, \tag{4.A.15}$$

which is the result shown in (4.6). A comparison to the dominant wavelength Λ_p in (4.4) shows that

$$L_{c1} = \frac{\sqrt{3\pi}}{16}\Lambda_p \cong 0.19\Lambda_p \tag{4.A.16}$$

Let us now turn our attention to the alternative definition of the correlation length given in (4.A.2). Note that the integral in the denominator of this expression is, in fact, I (cf. (4.A.4)) which we have just evaluated in (4.A.13). Hence, we focus on the integral in the numerator,

$$I_1 \equiv \int_{-\infty}^{\infty} x^2 C^2(x)dx \tag{4.A.17}$$

Once again we use (3.17) and rewrite (4.A.17) as

$$I_1 = \int_{-\infty}^{\infty} dx\left(x\int_{-\infty}^{\infty} dK\, W(K)\, e^{-jKx}\right)^2 \tag{4.A.18}$$

Consider the expression in the brackets in (4.A.18). First, we write it using a derivative:

$$x\int_{-\infty}^{\infty} dK\, W(K)\, e^{-jKx} = j\int_{-\infty}^{\infty} dK\, W(K)\frac{d(e^{-jKx})}{dK} \tag{4.A.19}$$

The right-hand side in (4.A.19) can be integrated by parts:

$$j\int_{-\infty}^{\infty} dK\, W(K)\frac{d(e^{-jKx})}{dK} = j\left\{W(K)e^{-jKx}\Big|_{K=-\infty}^{\infty} - \int_{-\infty}^{\infty} dK\, e^{-jKx}\,\frac{dW(K)}{dK}\right\} \quad (4.A.20)$$

Since the P-M spectrum in (4-2) vanishes at $K = \pm\infty$ the first term in the curly brackets in (4.A.20) is zero. Noting this and substituting (4.A.20) in (4.A.19) we obtain

$$x\int_{-\infty}^{\infty} dK\, W(K)\, e^{-jKx} = -j\int_{-\infty}^{\infty} dK\, e^{-jKx}\,\frac{dW(K)}{dK} \quad (4.A.21)$$

(4.A.21) can, in turn, be used to write (4.A.18) as

$$\begin{aligned} I_1 &= -\int_{-\infty}^{\infty} dx\left(\int_{-\infty}^{\infty} dK\, e^{-jKx}\,\frac{dW(K)}{dK}\right)^2 \\ &= -\int_{-\infty}^{\infty} dx \int_{-\infty}^{\infty}\int_{-\infty}^{\infty} dK dK'\, e^{-j(K+K')x}\,\frac{dW(K)}{dK}\frac{dW(K')}{dK'} \end{aligned} \quad (4.A.22)$$

In fact, (4.A.22) is quite similar to (4.A.5) and we can use essentially the same technique to simplify it. We exchange integration over x with integration over K's, use (4.A.6) and the fact that $W(K)$ is even (and, consequently, its derivative is odd) to arrive at the following expression

$$I_1 = 4\pi\int_0^{\infty} dK\left(\frac{dW(K)}{dK}\right)^2 \quad (4.A.23)$$

The derivative of the P-M spectrum in (4.2) is (for $K > 0$)

$$\frac{dW(K)}{dK} = \frac{\alpha}{4}e^{-\mu/(2K^2)}\left(\frac{\mu}{K^6} - \frac{3}{K^4}\right) \quad (4.A.24)$$

where we again used μ defined in (4.A.10) for compactness. The square of the derivative that we need in (4.A.23) is

$$\left(\frac{dW(K)}{dK}\right)^2 = \frac{\alpha^2}{16}e^{-\mu/K^2}\left(\frac{\mu^2}{K^{12}} - \frac{6\mu}{K^{10}} + \frac{9}{K^8}\right) \quad (4.A.25)$$

Substituting (4.A.25) in (4.A.23) and introducing a new integration variable $s = 1/K$ we obtain

$$I_1 = \frac{\pi\alpha^2}{4}\int_0^{\infty} ds\left(\mu^2 s^{10} - 6\mu s^8 + 9s^6\right)e^{-\mu s^2} \quad (4.A.26)$$

We use (4.A.12) and integrate (4.A.26) term-by-term. This yields:

$$I_1 = \frac{225\pi\alpha^2}{256}\sqrt{\frac{\pi}{\mu^7}} \tag{4.A.27}$$

Recalling (4.A.2) and the auxiliary definitions (4.A.17) and (4.A.4) we recognize that

$$L_{c2} = \left(\frac{I_1}{I}\right)^{1/2} \tag{4.A.28}$$

Substituting (4.A.27) for I_1 and (4.A.13) for I results in

$$L_{c2} = \left(\frac{75}{8}\frac{1}{\mu}\right)^{1/2} \tag{4.A.29}$$

Finally, using (4.A.10) for μ we obtain

$$L_{c2} = \frac{5}{4}\sqrt{\frac{3}{\beta}}\frac{U^2}{g} \tag{4.A.30}$$

L_{c2} can also be expressed in terms of Λ_p in (4.4) as

$$L_{c2} = \frac{5\sqrt{2}}{8\pi}\Lambda_p \cong 0.28\Lambda_p \tag{4.A.31}$$

Expressions in (4.A.16) and (4.A.31) demonstrate that the surface correlation lengths defined according to either (4.A.1) or (4.A.2) are proportional to the dominant surface wavelength Λ_p in (4.4). These expressions also indicate that values for L_{c1} and L_{c2} are close to each other and both are smaller than Λ_p.

Appendix 4.B The Limit of $P(x,x')$ as $x' \to x$

In this Appendix we demonstrate how the limit in (4.27) can be evaluated. We will perform a sample calculation for the vertical case only; similar procedure can be repeated for the horizontal-case propagator.

An explicit expression for the vertical propagator is obtained combining (2.14b) and (2.16):

$$P(x,x') = \frac{k}{2j}\frac{-\zeta_x(x')(x-x')+\zeta(x)-\zeta(x')}{\sqrt{(x-x')^2+(\zeta(x)-\zeta(x'))^2}}H_1^{(2)}(k\sqrt{(x-x')^2+(\zeta(x)-\zeta(x'))^2})$$

(4.B.1)

To calculate the limit as $x' \to x$, we expand all functions in series around x using $(x - x')$ as a small parameter. For the surface height and surface slope we use Taylor expansions (for the surface height in the numerator, accounting for the second-order terms is necessary):

$$\zeta(x') = \zeta(x) + \zeta_x(x)(x' - x) + \frac{1}{2}\zeta_{xx}(x' - x)^2 + o\left((x' - x)^2\right) \tag{4.B.2}$$

and

$$\zeta_x(x') = \zeta_x(x) + \zeta_{xx}(x)(x' - x) + o\left((x' - x)\right) \tag{4.B.3}$$

For the Hankel function we use (cf. (4.28), $z \to 0$)

$$H_1^{(2)}(z) = \frac{2j}{\pi z} + o\left(\frac{1}{z}\right) \tag{4.B.4}$$

The notation $f(\varepsilon) = o\left(g(\varepsilon)\right)$ means that

$$\lim_{\varepsilon \to 0} \frac{f(\varepsilon)}{g(\varepsilon)} = 0$$

With (4.B.2), we write for (4.B.1):

$$\lim_{x' \to x} P(x, x') = \frac{k}{2j} \lim_{x' \to x} \left\{ \frac{-\zeta_x(x')(x - x') + \zeta(x) - \zeta(x')}{\sqrt{(x - x')^2 + (\zeta(x) - \zeta(x'))^2}} \times \right.$$

$$\left. \times \left[\frac{2j}{\pi k \sqrt{(x - x')^2 + (\zeta(x) - \zeta(x'))^2}} + o\left(\frac{1}{\sqrt{(x - x')^2 + (\zeta(x) - \zeta(x'))^2}} \right) \right] \right\}$$

$$= \frac{1}{\pi} \lim_{x' \to x} \left\{ \frac{-\zeta_x(x')(x - x') + \zeta(x) - \zeta(x')}{(x - x')^2 + (\zeta(x) - \zeta(x'))^2} \right\} \tag{4.B.5}$$

Using the expansions in (4.B.2) and (4.B.3) we continue as:

$$\lim_{x' \to x} P(x, x') = \frac{1}{\pi} \lim_{x' \to x} \left\{ \frac{1}{(x - x')^2 + \left(\zeta(x) - \zeta(x) - \zeta_x(x)(x' - x) + o\left((x' - x)\right)\right)^2} \times \right.$$

$$\times \left(-\zeta_x(x)(x - x') + \zeta_{xx}(x)(x' - x)^2 + \zeta(x) - \zeta(x) - \zeta_x(x)(x' - x) - \right. \tag{4.B.6}$$

$$\left. \left. - \frac{1}{2}\zeta_{xx}(x)(x' - x)^2 + o\left((x' - x)^2\right) \right) \right\}$$

Collecting similar terms in the numerator and denominator of (4.B.6) we obtain

$$\lim_{x' \to x} P(x, x') = \frac{1}{\pi} \lim_{x' \to x} \frac{\zeta_{xx}(x)(x' - x)^2 / 2}{(x' - x)^2 (1 + \zeta_x^2(x))} = \frac{\zeta_{xx}(x)}{2\pi(1 + \zeta_x^2(x))} \tag{4.B.7}$$

The result in (4.B.7) is the one we are looking for.

In a similar manner one can show that for both horizontal and vertical polarizations

$$\lim_{x' \to x} P(x, x') = \lim_{x \to x'} P(x, x') \tag{4.B.8}$$

Finally, using essentially the same steps as above one can show that the following, more general limit

$$\lim_{\substack{x \to x_0 \\ x' \to x_0}} P(x, x')$$

exists and is still equal to

$$\lim_{\substack{x \to x_0 \\ x' \to x_0}} P(x, x') = \pm \frac{\zeta_{xx}(x_0)}{2\pi(1 + \zeta_x^2(x_0))} \tag{4.B.9}$$

As in (4.27), the upper sign corresponds to the vertical case and the lower to the horizontal case.

Chapter 5

Effects of Tapered Incident Field in Rough Surface Scattering Simulations

When presenting the simulation results in Chapter 4 we noted that the incident field taper that guards against the "edge effects" due to a finite surface size can affect the precision and validity of the scattering calculations. This is especially true at low grazing incident angles. This chapter studies the suitability of the tapered plane-wave incident field using both the Gaussian and the more advanced Thorsos tapers for low grazing angle (LGA) rough surface scattering problems. For surface scattering problems, it is known that as the angle of incidence approaches grazing, the tapered beam waist should be made larger and several criteria relating these two parameters have been proposed for both the Gaussian and Thorsos tapers. Our 2-D scattering simulations with the ocean-like Pierson-Moskowitz surfaces show that the failures of both the Thorsos and Gaussian tapers for TE polarization are characterized by a distinctive and consistent anomalous jump in the backscatter cross section as grazing incidence is approached. These observations have led to a refined version of one of the above mentioned "beam waist – angle of incidence" criterion and its robustness is demonstrated below.

5.1. Introduction

Numerical studies of extended surface scattering usually require a tapering of the incident field because the integral equations for surface scattering problems are formulated assuming infinite surfaces. In practice, tapering the incident field effectively truncates the surface to a finite size and thus makes the problem amenable for numerical solution. Failure to taper the incident field may result, in particular, in noticeable errors in the calculated average normalized radar cross section (NRCS) especially at low grazing angles (e.g. [Marchand, 1998]), the phenomenon commonly referred to as "edge effects".

Probably, the simplest and the most popular “incident beam” used in such problems is the plane wave modulated by a Gaussian taper function. Unfortunately, such an incident field does not exactly satisfy the Helmholtz scalar wave equation. This prompted E. Thorsos to derive a modified Gaussian taper which more “closely satisfied” the wave equation [Thorsos, 1988]. This form of tapered field has found a broad acceptance within the electromagnetics community (e.g. [Kapp and Brown, 1996], [Donohue *et al*, 1997], [Johnson, 1998]) and will be referred to herein as the "Thorsos taper".

It is generally known that as the angle of incidence moves down to grazing, the beam waist should be made larger, regardless of whether the Gaussian or the Thorsos tapers are used. A number of different criteria have been proposed relating the beam waist to the incident angle. For the Gaussian taper, this is the "resolvability criterion" suggested in [Ngo and Rino, 1994]. For the Thorsos taper, a similar criterion was proposed by D. Kapp [Kapp, 1995, p. 112] and further discussed by R. Marchand [Marchand, 1996]. Our simulations of scattering from 1-D Pierson-Moskowitz (P-M) surfaces have shown a very characteristic signature associated with the "failure" of the Thorsos taper, both in the backscattered cross section and the surface current. We found that for such surfaces the Kapp criterion is quite robust and we were further able to specify the value of the constant involved in this criterion. In addition, we found that for the cases studied the use of the Thorsos taper offered little advantage over the Gaussian taper in the sense that they yielded very similar values for the radar cross sections and failed at about the same incident angle while moving toward grazing. Still, the results do demonstrate that the Thorsos taper is somewhat more robust and is therefore preferable to its Gaussian counterpart.

5.2 Gaussian-Like Incident Field Approximation

5.2.1 Gaussian and Thorsos Tapers

As we discussed in Chapter 2, rough surface scattering simulations are usually based on the repeated numerical solution of an integral equation which gives the total field or its normal derivative on the surface. In particular, we showed that when scattering from a perfect electric conductor (PEC) is of interest, either the electric field integral

equation (EFIE) or the magnetic field integral equation (MFIE) can be set up and used. In the derivation of these integral equations, the surface is assumed to have an infinite extent. This follows from the fact that the equations are formulated for a closed body and in the case of the surface scattering such a closure is usually accomplished by the auxiliary surface of infinite radius on which the field vanishes and thus its contribution is zero (cf. Fig. 2-2, and the discussion preceding (2.6)). Then, in principle, the limits in the integrals in either the MFIE or EFIE should be taken to plus and minus infinity. To make the problem amenable for a numerical solution, the region of integration must be truncated. This can be justified if the incident field (and, consequently, the total field) on the surface is localized i.e. the beam is tapered. Briefly put, the taper is necessary to guard against the "edge effects" associated with a finite surface size.

In a 2-D Cartesian coordinate system (x, z) introduced in Chapter 2 (cf. Fig. 2-3) the expression for an incident field that is a tapered plane wave is as follows

$$\psi^i(x,z) = T(x,z)\exp\{-j\vec{k}_i \cdot \vec{r}\} \equiv T(x,z)\exp\{-jk(x\sin\theta_i - z\cos\theta_i)\} \tag{5.1}$$

The incident angle θ_i is defined with respect to z-axis and is positive in the counterclockwise direction, $k = \omega / c$, and $T(x,z)$ is a taper function. The taper function $T(x,z)$ in (5.1) is often assumed to be Gaussian and of the form;

$$T_G(x,z) = \exp\left\{-\frac{(x + z\tan\theta_i)^2}{g^2}\right\} \tag{5.2}$$

In (5.2), g is the parameter that controls the beam waist. Thorsos pointed out [Thorsos, 1988] that the incident field in (5.1) with the taper in (5.2) satisfies the wave equation only approximately with one of the consequences being that for the TE case the solutions obtained using the MFIE differ from those obtained using the EFIE. Consequently, he proposed the modified Gaussian taper, which we will call the "Thorsos taper":

$$T_T(x,z) = \exp\left\{-\frac{(x + z\tan\theta_i)^2}{g^2} - j\frac{k(x\sin\theta_i - z\cos\theta_i)}{(kg\cos\theta_i)^2}\left(\frac{2(x + z\tan\theta_i)^2}{g^2} - 1\right)\right\} \tag{5.3}$$

This taper was used for the incident field in Chapter 4, cf. (4.12). The incident field (5.1) with such a taper satisfies the wave equation more closely resulting, in particular, in a better agreement between the solutions to the MFIE in (2.12) and the EFIE in (2.10) in

the TE case. This taper was obtained by considering the following integral representation for the incident field [Thorsos, 1988];

$$\psi^i(x,z) = \frac{1}{\sqrt{\pi}\Delta\theta}\int_{-\pi/2}^{\pi/2} \exp\left(-\frac{(\theta-\theta_i)^2}{(\Delta\theta)^2}\right)\exp\left(-j\vec{k}\cdot\vec{r}\right)d\theta \ , \tag{5.4}$$

with

$$\Delta\theta \equiv 2/kg\cos\theta_i \tag{5.5}$$

and

$$\vec{k}\cdot\vec{r} \equiv k(x\sin\theta - z\cos\theta)\,. \tag{5.6}$$

Being a superposition of plane waves, the incident field (5.4) completely satisfies the wave equation. Such an incident field can be calculated numerically and used in simulations as well. In what follows we will refer to (5.4) as to the incident field with an "integral taper", or simply an "integral taper". Other linear superpositions of plane waves are possible as well giving rise to somewhat different expressions for the incident field that completely satisfy the wave equation (e.g. [Tran and Maradudin, 1994], [Chan *et al*, 1998], [Wagner *et al*, 1997]). However, it should be remembered that numerical implementation of (5.4) or a similar superposition-based expression is far more computationally expensive than an approximate closed-form incident field such as in (5.1).

Fig. 5-1 gives examples of the absolute value of the incident field $\psi^i(x, z=0)$ for different types of taper. The beam waist parameter g is the same that we used in Chapter 4, i.e. 136.5λ ($\lambda = 23$ cm). For Gaussian or Thorsos tapers $|\psi^i(x, z=0)|$ does not depend on the incident angle, as can be readily seen from (5.2) and (5.3) (also, the *absolute* value of both (5.2) and (5.3) is the same). In contrast, the field with the integral taper in (5.4) does depend on θ_i and as the incident angle increases this taper provides increasingly poorer suppression at the edges. This is further demonstrated in Fig. 5-2 which compares the levels (with respect to the center of the beam) of the Thorsos/Gaussian tapers and the integral taper with $g = 136.5\lambda$ at the ends of the flat surface of length $L = 819.2\lambda$. The edge levels are calculated using (5.1)-(5.4) as $|\psi^i(L/2, 0)|^2 / |\psi^i(0,0)|^2$ (the level at the opposite edge $x = -L/2$ is the same).

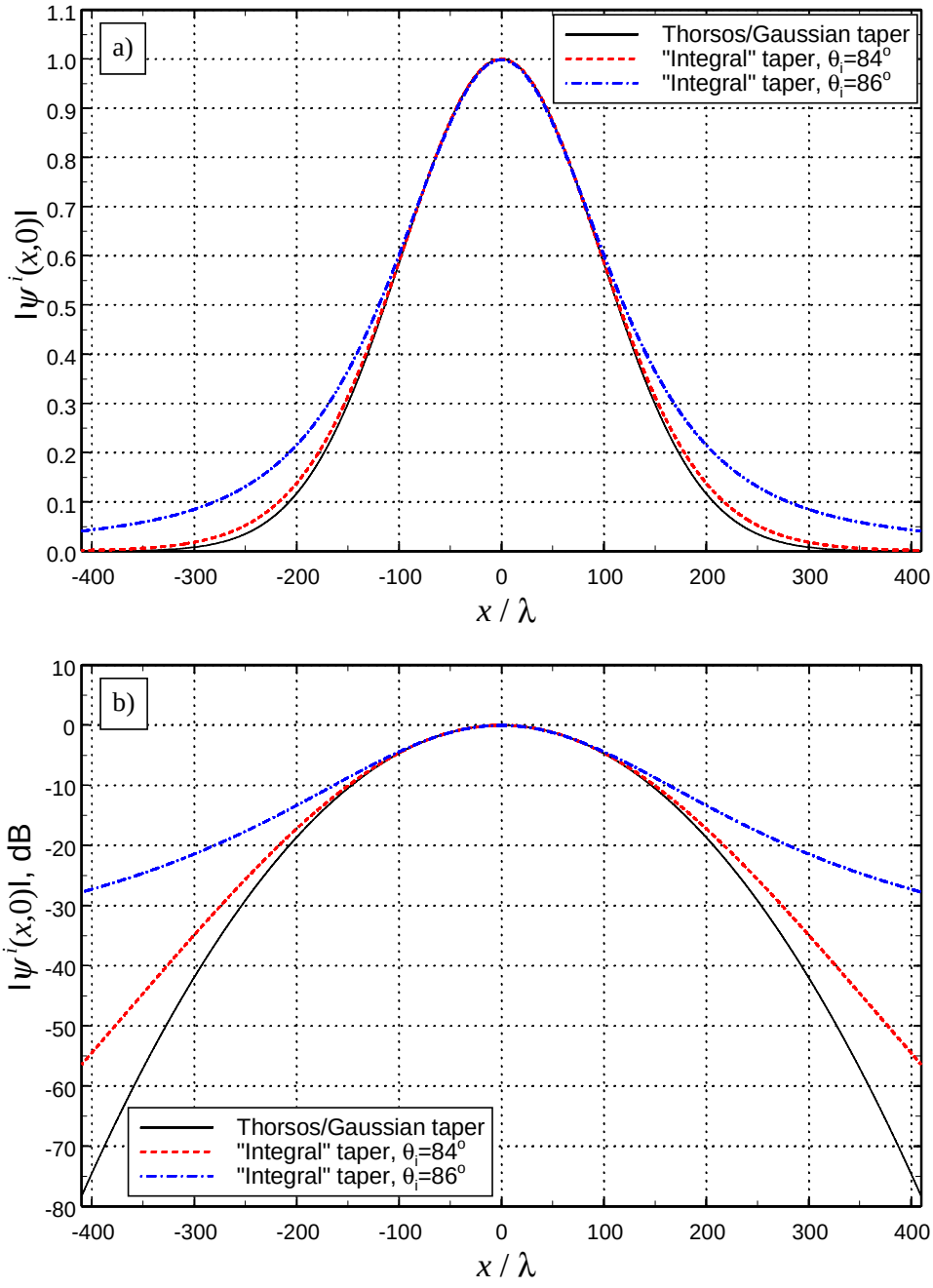

Figure 5-1. Examples of the amplitude of the incident field in the mean surface plane ($z = 0$) with different types of taper. (a) Linear scale; (b) dB scale. Beam waist g is 136.5λ .

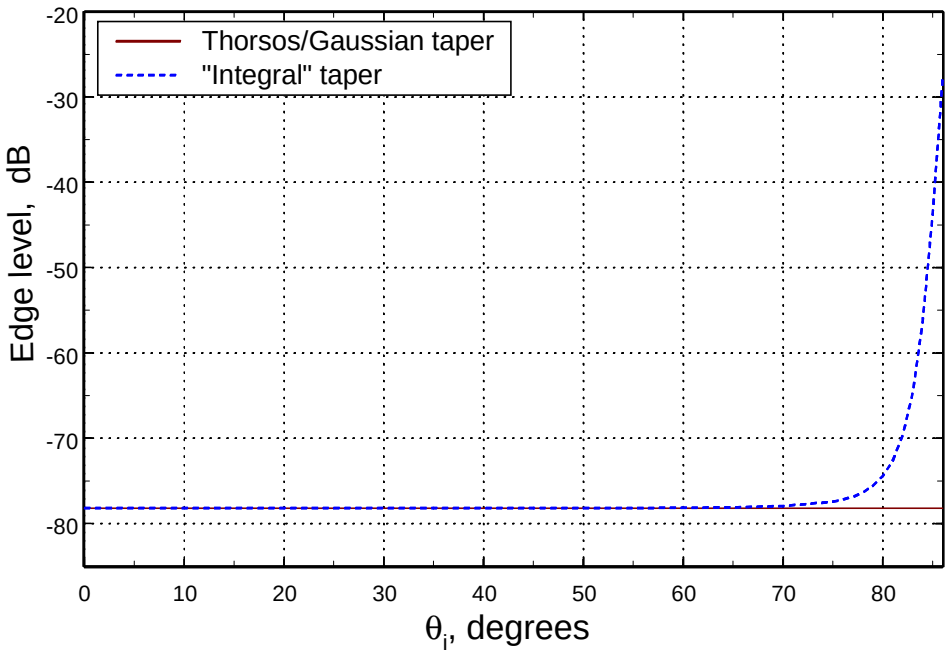

Figure 5-2. Relative level (with respect to the center of the beam) of the incident field at the edges of a flat ($z = 0$) surface of length $L = 819.2\lambda$. The beam points at the center of the surface and has the waist $g = L/6 = 136.5\lambda$.

5.2.2 Criteria for the Beam Waist

As a condition for the validity of the taper (5.3), Thorsos set

$$kg\cos\theta_i >> 1$$

or, equivalently,

$$g >> \frac{1}{k\cos\theta_i} \tag{5.7}$$

However, Kapp later proposed the following criterion for the taper applicability [Kapp, 1995, p. 112]

$$g > \frac{A}{k(\pi/2-\theta_i)\cos\theta_i}, \tag{5.8}$$

where A is some constant. This restriction emerges naturally when one considers the derivation of the approximate taper in (5.3). Some details of this derivation are given in the original paper [Thorsos, 1988], and it is examined in much greater detail in [Toporkov *et al*, 1998] (with the credit going mostly to the second author R. Awadallah). If $\Delta\theta$ in (5.5) is large as is assured by (5.7), the first exponential in (5.4) is highly peaked around $\theta = \theta_i$, which suggests an asymptotic evaluation of the integral via the Laplace's method [Bleistein and Handelsman, 1986]. It should be noted, however, that at large values of x the second exponential in (5.4) becomes highly oscillatory and Laplace's method will fail. The deviation of the tails of the integral taper from the Gaussian behavior in Fig.5-1 is a manifestation of this fact. It is shown in [Toporkov *et al*, 1998] that at large x one should rather apply the method of stationary phase which predicts a $1/\sqrt{x}$ decay of the tails of the field with the integral taper. If one proceeds with the Laplace's method, the exponent $j\vec{k}\cdot\vec{r}$ is then expanded in a Taylor series around θ_i retaining the terms up to the second order in $(\theta-\theta_i)$:

$$j\vec{k}\cdot\vec{r} \approx j\left(\vec{k}\cdot\vec{r}\Big|_{\theta=\theta_i} + \frac{d(\vec{k}\cdot\vec{r})}{d\theta}\Big|_{\theta=\theta_i}(\theta-\theta_i) + \frac{1}{2}\frac{d^2(\vec{k}\cdot\vec{r})}{d\theta^2}\Big|_{\theta=\theta_i}(\theta-\theta_i)^2\right) \tag{5.9}$$

If one recalls (5.6) and introduces a new variable $\delta \equiv \theta - \theta_i$, (5.4) becomes:

$$\psi^i(x,z) \approx \frac{1}{\sqrt{\pi}\Delta\theta}\exp\{-j\vec{k}_i\cdot\vec{r}\}\int_{-\pi/2-\theta_i}^{\pi/2-\theta_i}\exp\{-a\delta^2 - jb\delta\}\,d\delta \tag{5.10}$$

with

$$b = k(x\cos\theta_i + z\sin\theta_i)$$

and

$$a = \frac{1}{(\Delta\theta)^2} + j\frac{k}{2}(z\cos\theta_i - x\sin\theta_i), \tag{5.11}$$

In (5.10) the factor

$$\exp\{-j\vec{k}_i \cdot \vec{r}\} \equiv \exp\{-jk(x\sin\theta_i - z\cos\theta_i)\} \tag{5.12}$$

represents the plane wave (compare to (5.1)); other factors, upon further manipulations, are supposed to yield the taper $T_T(x,z)$ as given in (5.3). The next step in the application of Laplace's method is to extend the limits of integration in (5.10) to $\pm\infty$. However, if θ_i which we assume to be positive is close to $\pi/2$ such an extension may result in picking up significant contributions not present in (5.10). Referring to (5.4), we can interpret this extension of limits as including contributions of plane waves propagating at angles greater than 90°, i.e. coming from beneath the surface. To guard against this, we choose $\Delta\theta$ such that the amplitude of these contributions is very small. Specifically, we require that in (5.10)

$$\mathrm{Re}(a)(\pi/2 - \theta_i)^2 > B \tag{5.13}$$

where B is some constant. This assures that at $\delta = \pi/2 - \theta_i$, i.e. at the upper limit, the integrand will have an amplitude that does not exceed $\exp(-B)$. All contributions included as a result of extending the integration limits to infinity will have smaller, exponentially vanishing amplitudes. Recalling (5.11) and (5.5) we rewrite (5.13) as

$$g > \frac{2\sqrt{B}}{k(\pi/2 - \theta_i)\cos\theta_i} \tag{5.14}$$

If we make a replacement $2\sqrt{B} \equiv A$, we obtain the criterion in (5.8). It should be emphasized that the development outlined above does not provide a clear value for the constant B in (5.14) or A in (5.8). The choice may depend on various considerations such as surface statistics, polarization, etc. Studying the overall applicability of the criterion in (5.8) for P-M surfaces and determining what the constant in (5.8) should be is the subject of this Chapter.

Another "angle of incidence – beam waist" criterion called "a resolvability criterion" was formulated in [Ngo and Rino, 1994] for beams with Gaussian tapers (5.2). They first introduce a quantity called "resolvability":

$$P = \frac{\int_{-k}^{k} \tilde{\psi}^i(K_x;0)dK_x}{\int_{-\infty}^{\infty} \tilde{\psi}^i(K_x;0)dK_x}, \tag{5.15}$$

with $\tilde{\psi}^i(K_x;0)$ being a Fourier transform of the incident field in (5.1) in the $z=0$ plane. Unlike its counterpart in the numerator, the integral in the denominator of (5.15) allows the inclusion of the evanescent components ($|K_x|>k$); the less the evanescent components contribute to the beam $\psi^i(x,z)$, the closer the resolvability P is to unity. Ideally, the fully Maxwellian beam as in (5.4) should not contain any evanescent components and will have $P=1$. In this sense, P supposedly serves as a measure of the quality of the approximate beam. It is shown in the same reference [Ngo and Rino, 1994] that to achieve a given resolvability for the Gaussian beam (5.2)-(5.1) one should have

$$g > \frac{\sqrt{2}\chi}{k(1-\sin\theta_i)} \tag{5.16}$$

with the constant χ related to the resolvability P as

$$P = P(\chi) = \frac{1}{\sqrt{2\pi}} \int_{-\infty}^{\chi} \exp\{-t^2/2\}dt \tag{5.17}$$

The authors, however, do not provide any definite recipe for the choice of P (and hence of the constant χ in (5.16)); they cite a broad range of values (from 0.85 to greater than 0.99) that might be necessary depending on factors such as the surface roughness. In this regard, the "resolvability criterion" (5.16) as introduced in [Ngo and Rino, 1994] was more useful to illustrate that the beam waist should rapidly increase as θ_i approaches grazing and provide a motivation for the method of beam simulation (synthesis of a large beam from a number of smaller subbeams) used in the cited reference.

One can show that at large incident angles the resolvability criterion (5.16) and the Kapp criterion (5.8) are essentially equivalent. Indeed, for large incident angles (say larger than 70°) the cosine in the denominator of (5.8) can be approximated as follows:

$$\cos\theta_i = \cos\big(\pi/2 - (\pi/2 - \theta_i)\big) = \sin(\pi/2 - \theta_i) \cong \pi/2 - \theta_i \tag{5.18}$$

This is well justified since the criteria (5.8) and (5.16) are mainly of interest at low grazing angles. Consequently, we can rewrite (5.8) approximately as

$$g > \frac{A}{k(\pi/2 - \theta_i)^2} \tag{5.19}$$

We can use a similar approximation for the sine in the denominator of (5.16) to rewrite the "resolvability criterion" as:

$$g > \frac{2\sqrt{2}\chi}{k(\pi/2 - \theta_i)^2} \tag{5.20}$$

We see that (5.19) and (5.20) predict the same dependence on θ_i. The constants in the numerators are so far arbitrary and must be determined. Since the criteria (5.19) and (5.20) were derived for different tapers (given in (5.3) and (5.2), respectively), the constants A and $2\sqrt{2}\chi$ may differ. However, the similarity of the two criteria exhibited in (5.19) and (5.20) is encouraging. In fact, it has been shown [Toporkov *et al*, 1998] that the Gaussian taper in (5.2) can be obtained from the integral form in (5.4) with some additional approximations beyond those leading to the Thorsos taper in (5.3). In what follows, we will focus on the criterion (5.8) (or its approximate form in (5.19)) for the Thorsos taper. However, on many occasions we will examine the Gaussian taper as well and find that the same criterion (5.8) can be applied to it with only a slightly larger constant in the numerator.

From (5.19) one can also see that at large grazing angles the Kapp criterion is stricter than the Thorsos requirement in (5.7). Indeed, for large incident angles we can approximate (5.7) as

$$g >> \frac{1}{k(\pi/2 - \theta_i)} \tag{5.21}$$

This expression behaves as $(\pi/2-\theta_i)^{-1}$ and should be compared to (5.19), which goes as $(\pi/2-\theta_i)^{-2}$. Since we will find that the constant A in (5.8) or (5.19) is larger than one, the compliance with (5.8) will enforce (5.7) for all incident angles of interest to us.

For (5.8) to be of practical use, the value of A should be determined. Also, for the criterion to be robust A can depend on the type of the surfaces used in simulations but should not depend on either θ_i or the electromagnetic wavelength. There have been some recommendations for the value of A. In particular, Kapp in [Kapp, 1995] suggested the value $A=3\sqrt{2}$. Marchand stated that the values of A in (5.8) ranging from $3\sqrt{2}$ to $4\sqrt{2}$ appear to be an effective threshold [Marchand, 1996]. In later publication he arbitrarily increased this estimate by $\sqrt{2}$ [Marchand and Brown, 1998]. However, to our knowledge, there has been no dedicated study of the applicability and the robustness of the criterion (5.8) and the above-mentioned recommendations for the choice of A are rather heuristic.

5.3 The Taper and Scattering Simulations at Large Incident Angles

5.3.1 Taper-Induced Effects in the Average Cross Section and the Kapp Criterion

In this section, we present the simulation results for scattering from perfectly conducting ocean-like P-M surfaces that demonstrate a pattern of failures at low grazing angles for the Gaussian-like taper. We show that the Kapp criterion (5.8) is quite robust and we determine a value for the constant A that turns out to be larger than the ones cited above. Unless stated otherwise, the simulation details are the same as described in Section 4.2 of Chapter 4. In particular, we use the surfaces with the spectrum in (4.9), (4.2); the windspeed is 5 m/s and the surface spectral cutoff K_c in (4.9) is always chosen to be five times the electromagnetic wavenumber.

We start with the analysis of the horizontal polarized backscatter cross section calculated using the Thorsos taper. It is established that an anomalous jump in the $\langle\sigma^0_{bsc}\rangle$ at low grazing angles can be associated with the failure of the Thorsos taper and that the angle at which this anomaly occurs is predicted by the Kapp criterion. The same anomaly

is observed for the Gaussian taper, while the behavior of the $\langle \sigma^0_{bsc} \rangle$ with the "exact" integral taper is quite different. We closer examine the results obtained with the integral taper and find that some distortions in the cross section observed for this taper are due to insufficient incident field suppression at the surface ends. We further establish the range of incident angles where the results with the integral taper are not affected by edge effects and are valid. This, in turn, allows a more detailed investigation of the distortions introduced in the bistatic cross section by the approximate Gaussian-like tapers by using the results with integral taper as a check. Finally, we study the effects of the approximate tapers in the case of vertical polarization and find them negligible for the incident angles under consideration. It is also found that the poor edge suppression by the integral taper that distortes $\langle \sigma^0 \rangle$ at low grazing angles in the horizontal case does not have these consequences in the vertical case. To facilitate navigation through the material of this Section, Table 5-1 gives a summary of the examples considered and the parameters used therein.

Table 5-1. A summary of the examples in Section 5.3.1

Fig.	Quantity Shown	Polarization	em λ	Taper	Beam waist g	Surface Length L	Description
5-3	$\langle\sigma^0_{bsc}(\theta_i)\rangle$	H	$\lambda_1 = 23\,\text{cm}$ and $\lambda_2 = 10\,\text{cm}$	T	$136.5\lambda_1$, $49.3\lambda_1$, and $314.0\lambda_2$	188.42 m ($=819.2\lambda_1$ $=1884.2\lambda_2$)	An anomalous pattern (a jump) in $\langle\sigma^0_{bsc}\rangle$ at low grazing angles indicating a failure of the Thorsos taper.
5-4	$\langle\sigma^0_{bsc}(\theta_i)\rangle$	H	$\lambda_1 = 23\,\text{cm}$	T, G, I	$136.5\lambda_1$	$819.2\lambda_1$	A comparison of the failure patterns in the $\langle\sigma^0_{bsc}\rangle$ for Thorsos, Gaussian and integral tapers.
5-5	$\langle\sigma^0(86^\circ,\theta_s)\rangle$	H	$\lambda_1 = 23\,\text{cm}$	I	$136.5\lambda_1$	$819.2\lambda_1$ and $1638.4\lambda_1$	A demonstration that the jump in the integral taper result in Fig. 5-4 is due to edge effects. The longer surface results in a stronger taper suppression at the edges.
5-6	$\langle\sigma^0(84^\circ,\theta_s)\rangle$	H	$\lambda_1 = 23\,\text{cm}$	I	$136.5\lambda_1$	$819.2\lambda_1$ and $1638.4\lambda_1$	A demonstration that the edge effects are not a factor for the integral taper at $\theta_i = 84^\circ$.
5-7	$\langle\sigma^0(86^\circ,\theta_s)\rangle$	H	$\lambda_1 = 23\,\text{cm}$	T	$136.5\lambda_1$	$819.2\lambda_1$ and $1638.4\lambda_1$	This figure is a reiteration of Fig. 5-5, but for the Thorsos taper (that is in the failure mode at this θ_i). $\langle\sigma^0\rangle$ shows an unexpected growth with the increase in the surface length.

Polarization: H=horizontal, V=vertical.
Taper: T=Thorsos, G=Gaussian, I=integral.

Table 5-1 (continued).

Fig.	Quantity shown	Polarization	Em λ	Taper	Beam waist g	Surface length L	Description
5-8 a, b	$\langle\sigma^0(84^\circ,\theta_s)\rangle$	H	$\lambda_1 = 23\,\text{cm}$	T, G, I	$136.5\lambda_1$	$819.2\lambda_1$	A study of the *bistatic* cross sections for Thorsos and Gaussian tapers at $\theta_i = 84^\circ$ (the analysis of the *back-scattered* cross section in Fig. 5-4, identified this θ_i as a "pre-breakdown" angle). Integral taper serves as a check.
5-9	$\langle\sigma^0(85^\circ,\theta_s)\rangle$	H	$\lambda_1 = 23\,\text{cm}$	T, G, I	$136.5\lambda_1$	$819.2\lambda_1$	Same as Fig. 5-8a, but for $\theta_i = 85^\circ$.
5-10	$\langle\sigma^0(85^\circ,\theta_s)\rangle$	H	$\lambda_1 = 23\,\text{cm}$	T, G, I	$136.5\lambda_1$	$819.2\lambda_1$	Same as Fig. 5-9, but for $\theta_i = 86^\circ$.
5-11	$\langle\sigma^0_{bsc}(\theta_i)\rangle$	V	$\lambda_1 = 23\,\text{cm}$	T, G, I	$136.5\lambda_1$	$819.2\lambda_1$	A study of $\langle\sigma^0_{bsc}\rangle$ similar to one presented in Fig. 5-4 but for *vertical* polarization.
5-12	$\langle\sigma^0(86^\circ,\theta_s)\rangle$	V	$\lambda_1 = 23\,\text{cm}$	I	$136.5\lambda_1$	$819.2\lambda_1$ and $1638.4\lambda_1$	An investigation if poor edge suppression by the integral taper is a factor for the *vertical* polarization. This figure is similar to Fig. 5-5.
5-13	$\langle\sigma^0(86^\circ,\theta_s)\rangle$	V	$\lambda_1 = 23\,\text{cm}$	I	$136.5\lambda_1$	$819.2\lambda_1$	A study of the bistatic cross sections for Thorsos and Gaussian tapers for the *vertical* polarization; the integral taper servs as a check. This figure is similar to Fig. 5-10.

Polarization: H=horizontal, V=vertical.
Taper: T=Thorsos, G=Gaussian, I=integral.

Consider the incident field (5.1) with the Thorsos taper in (5.3). Fig. 5-3 shows (solid and dashed curves) the calculated average backscattered NRCS $\langle \sigma^0_{bsc}(\theta_i) \rangle \equiv \langle \sigma^0(\theta_i, \theta_s = -\theta_i) \rangle$ (cf. (2.33) and (2.34)) for the horizontal (TE) polarization

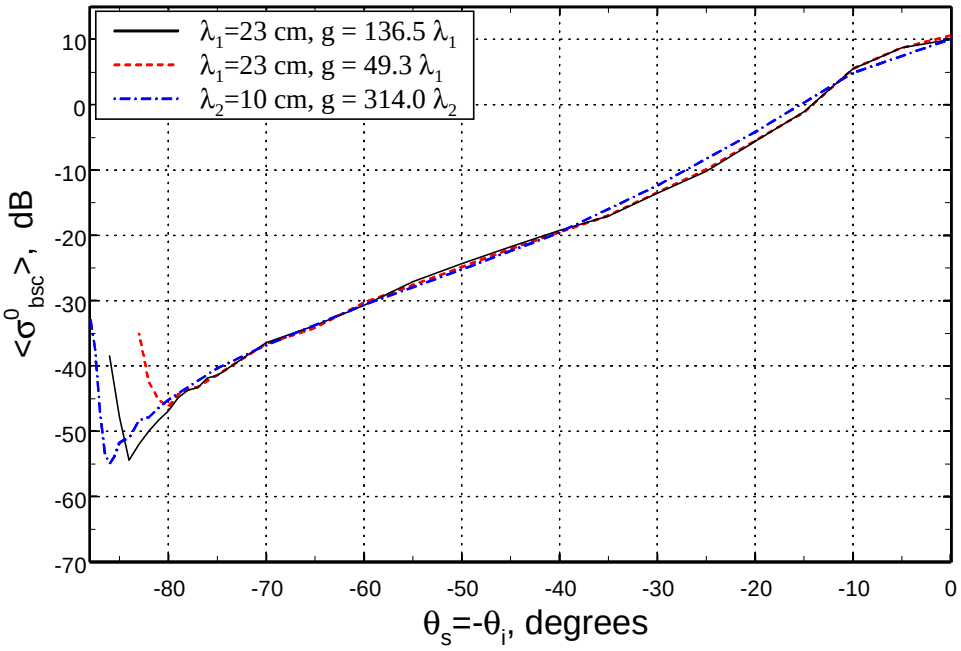

Figure 5-3. Average normalized radar cross section in the backscattered direction demonstrating an anomalous pattern at low grazing angles. Horizontal (TE) polarization, plane-wave incident field with the Thorsos taper. The average is taken over 100 realizations of P-M surfaces with a wind speed of 5 m/s.

at the electromagnetic wavelength $\lambda_1 = 23\,\text{cm}$. The surface length was $L = 819.2\,\lambda_1 = 188.42\,\text{m}$. The solid line corresponds to the beam waist $g = L/6 = 136.5\,\lambda_1$; such a choice of g provides a –78 dB suppression of the incident field at the edges $x = \pm L/2$ and was used in our simulations in Chapter 4. The plot shows a very characteristic jump after one moves from $\theta_i = 84^\circ$ to $\theta_i = 85^\circ$ (the step

used in the near-grazing region was 1°). Attributing this jump to the failure of the taper (5.3), we can try to determine the constant A in (5.8). Assuming that the largest incident angle for which the taper holds is $\theta_i = 84^\circ$ and writing (5.8) as an equality we get $A = 9.4$. To convince ourselves that the jump observed is really related to the taper failure and that the criterion (5.8) works, let us consider the average backscattered NRCS for simulations with different beam waists. For example, the criterion (5.8) with $A = 9.4$ predicts that, all other parameters being the same, the beam that fails after $\theta_i = 80^\circ$ should have the waist of $g = 49.3\lambda_1$. This prediction is tested in Fig. 5-3 where the dashed plot corresponds to the average NRCS calculated with this smaller g. Again, it demonstrates a characteristic jump, this time right after $\theta_i = 80^\circ$. So, the jump in the backscattered NRCS as the incident angle moves down to grazing is indeed an indication of the taper failure and the criterion (5.8) with the value for A determined above seems to be quite practical.

Let us check if the criterion (5.8) works for another electromagnetic wavelength, say $\lambda_2 = 10\,\text{cm}$. We will still use an ensemble of the randomly rough P-M surfaces corresponding to the windspeed $U = 5\,\text{m/s}$ and the spectral cutoff again being five times the new electromagnetic wavenumber. Due to the smaller λ, our surfaces are now rougher in an electromagnetic sense; the rms height is given by $1.33\,\lambda_2$ in this example as compared to the value $0.58\lambda_1$ for the previous example. The surface length is $L = 1884.16\lambda_2$ and the beam waist is chosen to be $g = L/6 = 314.0\,\lambda_2$. The criterion (5.8) with $A = 9.4$ predicts that the Thorsos taper will hold as far as $\theta_i = 86.0^\circ$ (we used an approximate form (5.19) to solve for θ_i). Indeed, the dash-dotted curve in Fig. 5-3 corresponding to this example exhibits the jump as the incident angle goes from 86° to 86.5° (this time the step of 0.5° was used in the near-grazing region).

Further proof that this jump is due to the approximate nature of the taper in (5.3) can be seen from Fig.5-4. This Figure compares the average backscattered NRCS calculated with the incident field (5.1) and the taper (5.3), with the integral representation of the incident field in (5.4) for TE polarization. Also shown is the average NRCS for the

incident field having the Gaussian taper in (5.2). We again consider the electromagnetic wavelength wavelength $\lambda_1 = 23\,\text{cm}$; the beam waist g is $136.5\,\lambda_1 = L/6$. The solid

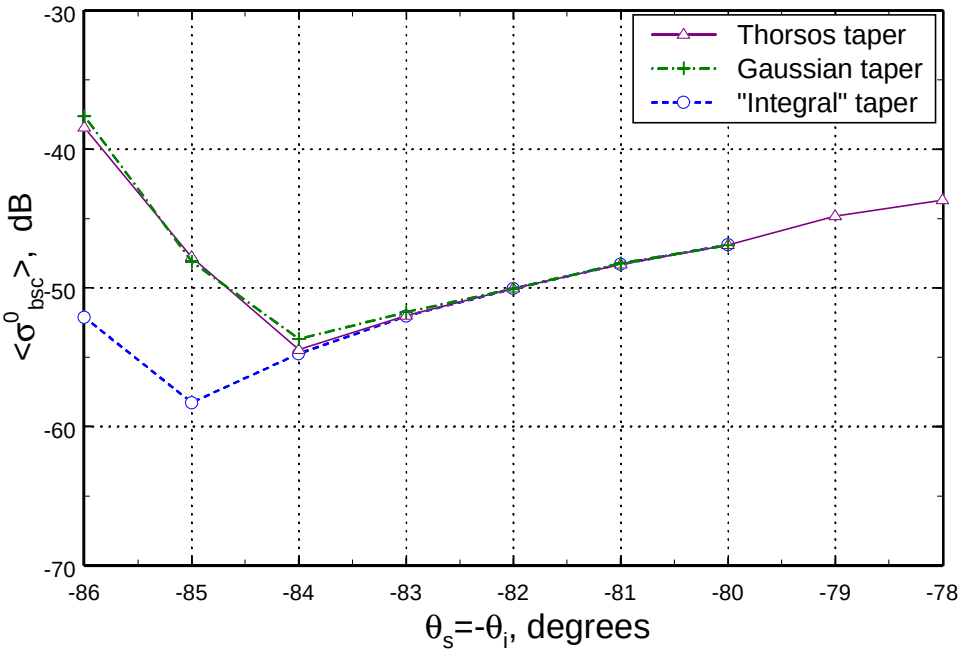

Figure 5-4. Failure patterns in the average backscattered normalized radar cross section for different types of taper. Horizontal (TE) polarization, em wavelength $\lambda_1 = 23\,\text{cm}$, beam waist $g = 136.5\,\lambda_1$. The average is taken over 100 realizations of P-M surfaces with a wind speed of 5 m/s.

curve is the same plot that we had in Fig. 5-3, with the axes scales expanded. It corresponds to $\langle \sigma^0_{bsc}(\theta_i) \rangle$ calculated with the Thorsos taper (5.3). The dashed curve corresponds to the average NRCS with the integral-taper incident field (5.4). The Figure shows that although in both cases the beam waist is the same, the average NRCS for the incident field (5.4) keeps decreasing for $\theta_i > 84^\circ$ while the NRCS obtained with the Thorsos taper experiences the anomalous jump. The $\langle \sigma^0_{bsc}(\theta_i) \rangle$ for the integral taper

does exhibit the jump after $\theta_i = 85^\circ$, but, as will be discussed shortly, these jumps are due to different mechanisms. As for the Gaussian taper, its NRCS (dash-dotted curve) has the jump at the same incident angle as the NRCS for the Thorsos taper. The criterion in (5.8) is thus applicable to the Gaussian taper as well.

The jump observed in the average NRCS curve corresponding to the integral taper in Fig.5-4 occurs because of the increasingly poor tapering at the edges provided by the incident field in (5.4) at large incident angles. Indeed, Fig. 5-2 shows that the integral taper at large incident angles provides increasingly poor suppression at the edges; at $\theta_i = 86^\circ$ this level is about –28 dB, while at $\theta_i = 85^\circ$ and $\theta_i = 84^\circ$ these levels are

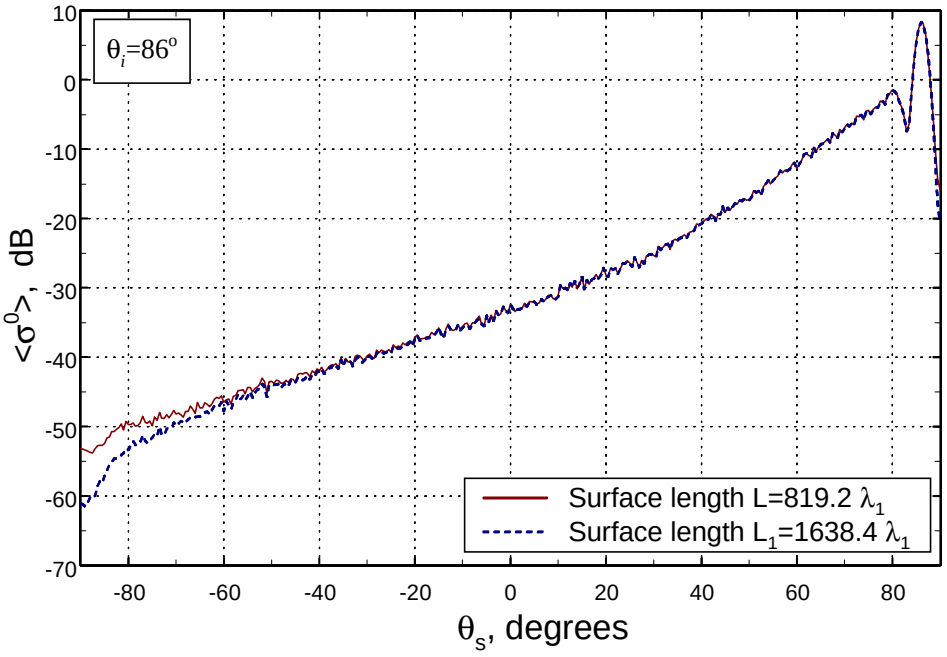

Figure 5-5. Effects of poor edge suppression by the *integral taper* in the average bistatic normalized radar cross section. The longer surface results in stronger edge suppression. $\theta_i = 86^\circ$, horizontal (TE) polarization, $g = 136.5\lambda_1$. The average is taken over 100 realizations of P-M surfaces with a wind speed of 5 m/s.

approximately –44 dB and –56 dB, respectively. Fig. 5-5 compares average bistatic NRCS's for 86° incidence calculated with the integral taper with the waist $g = 136.5\lambda_1$ using different surface lengths. The solid line corresponds to the surface length $L = 819.2\lambda_1$ used in the simulations shown in Fig. 5-4; as we mentioned, it provides –28 dB suppression at the edges. The dashed line corresponds to the MFIE solved with twice as large a surface length ($L_1 = 1638.4\lambda_1$). The incident beam still points at the center of the surface and now provides –38 dB suppression at surface ends. We observe that for large negative scattering angles the average NRCS for the longer surface has noticeably smaller values. In particular, at $\theta_s = -86^\circ$ (backscattering) the two curves differ by 5 dB. This clearly suggests that the abnormally high backscattering level observed in Fig. 5-4 for the integral taper at $\theta_i = 86^\circ$ is due to the poor tapering of the incident field at the edges. In fact, it is quite possible that even the tapering level of –38 dB achieved by elongating the surface to twice the original size may be insufficient and further extension of the surface size will result in even smaller value for $\langle \sigma^0_{bsc}(86^\circ) \rangle$. For a reference, the average bistatic NRCS for $\theta_i = 84^\circ$ calculated using the integral taper and surfaces of two different lengths are compared in Fig. 5-6. As can be seen from Fig. 5-2, at this incident angle the integral taper with $g = 136.5\lambda_1$ provides a –56 dB edge suppression for the surface with the length of $L = 819.2\lambda_1$. Doubling the surface size results in –121 dB tapering level; however, there is virtually no difference in two NRCS curves in Fig. 5-6 and this suggests that the original –56 dB tapering is acceptable.

Although we are certain that for the Gaussian/Thorsos taper it is not the insufficient edge suppression that causes the jump in the NRCS observed in Figs. 5-3 and 5-4, let us examine how the surface length affects the results in this case. In particular, let us again choose $\theta_i = 86^\circ$ as we did for the integral taper in Fig. 5-5 (from Fig. 5-4, we concluded that for this incident angle the Thorsos taper is well in the failure mode) and examine the average bistatic NRCS for the surfaces with the lengths $L = 819.2\lambda_1$ and $L_1 = 1638.4\lambda_1$ while keeping the beam waist the same and equal to $136.5\lambda_1$. This g results in a –78 dB suppression at the edges for the surface with $L = 819.2\lambda_1$; extending

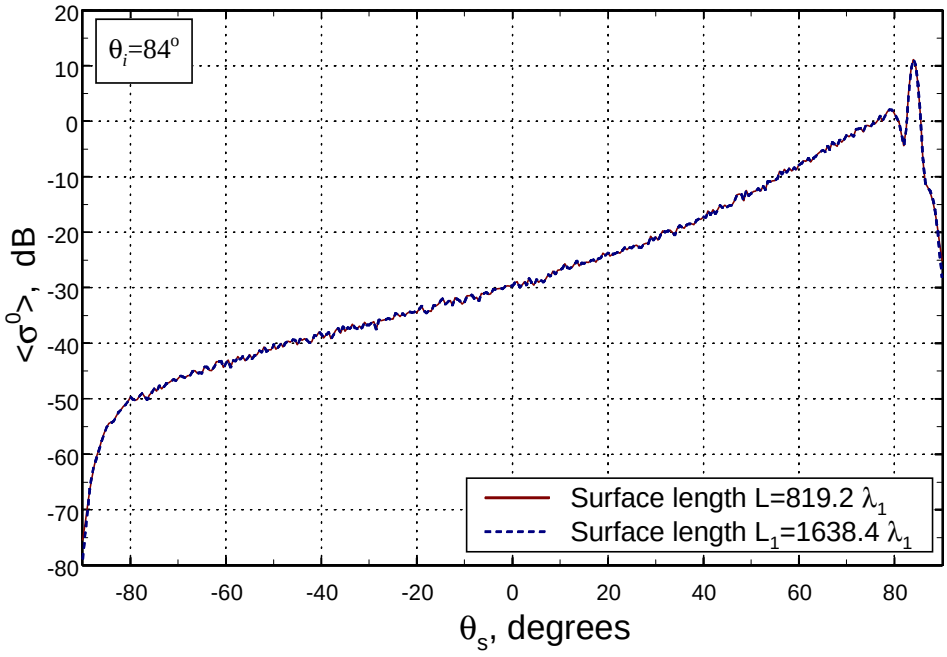

Figure 5-6. Examination of the edge effects in the average bistatic normalized radar cross section for the *integral taper* and $\theta_i = 84^\circ$. Horizontal (TE) polarization, $g = 136.5\lambda_1$. The average is taken over 100 realizations of P-M surfaces with a wind speed of 5 m/s.

the surface to twice that length assures a –313 dB level at the edges. The average bistatic NRCS's are shown in Fig. 5-7 and, in fact, they do display a dependence on the surface length. However, in contrast to the situation depicted in Fig. 5-5 for the integral taper, this time *surface extension resulted in the increased level of the calculated cross section.* We will further discuss this somewhat surprising result in the next Section where the effects of the taper on the surface current (the solution to the MFIE) will be examined. Right now, we can conclude that the increase in the surface length in the case of the Thorsos taper does not eliminate or alleviate the anomalous jump in the average backscattered NRCS as it does in the case of the integral taper (cf. Fig. 5-5). On the contrary, for such an incident field this surface extension seems to make this jump even worse. The same effect is observed for the Gaussian taper in (5.2).

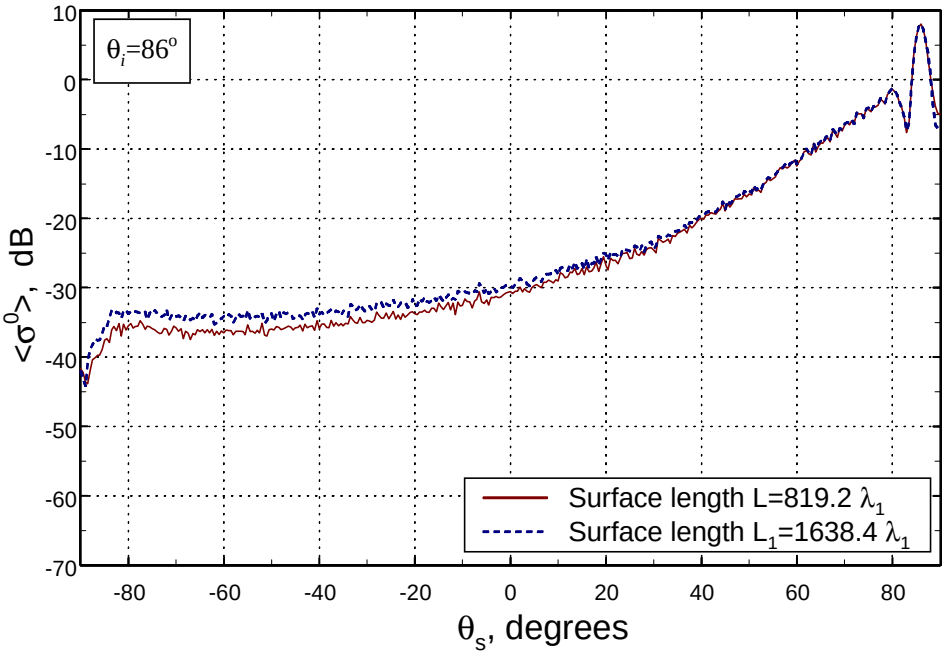

Figure 5-7. Effects of the surface length on the average bistatic normalized radar cross section for the *Thorsos taper* (this figure is similar to Fig. 5-5 where the integral taper was studied). $\theta_i = 86^\circ$, horizontal (TE) polarization, $g = 136.5\lambda_1$. The average is taken over 100 realizations of P-M surfaces with a wind speed of 5 m/s.

We have established that the criterion (5.8) with $A = 9.4$ does tell how close to $\theta_i = 90^\circ$ one can go before there is a taper "failure" (the jump in backscattered NRCS plots). It would be useful to check if at this largest incidence angle the NRCS we get is valid or incorrect. Let us turn our attention once again to Fig. 5-4. There we established that the Thorsos and the Gaussian tapers failed after $\theta_i = 84^\circ$. At this incident angle the average cross section obtained with the integral taper is free from "edge effects" (in Fig. 5-6, the difference between the two curves at $\theta_s = -84^\circ$ is 0.03 dB) and can be used as a gauge. It can then be seen that at this incident angle the result obtained with the Thorsos taper is very close to the "true value" (differing by only about 0.3 dB) while the Gaussian tapered NRCS is approximately 1 dB off. This suggests that at the pre-breakdown angle determined from (5.8), the Thorsos taper still provides valid results in the backscattered direction, and it is somewhat superior to the Gaussian taper. In fact, it may well be that the Gaussian taper fails a fraction of a degree earlier than the Thorsos taper (and, hence, somewhat larger value of the constant is required in the criterion (5.8) or (5.19)), but the step of 1° used in this example does not allow pinpointing this effect.

Let us further examine the bistatic cross sections corresponding to the tapers (5.2) and (5.3) at the pre-breakdown incident angle of 84° for the example considered in Fig. 5-4. Fig. 5-8 shows $\langle \sigma^0(\theta_i = 84^\circ, \theta_s) \rangle$ for the Thorsos, Gaussian and the integral taper, the latter again serving as a check (Fig. 5-8a gives the overall picture while Fig. 5-8b focuses on the region of scattered angles close to $\theta_s = -90^\circ$). The Thorsos taper yields values for the average NRCS that follow the integral-taper results very closely until about $\theta_s = 88.5^\circ$ at which point they deviate by approximately 0.8 dB. The results with the Gaussian taper display greater discrepancies when compared to the integral-taper results and once again suggest that the Thorsos taper is somewhat preferable.

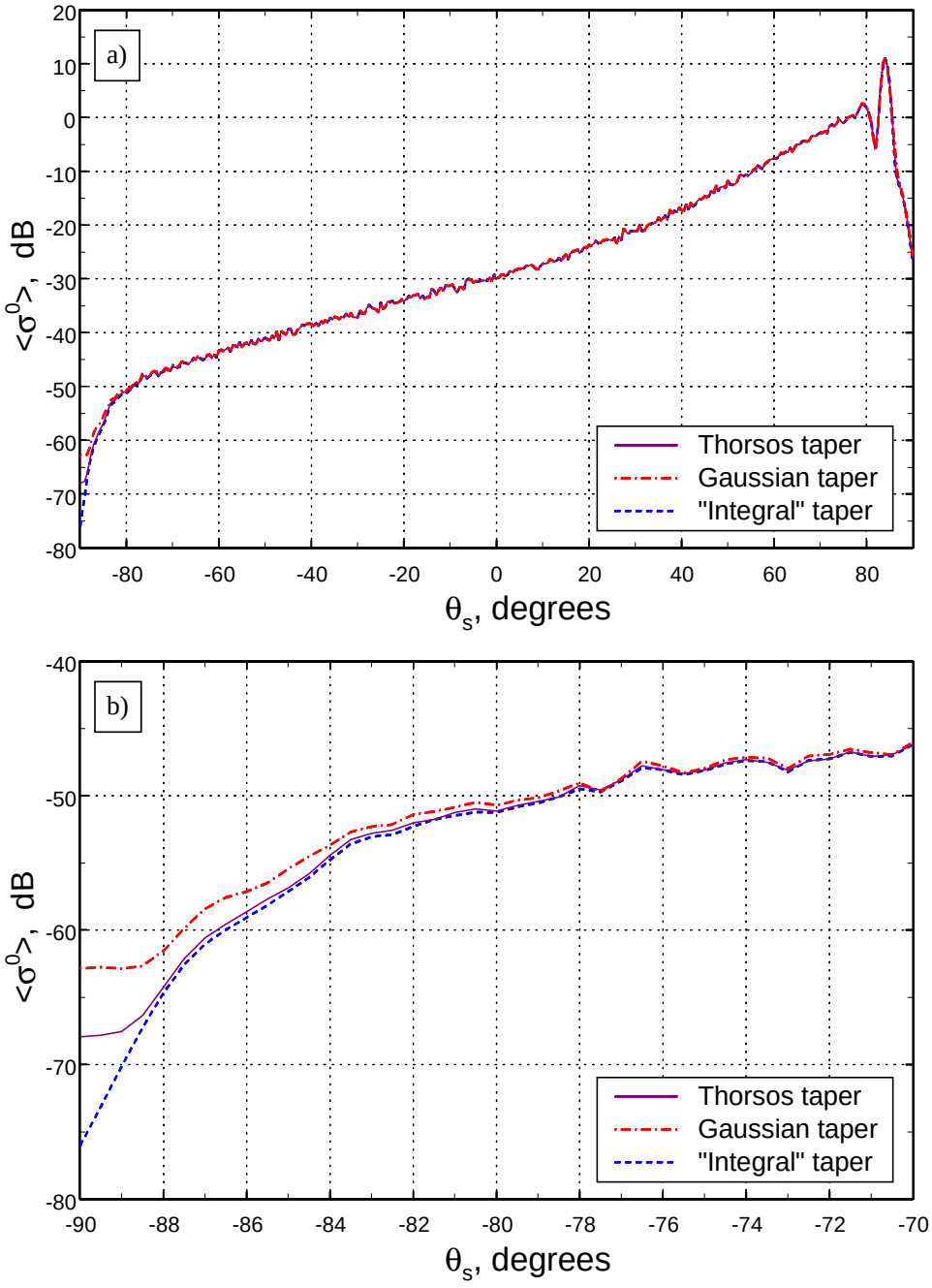

Figure 5-8. Distortions in the average bistatic normalized radar cross section due to approximate taper at the "pre-breakdown" point $\theta_i = 84^\circ$ (cf. Fig. 5-4). The integral taper serves as a check. Horizontal (TE) polarization; em wavelength $\lambda_1 = 23\,\text{cm}$, beam waist $g = 136.5\,\lambda_1$. The average is taken over 100 realizations of P-M surfaces with a wind speed of 5 m/s.

For comparison, Figs. 5-9 and 5-10 show similar graphs for $\theta_i = 85^\circ$ and $\theta_i = 86^\circ$, respectively, where the Thorsos/Gaussian tapers have already failed (cf. Fig. 5-4). The calculated $\langle \sigma^0 \rangle$ for the integral taper at 86° is definitely affected by the insufficient tapering at the edges (we used surfaces of length $L = 819.2\lambda_1$) and thus does not present the correct value for large negative θ_s (cf. the discussion regarding Fig. 5-5).

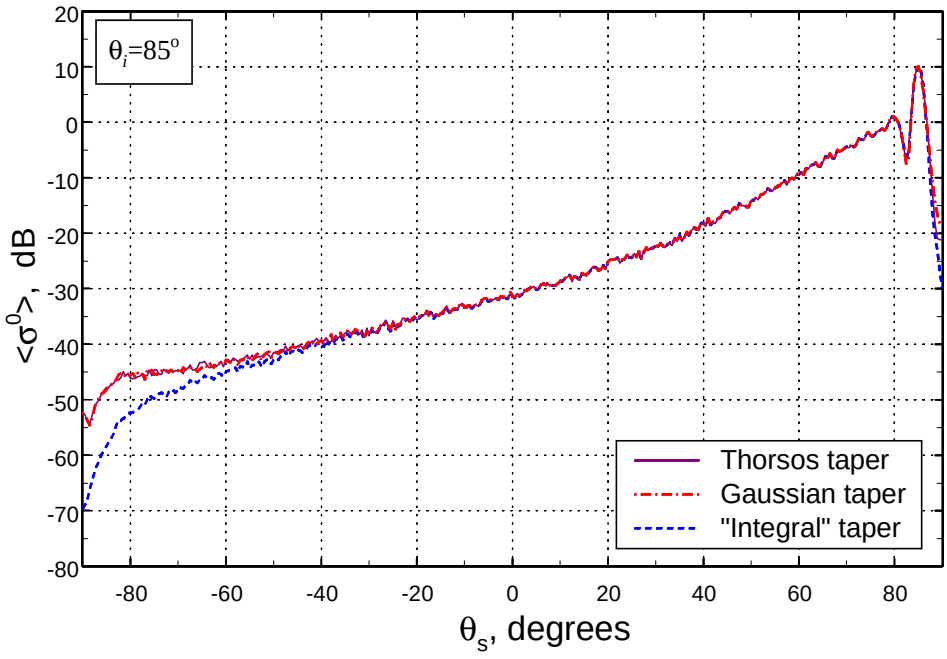

Figure 5-9. Distortions in the average bistatic normalized radar cross section due to the approximate taper at $\theta_i = 85^\circ$. The integral taper serves as a check. Horizontal (TE) polarization; em wavelength $\lambda_1 = 23\,\text{cm}$, beam waist $g = 136.5\,\lambda_1$. The average is taken over 100 realizations of P-M surfaces with a wind speed of 5 m/s.

However, it can still serve as a good reference to illustrate the distortion that the cross section with the Thorsos or Gaussian taper suffer if the incident angle and the beam waist do not agree according to the criterion (5.8).

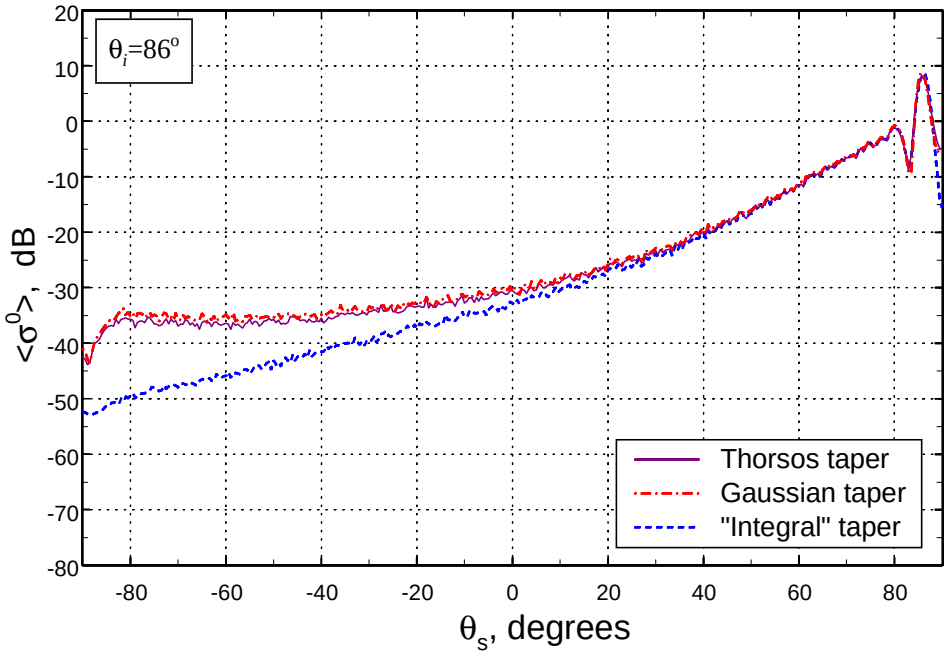

Figure 5-10. Distortions in the average bistatic normalized radar cross section due to the approximate taper at $\theta_i = 86^\circ$. The integral taper, although corrupted near $\theta_s = -90^\circ$ by edge effects, still can serve as a useful check (cf. Fig.5-5). Horizontal (TE) polarization; em wavelength $\lambda_1 = 23\,\text{cm}$, beam waist $g = 136.5\,\lambda_1$. The average is taken over 100 realizations of P-M surfaces with a wind speed of 5 m/s.

All examples considered so far are for horizontal (TE) polarization. For the vertical (TM) polarization, we observed no indications of the taper breakdown effects at the angles where Thorsos and Gaussian tapers failed in the TE case. The average backscattered NRCS's with Thorsos and Gaussian tapers are shown in Fig.5-11 (all simulation parameters except for polarization are the same as used in Fig. 5-4) and they clearly display no anomalous jumps for the incident angles as large as 86°. Also, the results obtained with the approximate tapers remained virtually identical to those obtained using the integral taper. The latter appear to be valid even at such low incident angle, as the comparison to the results for larger surface length and the same waist

$g = 136.5\lambda_1$ shown in Fig. 5-12 indicate. In particular, at $\theta_s = -86^\circ$ (the backscattering direction) the difference between two curves is less than 0.1 dB.

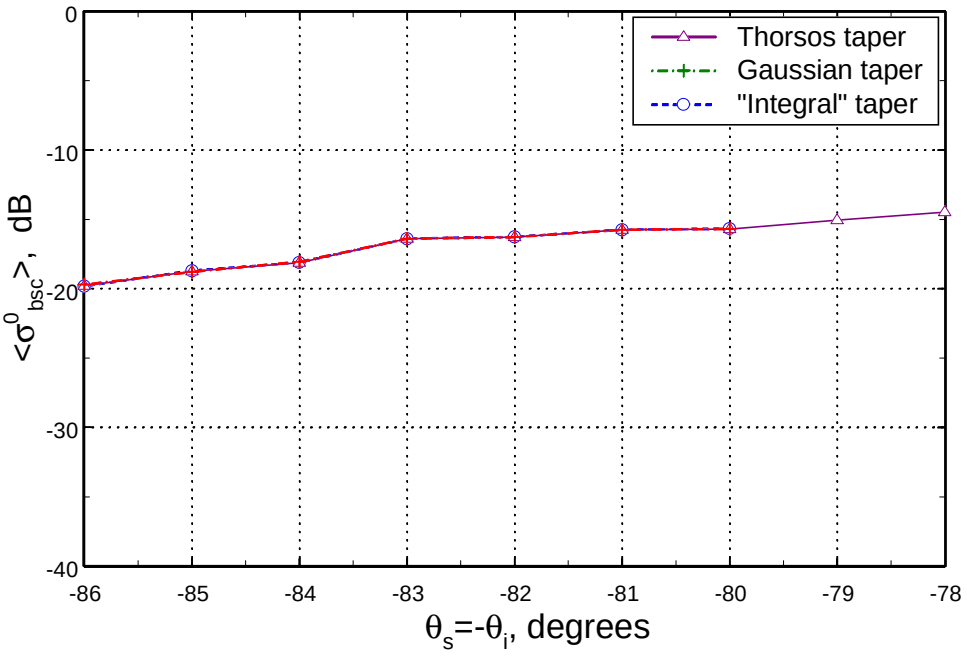

Figure 5-11. Average backscattered normalized radar cross section for vertical (TM) polarization, unlike its horizontal counterpart in Fig. 5-4, shows no signs of taper failure. Em wavelength $\lambda_1 = 23$ cm, beam waist $g = 136.5\,\lambda_1$. The average is taken over 100 realizations of P-M surfaces with a wind speed of 5 m/s.

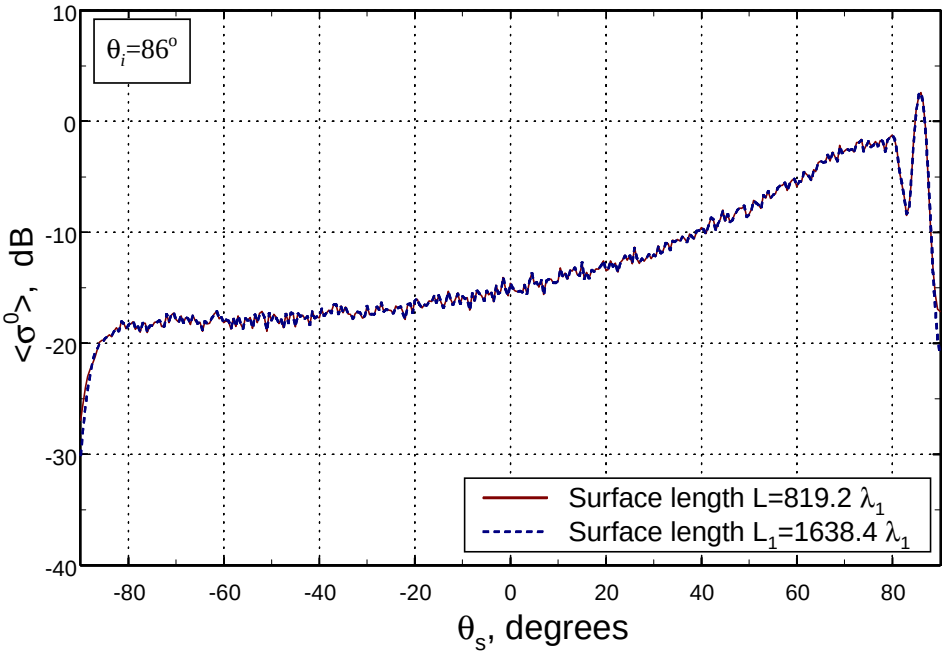

Figure 5-12. Study of the sensitivity of the average bistatic normalized radar cross section to the edge suppression levels provided by the *integral taper*. The longer surface results in stronger edge suppression. $\theta_i = 86^\circ$, vertical (TM) polarization, $g = 136.5\lambda_1$. $\theta_i = 86^\circ$. The average is taken over 100 realizations of P-M surfaces with a wind speed of 5 m/s.

As in the case of horizontal polarization, we can look at the effects of the approximate taper on the bistatic cross section as well. Fig. 5-13 examines the average bistatic NRCS for the Thorsos and Gaussian tapers at $\theta_i = 86^\circ$, the result obtained with the integral taper again serving as a check. All simulation parameters except polarization are identical to those used in Fig. 5-11. In contrast to what we observed at this incident

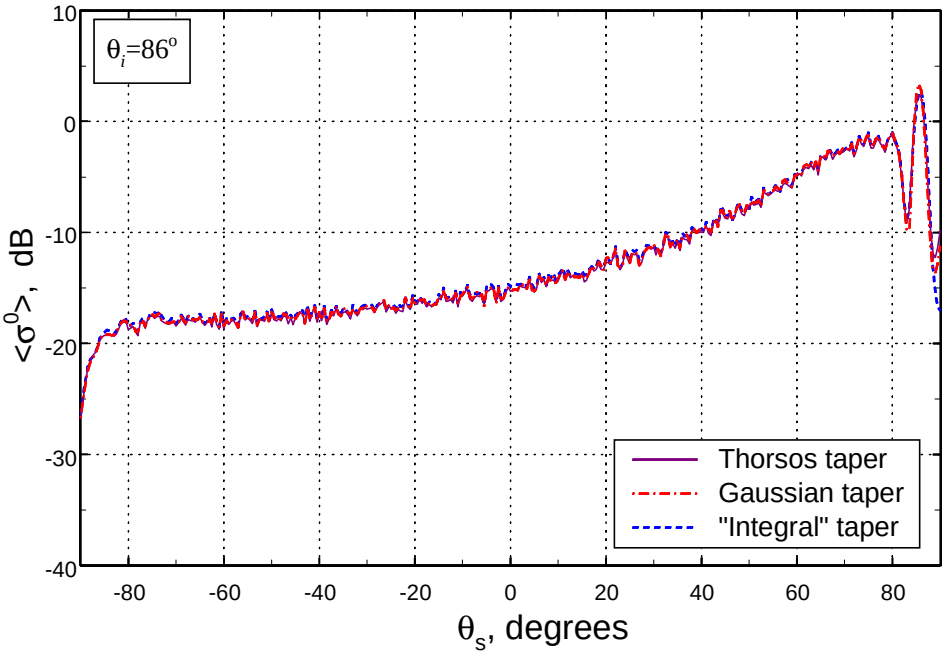

Figure 5-13. Comparison of the average bistatic normalized radar cross sections ($\theta_i = 86^\circ$) obtained with approximate tapers to a "check-case" result with the integral taper. for. Vertical (TM) polarization; em wavelength $\lambda_1 = 23\,\text{cm}$, beam waist $g = 136.5\,\lambda_1$. The average is taken over 100 realizations of P-M surfaces with a wind speed of 5 m/s.

angle in the case of horizontal polarization (Fig. 5-10), for vertical polarization the average bistatic NRCS remains virtually unaffected by the approximate nature of the taper. We do observe some discrepancy around the specular peak and somewhat higher

levels of Thorsos/Gaussian-tapered $\langle \sigma^0 \rangle$ close to $\theta_s = 90^\circ$. These deviations from the reference result with the integral taper disappear at smaller incident angles (they are already not present at $\theta_i = 85^\circ$) and are probably the only observable effect introduced by the approximate nature of the Gaussian-like tapers in (5.2) or (5.3) as far as the NRCS is concerned.

This observation again underscores the fact that the applicability of the criterion (5.8) depends on such factors as polarization and also the type of rough surfaces. For example, for smooth surfaces characterized by Gaussian spectra (when the levels of backscatter are very low) a much larger constant A may be required, or the criterion in (5.8) might not work so well. Nevertheless, the above examples show that for P-M surfaces this criterion is very robust with $A = 9.4$ in the case of horizontal polarization. Failure to follow this criterion, which can serve as a guideline for the Gaussian taper (5.2) as well, may result in severe distortions in the average backscattered and bistatic cross sections for horizontal (TE) polarization.

5.3.2 Taper-Induced Effects in the MFIE Current

The distinctive features associated with the breakdown in the Thorsos/Gaussian taper can be observed in the surface current $J(x)$ (which is the solution to the MFIE (2.13)) as well. While, in general, errors in the current do not necessarily translate into errors in the NRCS, the latter being of greater practical interest, the analysis of surface currents can provide some useful insights. For example, we will be able to give a qualitative explanation to the behavior of $\langle \sigma^0 \rangle$ vs. the surface length observed in Fig. 5-7.

Fig. 5-14 examines the surface current for a single surface realization in the case of the Thorsos taper with $g = 136.5\,\lambda_1$. Fig. 5-14a shows $|J|$ for the field incident at $\theta_i = 84^\circ$ while Fig. 5-14b and Fig. 5-14c show the same quantity in the case of

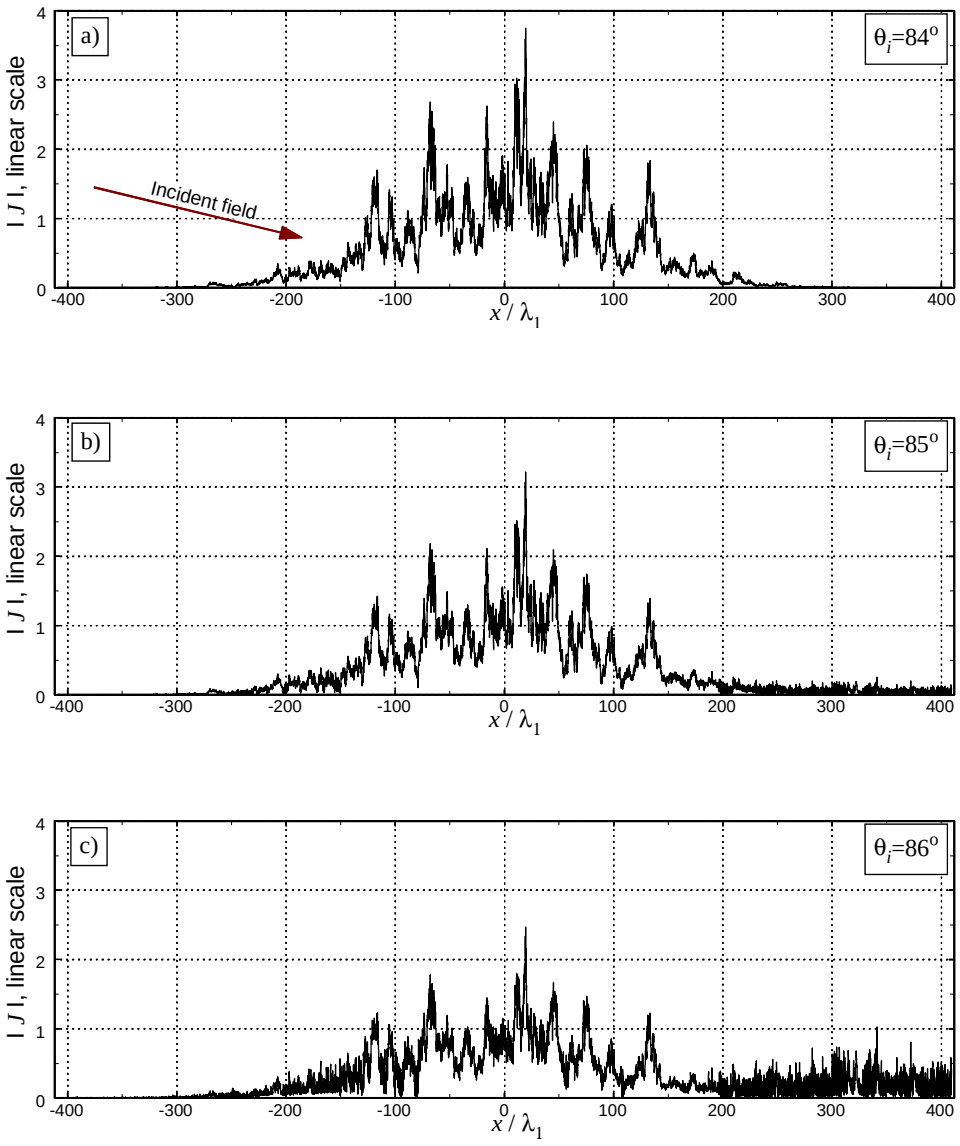

Figure 5-14. Examples of the surface current for a single realization of P-M surface (windspeed = 5 m/s). Thorsos taper, horizontal (TE) polarization, em wavelength $\lambda_1 = 23\,\text{cm}$, beam waist $g = 136.5\,\lambda_1$.

$\theta_i = 85^\circ$ and $\theta_i = 86^\circ$, respectively. For the latter two incident angles, as we concluded earlier, the Thorsos taper with this value of the beam waist fails. The remarkable feature of the current in Fig. 5-14b is the noisy "tail" on the right (the incident field is coming from the left). And this tail is especially pronounced in Fig. 5-14c. The same "tail" effect

is observed when the Gaussian taper (5.2) is used. For comparison, Fig. 5-15 shows the surface currents for the same incident angles when the integral taper is used. This time no

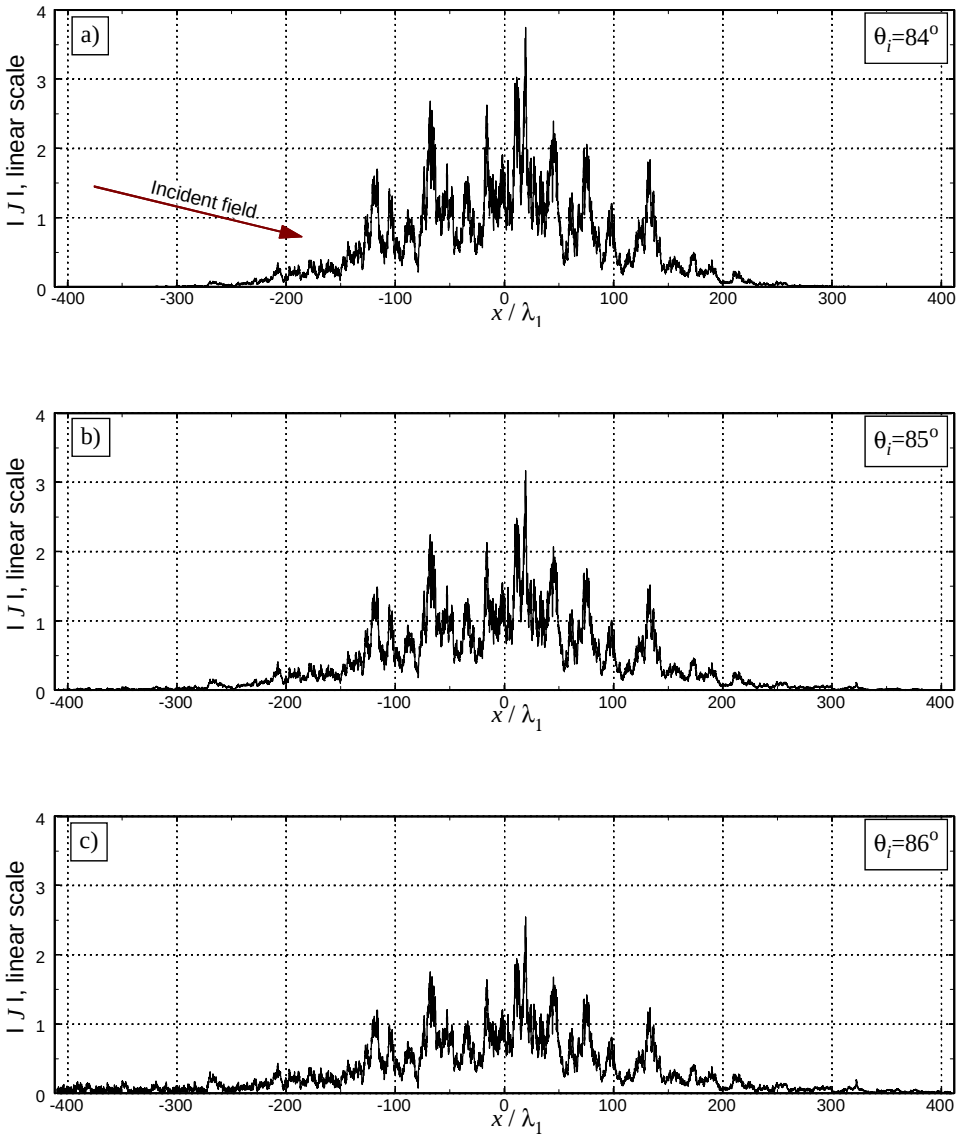

Figure 5-15. Examples of the surface current for a single realization of P-M surface (windspeed = 5 m/s). Integral taper, horizontal (TE) polarization, em wavelength $\lambda_1 = 23\,\text{cm}$, beam waist $g = 136.5\,\lambda_1$.

appreciable tail is evident for 84° or 85° incident angles. The current in Fig. 5-15c corresponds to the incident angle of 86° and has quite noticeable levels at the edges, especially on the left side. Those high levels appear to be the result of the insufficient tapering at the edges provided by the integral taper, as we discussed in the previous Section.

The tail observed in Figs.5-14b and 5-14c is thus yet another anomalous effect associated with the failure of the Gaussian-like approximate tapers. *In fact, it is this tail that caused the average bistatic NRCS to increase with the increase in the surface length,*

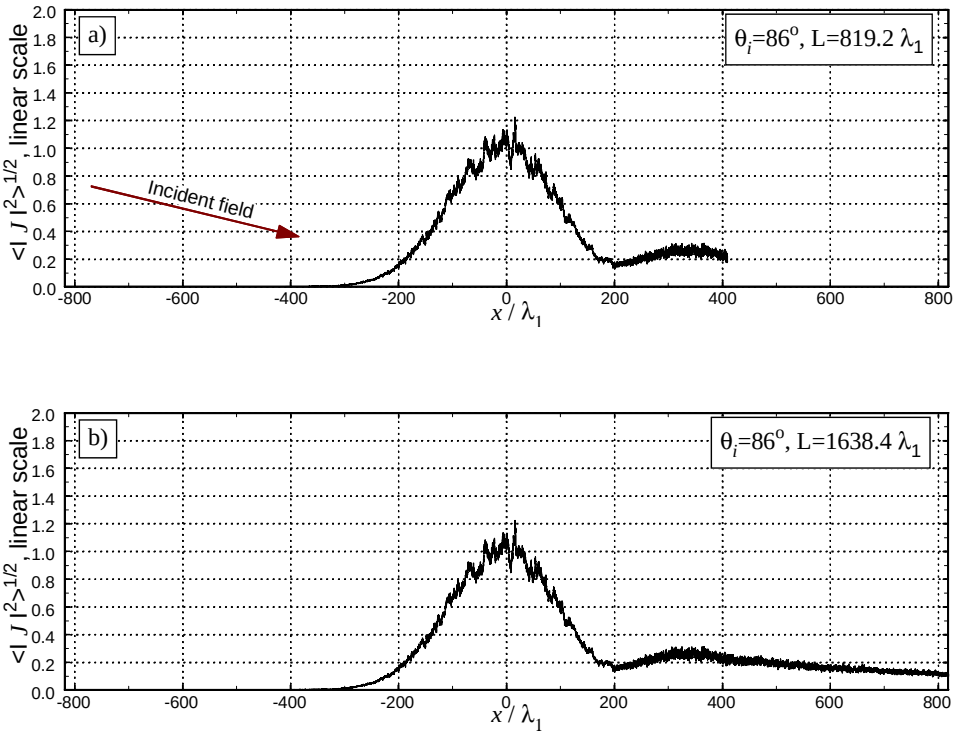

Figure 5-16. Rms surface current for two different surface lengths. Thorsos taper, $g = 136.5\,\lambda_1$, horizontal (TE) polarization. The average is taken over 100 P-M surfaces with a windspeed of 5 m/s.

as we observed in Fig. 5-7. Fig. 5-16 shows the root mean square MFIE currents calculated with the Thorsos taper at $\theta_i = 86^\circ$ using the surfaces of the length $L = 819.2\lambda_1$ (Fig. 5-16a) and extended surfaces with the length $L_1 = 1638.4\lambda_1$ (Fig. 5-16b), all other parameters including the beam waist $g = 136.5\lambda_1$ being the same. From the Figure we see that when the larger surfaces are used, the anomalous tail in the current continues further to the right, decaying only slowly. When we calculate the cross-section using extended surfaces, we include more of this tail and this is likely to introduce additional error in the average NRCS. To see if this is the case, let us compare $\langle \sigma^0 \rangle$ calculated for the surfaces of the length $L = 819.2\lambda_1$ to the average NRCS obtained from the MFIE currents solved for the extended surfaces of the length $L_1 = 1638.4\lambda_1$ with the integration in (2.30) performed over $x \in [-L/2, L/2]$. That is, when calculating the scattered field for the extended surfaces, we do not use the values of the current for $|x| > L/2 = 409.6\lambda_1$, cf. Fig. 5-16. By doing so, we cut off the part of the current tail that continues to the right in Fig. 5-16b. The two average cross sections are shown in Fig. 5-17. This Figure should be compared to Fig. 5-7 where the NRCS for the extended surface was calculated using the MFIE current on the whole interval $[-L_1/2, L_1/2]$. This time, unlike the situation in Fig. 5-7, the two curves show virtually no differences except for a small region close to $\theta_s = -90^\circ$. Of course, it should be remembered that for this incidence angle $\langle \sigma^0 \rangle$ shown in Figs. 5-7 and 5-17 is already a distorted one (cf. Fig. 5-10) and this analysis merely explains why the extension of the surface in Fig. 5-7 results in even more distorted cross section for the Thorsos taper.

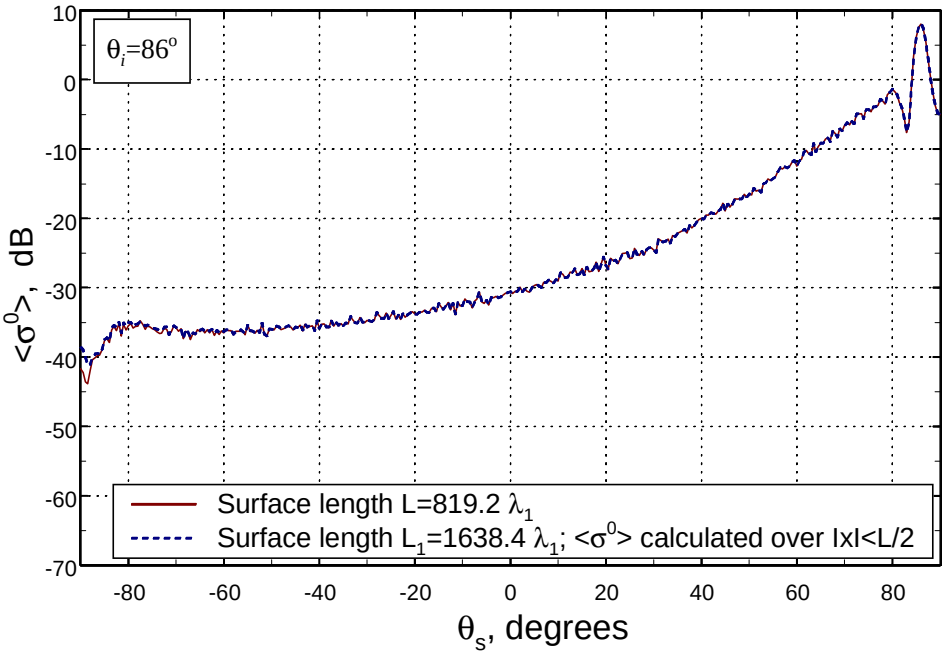

Figure 5-17. Average bistatic normalized radar cross section for $\theta_i = 86^\circ$. Horizontal (TE) polarization, incident field with the Thorsos taper, $g = 136.5\lambda_1$. Only the values of the surface current with $x \in [-L/2, L/2]$ are used to calculate NRCS in the case of the extended surface. The average is taken over 100 realizations of P-M surfaces with a wind speed of 5 m/s.

Let us turn again to Fig. 5-15. We have noticed that while the surface currents in the case of the integral taper lack the tail on the right side so characteristic of the approximate Gaussian-like taper (Fig. 5-14), they exhibit a noticeably high level on the left side, especially at large incident angles. This is apparently a consequence of poor tapering at the edges provided by the integral taper at these angles. This is demonstrated in Fig. 5-18 which shows (on a dB scale) the mean square surface current $\langle |J|^2 \rangle$ calculated by solving the MFIE with the integral-taper incident field at $\theta_i = 86^\circ$ and the mean square Kirchhoff current $\langle |J^i|^2 \rangle$ for the same taper. (Recall that J^i is related to

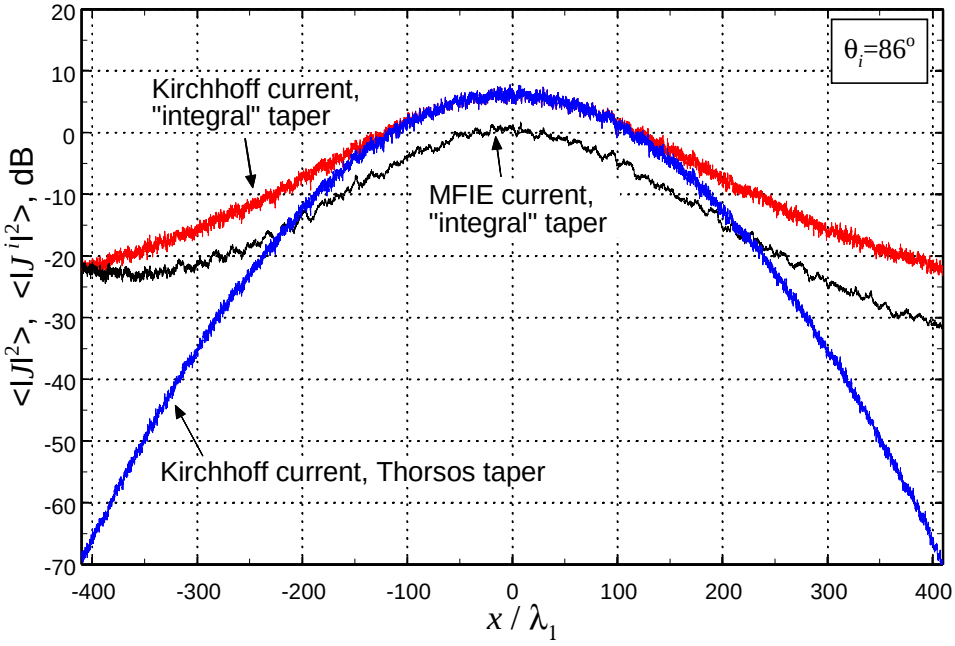

Figure 5-18. Mean square surface current (solution to the MFIE) and mean square Kirchhoff currents. Horizontal (TE) polarization; em wavelength $\lambda_1 = 23\,\text{cm}$, beam waist $g = 136.5\,\lambda_1$. The average is taken over 100 realizations of P-M surfaces with a wind speed of 5 m/s.

the incident field through (2.15a)). The mean square Kirchhoff current for the Thorsos taper is also shown for comparison. First, one can see that the edge levels of the Kirchhoff current for the integral taper are much higher than those for the Thorsos taper. On the other hand, the levels of the surface current $\langle |J|^2 \rangle$ at the edges are quite consistent with the edge levels of the Kirchhoff current with the same integral taper. In particular, the high level of the integral-taper Kirchhoff current obviously drives up the level of the MFIE current at the left surface end.

The behavior of the current levels at surface edges vs. incident angle is further examined in Fig. 5-19 (Thorsos taper) and Fig. 5-20 (integral taper). Ideally, we would like to study the quantities $\langle |J(-L/2)|^2 \rangle / \langle |J(0)|^2 \rangle$ and $\langle |J(L/2)|^2 \rangle / \langle |J(0)|^2 \rangle$. However, since the mean square current estimates that we obtain from 100 realizations are still somewhat noisy (cf. Fig. 5-16 for example) we took an additional spatial average over the intervals of $20\lambda_1$ to get more robust estimates of $\langle |J|^2 \rangle$ near the edges and at the center. In both cases the edge level of the appropriate taper is also shown for a reference using the data from Fig. 5-2.

In case of the Thorsos taper, the current levels at both surface ends are essentially equal at small angles of incidence, as can be seen in Fig. 5-19a. As the incident angle increases, the right-edge current level slowly increases (according to our convention in Fig. 2-4, the positive θ_i correspond to the field coming from the left). In contrast, the current level at the left edge remains unchanged and basically follows the constant edge level of the Thorsos taper. However, at about $\theta_i = 84^\circ$ the current levels at both edges start increasing rapidly with the incidence angle (Fig. 5-19b), with the level at the right edge being much higher. This is a manifestation of the anomalous right "tail" in the current that we observed in Figs. 5-14 and 5-16.

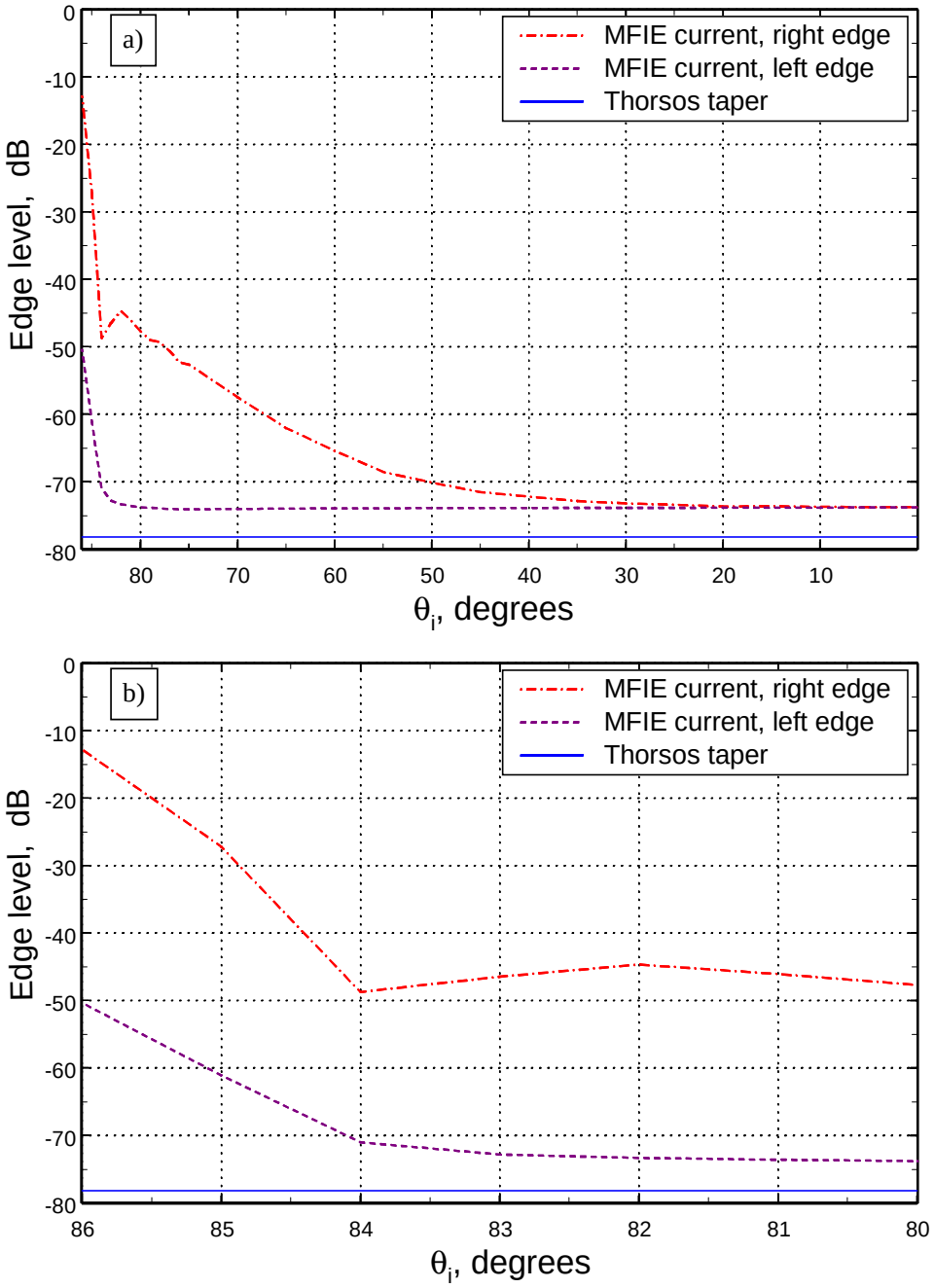

Figure 5-19. Relative levels of the mean-square MFIE current at the edges (edge level of the taper is also shown). Thorsos taper, $g = 136.5\,\lambda_1$, horizontal (TE) polarization, surface length $L = 819.2\lambda_1$. The average is taken over 100 P-M surfaces with a windspeed of 5 m/s. (a) Total range of incident angles; (b) close-up at low grazing incident angles.

Fig. 5-19b can be compared to Fig. 5-20 that displays the current levels when the integral taper is used (we ran simulations with the integral taper only for the range of incident angles shown; however at smaller θ_i the approximate Thorsos taper is virtually identical to the integral taper, cf. Figs. 5-1 and 5-2, and we expect the currents for these smaller angles to behave no different than shown in Fig. 5-19a). At $\theta_i = 80^\circ$ the edge

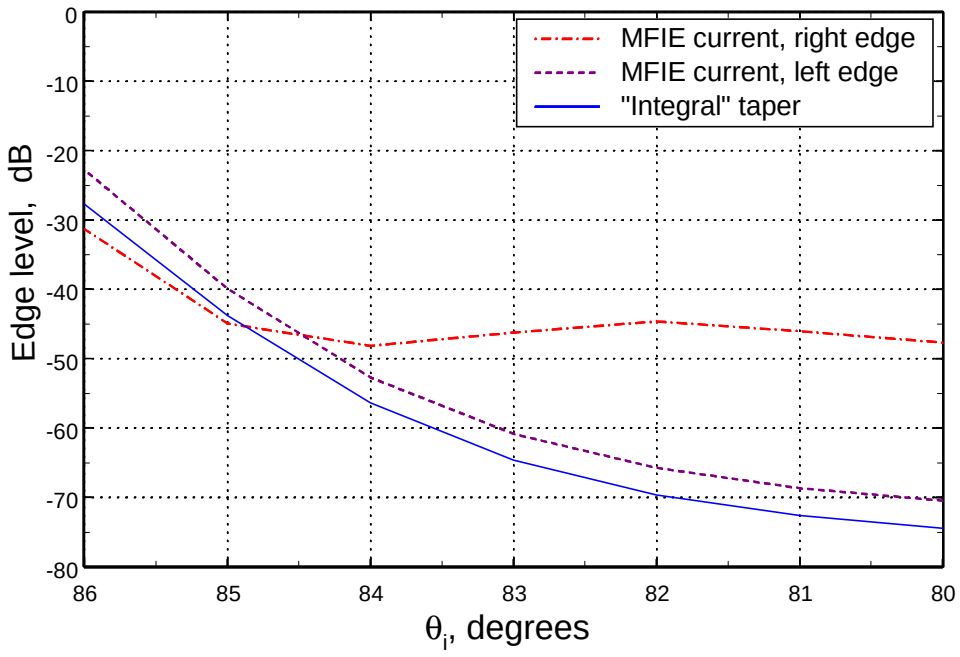

Figure 5-20. Relative levels of the mean-square MFIE current at the edges (edge level of the taper is also shown). Integral taper, $g = 136.5\,\lambda_1$, horizontal (TE) polarization, surface length $L = 819.2\lambda_1$. The average is taken over 100 P-M surfaces with a windspeed of 5 m/s.

levels of the current and the taper are roughly equal to those in the case of the Thorsos taper. However, their behavior as the incident angle increases is quite different from what we saw in Fig. 5-19b. Now the edge levels of the integral taper increase, and the current level at the left surface end also increases while obviously following the taper level. At

$\theta_i \geq 85^\circ$ it exceeds the current level at the right surface end, as we have already noticed in Figs. 5-15 and 5-18.

For vertical (TM) polarization, where we did not see any significant effect of the approximate Gaussian-like taper on the average NRCS (cf. Section 5.3.1), manifestations of the approximate nature of the taper in the MFIE current are also not as pronounced as in the TE case. Fig. 5-21 gives examples of the MFIE currents for a single surface realization in the case of the Thorsos taper and vertical polarization; it is similar to Fig. 5-14 that we had for the horizontal polarization case. Examples of the current for the same surface realization and the integral taper are considered in Fig. 5-22. For the Thorsos taper, one can notice that the current corresponding to $\theta_i = 86^\circ$ in Fig. 5-21c decreases rather slowly towards the right end of the surface. However, the effect is not nearly as pronounced as for the horizontal polarization (Fig. 5-14), and for vertical polarization the current is decaying rather slowly to the right when the integral taper is used as well (Fig. 5-22c). As in the case of horizontal polarization, visibly high levels of the currents near left surface end in Fig. 5-22 are attributed to the poor edge suppression of integral taper.

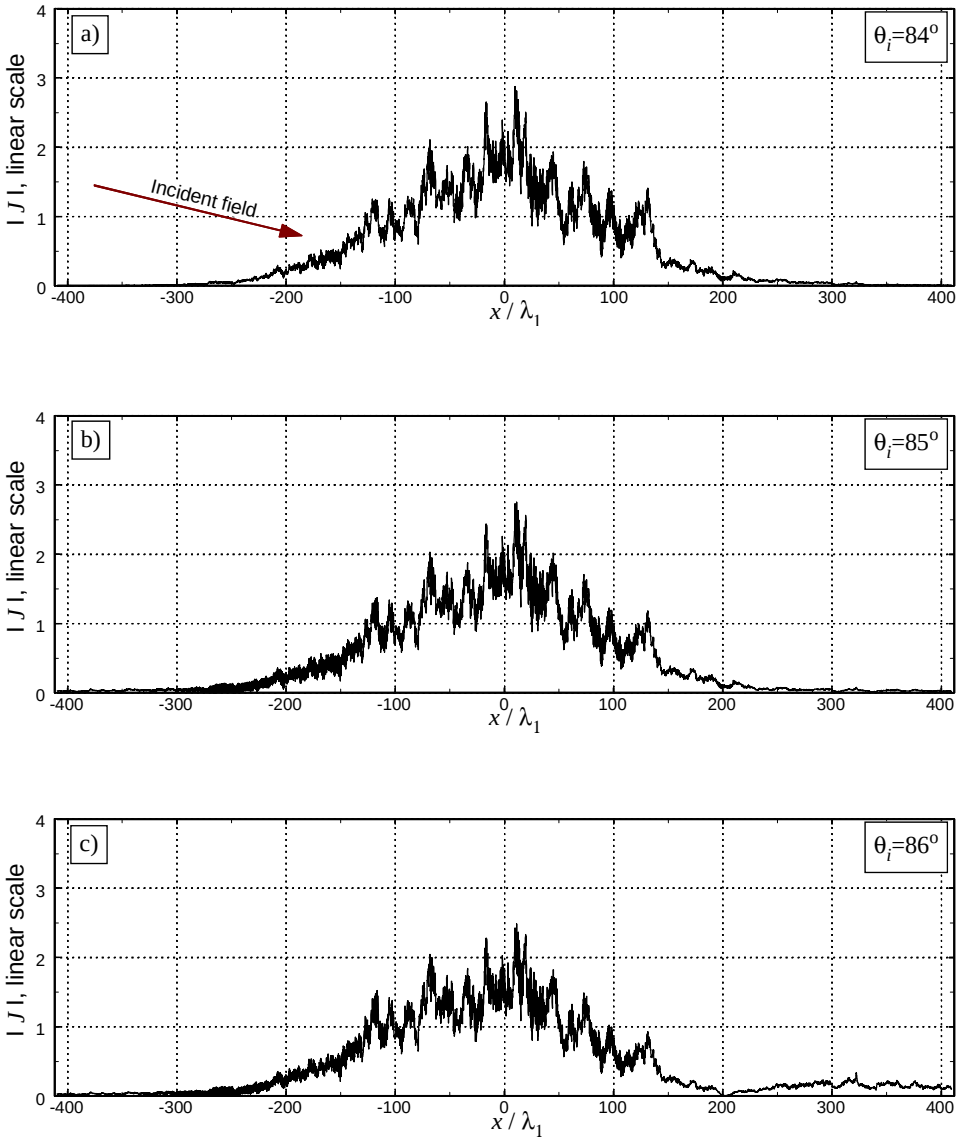

Figure 5-21. Examples of the surface current for a single realization of P-M surface (windspeed = 5 m/s). Thorsos taper, vertical (TM) polarization, em wavelength $\lambda_1 = 23\,\mathrm{cm}$, beam waist $g = 136.5\,\lambda_1$.

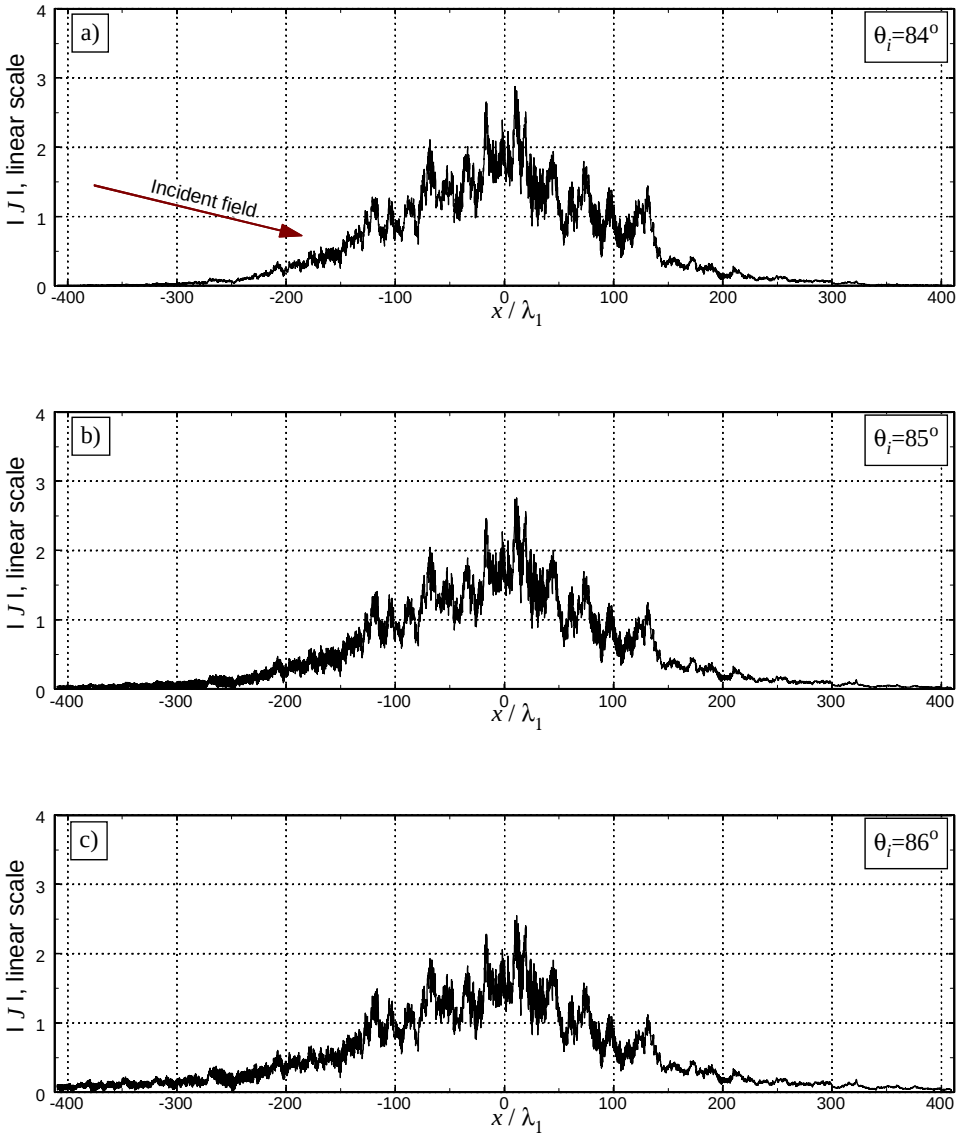

Figure 5-22. Examples of the surface current for a single realization of P-M surface (windspeed = 5 m/s). Integral taper, vertical (TM) polarization, em wavelength $\lambda_1 = 23\,\text{cm}$, beam waist $g = 136.5\,\lambda_1$.

The edge levels of the mean square surface current for vertical polarization are shown in Fig. 5-23 for the Thorsos taper and in Fig 5-24 for the integral taper. All parameters used are the same as in Figs. 5-19 and 5-20 where we examined same quantities for the horizontal polarization. From Fig. 5-23, one can notice that the edge levels of the current for vertical polarization are higher than for horizontal polarization (Fig. 5-19). Similar to the TE case, the current at the left edge remains virtually constant through the whole range of incident angles while the current at the right edge grows slowly as θ_i increases, cf. Fig 5-23a. For the Thorsos taper the current level at the right edge displays quite rapid growth after $\theta_i = 85^\circ$ staying higher than the current at the left surface end that still remains essentially constant (Fig. 5-23b). For the integral taper (Fig. 5-24), the picture is quite similar to that in Fig. 5-20 for the horizontal polarization case. Namely, at low grazing incidence angles the edge levels of the current start increasing apparently following the increase in the taper edge level, with the current at the left edge becoming larger than its counterpart at the right edge. *We would like to point out once again that the current features associated with the Thorsos or integral taper in the vertical polarization case, though identifiable, are not as pronounced as for the horizontal polarization*. And, in contrast to the horizontal polarization case, at the incident angles studied (up to 86°) there are virtually no visible distortions in the vertical polarization cross section (cf. Section 5.3.1) with which these features in the current could be correlated.

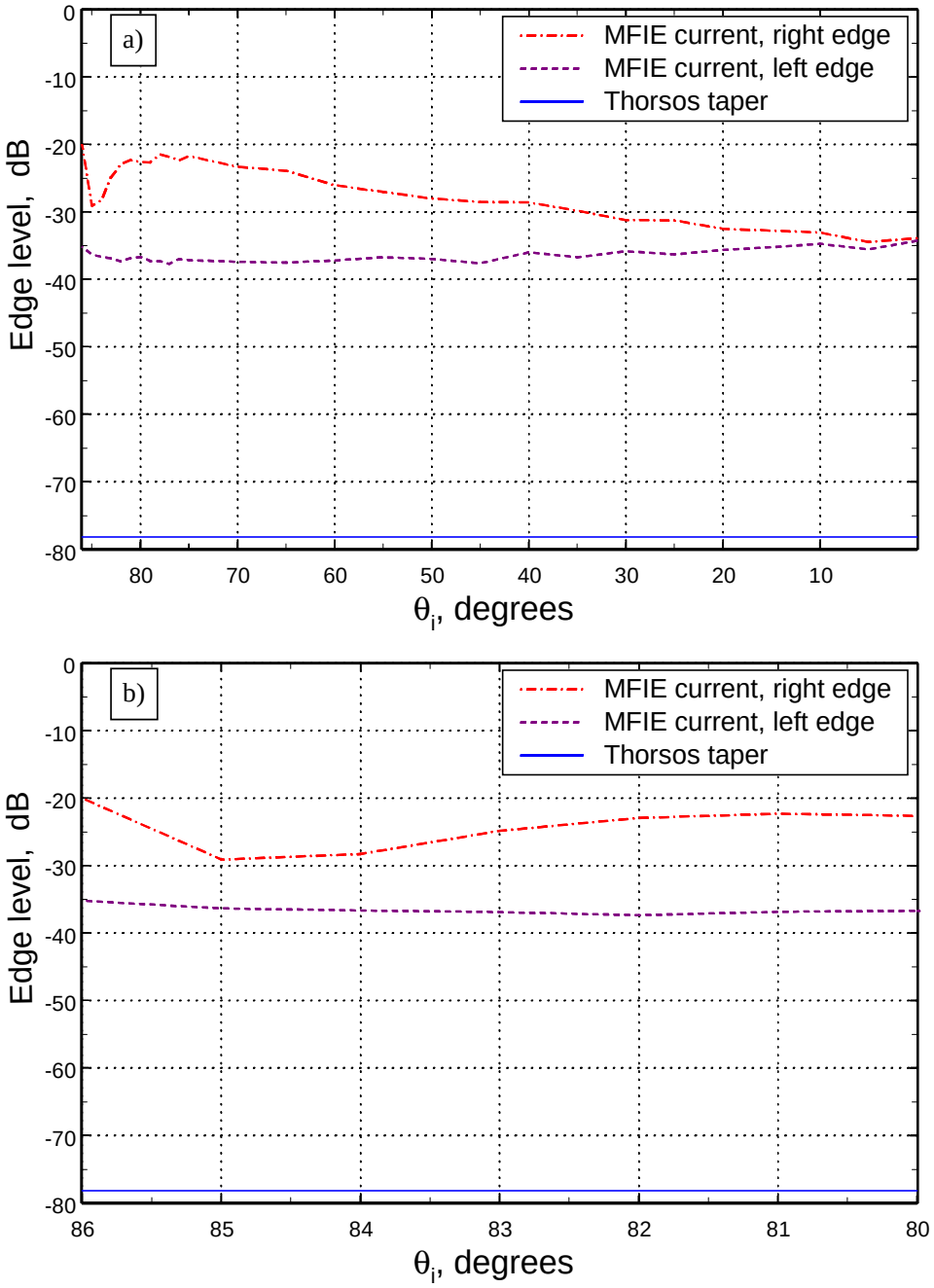

Figure 5-23. Relative levels of the mean-square MFIE current at the edges (edge level of the taper is also shown). Thorsos taper, $g = 136.5\,\lambda_1$, vertical (TM) polarization, surface length $L = 819.2\lambda_1$. The average is taken over 100 P-M surfaces with a windspeed of 5 m/s. (a) Total range of incident angles; (b) close-up at low grazing incident angles.

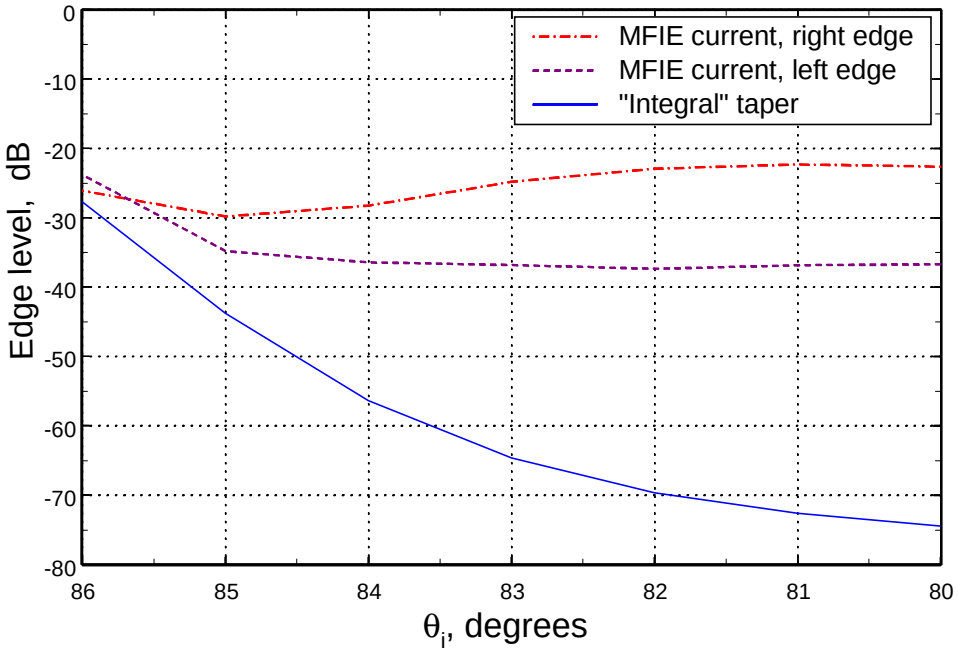

Figure 5-24. Relative levels of the mean-square MFIE current at the edges (edge level of the taper is also shown). Integral taper, $g = 136.5\,\lambda_1$, vertical (TM) polarization, surface length $L = 819.2\lambda_1$. The average is taken over 100 P-M surfaces with a windspeed of 5 m/s.

5.3.3 The Effect of the Thorsos Taper Edge Levels on the Average NRCS for P-M Surfaces

In Section 5.3.1, we established that the Kapp criterion in (5.8), that requires an increase in the beam waist as the incidence angle approaches grazing, is quite robust and should be followed to avert severe distortions in the calculated cross sections. This in turn requires a larger surface length L. Once the required value of g is obtained from (5.8), the surface length is determined from the condition that a certain suppression level at the edges is assured. For example, setting $L = 6g$ assures a –78 dB tapering at the edges. Indeed, using (5.1), (5.2) for the Gaussian taper or (5.1), (5.3) for the Thorsos taper we can write for the edge suppression level

$$S_{dB} = 10\log_{10}(|\psi^i(L/2,0)|^2 / |\psi^i(0,0)|^2) = 10\log_{10}(\exp\{-L^2/2g^2\}) = \\ = -2.17(L/g)^2 \tag{5.22}$$

and for the ratio $L/g = 6$ this yields $S_{dB} \cong -78.1\,\text{dB}$. In the simulations that we carried out in Chapter 4 and in most of the simulations involving Gaussian/Thorsos tapers in this Chapter we kept the L/g ratio equal to 6. However, the results with the integral taper indicated that much weaker edge suppression resulted in little effect on $\langle\sigma^0\rangle$ (cf., for example, Fig. 5-6). In this Section, we study in detail how the edge suppression level affects the average NRCS in the case of the Thorsos taper. Since, according to (5.22), for the Thorsos taper this edge level is defined entirely by the ratio L/g, this would tell how large the surface should be, provided that the beam waist is chosen appropriately. From the results we have already seen in this Chapter, one should expect that the average NRCS will be more sensitive to the edge suppression in the case of horizontal polarization and large angles of incidence.

In the simulations reported below we once again considered scattering from P-M surfaces characterized by the windspeed of 5 m/s at the electromagnetic wavelength $\lambda_1 = 23\,\text{cm}$. The surface length was fixed at the "usual" value of $L = 819.2\lambda_1$; the taper level at the edges was varied by changing the beam waist. We considered the values of g in the range of $L/6 = 136.5\lambda_1$ to $L/3 = 273.1\lambda_1$. According to (5.22), the taper suppression at the surface ends varied correspondingly from –78.1 dB to –19.5 dB. From

the criterion (5.8) and Section 5.3.1, the smallest value of $g = 136.5\lambda_1$ allows for the incidence angles as large as 84°.

Fig. 5-25 shows the average backscattered NRCS for several incident angles vs. the taper level at the edges, S_{dB} as defined in (5.22). In this figure we also included the

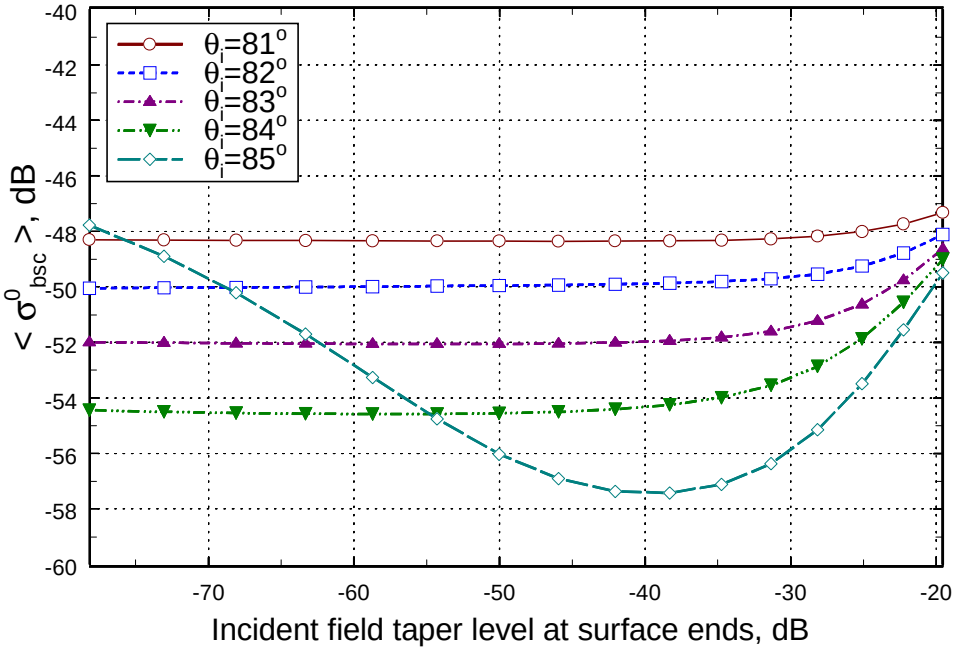

Figure 5-25. Average normalized radar cross section in the backscattered direction vs. the taper edge level. Thorsos taper, horizontal (TE) polarization, the average is taken over 100 realizations of P-M surfaces with a wind speed of 5 m/s.

NRCS plot for $\theta_i = 85^\circ$ for which the Thorsos taper with $g = 136.5\lambda_1$ fails, cf. Fig.5-4; we will discuss the behavior of this plot below. For other incidence angles ($81^\circ - 84^\circ$) we observe that the average backscattered NRCS remains quite insensitive to the taper edge levels over a broad range of values of the latter. In particular, for $\theta_i = 84^\circ$ $\langle \sigma^0_{bsc} \rangle$ starts showing some variation only for S_{dB} above –40 dB (from (5.22), $L/g \cong 4.3$). For

smaller incidence angles the threshold is even higher: for $\theta_i = 81^\circ$ noticeable variation occurs only after the taper level exceeds –30 dB ($L/g \cong 3.7$).

Let us consider the behavior of $\langle \sigma^0_{bsc}(85^\circ) \rangle$. As we mentioned, the value of $g = L/6 = 136.5\lambda_1$ that provides –78.1 dB tapering is insufficient for this incident angle. The Thorsos taper is failing and this results in abnormally high values of the cross section. As we weaken the taper edge suppression by increasing g, the taper failure effects are reduced, and the average backscattered NRCS decreases. The criterion in (5.8) with $A = 9.4$ predicts that for this incident angle the beam waist g should be at least $196.7\lambda_1$. When combined with the surface length $L = 819.2\lambda_1$ this results in, from (5.22), a -37.6 dB taper level at the edges. Indeed, in Fig. 5-25 the line corresponding to $\langle \sigma^0_{bsc}(85^\circ) \rangle$ keeps descending until the taper level is about –38 dB. However, at this point it apparently starts being affected by the insufficient tapering at the edges and begins rising immediately. If we regard the value of $\langle \sigma^0_{bsc}(85^\circ) \rangle = -58.4$ dB obtained with the integral taper (cf. Fig. 5-4) to be the "true" one, the average NRCS in Fig. 5-25 never reaches this "true" value: at its lowest point it is equal to –57.4 dB. The plot corresponding to $\theta_i = 85^\circ$ in Fig. 5-25 is thus a good example how, for a fixed surface length, either taper failure effects or edge effects come into play and prevent us from obtaining the correct result.

We can further examine how the edge tapering affects the bistatic cross section. Fig. 5-26 shows $\langle \sigma^0(\theta_i, \theta_s = -89^\circ) \rangle$, i.e. the average NRCS for different incidence angles and one particular scattering angle $\theta_s = -89^\circ$. At this scattering angle the cross sections have smaller values and, as should have been expected, are more sensitive to the taper edge levels, with the NRCS for $\theta_i = 81^\circ$ starting to show changes for as small taper level as -45 dB. The average NRCS for $\theta_i = 85^\circ$ this time apparently does not even approach the correct level, remaining abnormally higher than all other cross sections. $\langle \sigma^0 \rangle$ corresponding to $\theta_i = 84^\circ$ now exhibits the behavior that we observed in Fig. 5-25 for $\langle \sigma^0_{bsc}(85^\circ) \rangle$. This is not surprising since in Fig. 5-8 we concluded that at such large

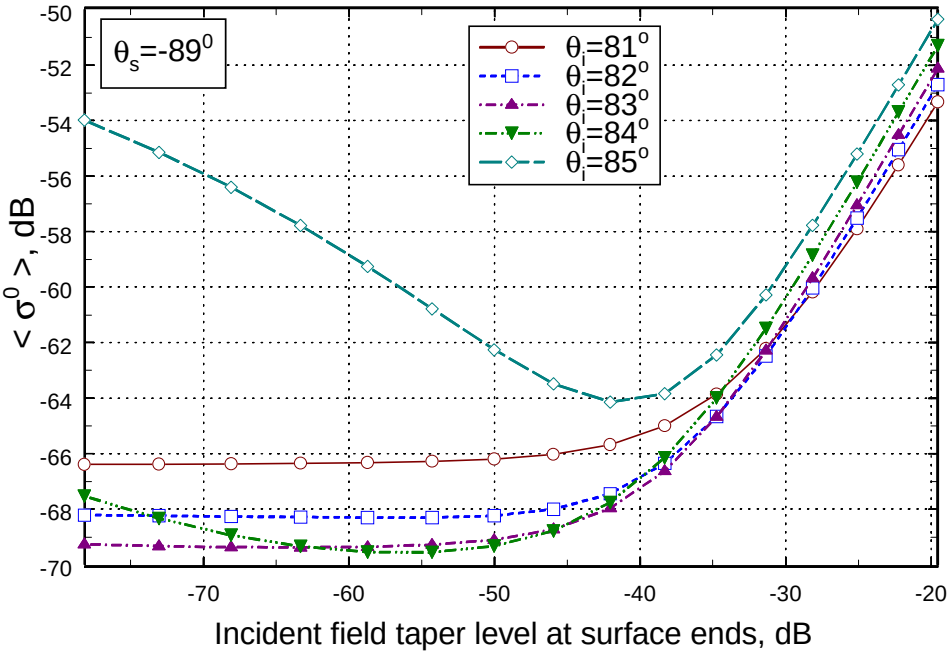

Figure 5-26. Average bistatic normalized radar cross section (for $\theta_s = -89^\circ$) vs. the taper edge level. Thorsos taper, horizontal (TE) polarization, the average is taken over 100 realizations of P-M surfaces with a wind speed of 5 m/s.

scattering angle the NRCS even for $\theta_i = 84^\circ$ can be influenced by the approximate taper effects.

Similar results for backscattering and bistatic scattering in the case of vertical (TM) polarization are presented in Figs. 5-27 and 5-28. Not surprisingly, the TM results show much less sensitivity to the taper edge levels.

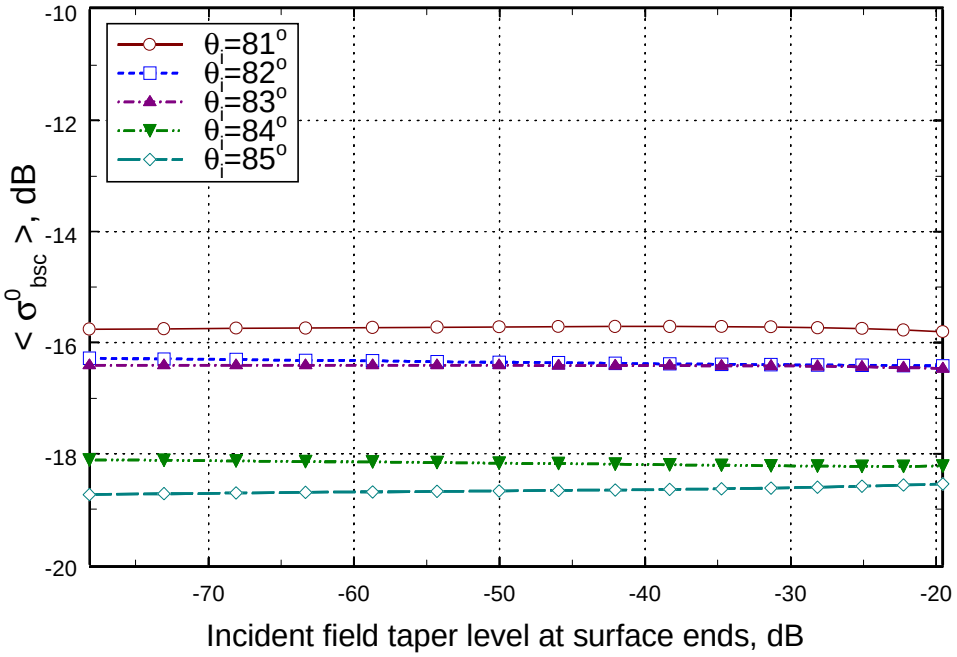

Figure 5-27. Average normalized radar cross section in the backscattered direction vs. the taper edge level. Thorsos taper, vertical (TM) polarization, the average is taken over 100 realizations of P-M surfaces with a wind speed of 5 m/s.

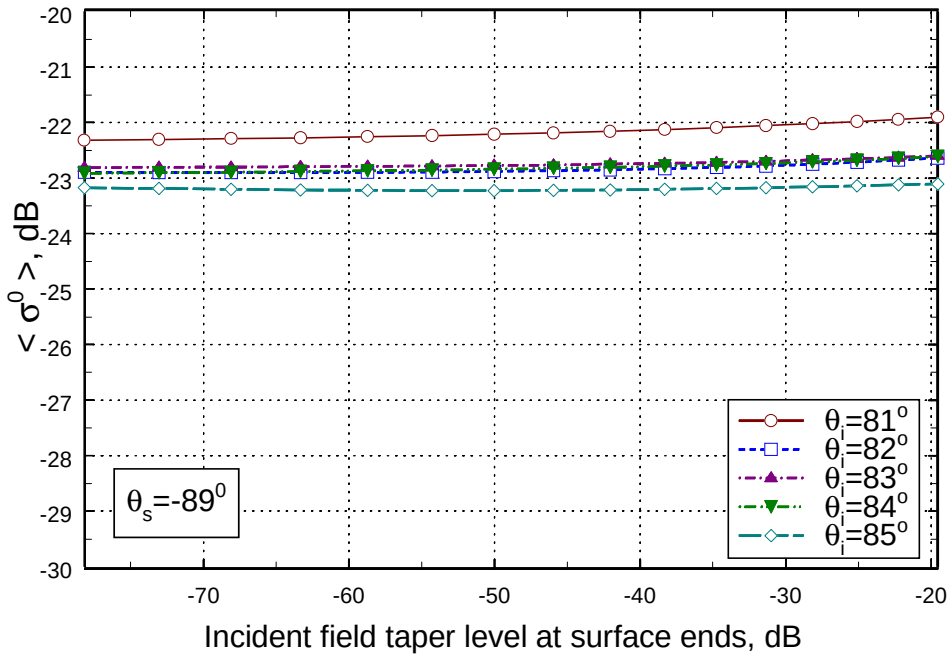

Figure 5-28. Average bistatic normalized radar cross section (for $\theta_s = -89^\circ$) vs. the taper edge level. Thorsos taper, vertical (TM) polarization, the average is taken over 100 realizations of P-M surfaces with a wind speed of 5 m/s.

Let us finally discuss the following question. We have seen that as the incident angle increases, the Thorsos/Gaussian taper fails and several solutions to this problem can be considered. One can:

(1) continue to use the Thorsos taper with larger g chosen in accordance with (5.8);

(2) use the integral taper with the same fixed g since, unlike its Thorsos/Gaussian approximation, it is not subject to a failure;

(3) use the integral taper with the increasing g (with the latter not necessarily satisfying (5.8)).

All these solutions, however, would eventually require an increase in the surface length to guard against poor edge tapering. Indeed, if the surface length is fixed, the option (1) results in insufficient edge tapering by the virtue of (5.22). The increase in the edge level of the integral taper with a fixed g (option (2)) as θ_i increases is depicted in Fig. 5-2. Since we find that the integral taper always provides poorer edge suppression as compared to the Thorsos approximation with the same g, the option (3) will also have increasingly higher edge levels for large θ_i, with (5.22) providing the lower bound for any given beam waist value. Consequently, a larger surface length will be required to assure a proper edge tapering and eliminate edge effects.

For example, the correct value for the Thorsos taper waist at $\theta_i = 86^\circ$ is, from (5.8), $g = 307.2\lambda_1$. However, for our "standard" surface length $L = 819.2\lambda_1$ such a g would result in the –15.4 dB taper level at the edges (cf. (5.22)). From Fig. 5-25 we see that such edge level is insufficient even for smaller incident angles; for $\theta_i = 86^\circ$ it is definitely unacceptable. Increasing the surface length by a factor of 2 to $L_1 = 1638.4\lambda_1$ will result in –61.7 dB edge suppression level (cf. again (5.22)). Although we do not have the relevant data in Fig. 5-25, from the behavior of the curves for smaller incident angles it seems likely that this edge level may be sufficient, or otherwise an even longer surface should be used.

On the other hand, we found earlier that using the integral taper with $g = 136.5\lambda_1$ at $\theta_i = 86^\circ$ (which in the context of the example of Fig. 5-4 corresponds to option (2) above) provides only –28 dB suppression at the edges of the surface of length

$L = 819.2\lambda_1$, and this high edge level affects the result (cf. Fig. 5-5). We found it necessary to double the surface length to $L_1 = 1638.4\lambda_1$ and this still resulted in the relatively high –38 dB taper level at the edges with apparent impact on the NRCS. Fig. 5-29 compares the average bistatic NRCS calculated using the integral taper with

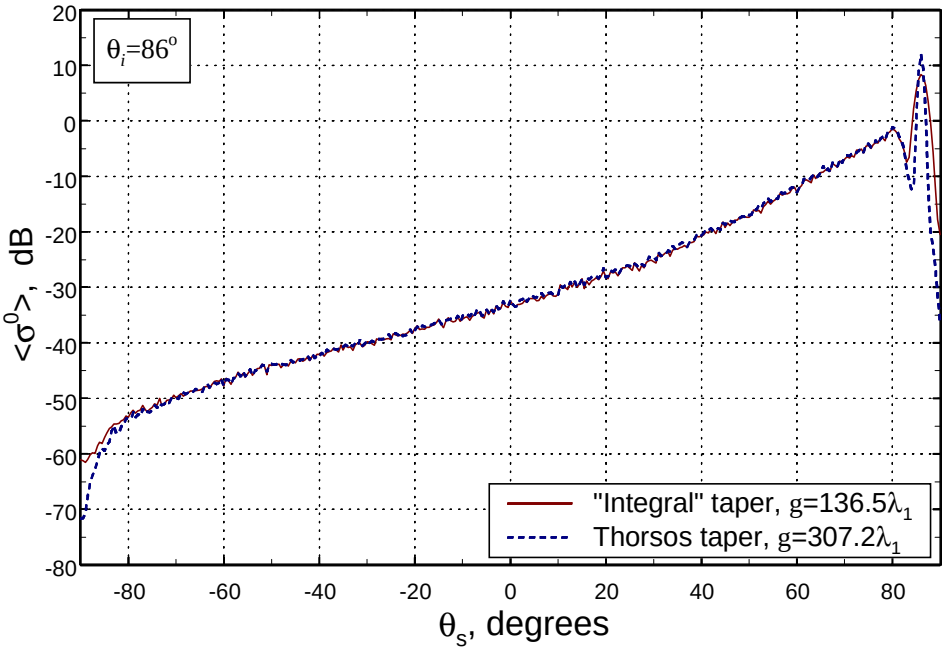

Figure 5-29. Average bistatic normalized radar cross section for $\theta_i = 86^\circ$. Horizontal (TE) polarization, the average is taken over 100 realizations of P-M surfaces with a wind speed of 5 m/s and surface length $L_1 = 1638.4\lambda_1$.

$g = 136.5\lambda_1$ (the curve is borrowed from Fig. 5-5) and the Thorsos taper with $g = 307.2\lambda_1$. The surface length in both cases is $L_1 = 1638.4\lambda_1$. One can see that the two curves are almost identical for the most of scattering angles; however, close to $\theta_s = -90^\circ$ the curve corresponding to the Thorsos taper has noticeably smaller values. While we did not have the data to check if the result with the Thorsos taper is a "true"

one (this would involve simulations with even larger surfaces), the general pattern of behavior in the vicinity of -90° suggests that the dashed curve in Fig. 5-29 is closer to to the "true" answer (cf. Figs. 5-6 and 5-9).

The example in Fig. 5-29 and the preceding discussion suggest that when one needs to go to the larger incident angles, it is more advantageous to use the Thorsos taper with a g that satisfies the Kapp criterion and increase the surface length accordingly than to use the integral taper with a smaller g and still be forced to use larger surface to reduce the taper edge levels. This means that if only the options (1) and (2) were considered, the preference should be given to the option (1). In Fig. 5-29 one can also notice a sharper specular peak in the case of the Thorsos taper which is due to a larger spotsize. This brings yet another consideration in favor of using the taper with a larger g (i.e. options (1) and possibly (3)): the larger spotsize allows determining the NRCS with a finer angular resolution, as was pointed out by [Ngo and Rino, 1994].

As was noted, the integral taper provides higher edge levels compared to its Thorsos/Gaussian counterparts with the *same* g (as can be observed in Fig. 5-2, cf. also [Toporkov *et al*, 1998]). So, if g in option (3) varies with θ_i as in (5.8), then the integral taper would have no apparent advantage to the Thorsos taper which will remain valid for such g's . However, the question of using the integral taper with the waist that increases with θ_i in a fashion other than in (5.8) may be of interest and probably deserves further study. Here we will give an example illustrating the possible issues involved. Fig. 5-30 shows the edge levels for the integral taper as a function of the beam waist for $\theta_i = 86^\circ$ and three surface lengths: $819.2\lambda_1$, $1638.4\lambda_1$ and $3276.8\lambda_1$ (while we used $\lambda_1 = 23\,\text{cm}$, the results as shown in Fig. 5-30 are valid for any electromagnetic wavelength used in place of λ_1). For small g's, high edge levels observed in Fig. 5-30 are understandable given the raised "tails" of the integral taper visisble in Fig. 5-1; at large g's the integral taper is well approximated by the Thorsos taper and we see the edge level rising as $(L/g)^2$ as predicted for the Thorsos/Gaussian taper by (5.22). It is evident from the figure that for every surface length considered there is a certain value of g that minimizes the edge level. For example, for the surface of the length $L_1 = 1638.4\lambda_1$

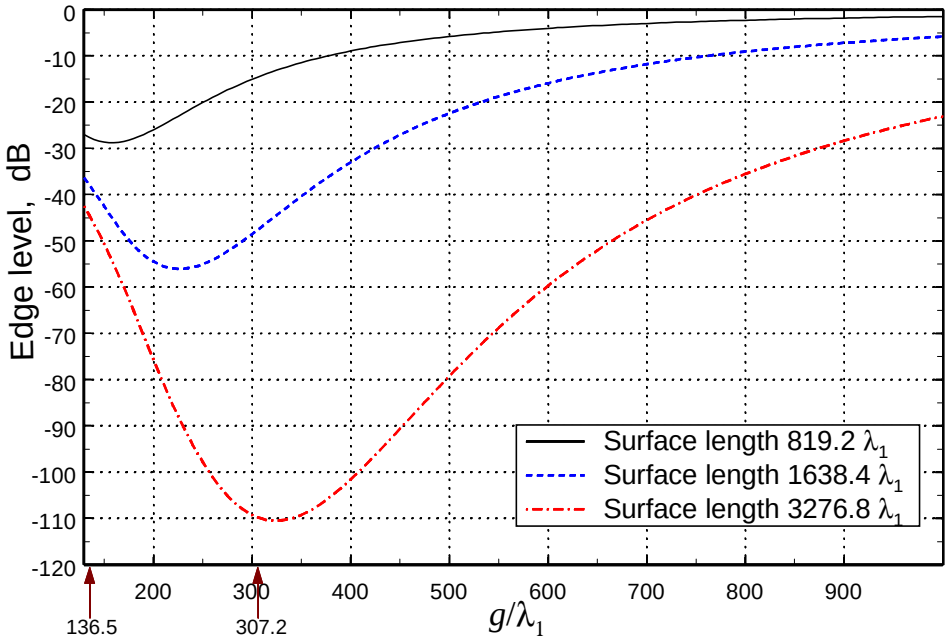

Figure 5-30. Suppression levels at surface ends provided by the integral taper vs. the beam waist parameter g ($\theta_i = 86^\circ$). The values of g used in other examples in this Section ($136.5\lambda_1$ and $307.2\lambda_1$) are marked for reference.

(dashed curve) this minimum occurs at approximately $g = 225\lambda_1$ and is about –56 dB. For comparison (we continue to follow the dashed curve for $L_1 = 1638.4\lambda_1$), should we used a smaller $g = 136.5\lambda_1$ (as we did in Fig. 5-5) this would have resulted in –38 dB edge level. The use of $g = 307.2\lambda_1$ predicted by (5.8) for the validity of the *Thorsos taper* would result in about –47 dB edge suppression. Both these values are higher than the minimal –56 dB. Note also that this minimal edge level is still higher than –61.7 dB what would be achieved if the Thorsos taper with a "correct" $g = 307.2\lambda_1$ were used with the same surface of the length $L_1 = 1638.4\lambda_1$.

This example demonstrates that for a given surface length there is an optimal beam waist, say, g^* that results in the lowest integral taper edge level possible. This "optimal waist" is different from the one predicted by (5.8) for the Thorsos taper. The

dependence of g^* on θ_i and L, as well as achievable suppression levels, deserve further investigation. This knowledge will be of certain use if the integral taper has to be employed; indeed, in some problems (like propagation over rough surfaces) the exact Maxwellian nature of the incident field is of a paramount concern and the integral taper emerges as a logical choice [Toporkov *et al*, 1998].

Although our understanding of the application of the integral taper is not yet complete, the discussion above indicates that in the rough surface scattering problems it is preferable to use the Thorsos taper with the waist governed by the Kapp criterion. In this case, tapering levels at the edges seem to be smaller than for the integral taper with even the "optimal" waist g^* and they are more controllable. Switching from Thorsos to integral taper while retaining the same g and the surface length does *occasionally* permit obtaining valid results for incident angles larger than the limit set by the Kapp criterion (cf. Fig. 5-4 for example). This happens if the increase in the edge levels resulting from such a switch is not large enough to affect $\langle \sigma^0 \rangle$. However, due to the reasons cited above the Thorsos taper seems to be the preferred choice *in general*. It should also be remembered that one of the most important considerations in favor of the Thorsos taper is its computational simplicity.

5.4 Conclusion

In this Chapter we have considered the applicability of the Gaussian and the Thorsos tapers to rough surface scattering a low grazing angles. In our scattering simulations with the ocean-like Pierson-Moskowitz surfaces we saw a distinctive signature of the Thorsos and Gaussian taper failure for the horizontal polarization (TE case): as the incident angle approaches grazing, the backscattered cross section consistently exhibits an anomalous jump. From these observations, we determined the value of an arbitrary constant involved in the Kapp "angle of incidence-beam waist" criterion and showed that this criterion is very reliable. We find that Gaussian and Thorsos tapers with the same waist fail at about the same incident angle, with the Thorsos taper being somewhat more robust. Once the incident angle is in the region where the taper fails, the surface current, which is the solution to the magnetic field integral

equation (MFIE), also displays quite distinctive features such as a slowly decaying "tail". For the vertical polarization (TM case), we find virtually no indication of a Gaussian-like taper failure either in the cross section, or in the MFIE current. These effects might, however, be present at larger incident angles that have not been studied.

The above effects associated with the failure of the approximate taper for horizontal polarization are not present if the exact Maxwellian integral taper is used. However, this taper provides poorer suppression at the surface edges and, as the incident angle increases, the results obtained with such a taper become invalid because of the insufficient edge tapering. This effect limits the applicability of the integral taper at large θ_i for a fixed surface length.

When either the integral taper or Thorsos taper that follow the Kapp criterion are used, the surface length has to be increased as the incidence angle moves to grazing, the reason being the deterioration in the edge tapering. The influence of the edge suppression provided by the Thorsos taper (or, equivalently, L/g ratio) on the average NRCS of P-M surfaces has been considered. It was found that in the horizontal case the valid backscattering cross section for the incident angles as low as $81^\circ - 84^\circ$ can be calculated with the tapering levels as high as -30 to -40 dB. However, this threshold grows with θ_i and lower incident angles will require stronger edge tapering, as should be expected. Stronger tapering at the edges may be required if the values of bistatic cross section at scattering angles close to -90° are of interest. For the vertical (TM) case, both backscattering and bistatic results display much larger tolerance to the taper edge levels.

Although the integral taper probably requires further study, its comparison to the Thorsos taper suggests that the latter (with the appropriate beam waist) provides lower edge levels. Also, in the case of the Thorsos taper the edge levels are easier to control. Combined with the fact that the Thorsos taper is much less computationally expensive, these considerations indicate that in general the Thorsos taper should be given a preference provided that the Kapp criterion is satisfied.

Chapter 6

Summary and Conclusions

This study considers 2-D numerical simulations of scattering from randomly rough perfectly conducting surfaces with the ocean-like Pierson-Moskowitz spectrum. The purpose of this work was to investigate and report on several issues found to be of importance relative to the validity of numerical scattering simulations, especially at low grazing incidence angles. These issues include the discretization of the integral equation for surface current and properly accounting for all terms that should result from such a procedure, and the choice of the sampling interval and the effect of the artificially introduced surface spectral cutoff. Another important factor that can affect simulation results at low grazing angles (LGA) is the use of an incident field having a Gaussian-like taper. The approximate nature of such an incident field (it does not satisfy the wave equation exactly) can result in significant distortion of the results unless certain precautions developed here are followed.

The electromagnetic and statistical foundations of Monte Carlo scattering simulations used in this study are reviewed in Chapters 2 and 3, respectively. Chapter 3 also presents a detailed development of the spectral method of generating realizations of randomly rough surfaces together with their higher derivatives. This ability to generate first and second surface height derivatives is important since the knowledge of these derivatives is required when solving the discretized Magnetic Field Integral Equation (MFIE) that constitutes the basis for the scattering simulations.

The main results of this dissertation are presented in Chapters 4 and 5. Chapter 4 addresses the questions of discretizing the MFIE, choosing the sampling interval and a related issue of selection of the surface spectral cutoff for simulation purposes. Chapter 5 focuses on the application of the incident field with a Gaussian-like taper in LGA simulations. The most important findings are listed at the end of each chapter in the "Conclusion" sections. Here we summarize these findings once again.

The results of numerical scattering simulations with Pierson-Moskowitz surfaces demonstrate that the so-called "curvature terms", previously regarded by many researchers as an optional correction must be included in the diagonal of the propagator matrix of the discretized MFIE. Otherwise, calculated values of the normalized radar cross section exhibit strong sensitivity to the sampling interval and very small intervals (such as a hundredth of an electromagnetic wavelength) may be required to achieve a stable and presumably correct value. This effect is especially pronounced in the case of the horizontal polarization at low grazing angles. For average quantities like the average normalized radar cross section, the observed discrepancies are not as dramatic as for single-realization cases but are still significant. An inclusion of the "curvature terms" in the propagator matrix remedies this problem completely. Subsequent analysis of the discretization of the MFIE reveals that these "curvature terms" must indeed appear in the diagonal of the kernel matrix as a result of the correct discretization procedure. This conclusion does not depend on the type of the surface spectrum; however the effect of neglecting these terms when P-M surfaces are used is especially strong since high local curvature is characteristic of such surfaces. The above finding regarding "curvature terms" also does not depend on what particular numerical technique is used to solve the discretized MFIE. Following this analysis, we develop a recommendation for the choice of a sampling interval to be used in simulations with P-M surfaces that is based on the electromagnetic wavelength and the surface spectral cutoff. Such a cutoff is present in natural ocean-like surfaces due to physical mechanisms and can have different values depending on several factors like the presence of certain surfactants. For numerical simulation purposes some artificial, much lower value of such a cutoff is usually assumed. The sensitivity of the scattering simulation results to the choice of this cutoff was studied. It was found that for both single-realization and average backscattered cross section this sensitivity increases at large incidence angles. At LGA significant changes in the *average* cross section are observed once the spectral cutoff falls below $2k$ ($k =$ the electromagnetic wavenumber). The spectral cutoff can be chosen as low as $2.5k$ for the average normalized radar cross section not to be affected. At moderate incident angles, these thresholds become lower. For single-realization cross sections, variations are observed until higher values of surface cutoff are reached; these values for low grazing

incident angles may be as high as $3k$ to $4k$. Further analysis of the relative rms error in the scattered *field* reveals that the cutoff value of $4k$ results in only a few percent error for incidence angles as low as 85°. Consequently, while the cutoff of $2.5k$ seems to be completely adequate for average cross section calculations, one should consider using a higher cutoff like $4k$ if quantities other than average cross section are of interest. Such choices will permit obtaining valid results that are representative of realistic surfaces with much larger natural spectral cutoffs. The conclusions regarding the choice of surface spectral cutoff remain much the same for both horizontal and vertical polarizations.

To guard against "edge effects" associated with the finite surface size used in numerical simulations, a taper is often applied to the plane-wave incident field thus reducing field levels towards the surface ends. The most popular taper functions are the Gaussian and Thorsos tapers. These Gaussian-like tapers provide strong suppression at the edges that can be easily controlled by choosing the taper waist/surface length ratio. However, the incident field with either taper satisfies the wave equation only approximately, with the Thorsos taper providing better compliance. Our simulation results show that for the horizontal polarization the average backscattered cross section obtained with these approximate tapers displays a characteristic anomaly that is associated with the taper "failure" at LGA. We used this observation to investigate the "beam waist – angle of incidence" criteria that have been proposed by several authors. These criteria sought to limit a fraction of evanecsent waves or wave components that can be interpreted as coming from below the surface by increasing the taper waist with the angle of incidence; at LGA they predict essentially the same dependence. For P-M surfaces, we refined one of the criteria by determining the value of an arbitrary constant involved and showed that this criterion is very robust. It was also shown that if one chooses the beam waist in accordance with this refined criterion the valid results are obtained not only in backscattered direction but for all scattering angles, except maybe those very close to -90°. The Gaussian and the Thorsos tapers having same waist were observed to fail at about the same incident angle with the Thorsos taper being somewhat more robust. The effects of the taper "failure" in the horizontal case were also observed in the surface current (the solution to the MFIE) as an abnormally large "tail". As far as

the vertical polarization is concerned, for the range of incident angles studied (up to 86°) we saw no indications of taper failure in either the average cross section or the surface current. During this study we investigated the application of the "exact" tapered incident field which, being a weighted superposition of plane waves, satisfied the wave equation exactly (this was done mainly to have a check case to which the approximate taper results could be compared). It was found that the main problem associated with such an incident field was an increasingly weak suppression at the finite length surface edges at large incident angles that eventually lead to the distortions in the calculated cross sections. For both the "exact" incident field and the field with the approximate Gaussian-like taper that satisfies the beam waist criterion, the edge suppression level is controlled by the surface length, and at large incident angles the increasingly long surfaces are required. While for Gaussian-like tapers the relationship between the beam waist, surface length and the edge levels is simple, for the incident field with the "exact" taper such a relationship seems to be more complex and this issue may deserve further study.

This work uncovers the problems associated with numerical simulations of rough surface scattering, especially in the demanding LGA regime, and presents solutions and recommendations to avoid or eliminate these problems. These results provide further progress in the newly emerging area of numerical studies of surface scattering at low grazing angles.

References

Adams, R. J., Private communication, 1998.

Allen, K. R., and Joseph, R. I., "A canonical statistical theory of oceanic internal waves", *Journal of Fluid Mechanics*, vol. 204, pp. 185-228, 1989.

Allen, K. R., and Joseph, R. I., "A canonical statistical theory of surface wind waves", *EOS Transactions AGU*, vol. 71, p. 73, 1990.

Apel, J. R., "An improved model of the ocean surface wave vector spectrum and its effects on radar backscatter", *Journal of Geophysical Research*, vol. 99, no C8, pp. 16269-16291, 1994.

Arfken, G. B., Weber, H. J., *Mathematical Methods for Physicists*, Academic Press, N.Y., 1995.

Beckmann, P., Spizzichino, A., *The Scattering of Electromagnetic Waves from Rough Surfaces*, Pergamon Press, N.Y., 1963.

Bleistein, N. and Handelsman, R. A., *Asymptotic Expansions of Integrals, Dover Publications*, Inc., N.Y., 1986.

Bracewell, R., *The Fourier Transform and Its Applications*, McGraw Hill, N.Y., 1965.

Brigham, E. O., *The Fast Fourier Transform*, Prentice-Hall, Inc., Englewood Cliffs, NJ, 1974.

Brown, G. S. and Kapp, D. A., "The effect of surface curvature on the sampling interval and convergence rate of the Method of Ordered Multiple Interactions", *IEEE Antennas*

and Propagation International Symposium and URSI Radio Science Meeting, Baltimore, MD, p. 144, July 1996.

Chan, C. H., Tsang, L., and Li, Q., "Monte Carlo simulations of large-scale one-dimensional random rough-surface scattering at near-grazing incidence: penetrable case", *IEEE Trans. Antennas & Propagat.*, vol. 46**,** no 1, pp. 142-149, January 1998.

Chew, W. C., *Waves and Fields in Inhomogeneous Media*, IEEE Press, N.Y., 1995.

Courant, R., Hilbert, D., *Methods of Mathematical Physics*, vol.1, Interscience Publishers, Inc., N.Y., 1953.

Davenport, W. B., Root, W. L., *An Introduction to the Theory of Random Signals and Noise*, IEEE Press, N.Y., 1987.

Donohue, D. J., Ku, H.-C., Thompson, D. and Sadowsky, J., "Direct numerical simulation of electromagnetic rough surface and sea scattering by an improved banded matrix iterative method", *Johns Hopkins APL Technical Digest*, vol.18, no 2, pp. 204-216, 1997.

Donohue, D. J., Ku, H.-C., Thompson, D., "Application of Iterative Moment-Method Solutions to Ocean Surface Radar Scattering", *IEEE Trans. Antennas & Propagat.*, vol. 46**,** no 1, pp. 121-132, January 1998.

Feynman, R. P., Hibbs, A. R., *Quantum Mechanics and Path Integrals*, McGraw Hill, N.Y., pp.322-356, 1965.

Gradshteyn, I.S., Ryzhik, I. M., *Table of Integrals, Series and Products*, Fifth Edition, A. Jeffrey, Editor, Academic Press, Inc., N.Y., 1994.

Harrington, R., *Field Computation by Moment Methods*, IEEE Press, N. Y., 1993.

Holliday, D., DeRaad, L. L. and St-Cyr, G. J., "Forward-Backward: a new method for computing low-grazing angle scattering", *IEEE Trans. Antennas & Propagat.*, vol. 44**,** no 5, pp**.** 722-729, May 1996.

Ishimaru, A. *Electromagnetic Wave Propagation, Radiation, and Scattering*, Prentice-Hall, Inc., N. J., 1991.

Jackson, J. D., *Classical Electrodynamics*, John Wiley & Sons, Inc., N. Y., 1975.

Johnson, J. T., "A numerical study of low grazing angle backscatter from ocean-like impedance surfaces with the canonical grid method", *IEEE Trans. Antennas & Propagat.*, vol. 46**,** no 1, pp. 114-120, January 1998.

Kapp, D. A., *A New Method to Calculate Wave Scattering From Rough Surfaces at Low Grazing Angles*, Ph.D. dissertation, Virginia Polytechnic Institute and State University, Blacksburg, VA, 1995.

Kapp, D. A. and Brown, G. S., "A new numerical method for rough surface scattering calculations", *IEEE Trans. Antennas & Propagat.*, vol. 44**,** no 5, pp**.** 711-721, May 1996.

Lentz, R. R., "A numerical study of electromagnetic scattering from ocean-like surfaces", *Radio Science*, 9, 1139-1146, 1974.

Leskova, T. A., Maradudin, A. A., Schegrov, A.V., Mendez E. R., "Numerical generation of a one-dimensional random surface with a prescribed pdf of slopes", *URSI National Radio Science Meeting*, Boulder, CO, p. 174, January 1998.

Longuet-Higgins, M. S., "The effect of non-linearities on statistical distribution in the theory of sea waves", *Journal of Fluid Mechanics*, 17, pp. 459-480, 1963.

Mandel, L. and Wolf, E., *Optical Coherence and Quantum Optics*, Cambridge University Press, N.Y., p. 44, 1995

Marchand, R. T., *Numerical Study on the Validity of the Quasi-Specular and Two-Scale Models for Rough Surface Parameter Estimation: One Dimensional Surfaces,* Ph.D. dissertation, Virginia Polytechnic Institute and State University, Blacksburg, VA, pp. 87-89, 1996.

Marchand, R. T. and Brown G. S. "On the use of finite surfaces in the numerical prediction of rough surface scattering", submitted to *IEEE Trans. Antennas & Propagat.*, 1998.

Middleton, D., *An Introduction to Statistical Communication Theory*, McGraw Hill, New York, 1960.

Morita, N., Kumagi, N. and Mautz, J., *Integral Equation Methods for Electromagnetics*, Artech House, Boston, 1990.

Ngo, H. D., and Rino, C. L., "Application of beam simulation to scattering at low grazing angles. 1. Methodology and validation", *Radio Science*, vol. 29**,** no 6, pp. 1365-1379 1994.

Ogilvy, J. A., *Theory of Wave Scattering from Random Rough Surfaces*, Adam Hilger, N.Y., 1991.

Papoulis, A., *Probability, Random Variables, and Stochastic Processes*, 3rd Edition, McGraw-Hill, Inc., N.Y., 1991.

Pak, K, Tsang, L, Chan, C. H., and Johnson, J., "Backscattering enhancement of electromagnetic waves from two-dimensional perfectly conducting random rough

surfaces based on Monte Carlo simulations", *Journal of the Optical Society of America A*, vol. 12, no. 11, pp. 2491-2499, November 1995.

Rayleigh, Lord, *The Theory of Sound*, 3rd edition, MacMillan, London, 1896.

Thorsos, E., "The validity of the Kirchhoff approximation for rough surface scattering using a Gaussian roughness spectrum", *The Journal of the Acoustical Society of America*, vol. 83, no 1, pp. 78-92, Jan. 1988.

Thorsos, E., "Acoustic scattering from "Pierson-Moskowitz" sea surface", *The Journal of the Acoustical Society of America*, vol. 88, no 1, pp. 335-349, Jul. 1990.

Toporkov, J. V., and Brown, G. S., "Radar Imaging of a Simple Model of Non-Gaussian One–Dimensional Random Surface", *IEEE Antennas and Propagation International Symposium and URSI Radio Science Meeting*, Baltimore, MD, pp. 2171-2174, July 1996.

Toporkov, J. V., Marchand, R. T., and Brown, G. S., "On the discretization of the integral equation describing scattering by rough conducting surfaces", *IEEE Trans. Antennas & Propagat.*, vol. 46**,** no 1, pp. 150-161, January 1998.

Toporkov, J. V., Awadallah, R. S., and Brown, G. S., "Failure of Gaussian-like incident angle field approximation at low grazing angles", submitted to *Journal of the Optical Society of America A*, 1998.

Tran, P., and Elson, J. M., "Banded method of ordered multiple interaction for the scattering of electromagnetic waves from a rough surface", submitted to *Journal of the Optical Society of America A*, 1997.

Tran, P., and Maradudin, A. A., "The scattering of electromagnetic waves from a randomly rough 2D metallic surface", *Optics Communications*, 110, pp. 269-273, 1994.

Van Trees, H., *Detection, Estimation, and Modulation Theory*, John Wiley and Sons, Inc., N.Y., 1968.

Wagner, R. L., Song J., and Chew, W. C., "Monte Carlo simulation of electromagnetic scattering from two-dimensional random rough surfaces", *IEEE Trans. Antennas & Propagat.*, vol. 45**,** no 2, pp. 235-245, February 1997.

Wingham, D. J. and Devayya, R. H., "A note on the use of the Neumann expansion in calculating the scatter from rough surfaces", *IEEE Trans. Antennas & Propagat.*, vol. 40**,** no 5, pp. 560-563, May 1992.

Zinn-Justin, J. *Quantum Field Theory and Critical Phenomena*, Oxford University Press, N.Y., 1989.